Spring 1-1-2015

Non-linear Tidal Interactions and Their Role in Determining the Mean State and Variability of the Ionosphere-Thermosphere (IT) System

McArthur Jones Jr.
University of Colorado Boulder, mcarthur.jonesjr@colorado.edu

Recommended Citation

Jones, McArthur Jr., "Non-linear Tidal Interactions and Their Role in Determining the Mean State and Variability of the Ionosphere-Thermosphere (IT) System" (2015). *Aerospace Engineering Sciences Graduate Theses & Dissertations*. 103.
https://scholar.colorado.edu/asen_gradetds/103

Non-linear Tidal Interactions and Their Role in Determining the Mean State and Variability of the Ionosphere-Thermosphere (IT) System

by

McArthur Jones Jr.

B.S., Millersville University of Pennsylvania, 2010

M.S., University of Colorado, 2013

A thesis submitted to the
Faculty of the Graduate School of the
University of Colorado in partial fulfillment
of the requirements for the degree of
Doctor of Philosophy
Department of Aerospace Engineering Science
2015

This thesis entitled:
Non-linear Tidal Interactions and Their Role in Determining the Mean State and Variability of the Ionosphere-Thermosphere (IT) System
written by McArthur Jones Jr.
has been approved for the Department of Aerospace Engineering Science

Professor Jeffrey M. Forbes

Dr. Maura E. Hagan

Professor Scott E. Palo

Professor Cora E. Randall

Professor Jeffrey P. Thayer

Date ____________

The final copy of this thesis has been examined by the signatories, and we find that both the content and the form meet acceptable presentation standards of scholarly work in the above mentioned discipline.

Jones Jr., McArthur (Ph.D., Aerospace Engineering Sciences)

Non-linear Tidal Interactions and Their Role in Determining the Mean State and Variability of the
Ionosphere-Thermosphere (IT) System

Thesis directed by Professor Jeffrey M. Forbes

Atmospheric tides are vertically-propagating waves generated in the lower and middle atmosphere that are widely known to affect the dynamics and electrodynamics of the ionosphere-thermosphere (IT) system. The tidal spectrum evolves with height due to wave-mean flow, wave-wave, and wave-plasma interactions, leading to the tidal spectrum observed by ground- and space-based observing platforms in the IT. Some of these observations and prior theoretical work suggest that non-linear interactions may produce important effects. However, one can only speculate about how non-linear tidal interactions and their various generation mechanisms might result in mean state, spatial, and temporal variations in the IT system based on prior work. Through numerical experiments performed with the National Center for Atmospheric Research Thermosphere General Circulation Models, this work seeks to quantify and understand how non-linear tidal interactions affect the IT system.

The main results to emerge from this study are as follows: (1) Interaction between the zonally-symmetric solar-driven circulation and the longitude-dependent ionospheric magneto-plasma produce non-migrating atmospheric tides that reconcile existing data-model disparities, mainly under solar maximum conditions; (2) Dissipating tides of lower atmospheric origin act to alter the pressure gradient force via the eddy heat transport causing zonal-mean wind differences of up to 30 m s^{-1} in the dynamo region; (3) Variations of up to 30 K in zonal-mean temperatures of the IT between solar minimum and maximum result from a combination of net eddy heat transport effects and tidal modulation of net nitric oxide cooling; (4) The net transport of atomic oxygen produced by dissipating tides is shown to significantly contribute to atomic oxygen changes in the IT; (5) Measurable solar cycle variations in electron density in the F-region result from tidally driven net changes in the major constituents of the thermosphere. The major computational results from this work will provide additional insight into current and future tidal diagnostics and related non-linear processes observed from a range of ground-based and space-based platforms.

Dedication

To Grace Jones for your love and sacrifice throughout the years. I cannot thank you enough for all the support you have given me in pursuit of this goal. To McArthur Jones III for all the joy that you are currently bringing and are going to bring your mother and I in the future. To McArthur Jones Sr., Shirley Jones, and Rachel Jones for your love, guidance, and support over the years.

Acknowledgements

First and foremost the author would like to thank my co-advisors Dr. Jeffrey M. Forbes and Dr. Maura E. Hagan for all of their mentorship, support, and understanding throughout my five years at the University of Colorado. Without the two of you the work presented herein would not be possible. My hope is that all of my future professional endeavors are worthy of the time and effort you spent advising me over these last five years. Additionally, the author wishes to thank Dr. Astrid Maute and Dr. Arthur Richmond for all their assistance and insight with the TGCMs run at the High Altitude Observatory (HAO); Dr. Xiaoli Zhang for providing the Climatological Tidal Model of the Thermosphere (CTMT), Sounding of the Atmosphere using Broadband Emission Radiometry (SABER) data, and Global Scale Wave Model (GSWM) data, as well as the IDL and FORTRAN coding assistance you provided as part of this study. The author also wishes to acknowledge Dr. Alan Burns, Dr. Stanley C. Solomon, and Dr. Wenbin Wang at the HAO for educational discussions regarding the zonal-mean thermodynamic energy equation and chemistry in the TIE-GCM.

The author also wishes to thank the committee for all the assistance and mentorship throughout my years here at the University of Colorado. Thank you to the Ford Fellowship Foundation, the Significant Opportunities in Atmospheric Research and Science (SOARS), and the Minorities Striving and Pursuing Higher Degrees of Success (MS PHD'S) in Earth System Science Programs for the continued financial and mentoring support, which has made this dissertation possible. Special thanks to Rajul Pandya and Rebecca Haacker-Santos for your kind words of encouragement, continued support, and mentorship. To my fellow graduate students thank you for your support,

assistance, encouragement, and inspiration to become a better scientist, as well as a better person. Finally, thank you Reverend Dr. Stanley E. Adamson for helping me to continue to grow spiritually and completely realizing that through God's love and grace all things are possible.

Contents

Chapter

1 Introduction and Background 1

1.1 Atmospheric Tides in the Ionosphere and Thermosphere 1

1.2 Classical Tidal Theory 5

1.2.1 Mathematical Formulation 5

1.2.2 The Zonally- and Diurnally-Averaged Equations 7

1.2.3 The Perturbation Equations 8

1.2.4 Tidal Nomenclature 11

1.2.5 Limitations of Classical Tidal Theory 12

1.3 Manifestations of Non-Linear Tidal Interactions in Observations and Models 15

1.3.1 Plasma-Neutral Interactions 16

1.3.2 Non-linear Tidal Interaction Effects on the Mean IT 20

1.4 Objective and Science Questions 24

2 Model Descriptions and Methodology 26

2.1 NCAR TGCMs and their Lower Boundary Conditions 26

2.1.1 TIME-GCM 26

2.1.2 TIE-GCM 29

2.2 Validation of the TIE-GCM Solutions Near its Lower Boundary 36

2.3 Zonally- and Diurnally-Averaged Equations in the IT from the NCAR TGCMs . . . 45

2.4 Analysis Methodology 49
  2.4.1 Spectral Analysis 49
  2.4.2 Difference Fields 50

3 Non-migrating Tides in the IT: In situ versus Tropospheric Sources 51
3.1 Introduction and Motivation 51
3.2 TIME-GCM Simulations and Methodology 54
3.3 Hydromagnetic Coupling 57
3.4 Spatial Variability Introduced by a Realistic Magnetic Field 67
3.5 In-Situ Generated Non-migrating Tides at High-Latitudes 72
3.6 Summary of Important Results 75

4 Tidal Impacts on the Mean State and Variability of the IT System: Momentum Equations 78
4.1 Introduction and Motivation 79
4.2 TIE-GCM Simulations and Methodology 81
4.3 Tidal Impacts on the Zonal-Mean Zonal Winds 82
  4.3.1 Interpreting the Zonal Wind Differences, Seasonal and Solar Cycle Variability 87
4.4 Tidal Impacts on the Zonal-Mean Meridional Winds 103
  4.4.1 Interpreting the Meridional Wind Differences, Seasonal and Solar Cycle Variability 107
  4.4.2 Tidal Induced Meridional Wind Effects on h_mF_2 113
4.5 Summary of Important Results 115

5 Tidal Impacts on the Mean State and Variability of the IT System: Thermodynamic Energy Equation 118
5.1 Introduction, Motivation, TIE-GCM Simulations, and Methodology 118
5.2 Tidal Impacts on the Zonal-Mean Temperature 120

5.2.1 Diagnosing the Temperature Differences and associated Seasonal Variability . 123
5.3 Solar Cycle Variability 132
5.4 Summary of Important Results 139

6 Tidal Impacts on the Mean State and Variability of the IT System:
Contiunity Equation and Composition 142
6.1 Introduction, Motivation, TIE-GCM Simulations, and Methodology 143
6.2 The Continuity Equation and Mass Flow Stream Function 144
6.3 Tidal Impacts on the Major Constituents 148
6.4 Tidal-Induced Net Transport Effects on the O Distribution in the Thermosphere . . 155
6.5 Solar Cycle Variations in the Major Constituents of the IT 165
6.6 Solar Cycle Variations in NO 170
6.7 Tidal-Induced Constituent Effects on N_mF_2 and Their Associated Variability 176
6.8 Summary of Important Results 179

7 Conclusions 181
7.1 Summary and Discussion 181
7.2 Recommendations for Future Study 185

Bibliography 187

Appendix

A Glossary of Atmospheric Variables and Symbols 197

B Supplemental Figures: Non-migrating Tides in the IT Study 201

C Supplemental Figures: Tidal Impacts on the Zonal-Mean Winds 215

D Supplemental Figures: Tidal Impacts on the Zonal-Mean Temperatures 233

E Supplemental Figures: Tidal Impacts on the Zonal-Mean Composition 235

Tables

Table

3.1 Hydromagnetic Coupling Momentum Source Terms 63

Figures

Figure

1.1 Meteorological forcing of the Ionosphere-Thersmosphere System 2
1.2 TIME-GCM Differences due to Tides 4
1.3 Monthly Mean September DE3 Zonal Wind Amplitudes from TIDI and GSWM-2002 adapted from Oberheide et al. [89] 13
1.4 Monthly Mean September D0 Zonal Wind Amplitudes from TIDI, GSWM-2002, and TIME-GCM adapted from Oberheide et al. [89] 14
1.5 CHAMP Non-migrating Tides at ∼400 km from Häusler and Lühr [48] 17
1.6 CHAMP and HME D0, DW2, SW3, and SW1 density amplitudes from Oberheide et al. [87] 18
1.7 TIGCM Zonal-Mean Differences due to Observationally-based Migrating Tidal Lower Boundary Conditions from Forbes et al. [31] 22
1.8 Zonal-Mean Zonal Wind Differences due to Non-migrating Tides in the TIME-GCM from Hagan et al. [45] 23

2.1 Observationally-Based TIE-GCM Background Lower Boundary Conditions versus Empirically Modeled TIE-GCM Background Lower Boundary Conditions 33
2.2 Comparison between CTMT and GSWM-02 Tidal Lower Boundary Conditions in the TIE-GCM 37
2.3 Validation of TIE-GCM Solutions Near Its Lower Boundary using Zonal-Mean Zonal Winds, DE3, and SW2 39

2.4 Validation of TIE-GCM Solutions in the Ionosphere using h_mF_2, N_mF_2, and f_oF_2 . . 40

2.5 Background Lower Boundary Conditions from the TIME-GCM, HWM07, NRLM-SISE00, WINDII-HRDI, and SABER during September 42

2.6 TIME-GCM Tidal Lower Boundary Conditions at the TIE-GCM Lower Boundary . 43

2.7 Zonal-Mean Zonal Wind Differences from TIE-GCM Simulations under different Background Wind Conditions 44

3.1 Idealized, Modified, and Realistic TIME-GCM simulations under Varying Solar Cycle Conditions 55

3.2 Idealized Ion Drag Components at Solar Maximum 60

3.3 Modified Ion Drag Components at Solar Maximum 61

3.4 Idealized, Modified, and Realistic Zonal Wind Components at Solar Maximum . . . 62

3.5 Idealized, Modified, and Realistic Zonal Wind Spectra at Solar Maximum 64

3.6 Idealized, Modified, and Realistic Zonal Wind Spectra at Solar Minimum 66

3.7 Zonal Wind Differences between Modified and Idealized Circulations at Solar Maximum 68

3.8 Temperature Differences between Modified and Idealized Circulations at Solar Maximum 69

3.9 Temperature Differences between Modified and Idealized Circulations at Solar Minimum 70

3.10 Zonal-Mean Wind and Temperature Differences between Modified and Idealized Circulations 71

3.11 Zonal Wind Spectra at Northern High Latitudes 73

3.12 Zonal Plasma Drift Spectra at Northern High Latitudes 74

4.1 TIE-GCM Zonal-Mean Zonal Winds at 140 km under Solar Medium Conditions . . 83

4.2 Zonal-Mean Zonal Wind Differences at 115 and 140 km under Solar Medium Conditions 85

4.3 SW2, DE3, and DW1 Zonal Wind Amplitudes at 115 and 140 km under Solar Medium Conditions 86

4.4 Forcing Terms from All Tides TIE-GCM Simulation under March and Solar Medium Conditions . . . 89

4.5 TIE-GCM Forcing Term Differences under March and Solar Medium Conditions . . 93

4.6 TIE-GCM Forcing Term Differences under July and Solar Medium Conditions . . . 96

4.7 TIE-GCM Forcing Term Differences under September and Solar Medium Conditions 97

4.8 Zonal-Mean Zonal Wind Differences during March, July, and September under Solar Medium Conditions . . . 98

4.9 Zonal-Mean Zonal Wind Differences during March, July, and September under Solar Minimum and Solar Maximum Conditions . . . 100

4.10 TIE-GCM Forcing Terms Difference during March under Solar Minimum and Maximum Conditions . . . 102

4.11 TIE-GCM Zonal-Mean Meridional Winds at 140 km under Solar Medium Conditions 104

4.12 Zonal-Mean Meridional Wind Differences at 140 km under Solar Medium Conditions 105

4.13 SW2 and DW1 Meridional Wind Amplitudes at 140 km under Solar Medium Conditions . . . 106

4.14 Forcing Terms from All Tides TIE-GCM Simulation under September and Solar Medium Conditions . . . 108

4.15 TIE-GCM Forcing Term Differences under September and Solar Medium Conditions in the Lower IT . . . 110

4.16 TIE-GCM Forcing Term Differences under September and Solar Medium Conditions in the Upper IT . . . 111

4.17 Zonal-Mean Meridional Wind Differences at 140 km under Solar Minimum and Maximum Conditions . . . 113

4.18 Zonal-Mean h_mF_2, Meridional Wind, and Field-Aligned Plasma Motion Differences under Solar Medium Conditions . . . 114

5.1 TIE-GCM Zonal-Mean Temperature Differences under Solar Medium Conditions . . 121

5.2 SW2 and DW1 Temperature Amplitudes at 130 km Under Solar Medium Conditions 122

5.3 Temperature Equation Forcing Terms from All Tides TIE-GCM Simulation under September and Solar Medium Conditions 125

5.4 Forcing Term and Zonal-Mean Temperature Differences under September and Solar Medium Conditions 127

5.5 Diabatic Heating Term Differences under September and Solar Medium Conditions . 129

5.6 Forcing Term and Zonal-Mean Temperature Differences under July and Solar Medium Conditions 130

5.7 TIE-GCM Diabatic Heating Term Differences under July and Solar Medium Conditions 131

5.8 TIE-GCM Zonal-Mean Temperature Differences under Solar Minimum and Maximum Conditions 133

5.9 SW2 and DW1 Temperature Amplitudes at 130 km Under Solar Minimum and Maximum Conditions 134

5.10 Zonal-Mean Temperature Differences under Solar Minimum and Maximum Conditions in July and September 135

5.11 Forcing Term and Zonal-Mean Temperature Differences under September and Solar Minimum Conditions 136

5.12 Forcing Term and Zonal-Mean Temperature Differences under September and Solar Maximum Conditions 137

5.13 Diabatic Heating Term Differences under September and Solar Minimum and Maximum Conditions 139

6.1 Forcing Terms in the Continuity Equation under September and Solar Medium Conditions 146

6.2 Mass Flow Stream Function under September and Solar Medium Conditions 148

6.3 Percent Changes in IT Constituents under Solar Medium Conditions 149

6.4 Percent Changes in IT Constituents under September and Solar Medium Conditions 150

6.5 Percent Changes in [O] and [O_2] under September and Solar Medium Conditions at 1.25° S . . . 153

6.6 TIME-GCM Percent Changes in [O] under September and Solar Medium Conditions 155

6.7 Time Constants of O Recombination, Transport, Diffusion . . . 157

6.8 Meridional Tidal and Advective O Transport under September and Solar Medium Conditions . . . 160

6.9 Vertical Tidal and Advective O Transport under September and Solar Medium Conditions . . . 160

6.10 Forcing Term Difference Fields from the O Continuity Equation under September and Solar Medium Condtions . . . 162

6.11 Percent Changes in IT Constituents under Solar Minimum and Maximum Conditions 166

6.12 Percent Changes in IT Constituents under September and Solar Minimum and Maximum Conditions . . . 167

6.13 Solar Cycle Variability Associated with Changes in N(^{2}D) and NO during September 172

6.14 Solar Cycle Variability Associated with Changes in the Major Constituents during September . . . 173

6.15 Time Constants of the Different Forcing Terms in the Thermodynamic Energy Equation 174

6.16 Percent Changes in N_mF_2 and Major Constituents at 330 km during September under Solar Medium Condition . . . 177

6.17 Percent Changes in N_mF_2 and Major Constituents at 330 km during September under Solar Minimum and Maximum Conditions . . . 178

B.1 Idealized and Modified Height Integrated Joule Heating in the Northern Hemisphere 201

B.2 Idealized and Modified Height Integrated Joule Heating in the Southern Hemisphere 202

B.3 Idealized Atomic Oxygen and Electron Density at 15 LT . . . 203

B.4 Realistic Ion Drag Components at Solar Maximum . . . 204

B.5 Modified Ion Drag Components at Solar Minimum . . . 205

B.6 Idealized, Modified, and Realistic Zonal Wind Components at Solar Minimum 206
B.7 Zonal Wind Differences between Modified and Idealized Circulations at Solar Minimum 207
B.8 Meridional Wind Differences between Modified and Idealized Circulations at Solar Maximum 208
B.9 Meridional Wind Differences between Modified and Idealized Circulations at Solar Minimum 208
B.10 Zonal Wind Spectra at Southern High Latitudes 209
B.11 Zonal Plasma Drift Spectra at Southern High Latitudes 210
B.12 Zonal Plasma Drift Spectra at Northern High Latitudes and Solar Minimum 211
B.13 Zonal Plasma Drift Spectra at Northern High Latitudes and Solar Minimum 212
B.14 Zonal Wind Spectra at Southern High Latitudes and Solar Minimum 213
B.15 Zonal Plasma Drift Spectra at Southern High Latitudes and Solar Minimum 214

C.1 SW2, DE3, and DW1 Zonal Wind Amplitudes at 115 and 140 km under Solar Medium Conditions without CTMT Tidal Forcing 215
C.2 $f - \overline{\lambda_{yx}}$ during March, July, and September under Solar Medium Conditions 216
C.3 Forcing Terms from No Tides TIE-GCM Simulation under March and Solar Medium Conditions 217
C.4 Forcing Terms from All Tides TIE-GCM Simulation under July and Solar Medium Conditions 218
C.5 Forcing Terms from No Tides TIE-GCM Simulation under July and Solar Medium Conditions 219
C.6 Forcing Terms from All Tides TIE-GCM Simulation under September and Solar Medium Conditions 220
C.7 Forcing Terms from No Tides TIE-GCM Simulation under September and Solar Medium Conditions 221

C.8 SW2, DE3, and DW1 Zonal Wind Amplitudes at 115 and 140 km under Solar Minimum Conditions . . . 222
C.9 SW2, DE3, and DW1 Zonal Wind Amplitudes at 115 and 140 km under Solar Maximum Conditions . . . 223
C.10 TIE-GCM Forcing Term Differences during July under Solar Minimum and Maximum Conditions . . . 224
C.11 TIE-GCM Forcing Term Differences during September under Solar Minimum and Maximum Conditions . . . 225
C.12 SW2 and DW1 Meridional Wind Amplitudes at 140 km under Solar Medium Conditions without CTMT Tidal Forcing . . . 226
C.13 Forcing Terms from No Tides TIE-GCM Simulation under September and Solar Medium Conditions . . . 227
C.14 TIE-GCM Forcing Term Differences under March and Solar Medium Conditions in the Lower IT . . . 228
C.15 TIE-GCM Forcing Term Differences under July and Solar Medium Conditions in the Lower IT . . . 229
C.16 TIE-GCM Forcing Term Differences under March and Solar Medium Conditions in the Upper IT . . . 230
C.17 TIE-GCM Forcing Term Differences under July and Solar Medium Conditions in the Upper IT . . . 230
C.18 SW2 and DW1 Meridional Wind Amplitudes at 140 km under Solar Minimum and Maximum Conditions . . . 231
C.19 Zonal Mean h_mF_2, Meridional Wind, and Field-Aligned Plasma Motion Differences under Solar Minimum and Maximum Conditions . . . 232

D.1 TIE-GCM Temperature Forcing Term Differences under September and Solar Medium Conditions . . . 233

D.2 Diabatic Heating Term Differences under March and Solar Medium Conditions . . . 234

D.3 SW2 and DW1 Temperature Amplitudes at 130 km Under Solar Minimum and Maximum Conditions without CTMT Tidal Forcing 234

E.1 Forcing Terms in the Continuity Equation under July and Solar Medium Conditions 235

E.2 Mass Flow Stream Function under September and Solar Minimum and Maximum Conditions 236

E.3 Percent Changes in IT Constituents under March, July, and Solar Medium Conditions 237

E.4 Percent Changes in IT Constituents at Low Latitudes under September and Solar Medium Conditions 238

E.5 Percent Changes in IT Constituents under July and Solar Minimum and Maximum Conditions 239

E.6 Percent Changes in [O] and [O_2] under September and Solar Minimum Conditions at 1.25° S 240

E.7 Percent Changes in [O] and [O_2] under September and Solar Maximum Conditions at 1.25° S 241

E.8 Percent Changes in IT Constituents at Low Latitudes under September and Solar Minimum and Maximum Conditions 242

E.9 Tidal-Induced Residual Meridional Circulation under September and Solar Medium Conditions 242

Chapter 1

Introduction and Background

This thesis is aimed at understanding and quantifying the role that atmospheric tides play in determining the overall mean state, structure, longitudinal, seasonal, and solar cycle variability of the ionosphere-thermosphere (IT; ca. 100-500 km), with specific attention to the role of non-linear processes. Contrary to linear tidal effects (i.e., single-component propagation and dissipation), non-linear tidal effects on the dynamics, electrodynamics, and composition of the IT are not well understood. By performing numerical experiments with self-consistent Thermospheric General Circulation Models (TGCMs), and considering those results in light of tidal diagnostics from space-based observing platforms, a better understanding can be gained on the effects that non-linear tidal interactions have on the IT. In this chapter, an introduction to atmospheric tides is offered including the equations that govern tidal perturbations in Earth's atmosphere. The conservation equations that govern atmospheric motion, temperature, and compositional structure are reviewed and discussed, a literature review is provided, and the overall objective and science questions are presented.

1.1 Atmospheric Tides in the Ionosphere and Thermosphere

The upper portion of Earth's atmosphere, the thermosphere, extends from approximately 90 to 1000 km, depending upon solar cycle. Embedded within the thermosphere is Earth's ionosphere, which is a weakly ionized plasma containing free electrons and ions. The IT system represents the transition region from Earth's atmosphere to geospace. Furthering our understanding of IT dynamics, electrodynamics, and chemistry is essential to the increased need for more accurate space weather forecasts in support of tracking and monitoring near Earth orbiting satellites and space debris (e.g., Leonard et al., [63]) , as well as predicting ionospheric conditions relevant to communications and navigation systems. Additionally, a better understanding of the underlying physics responsible for changes in the IT, specifically the longitudinal and seasonal variability, will prove useful when preparing for upcoming satellite missions that are focused on studying the IT (e.g. Ionospheric Connection Explorer (ICON) and Global-scale Observations of the Limb and Disk (GOLD)).

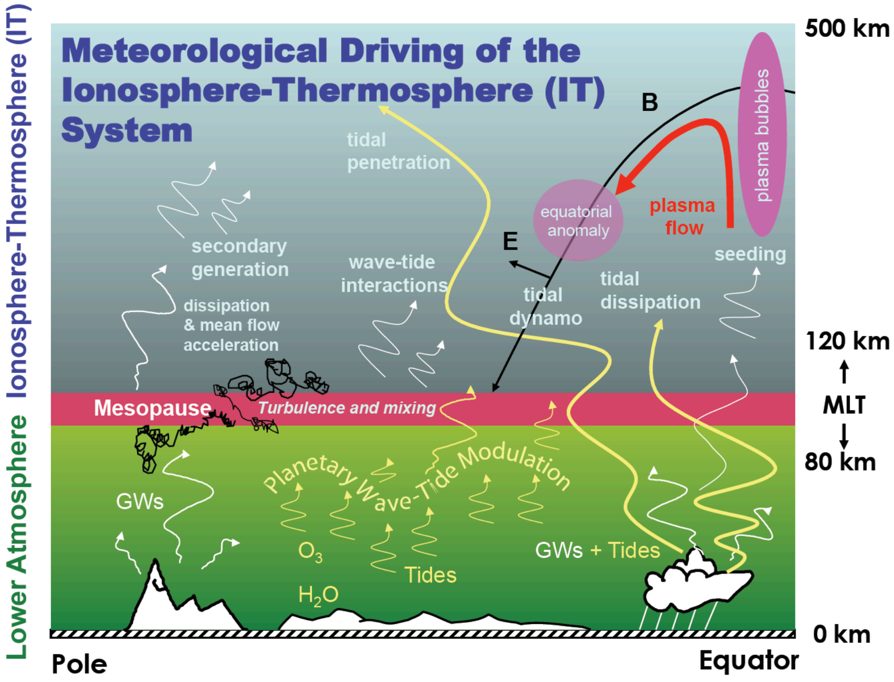

Figure 1.1: Schematic of Meteorological Forcing of the IT System. Figure from National Research Council [9].

Due to the location of the IT in Earth's atmosphere it is subject to regular and repeatable forcing from both above and below. Specifically, Figure 1.1 shows an illustration of the different meteorological influences (i.e., forcing from below) that affect the IT system. A spectrum of different wave components whose origins lie throughout the atmosphere include gravity waves (white graphics in Figure 1.1), planetary or Rossby waves, and atmospheric tides (yellow graphics in Figure 1.1). Gravity waves are small-scale (approximately < 1000 km) dynamical features with periods of minutes to hours that are generated in the troposphere, stratosphere, and mesosphere (green region of Figure 1.1) via flow over topography, convective processes, and shear instabilities. Global-scale oscillations (horizontal wavelengths ranging from 1000s to 10,000 km) with periods longer than a day (i.e., periods of 2 to 20 days) are termed planetary waves. Planetary waves can be generated by longitudinally-dependent heating and flow over topography, or they can be resonant (forced-free) oscillations of the atmosphere. Planetary waves that have zero phase speed are referred to as stationary planetary waves, and do not propagate horizontally. Another major momentum and energy source from the lower atmosphere, and the main focus of this dissertation work, is a special class of internal gravity waves, commonly referred to as atmospheric thermal tides. Atmospheric tides are global scale dynamical perturbations in pressure, wind, temperature, and density that result from the daily cyclic absorption of solar radiation by water vapor (H_2O) in the troposphere and ozone (O_3) in the stratosphere. Thermal tides can also be generated by latent heat release due to raindrop formation in deep tropical convective clouds, as well as the absorption of far ultraviolet (FUV) and extreme ultraviolet (EUV) radiation in the thermosphere by atomic oxygen (O), molecular oxygen (O_2), and molecular nitrogen (N_2). Due to their large horizontal wavelengths (ranging from 1000s to 10,000 km), atmospheric tides are considered inertio-gravity waves, as their propagation characteristics are determined by both buoyancy and Coriolis forces (i.e., inertial forces). Further distinguishing atmospheric thermal tides from gravity and planetary waves are their period, which are subharmonics of a solar day or 24 hours.

Tidal perturbations generated in the lower atmosphere can propagate to higher altitudes, growing in amplitude with height due to the conservation of energy and an exponential decrease in density with altitude. Dissipation of the shorter vertical wavelength (e.g., < 30 km) tidal perturbations is most prevalent within the upper mesosphere and lower thermosphere (MLT, ca. 70-150 km; pink region in Figure 1.1) due to eddy and molecular diffusion, as well as ion drag. Longer vertical wavelength (e.g., > 30 km) tidal perturbations can propagate to higher altitudes into the IT before they are dissipated by molecular diffusion and ion drag. As a result, the dissipation of vertically-propagating atmospheric tides serves as an important mechanism for transporting and depositing energy and momentum from the lower atmosphere into the MLT and IT, driving what is commonly referred to as geomagnetically quiescent "space weather."

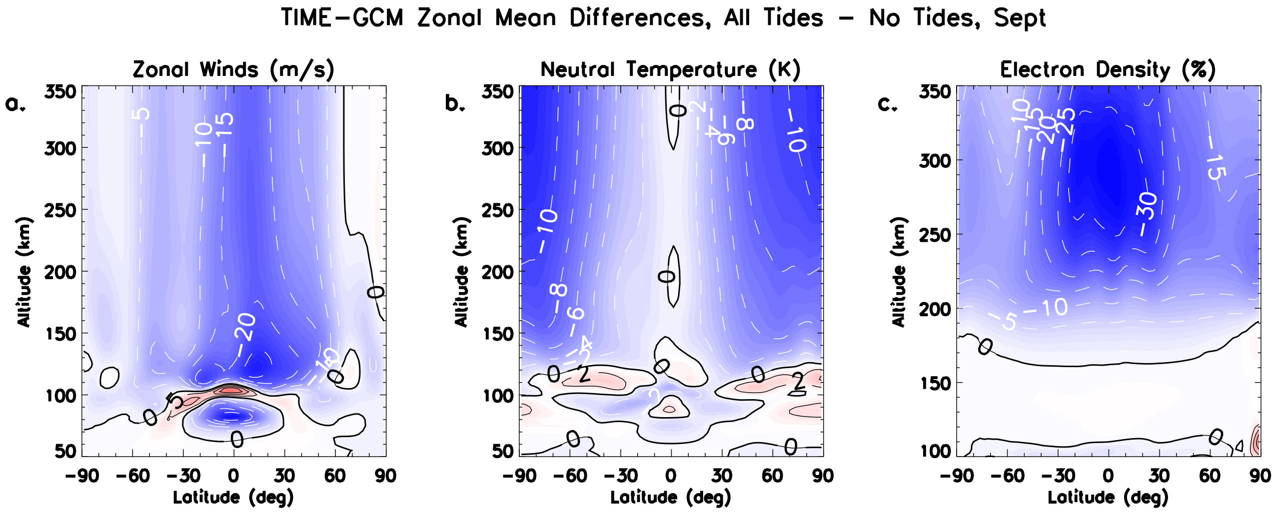

Figure 1.2: September zonally- and diurnally-averaged zonal wind (a), temperature (b), and electron density (c) differences between simulations from the TIME-GCM including and excluding lower boundary tidal forcing for solar minimum conditions.

Figure 1.2 presents a summary result from the National Center for Atmospheric Research (NCAR) Thermosphere-Ionosphere-Mesosphere-Electrodynamics General Circulation Model (TIME-GCM), which shows the differences in the zonal winds, neutral temperatures, and electron densities from simulations that include and exclude atmospheric tides at the model lower boundary (ca. 30 km). Figure 1.2 clearly illustrates that differences in the zonally- and diurnally-averaged zonal winds, temperatures, and electron densities of up to 25 m s^{-1}, 10° K, and 30%, respectively, stem from tidal propagation and dissipation effects at both MLT and IT altitudes in the TIME-GCM. Vertically-propagating tides are also responsible for modulating the E-region wind dynamo processes that affect the plasma in the F-region ionosphere (Sagawa et al., [109]; Immel et al., [56]; Hagan et al., [46]). Additionally, the direct penetration of upward propagating tides into the upper portions of the IT and that originate in the troposphere contribute to the longitudinal, interannual, and solar cycle variability of the IT, especially at low and middle latitudes (Forbes et al., [27];

Oberheide et al., [85]). Consistent with what is depicted in Figure 1.2, Miyahara et al. [79], Forbes et al. [31], Portnyagin et al. [96], and references therein have shown that tidal dissipation alters the zonal-mean dynamics, thermal, and compositional structure of the MLT and IT. Given the effects atmospheric tides have on the IT system, furthering our knowledge on how these waves non-linearly interact with the background IT provides useful insight when interpreting the data collected by near-Earth orbiting satellites including the CHAMP (CHAllenging Minisatellite Payload), COSMIC (Constellation Observing System for Meteorology, Ionosphere, and Climate), GOCE (Gravity field and steady-state Ocean Circulation Explorer), TIMED (Thermosphere Ionosphere Mesosphere Energetics and Dynamics), and UARS (Upper Atmosphere Research Satellite) missions.

1.2 Classical Tidal Theory

Tidal perturbations generated in the troposphere and stratosphere through the absorption of solar radiation by H_2O and O_3 propagate to higher altitudes, grow exponentially with height and dominate the "weather" in the MLT, as well as the IT. Damping of these tidal perturbations is most prevalent within the MLT, where their maximum amplitudes typically occur, although specific tidal components can directly penetrate into the IT and affect the "weather" at higher altitudes.

1.2.1 Mathematical Formulation

The theoretical framework for atmospheric thermal tides is provided in the seminal work of Chapman and Lindzen [5]. Atmospheric tides are linearized solutions to the conservation of momentum, mass, and energy that govern atmospheric motions, along with the ideal gas law. These equations are given in vector form below,

$$\frac{D}{Dt}\mathbf{V} = -2\Omega \times \mathbf{V} - \frac{1}{\rho}\nabla\mathbf{p} + \mathbf{g} + \mathbf{OF_V}, \tag{1.1}$$

$$\rho c_v \frac{DT}{Dt} = RT\frac{D\rho}{Dt} + \rho J + \mathbf{OF}_T, \tag{1.2}$$

$$\frac{\partial\rho}{\partial t} + \nabla\cdot(\rho\mathbf{V}) = 0, \tag{1.3}$$

$$p = \rho RT. \tag{1.4}$$

All of the variables presented in this subsection, subsequent subsections, and other chapters are defined in the Glossary in Appendix A.

In the context of classical tidal theory, we first consider the Navier-Stokes equations (1.1 - 1.4), including the following assumptions and approximations:

(1) The atmosphere is in local thermodynamic equilibrium.

(2) The atmosphere is a perfect gas.

(3) The atmosphere is a geometrically thin layer of fluid compared to the radius of the Earth. This implies that only the vertical component of Earth's rotation vector is considered in the equations below.

(4) The atmosphere (and thus tidal oscillations) is in hydrostatic equilibrium (i.e., vertical accelerations are small).

(5) The Earth's ellipticity and topography are ignored, and that $w = 0$ at the ground.

Invoking the above assumptions and approximations, the equations 1.1 - 1.3 can be rewritten in vector form as:

$$\frac{\partial \mathbf{V_h}}{\partial t} + \mathbf{V} \cdot \nabla \mathbf{V_h} = -\frac{1}{\rho}\nabla_h p - \hat{k} \times f\mathbf{V_h} + \mathbf{OF}_{\mathbf{V_h}}, \tag{1.5}$$

$$\frac{\partial p}{\partial z} = -\rho g, \tag{1.6}$$

$$\rho c_v\Big(\frac{\partial T}{\partial t} + \mathbf{V} \cdot \nabla T\Big) = RT\Big(\frac{\partial \rho}{\partial t} + \mathbf{V} \cdot \nabla \rho\Big) + \rho J + \mathbf{OF}_T \tag{1.7}$$

$$\frac{\partial \rho}{\partial t} + \mathbf{V} \cdot \nabla \rho + \rho \nabla \cdot \mathbf{V} = 0. \tag{1.8}$$

where ∇ represents the full gradient in spherical coordinates, ∇_h is the horizontal gradient in spherical coordinates (i.e., the gradient in the longitude and latitude directions), $\mathbf{V_h}$ is the vector horizontal wind (i.e., u and v), $\hat{z}$ is the unit vector in the vertical direction, and f is the Coriolis frequency (or parameter). The above equations correspond to the horizontal momentum equations, the hydrostatic equation, the thermodynamic energy equation, and the continuity equation, respectively. We must note here that the ideal gas law presented in equation 1.4 remains unchanged.

1.2.2 The Zonally- and Diurnally-Averaged Equations

Following the classical tidal theory derivation, we arrive at the zonally- and diurnally-averaged (hereafter "zonal mean") equations by making some additional assumptions including:

(6) The atmosphere is inviscid (i.e., we neglect all forms of dissipation).

(7) Tidal fields are linearizable perturbations about some zonally-averaged basic (or mean) state.

(8) The basic (mean) state fields are in steady state. Given (7) and (8) the dependent atmospheric field variables (e.g., zonal, meridional, and vertical winds, temperature, pressure, density, and diabatic heating) take the following form:

$$\begin{bmatrix} u(\lambda,\theta,z,t) \\ v(\lambda,\theta,z,t) \\ w(\lambda,\theta,z,t) \\ T(\lambda,\theta,z,t) \\ p(\lambda,\theta,z,t) \\ \rho(\lambda,\theta,z,t) \\ J(\lambda,\theta,z,t) \end{bmatrix} = \begin{bmatrix} \overline{u}(\theta,z) + u'(\lambda,\theta,z,t) \\ \overline{v}(\theta,z) + v'(\lambda,\theta,z,t) \\ \overline{w}(\theta,z) + w'(\lambda,\theta,z,t) \\ T_0(\theta,z) + T'(\lambda,\theta,z,t) \\ p_0(\theta,z) + p'(\lambda,\theta,z,t) \\ \rho_0(\theta,z) + \rho'(\lambda,\theta,z,t) \\ \overline{J}(\theta,z) + J'(\lambda,\theta,z,t) \end{bmatrix} \tag{1.9}$$

where the barred quantities represent the zonal-mean background atmospheric conditions and the primed quantities represent the tidal perturbations.

(9) Perturbation quantities are small such that the products of any perturbation quantities are neglected (e.g., $u'\overline{v}$ or $u'v' = 0$). This implies that the mean fields must exactly satisfy the Navier-Stokes equations.

Applying (6) - (9) to equations 1.5 - 1.8, and writing the conservation laws in component form yields:

$$\frac{\overline{v}}{a}\frac{\partial \overline{u}}{\partial \theta} + \overline{w}\frac{\partial \overline{u}}{\partial z} - f\overline{v} - \frac{\overline{u}\,\overline{v}\tan\theta}{a} + \frac{\overline{u}\,\overline{w}}{a} = 0, \tag{1.10}$$

$$\frac{\overline{v}}{a}\frac{\partial \overline{v}}{\partial \theta} + \overline{w}\frac{\partial \overline{v}}{\partial z} + f\overline{u} + \frac{\overline{u}^2 \tan\theta}{a} + \frac{\overline{v}\,\overline{w}}{a} = -\frac{1}{a}\frac{\partial p_0}{\partial \theta}, \tag{1.11}$$

$$\rho_0 c_v\Big(\frac{\overline{v}}{a}\frac{\partial T_0}{\partial \theta} + \overline{w}\frac{\partial T_0}{\partial z}\Big) = RT_0\Big(\frac{\overline{v}}{a}\frac{\partial \rho_0}{\partial \theta} + \overline{w}\frac{\partial \rho_0}{\partial z}\Big) + \rho_0\overline{J} \tag{1.12}$$

$$\frac{\overline{v}}{a}\frac{\partial \rho_0}{\partial \theta} + \overline{w}\frac{\partial \rho_0}{\partial z} + \rho_0\Big(\frac{1}{a}\frac{\partial \overline{v}}{\partial \theta} + \frac{\partial \overline{w}}{\partial z}\Big) = 0. \tag{1.13}$$

Equations 1.10, 1.11, 1.12, and 1.13 are the zonal-mean zonal momentum equation, zonal-mean meridional momentum equation, zonal-mean thermodynamic energy equation, zonal-mean continuity equation, the zonal-mean hydrostatic equation is given by $\frac{\partial p_0}{\partial z} = \rho_0 g$, and the zonal-mean ideal gas law is given by $p_0 = \rho_0 R T_0$.

1.2.3 The Perturbation Equations

Recall that any field can be written as a linear superposition of that fields' zonal mean and a perturbation about that zonal mean. By subtracting the zonal-mean equations (i.e., equations 1.10 - 1.13) from the full conservation equations (i.e., equations 1.5, 1.7, and 1.8), neglecting dissipative effects and defining the basic state such that:

(10) The zonal-mean winds are set to zero (i.e., $\overline{u} = \overline{v} = \overline{w} = 0$). This implies that the basic state density (ρ_0), pressure (p_0), and temperature (T_0) are independent of longitude and latitude. This also implies that p_0 at the ground and the vertical profile of T_0 is specified (i.e., p_0 changes in altitude following the barometric law and ρ_0 is calculated via the ideal gas law $\rho_0 = \frac{p_0}{RT_0}$).

Applying (10) to the zonal-mean equations (equations 1.10-1.13) and then subtracting these from the full conservation equations (equations 1.5-1.8) allows one to arrive at the perturbation equations in component form in log-pressure and spherical coordinates after Chapman and Lindzen [5]:

$$\frac{\partial u'}{\partial t} - 2\Omega v' \sin\theta + \frac{1}{a\cos\theta}\frac{\partial p'}{\partial \lambda} = 0, \tag{1.14}$$

$$\frac{\partial v'}{\partial t} + 2\Omega u' \sin\theta + \frac{1}{a}\frac{\partial p'}{\partial \theta} = 0, \tag{1.15}$$

$$c_v\Big(\frac{\partial T'}{\partial t} + w'\frac{dT_0}{dz}\Big) = \Big(\frac{RT_0}{\rho_0}\Big)\Big(\frac{\partial \rho'}{\partial t} + w'\frac{d\rho_0}{dz}\Big) + J' \tag{1.16}$$

$$\frac{\partial \rho'}{\partial t} + w'\frac{d\rho_0}{dz} + \rho_0\Big(\frac{1}{a\cos\theta}\frac{\partial u'}{\partial \lambda} + \frac{1}{a\cos\theta}\frac{\partial v'}{\partial \theta} + \frac{\partial w'}{\partial z}\Big) = 0. \tag{1.17}$$

Equations 1.14 and 1.15 are the perturbation zonal and meridional momentum equations, 1.16 is the perturbation thermodynamic energy equation, and 1.17 is the perturbation continuity equation, $\frac{\partial p'}{\partial z} = \rho' g$ is the perturbation hydrostatic equation, and $\frac{p'}{p_0} = \frac{\rho'}{\rho_0} + \frac{T'}{T_0}$ is the perturbation ideal gas law, from which the specifics of atmospheric tides are derived.

Tidal perturbations result from the daily cyclic absorption of solar radiation throughout Earth's atmosphere (represented by J' in equation 1.16) and thus have periods that are subharmonics of solar day. Atmospheric tides propagate through the background atmosphere and have oscillations that vary in longitude and time. A specific tidal component is one that has a distinct zonal wavenumber (s) and associated frequency ($\sigma = m\Omega$, expressed as a multiple of Earth's rotation rate), which describes its oscillatory nature in longitude and time. Further, each perturbation field can be written as a superposition of all the tidal components present in Earth's atmosphere. Applying the previous two statements to 1.9 yields

$$\begin{bmatrix} u'(\lambda,\theta,z,t) \\ v'(\lambda,\theta,z,t) \\ w'(\lambda,\theta,z,t) \\ T'(\lambda,y,z,t) \\ p'(\lambda,y,z,t) \\ \rho'(\lambda,y,z,t) \end{bmatrix} = \sum_{\sigma}\sum_{s} \begin{bmatrix} \hat{u}(\theta,z) \\ \hat{v}(\theta,z) \\ \hat{w}(\theta,z) \\ \hat{T}(\theta,z) \\ \hat{\rho}(\theta,z) \\ \hat{p}(\theta,z) \end{bmatrix} e^{i(\sigma t + s\lambda)}. \tag{1.18}$$

By plugging in $\hat{u}$ and $\hat{v}$ from 1.18 above, into equations 1.14 and 1.15 it is possible to reduce equations 1.14-1.17, the perturbation hydrostatic equation, and the perturbation ideal gas law down to one second order partial differential equation. Recognizing that J', is not only periodic in longitude and time, but also in latitude and altitude, allows one to decompose J' (or for that matter the solar heating) into a complete set of mutually orthogonal modes, each of which is a product of a latitude varying function, and an altitude varying function. A mode for a specific wave component is described by a zonal wavenumber (s) and meridional index (n) pair (s,n). The latitude varying function is written as $\Theta_n^{\sigma,s}(\theta)$, and the altitude varying function is written as $J_n^{\sigma,s}(z)$. Specifically, each mode is called a "Hough" mode because each one of the latitudinal functions ($\Theta_n^{\sigma,s}(\theta)$), is a Hough function, which represent the eigenfunctions of Laplace's tidal equation. Each Hough modes' contribution to the complete tidal structure is determined by the superposition of the solar heating projection onto the particular Hough model of interest:

$$J'(\lambda,\theta,z,t)=\sum_{\sigma}\sum_{s}\sum_{n}\Theta_n^{\sigma,s}(\theta)J_n^{\sigma,s}(z)e^{i(\sigma t+s\lambda)}. \tag{1.19}$$

Using equation 1.19 in the linearized thermodynamic energy equation (1.16), one can see that projection of the solar heating amplitude onto mutually orthogonal modes would cause an analogous projection onto the other perturbed fields that can also be decomposed as follows:

$$\left.\begin{aligned}\hat{u}(\theta,z)&=\sum_n U_n^{\sigma,s}(\theta)u_n^{\sigma,s}(L_n^{\sigma,s}(z))\\ \hat{v}(\theta,z)&=\sum_n V_n^{\sigma,s}(\theta)v_n^{\sigma,s}(L_n^{\sigma,s}(z))\\ \hat{w}(\theta,z)&=\sum_n \Theta_n^{\sigma,s}(\theta)w_n^{\sigma,s}(L_n^{\sigma,s}(z))\\ \hat{T}(\theta,z)&=\sum_n \Theta_n^{\sigma,s}(\theta)T_n^{\sigma,s}(L_n^{\sigma,s}(z))\\ \hat{p}(\theta,z)&=\sum_n \Theta_n^{\sigma,s}(\theta)p_n^{\sigma,s}(L_n^{\sigma,s}(z))\\ \hat{\rho}(\theta,z)&=\sum_n \Theta_n^{\sigma,s}(\theta)\rho_n^{\sigma,s}(L_n^{\sigma,s}(z))\end{aligned}\right., \tag{1.20}$$

where the Hough functions are related to the latitudinal structures of the horizontal wind fields via the wind expansion functions $U_n^{\sigma,s}$ and $V_n^{\sigma,s}$:

$$\begin{aligned}U_n^{\sigma,s}(\theta)=&\ \frac{1}{(f_\Theta^2-\sin^2\theta)}\left[\frac{\sin\theta}{f_\Theta}\frac{d}{d\theta}+\frac{s}{\cos\theta}\right]\Theta_n^{\sigma,s}(\theta)\\ V_n^{\sigma,s}(\theta)=&\ \frac{1}{(f_\Theta^2-\sin^2\theta)}\left[\frac{d}{d\theta}+\frac{s\tan\theta}{f_\Theta}\right]\Theta_n^{\sigma,s}(\theta)\end{aligned}, \tag{1.21}$$

where $f_\Theta\equiv\frac{\sigma}{2\Omega}$. The vertical structure of each Hough mode is determined by its solution to the vertical structure equation (L_n). Specifically, the vertical structure equation describes whether or not a specific Hough mode is free to propagate vertically away from its source region or remains trapped (evanescent) close to its source region.

In summary, Laplace's tidal equation and the vertical structure equation provide a means to solve for the Hough functions ($\Theta_n^{\sigma,s}(\theta)$) for a tidal component of interest. Then for each Hough mode, one can solve for its vertical structure (L_n), assuming the vertical profile of solar heating is known. The vertical structure (L_n) specific to the Hough mode of interest can then be used in equations 1.20 and 1.21 to solve for the complex amplitudes of the tides present in Earth's atmosphere, the sum of which represents the total perturbation relative to the zonal mean. A more rigorous mathematical derivation and in-depth discussion regarding the specifics and solutions of Laplace's tidal and the vertical structure equations are offered in Chapman and Lindzen [5], Forbes [25], and Palo [90].

1.2.4 Tidal Nomenclature

The tidal nomenclature to be used throughout the remainder of this study is facilitated by rewriting the complex form of 1.18 using Euler's Formula and taking only the real part

$$A_{\sigma,s}(\theta,z)\cos(\sigma t + s\lambda - \phi_{\sigma,s}(\theta,z)), \tag{1.22}$$

which is the typical form of a tidal perturbation shown in most publications today, where t = time in UT, $\sigma = m\Omega$, Ω = rotation rate of the Earth ($\frac{2\pi}{24}$ hr^{-1}), λ = longitude, m (= 1,2,3,...) is the subharmonic of a solar day, s (=...-3,-2,...0,1,2...) is the zonal wavenumber, $\phi_{\sigma,s}$ is the phase as a function of latitude and altitude, and $A_{\sigma,s}$ is the amplitude as function of latitude and altitude. Writing out σ as $m\Omega$ and considering a constant local-time reference frame (i.e., the reference frame from a sun-synchronous satellite), expression 1.22 becomes

$$A_{m,s}(\theta,z)\cos(m\Omega t_{LT} + (s-m)\lambda - \phi_{m,s}(\theta,z)), \tag{1.23}$$

where t_{LT} is local time, since $t_{LT} = t + \frac{\lambda}{\Omega}$. The positive integer m = 1, 2, 3 ... corresponds to oscillation periods of 24 h, 12 h, ... and are referred to as diurnal and semidiurnal, respectively. In this context, $s > 0$ ($s < 0$) components correspond to westward (eastward) propagating tides. The phase is defined as the time of maximum at zero degrees longitude (i.e., the local time of maximum at Greenwich). When $s = m$ in 1.23 there is no longitude variability at a fixed local time and latitude; these tides are said to be migrating (i.e., sun-synchronous) because their phase speeds relative to a ground-based observer are all equal to the rotation rate of the Earth, $-\Omega$. When $s \neq m$ and local time is fixed, a given tide with a frequency $m\Omega$ and zonal wavenumber s has a longitudinal variation of $|s-m|$ (i.e., $|s-m|$ maxima and minima observed in longitude). These waves have zonal phase speeds (C_{ph}) equal to $\frac{-m\Omega}{s}$ and are referred to as non-migrating tides because they do not migrate with the Sun from the perspective of a ground-based observer. Henceforth, the notation DWs (SWs) or DEs (SEs) is used to signify westward or eastward propagating diurnal (semidiurnal) tides, respectively, with zonal wavenumber s. Standing oscillations (i.e., $s = 0$) are denoted as D0 and S0. Waves with $m = 0$ are stationary planetary waves (SPW), and with zonal wavenumber s are denoted as SPWs.

1.2.5 Limitations of Classical Tidal Theory

In order to derive the perturbation equations (1.14 - 1.17) used to arrive at Laplace's tidal equation and the vertical structure equation, which describe tidal oscillations in Earth's atmosphere, we made a number of assumptions, as outlined in the previous subsections. Some of the assumptions listed above are inappropriate given that the atmosphere is not windless, isothermal, or dissipationless. For instance, differential heating between the equator and the poles drives a meridional temperature gradient, which leads to large scale pressure gradients responsible for driving the general circulation (i.e., winds) of Earth's atmosphere. A number of dissipation processes including eddy and molecular diffusion, and ion drag play a major role in determining the circulation of Earth's atmosphere, especially in the mesosphere and IT. It is also assumed that the perturbations (i.e., tidal or planetary wave perturbations) are small, such that non-linear tide-tide (via the perturbation equations) and non-linear tide-mean flow (via the zonal-mean equations) interactions are neglected. It is not surprising that discrepancies between tidal observations and classical tidal theory predictions exist given the above assumptions.

Subsequently, linear tidal theory was then developed which extends the classical tidal framework to include non-zero mean winds, meridional temperature gradients, and dissipation. Inclusion of mean winds, temperature gradients, and dissipation render the perturbation equations (1.14 -

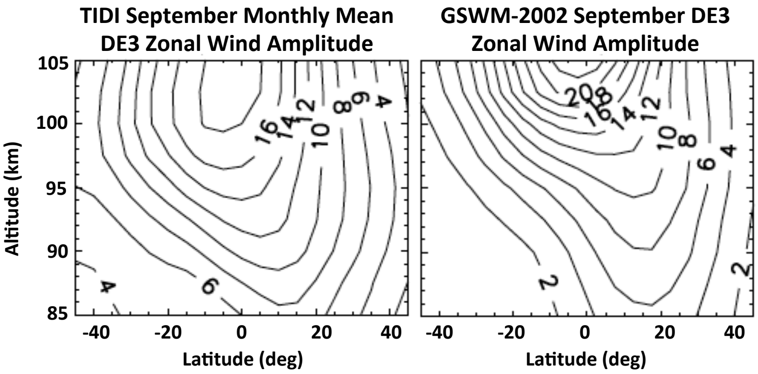

Figure 1.3: Monthly mean September DE3 zonal wind amplitude from the TIDI instrument (left) and the GSWM-2002 (right) at low and middle latitudes in the lower thermosphere. Figure adapted from Oberheide et al. [89].

1.17) inseparable in latitude and altitude; thus linearized tidal solutions must be solved for numerically. In the past a great deal of research has been conducted to understand the effects that mean winds, meridional temperature gradients, and dissipative forces have on tidal propagation and dissipation characteristics in Earth's atmosphere. Specifically, Lindzen and Hong [68], Forbes and Garrett [28], Forbes [23];[24], Vial [121], Forbes and Hagan [30], Forbes and Vincent [33], Forbes [25], Ekanayake et al. [16], McLandress [74], and references therein all investigate the effects that non-zero background winds, meridional temperature gradients, and/or realistic dissipation have on altering the classical tidal structures and comment on their numerical results in light of tidal observations. Linear tidal theory replicates the tidal structures quite well in situations where non-linear process (i.e., tide-mean flow, tide-tide, and tide-planetary wave interactions) are unimportant. For example, Figure 1.3 shows results presented in Oberheide et al. [89] of the monthly mean September DE3 zonal wind amplitude as a function of latitude and altitude measured by the TIMED Doppler Interferometer (TIDI) instrument and calculated from the Global Scale Wave Model version 2002 (GSWM-2002 or GSWM-02; model version described in Hagan and Forbes [42], [43], and references therein). The GSWM is a two-dimensional, steady-steady state tidal model that solves the linearized tidal equations including mean winds, meridional temperature gradients, and dissipation

(Hagan et al., [44], [41]; Hagan, [40]). Therefore, Figure 1.3 clearly illustrates that linear tidal models compare well to observations when non-linear interactions are unimportant.

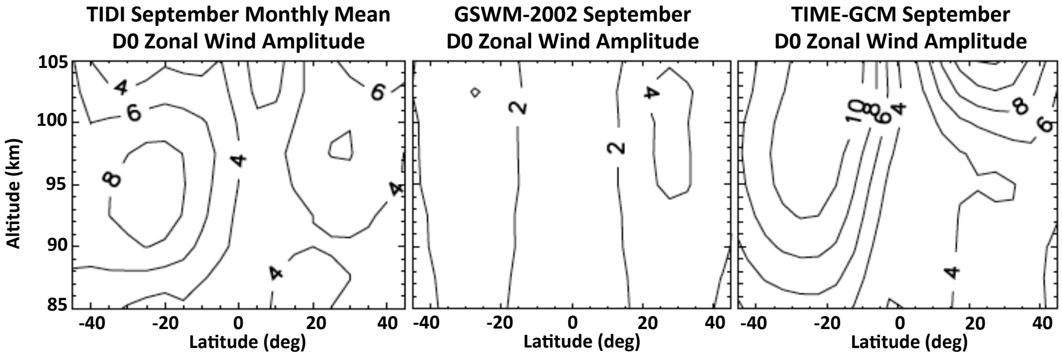

Figure 1.4: Monthly mean September D0 zonal wind amplitude from the TIDI instrument (left), the GSWM-2002 (middle), and the TIME-GCM (right) at low and middle latitudes in the lower thermosphere. Figure adapted from Oberheide et al. [89].

However, linear tidal theory is unable to reproduce measured tidal structures in the IT when non-linear interactions are important. Evidence to support the previous statement is provided by Figure 1.4, which depicts the monthly mean September D0 zonal wind amplitude reported on by Oberheide et al. [89] from the TIDI (left), GSWM-2002 (middle), and TIME-GCM (right). The lower boundary forcing at ~30 km of the D0 in the TIME-GCM results depicted in Figure 1.4 is from the GSWM-2002. In Figure 1.4, the GSWM-2002 does not reproduce the latitudinal and vertical structure of the D0 very well, whereas the D0 computed in the TIME-GCM does compare favorably to observations. This implies that the D0 zonal wind amplitude measured by TIDI in the lower thermosphere results from the superposition of the radiatively forced component in the lower atmosphere, and a non-linear component generated via a DW1-SPW1 interaction in the lower atmosphere or in-situ within the MLT. Figure 1.4 shows that the TIME-GCM provides a much better estimate of the D0 than that of the estimate from GSWM-2002 because it solves the full conservation equations (i.e., 1.1 - 1.4), which account for non-linear tidal interactions. Hence, one can conclude that in order to understand and interpret the processes and mechanisms responsible for producing the tidal spectrum in the IT a numerical model that solves the full conservation equations, including non-linear tidal interactions is required.

Over the years, considerably less attention has been paid to the effects that non-linear tidal interactions have on altering the classical tidal structure(s), and ultimately the role that non-linear tidal interactions play in determining the complete tidal spectrum and resulting mean state of the IT system observed by ground- or space-based instruments. But, there have been some studies that consider these non-linear tidal interactions, and these will be discussed in the subsequent section.

1.3 Manifestations of Non-Linear Tidal Interactions in Observations and Models

Non-linear terms in the conservation equations arise from the advective terms that result from the material derivatives in the Navier-Stokes equations shown in 1.1 - 1.3, as well as the ion drag terms in the conservation equations, which are discussed in Chapter 2. The product of two primed (perturbation) quantities represent the non-linear interaction of one tidal perturbation with another tidal perturbation (e.g. the eddy momentum and eddy heat source terms, as well as the ion drag terms that include the product of two perturbation quantities), which serves as an energy transfer mechanism between what is typically termed primary (i.e., two initial tidal or planetary wave oscillations) and secondary (the resulting two tidal or planetary oscillations) waves (Teitelbaum and Vial, [120]). For example, the interaction between two primary waves with frequencies (σ_1,σ_2) and zonal wavenumbers (s_1,s_2), results in the linear sum of two secondary waves:

$$cos(\sigma_1 t + s_1\lambda)cos(\sigma_2 t + s_2\lambda) = \frac{cos\Big((\sigma_1+\sigma_2)t + (s_1+s_2)\lambda\Big) + cos\Big((\sigma_1-\sigma_2)t + (s_1-s_2)\lambda\Big)}{2}. \tag{1.24}$$

one of which has a “summed” frequency, wavenumber pair ($\sigma_1+\sigma_2$,s_1+s_2) and another which has a “difference” frequency, wavenumber pair ($\sigma_1-\sigma_2$,s_1-s_2). It must also be noted that for perturbations undergoing dissipation, the zonal and diurnal average of two primed quantities represents energy and momentum being deposited into the zonal-mean IT system from the perturbations (tides).

1.3.1 Plasma-Neutral Interactions

As previously stated in Section 1.1, Earth's thermosphere is embedded within Earth's ionosphere, and so the motion of neutral particles in Earth's upper atmosphere are affected by the presence of charged particles and vice versa. In fact, Earth's magnetic field adds another layer of complexity to the neutral motion at IT altitudes, as charged particle motions are strongly influenced (i.e., through the Lorentz force) by the spatially varying geomagnetic field which is offset from Earth's rotation axis. Because of Earth's spatially varying magnetic field, the distribution of charged particles is anisotropic. At F-region altitudes (i.e., >150 km) ion drag (i.e., a "frictional" force by which neutral particles that are forced to move across magnetic field lines experience a momentum loss via collisions with charged particles) is one of the dominate drivers of neutral gas motion. In addition to ion drag, plasma drift motions (i.e., $\mathbf{E} \times \mathbf{B}$) can drive neutral motions through collisions at F-region altitudes. Richmond [100] showed that the ion drag term affects tidal motions propagating upward into the IT system by reducing the rate of exponential wave growth. A modeling study performed by Dickinson and Roble [13] showed that accelerations (decelerations) in neutral zonal wind speeds occur as incident zonal winds flow through regions of low (high) ionization levels relative to the global mean. Roble and Dickinson [105] used a three-dimensional semi-empirical model to show that small zonal wind differences (i.e., only a few m s^{-1}) occur when the geomagnetic poles are offset versus aligned from the geographic poles.

The historical works by Richmond [100], Roble and Dickinson [105], and Dickinson and Roble [13] clearly show that ion drag can affect the propagation and dissipation of atmospheric tides, as well as the modeled and observed tidal spectrum via variations in the neutral wind circulation within the IT. Dickinson et al. [10]; [11] where the first to show that momentum source terms in the zonal-mean momentum equations (i.e., only a longitudinal mean) arose from non-linear interactions in the ion drag terms. Dickinson et al. [10] defines the momentum source terms (M_x and M_y) as correlations of the diurnal zonal and meridional winds (u' and v'), with the departures of ion drag (λ'_{xx} and λ'_{yy}) from their zonal mean values, where $M_x = -\overline{u'\lambda'_{xx}}$ and $M_y = -\overline{v'\lambda'_{yy}}$. Using the neutral thermosphere from the three-dimensional semi-empirical model described by Roble and Dickinson [105] assuming a centered aligned dipole geomagnetic field, pressure gradients derived from the Jacchia [57] and Hedin et al. [51] empirical models, and global ion drag coefficients from the empirical model of Ching and Chiu [6], Dickinson et al. [10] (Dickinson et al. [11]) found that these momentum source terms ranged from -0.6 to 0.8 cm s^{-2} (-1.2 and 1.6 cm s^{-2}) at low and middle latitudes between 300 and 400 km under equinox (solstice), near solar maximum, and geomagnetically quite conditions. The M_x and M_y forcing calculated by Dickinson et al. [10] (Dickinson et al. [11]) leads to perturbations of the zonal-mean winds and temperatures on the order of 10 m s^{-1} (50 m s^{-1}) 40° K (50° K) between 300 and 400 km during equinox (solstice).

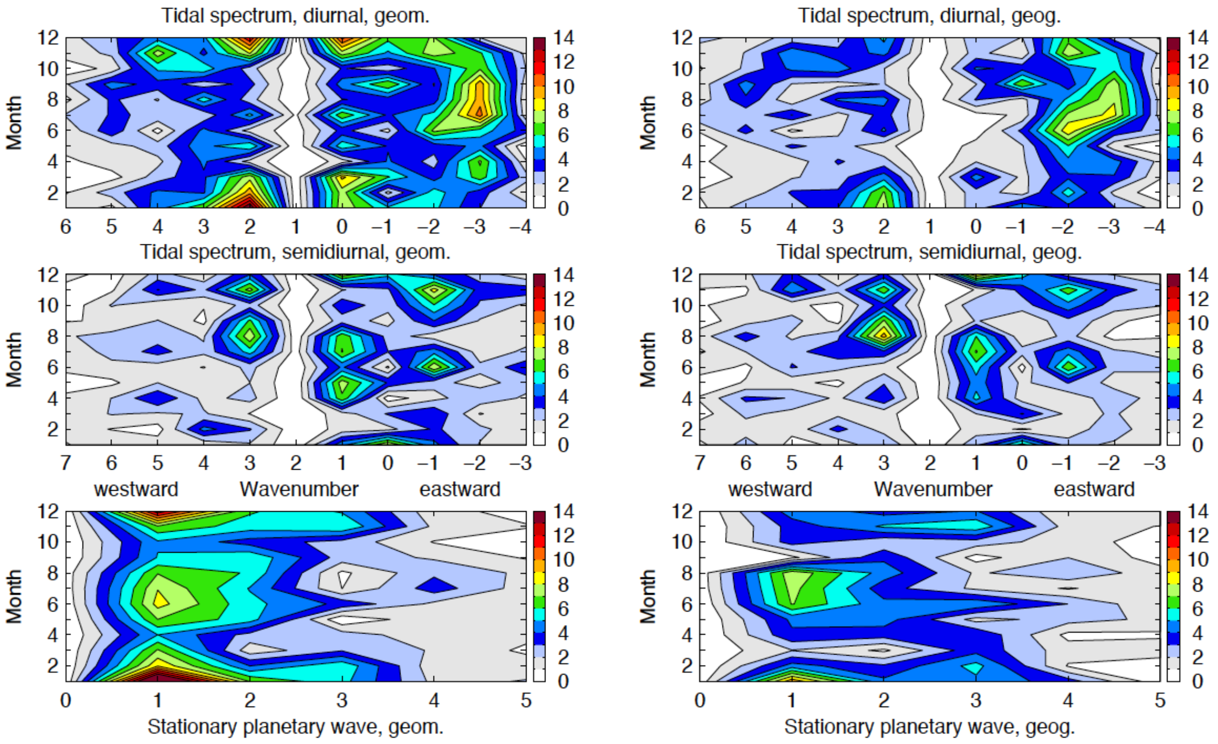

Figure 1.5: Diurnal (top), semidiurnal (middle), and stationary planetary wave (bottom) zonal wind amplitudes along the geomagnetic equator (left column) and geographic equator (right column). Figure from Häusler and Lühr [48].

The seminal work of Forbes and Garrett [28] was the first to discuss the generation of migrating tides via non-linear plasma-neutral interactions. Forbes and Garrett [28] showed mathematically that migrating tides could be generated in the IT by linearizing the hydromagnetic terms (i.e., ion drag terms) utilized in their eighth-order model equations including dissipation. More recently, Häusler and Lühr [48] derived tidal and stationary planetary wave amplitudes in the zonal wind field from the CHAMP satellite spanning data collected from 2002–2005 at ∼400 km (Figure 1.5). They concluded that the D0, DW2, SW3, and SW1 shown in Figure 1.5 all contribute to the longitudinal variability observed along the geomagnetic equator, however they were unsure of the mechanism responsible for generating these non-migrating tides. Using densities measured from CHAMP and Gravity Recovery and Climate Experiment (GRACE), Forbes et al. [27] found considerable (i.e., ±25° K at low latitudes) longitudinal variability in exospheric temperatures. Forbes et al. [27] suggested that the tidal components responsible for the observed longitudinal variability could have been influenced by a longitude-dependent ion drag term, similar to the hydromagnetic coupling process outlined in Forbes and Garrett [28].

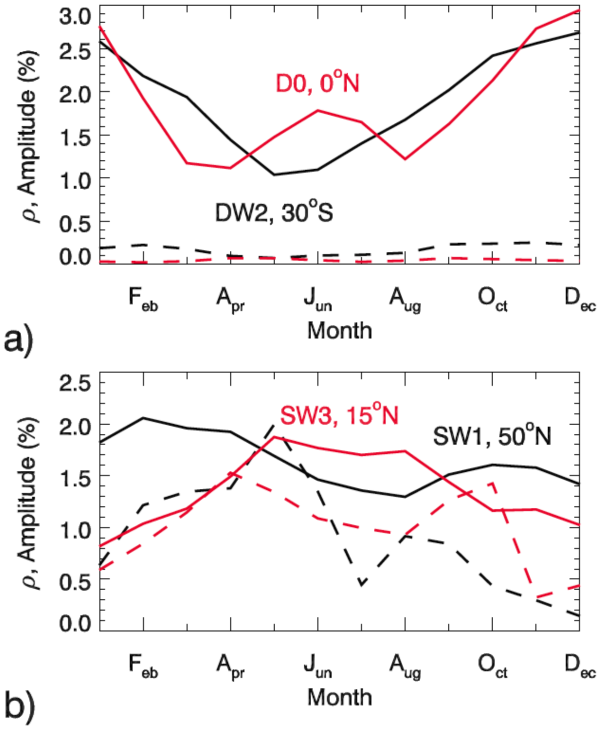

Figure 1.6: D0 (red) and DW2 (black) density amplitudes from CHAMP (solid line) and HME (dashed line) at 390 km at the equator and 30° S, respectively (a). Same as Figure 1.6a except for SW3 (red) and SW1 (black) at 15° N and 50° N, respectively (b). Figure from Oberheide et al. [87].

Oberheide et al. [87] found large D0 and DW2 density perturbations in the CHAMP measurements at 390 km, but not in their Climatological Tidal Model of the Thermosphere (CTMT), which is based on Hough Mode Extension (HME, see Lindzen et al., [69]; Forbes and Hagan, [29]) fits to TIDI and Sounding of the Atmosphere using Broadband Emission Radiometry (SABER) data in the MLT (Figure 1.6). Figure 1.6 also reveals noticeable differences in the annual structure of the SW3 and SW1 between the CHAMP measurements and CTMT at 390 km. Since the HME fitting can only account for tidal sources below the fit altitude (i.e., only for lower atmospheric sources in the CTMT), Oberheide et al. [87] suggested that the non-migrating tidal perturbations shown by the solid lines in Figure 1.6 are generated in-situ in the upper thermosphere via non-linear interactions. Specifically, they state the D0 and DW2 could be generated via a non-linear interaction between the in-situ generated DW1 (via EUV solar radiation absorption) and the SPW1 resulting from the offset between the geographic and geomagnetic fields (driven by plasma-neutral interactions). Forbes et al. [35] illustrated longitudinal variability introduced by non-migrating tides using density measurements from the Satellite Electrostatic Triaxial Accelerometer (SETA), CHAMP, and GRACE satellites. Forbes et al. [35] found a two-peaked longitudinal structure at high-latitudes and compared their results with results from the CTMT, and found that the CTMT was incapable replicating the observed longitudinal variability. Similar to Forbes et al. [27] and Oberheide et al. [87], Forbes et al. [35] proposed that a plasma-neutral interaction due to the offset between the geographic and geomagnetic fields was responsible for the in-situ generation non-migrating tides. However, all the works listed above (i.e., Häusler and Lühr, [48]; Forbes et al., [27]; Oberheide et al., [87]; Forbes et al., [35]) state that numerical experiments are required in order validate their proposed mechanisms of in-situ tidal generation in the upper thermosphere, and to determine if these in-situ generated tides affect the zonal-mean state and variability of the IT system.

1.3.2 Non-linear Tidal Interaction Effects on the Mean IT

Energy and momentum transport by wave motions serve as important drivers for the dynamics, electrodynamics, and chemistry responsible for determining the circulation, composition, and overall structure of planetary atmospheres (Forbes, [26]). As reviewed in Section 1.1 atmospheric tides excited in Earth's troposphere and stratosphere propagate vertically and grow to their maximum amplitudes until they are dissipated by ion drag, eddy and molecular diffusion processes in the lower IT (∼80-160 km), where they deposit energy and momentum into the zonal-mean IT. Vertically propagating tides may also interact non-linearly with one another or with planetary waves in the intervening regions of Earth's atmosphere, altering their otherwise exponential growth. The manifestation of such non-linear tidal interactions can also be expected to affect the circulation, composition, and thermal structure of the zonal-mean IT.

Hines [52] was the first to propose that internal atmospheric gravity waves (i.e., atmospheric tides are a special class of internal atmospheric gravity waves) could act to heat the mean IT by ∼10° K day^{-1} near 95 km and ∼100° K day^{-1} near 140 km. Lindzen and Blake [67] followed the work of Hines [52] and showed theoretically that specifically the semidiurnal tide could be responsible for maintaining exospheric temperatures on the order of 600° - 700° K in the absence of solar EUV heating. A series of studies performed in the late 1970s and early 1980s by Miyahara [75]; [76]; [77]; [78] quantified the induced zonal-mean winds in the lower IT due to the dissipating diurnal and semidiurnal migrating tides. Miyahara found that dissipation of the diurnal and semidiurnal migrating tides deposited momentum into the equatorial lower IT via the eddy momentum source terms, inducing strong zonal-mean easterlies on the order ∼100 m s^{-1}. Groves and Forbes [38] found that energy flux divergences generated by diurnal and semidiurnal tidal dissipation lead to global averaged energy inputs comparable to ultraviolet (UV) radiation absorption between 70 and 90 km. They also found that global average tidal heating was about 40% of that generated by EUV absorption heating above 300 km. Furthermore, Groves and Forbes [39] concluded that equatorial and mid-latitude tidal heating exceeds or is comparable to the daily average heating due to EUV absorption below ∼120 km.

A later study by Miyahara and Wu [80] showed that during solstice the dissipation of vertically propagating diurnal (semidiurnal) tides generated mean zonal winds of order 10 m s^{-1} (20 m s^{-1}) at low latitudes below (above) 120 km. Following the work of Miyahara and Wu [80], Miyahara et al. [79] showed that the dissipation of atmospheric tides were the primary source contributing to zonal-mean accelerations and heating of the 70 to 100 km height regime. Forbes et al. [31] utilized the NCAR Thermosphere-Ionosphere General Circulation Model (TIGCM, see Roble et al. [106]) with and without observationally-based tidal lower boundary conditions (∼97 km) to quantify the net acceleration, heating, and compositional changes in the IT due to upward propagating migrating diurnal and semidiurnal tides. Figure 1.7 shows the changes in the zonally- and diurnally-averaged winds, temperature, and composition of the IT system presented by Forbes et al. [31]. They concluded that dissipating upward propagating migrating tides enhance the zonal-mean winds in the equatorial lower thermosphere by 10–30 m s^{-1}, alter the zonal-mean temperature by $-5°$ to $+8°$ K, and increase (decrease) N_2 (O) number densities by 10–15% (30–50%) in the IT. Furthermore, Portnyagin et al. [96] used a climatological model based on global radar observations to identify tides as one of the main drivers of an annual mean circulation within in the MLT region.

Angelats i Coll and Forbes [54] reported on the secondary waves resulting from the SW2-SPW1 non-linear interaction (i.e., SW1 and SW3), showing that they contributed significantly to the zonal-mean circulation (i.e., 30 m s^{-1} in the zonal wind and 15 m s^{-1} in the meridional wind around 140 km), as well as induced significant longitudinal variability around 130 km. Model simulations by Forbes et al. [32] showed the dissipation of DW1 and DE3 produce an eastward jet of ∼20 m s^{-1} during boreal summer months between 100 and 120 km. A recent study by Hagan et al. [45] examined vertically propagating tidal effects on the zonal-mean circulation in the previously mentioned NCAR TIME-GCM. They found that the non-migrating tides (i.e., specifically DE3 and SE2), can enhance zonal wind speeds in the MLT by up to 50 m s^{-1} during the September equinox (Figure 1.8). Both Forbes et al. [31] and Hagan et al. [45], along with the historical work of Forbes and Garrett [28] showed that upward propagating tides typically reach their maximum

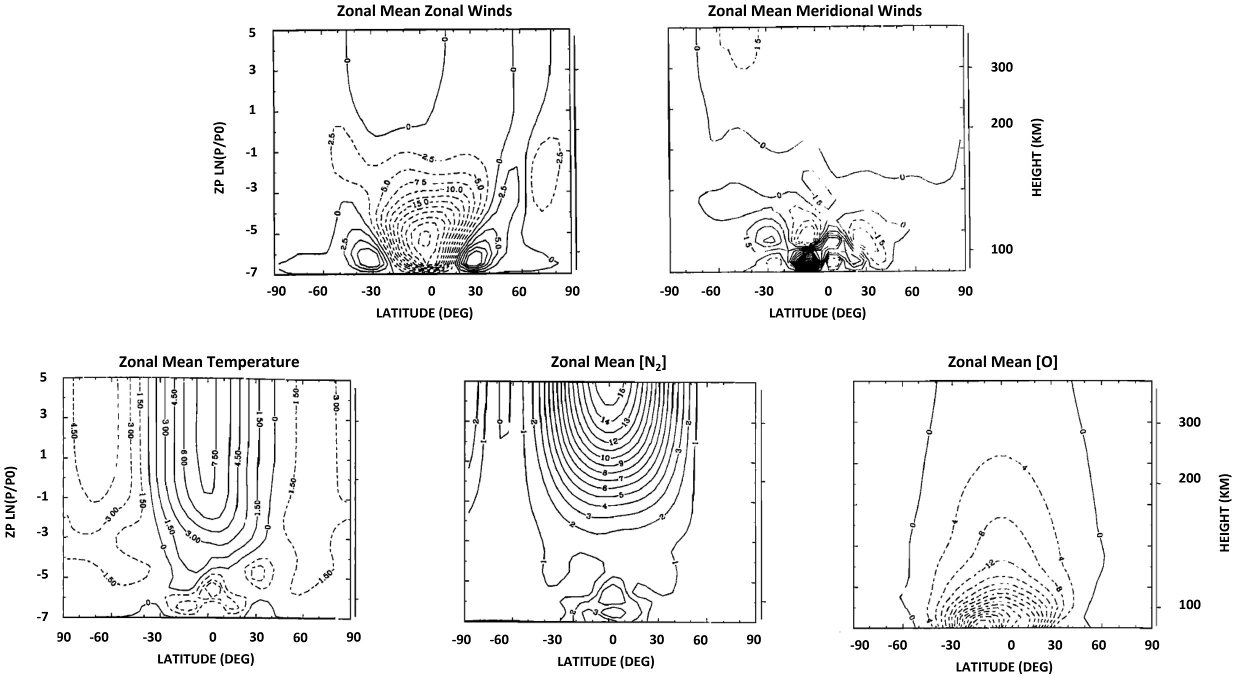

Figure 1.7: September zonally and diurnally differences between TIGCM simulations including and excluding migrating diurnal and semidiurnal lower boundary tidal forcing as a function latitude and log-pressure level ($\ln(\frac{p_0}{p})$ for the zonal winds (top left), meridional winds (top right), temperature (bottom left), percent change in [N_2] (bottom middle), and percent change in [O] (bottom right). Zonal winds were contoured every ± 2.5 m s^{-1}, meridional winds were contoured every ± 1.5 m s^{-1}, temperatures were contoured every $\pm 1.5°$ K, [N_2] were contoured every 1%, and [O] were contoured every -2%. Figure adapted from results presented in Forbes et al. [31].

amplitudes at lower IT altitudes (ca. 90-120 km). The region where upward propagating tides attain their maximum amplitudes (i.e., and thus experience maximum dissipation) coincides with the so-called dynamo region (ca. 100-170 km, indicated by the dashed lines in Figure 1.8). Hagan et al. [46] demonstrated that upward propagating non-migrating tides modulate the E-region wind-dynamo processes leading to four-peaked longitude structures observed in many F-region ionospheric measurements (e.g., Sagawa et al., [109]; Immel et al., [56]; England et al., [18]; Lin et al., [64]; Lühr et al., [73]; Häusler and Lühr, [48]; Pedatella et al., [92]).

It is clear from prior research efforts that upward propagating tides not only affect the zonal-mean state of the IT, but also the wind-dynamo processes responsible for generating electric fields at E-region altitudes. Due to restrictions imposed by space-based observing platforms, there exists

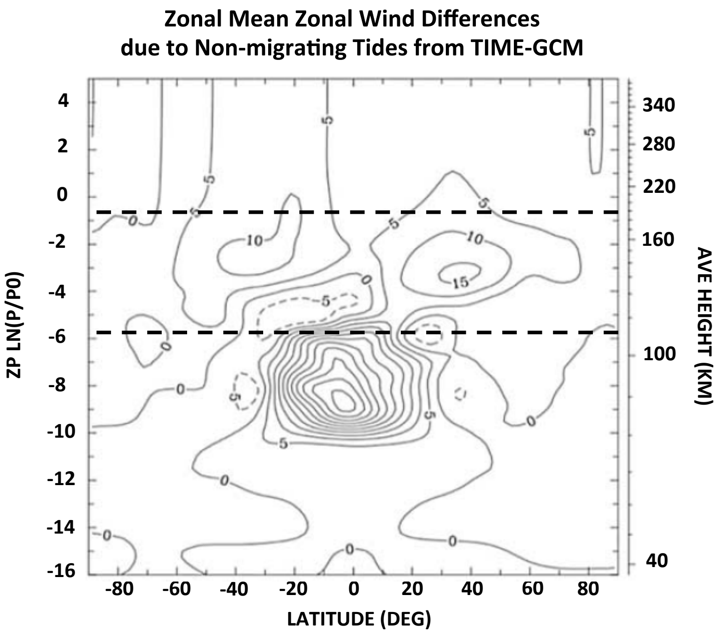

Figure 1.8: Contours of zonally- and diurnally-averaged zonal wind differences attributable to the presence of non-migrating tides in the TIME-GCM during September as a function of latitude and log-pressure level ($\ln(\frac{p_0}{p})$. Zonal wind differences are contoured every ±5 m s^{-1}. Figure from results presented in Hagan et al. [45].

a spatial data gap in global tidal observations, termed by Oberheide et al. [87] the "thermospheric gap", extending from the dynamo region to the upper thermosphere (ca. 120–400 km). Therefore, Oberheide et al. [87] derived the aforementioned observationally-based CTMT consisting of migrating and non-migrating tidal amplitudes and phases extending from 80 to 400 km aimed at ameliorating this deficiency. This new set of observationally-based tidal perturbations within and beyond the dynamo region, along with state-of-the-art general circulation modeling capabilities provides an unprecedented chance to study the upward propagating tidal affects on the mean state of the IT, especially in the dynamo region where observations are scarce.

1.4 Objective and Science Questions

The previous section clearly shows evidence for non-linear tidal interactions observed in the IT; however, while a few of the proposed mechanisms are now well understood, many of the other mechanisms have yet to be fully explored and understood by numerical experiments. **The primary objective of this dissertation is to quantify and better understand the role that atmospheric tides play in determining the mean state, longitudinal, seasonal, and solar cycle variability of the IT system, with specific attention to non-linear tidal interactions and their underlying physical mechanisms.** To accomplish this objective the NCAR TGCMs are used with the intent of aiding the interpretation and understanding of ground-based and satellite observations. The science questions we seek to answer from the NCAR TGCMs and our subsequent analyses in order to achieve this objective are as follows:

(1) **Does the offset between the geographic and geomagnetic fields introduce complexities via ion-neutral coupling that project onto diurnal and semidiurnal non-migrating tides in the neutral atmosphere?**

  As part of this larger question there are three sub-questions which we seek to answer, including:

  (a) How do these in-situ generated tides compare in amplitude with tropospherically-generated tides?

  (b) What are the underlying physical mechanisms and relationships?

  (c) How and why do these "pseudo-tides" vary with solar activity?

(2) **What role do vertically-propagating tides play in determining the zonal-mean thermal, dynamical, and compositional structure of the IT system?**

  As part of this larger question there are three sub-questions which we seek to answer, including:

(a) What are the zonal-mean wind variations brought about by the dissipation of vertically-propagating tides and how do these depend on season and solar cycle?

(b) How do dissipating tides affect the thermal balance and temperature structure of the IT system and how do these effects change with respect to season and solar cycle?

(c) How does dissipation of vertically-propagating tides affect the composition and densities of the IT system, and what are the seasonal and solar cycle dependencies?

The remaining content of this dissertation is organized into six chapters. Chapter 2 introduces the methodology for this study and provides more detailed information regarding the NCAR TGCMs and the lower boundary conditions utilized to produce the numerical modeling results analyzed as part of this study. Chapter 3 focuses on answering the first science question described above, in addition to all three sub-questions. Chapters 4, 5, and 6 concentrate on answering science questions (2a), (2b), and (2c), respectively. Finally, conclusions, major findings, and implications of this work are summarized in Chapter 7. A glossary of variables is provided in Appendix A. Appendix B, C, D, and E contain figures utilized to supplement the analyses presented in Chapters 3, 4, 5, and 6, respectively.

Chapter 2

Model Descriptions and Methodology

This chapter provides a detailed description of the NCAR TIME-GCM and Thermosphere-Ionosphere-Electrodynamics General Circulation Model (TIE-GCM) utilized as part of this dissertation work, as well as some general details regarding the numerical experiments described herein. Particularly, we describe the use of a new set of observationally-based lower boundary conditions in the TIE-GCM, and compare these observationally-based lower boundary conditions to results from the TIME-GCM, GSWM-02, and other empirical models. The zonal-mean conservation equations in the NCAR TGCMs are reviewed and discussed in the context of classical tidal theory and the zonal-mean equations presented in Chapter 1. Lastly, a brief description of the data analysis methods employed in this study are described.

2.1 NCAR TGCMs and their Lower Boundary Conditions

2.1.1 TIME-GCM

Beginning with the original development of the thermosphere general circulation model by Dickinson et al. [14], the TIME-GCM is the latest in a series of three-dimensional time-dependent non-linear general circulation models developed at NCAR. The NCAR TIME-GCM is numerical model extending from $\sim$30 km in the stratosphere to $\sim$600-750 km in altitude (depending on solar cycle) in the upper thermosphere designed to self-consistently calculate the dynamics, photoionization, photodissociation, chemical loss, neutral gas heating, electrodynamics, disspation, and chemistry from first-principles (e.g., from the conservation of mass, momentum, energy, charge, and electromagnetic energy equations, Lorentz force law, and Maxwell's equations) in order to replicate the circulation, temperature, electrodynamics, and compositional structure of the mesosphere, thermosphere, and ionosphere for a predetermined set of solar irradiance values (i.e., using a 10.7cm solar radio flux (F10.7) value as a proxy) and geomagnetic proxies (i.e., hemispheric power value after Evans [20] and cross-cap potential drop) to account for particle precipitation and magnetospheric drivers. The TIME-GCM performs numerical integration of the discretized conservation equations across the entire three-dimensional spatial domain, and propagates the resulting solutions to the conservation equations forward in time from a given three-dimensional initial state (e.g., specified month, day, and year). Inclusion of sub-grid scale gravity waves is necessary in order to properly simulate the mesopause region and are parameterized using a modified Lindzen [66] scheme. For more information of the historical development of the TIME-GCM, as well as more in-depth detail regarding all the conservation laws, chemical and ion species, etc. included in the model the reader is referred to Roble and Ridley [108], Roble [103]; [104], TIEGCM V1.94 Model Description [47], and references therein.

All the TIME-GCM simulations that contribute to this study were from model version 1.42 using a horizontal resolution of 2.5° x 2.5° (longitude x latitude), a vertical resolution of 4 points per scale height, and a time step of 120 s. Geomagnetic proxies representative of quiescent conditions were held constant in all the TIME-GCM simulations discussed henceforth utilizing a hemispheric power value of 8 GW, and cross-cap potential drop of 30 kV. Furthermore, all TIME-GCM results represent steady-state monthly average conditions i.e., the TIME-GCM is run for one day in the middle of the month of interest until the model reaches a diurnally-reproducible state.

2.1.1.1 Background and Tidal Lower Boundary Conditions

The lower boundary of the TIME-GCM is located in the stratosphere at log-pressure level ($\ln \frac{p_0}{p}$) = −17 or ∼12 mbar (∼30 km). Typically for climatological or steady-state simulations the zonal-mean geopotential height and temperature fields at the model lower boundary are from analytical fits to an empirical model named *zatmos*. These zonal-mean fields vary as function of latitude and day of year. The zonal-mean neutral wind fields at the TIME-GCM lower boundary are calculated from the zonal-mean temperature and geopotential height fields assuming geostrophic balance. A tunable Rayleigh friction parameter is utilized at equatorial latitudes where geostrophic approximation breaks down, in order to get realistic zonal-mean winds. For the remainder of this work we refer to the zonally- and diurnally-averaged (i.e., zonal mean) wind, temperature, and geopotential height input fields at the NCAR TGCMs lower boundaries as the "lower boundary background" wind, temperature, and geopotential height fields. Additionally, all four lower boundary background fields can be specified using daily average data from the European Center for Medium range Weather Forecasting (ECMWF) or the National Center for Environmental Prediction (NCEP) reanalysis products. For the TIME-GCM simulations performed herein we use the background fields from *zatmos*. Above the lower boundary, all the aforementioned atmospheric variables along with others are specified using output from a previous TIME-GCM simulation, which is chosen to match the desired solar cycle, geomagnetic, and seasonal conditions.

The TIME-GCM intrinsically accounts for atmospheric tides excited due to absorption of UV, EUV, and FUV in the stratosphere, mesosphere, and thermosphere. Atmospheric tides or global scale planetary waves with source regions in the troposphere must be introduced as lower boundary conditions. Recent TIME-GCM tidal studies (e.g., Hagan et al., [45]; England et al., [17]; Häusler et al., [49]; Pedatella et al., [94]) have perturbed the TIME-GCM lower boundary with migrating and non-migrating tidal results from the GSWM-02. GSWM-02 was recently updated by Zhang et al. [128], [129] to the GSWM version 2009 (GSWM-09). GSWM-09 now includes updated background temperature and wind fields derived from TIMED SABER measurements, as well as new tidal radiative and latent heating rates derived from the International Satellite Cloud Climatology Project (ISCPP) and Tropical Rainfall Measuring Mission (TRMM) data, respectively. GSWM-09 includes migrating and non-migrating diurnal and semidiurnal tidal components with zonal wavenumbers ranging between ±6 and may be used as input at the TIME-GCM lower boundary. An inter-comparison and assessment of TIME-GCM results that are forced with GSWM-02 and GSWM-09 at the lower boundary is beyond the purview of this report and the subject of a separate study. For this dissertation work, we use migrating and non-migrating tides (i.e., DE6 to DW6 and SE6 to SW6) calculated from the GSWM-09 at the TIME-GCM lower boundary. These GSWM-09 tides are then added to the background wind, temperature, and geopotential height fields specified by *zatmos*, resulting in the full wind, temperature, and geopotential height input fields at the TIME-GCM lower boundary. An example TIME-GCM result was shown in Figure 1.2 for differences between TIME-GCM simulations that included and excluded GSWM-09 tides at the model lower boundary. We must also note that in addition to lower boundary tidal forcing upward propagating planetary waves may also be forced at the TIME-GCM lower boundary using the National Center for Environmental Prediction (NCEP) Reanalysis or ECMWF Reanalysis values; although neither were considered in the present study.

The numerical experiments performed with TIME-GCM are used to address science question (1), and all of its subquestions, as well as science question (2c).

2.1.2 TIE-GCM

The NCAR TIE-GCM is analogous to TIME-GCM except the model lower boundary is at ∼97 km (in the upper mesosphere) and some of the TIME-GCM model physics is not included in the TIE-GCM. For example, the TIME-GCM includes the aforementioned gravity wave parameterization scheme after Lindzen [66], in addition to non-local thermodynamic equilibrium (NLTE) radiative cooling by carbon dioxide (CO_2), which leads to determination of atmospheric properties in the mesopause; whereas the TIE-GCM does not include these parameterizations and physical processes and cannot resolve the mesopause. A more detailed description of the current TIE-GCM is provided by Qian et al. [98] and Richmond and Maute [101], while Dickinson et al. [14], [12], Roble et al. [106], Richmond et al. [102], Wang [125] provide a historical development of the TIE-GCM.

TIE-GCM simulations reported on herein were performed using a horizontal resolution of 2.5° x 2.5° (longitude x latitude), a vertical resolution of 4 points per scale height, a time step of 120 s, and using model version 1.94. A set of monthly climatologies were simulated by running the TIE-GCM for the 15th day of every month until the model reached a diurnally-reproducible state. The TIE-GCM solar fluxes in the 8–70 Å range were multiplied by a factor of 4.4 following Fang et al. [21], in order to more realistically resolve E-region conductivities and electron densities in the TIE-GCM. Also, the eddy diffusion scheme in the TIE-GCM was updated to improve consistency with TIME-GCM eddy diffusivities near the TIE-GCM lower boundary. Specifically, the globally invariant eddy diffusion value of ∼186 m^2 s^{-1} was increased by ∼5-40% and includes spatial variations ranging between 196-260 m^2 s^{-1} at the TIE-GCM lower boundary. As with all the TIME-GCM simulations performed herein, all the TIE-GCM simulations analyzed henceforth utilized geomagnetic proxies representative of quiescent conditions were held constant with a hemispheric power value of 8 GW, and cross-cap potential drop of 30 kV. The numerical experiments performed with TIE-GCM employing the observationally-based lower boundary conditions described below are used to address science question (2). Please note that the solar fluxes in the 8-70 Å range in the TIME-GCM simulation used in our comparative sensitivity analysis performed below in Section 2.2 were not multiplied by any factor. This was omitted from the TIME-GCM simulation because we are performing a sensitivity analysis using TIME-GCM, whereas our TIE-GCM simulations are designed to best replicate the IT, especially within the dynamo region.

2.1.2.1 Background Lower Boundary Conditions

The lower boundary of the TIE-GCM is located within the mesopause region at $\ln \frac{p_0}{p} = -7$ or 5.483×10^{-4} mbar (∼97 km). For a standard TIE-GCM simulation the background wind fields at the TIE-GCM lower boundary are typically set to zero, while the background temperature and geopotential height fields are set to latitudinally and longitudinally invariant values of 181° K and 96.37 km, respectively. In the present work, we use more realistic background lower boundary conditions and assess the associated impacts. Longitudinally-invariant observationally-based temperatures and geopotential heights are identical to those computed in Zhang et al. [128];[129] from SABER measurements (Russell et al., [55]) onboard the TIMED spacecraft at 5.483×10^{-4} mbar. The TIMED satellite is in a 625 km and 73° inclination orbit so that the latitude coverage of the

SABER instrument on a given day extends from ∼53° in one hemisphere to ∼83° in the other hemisphere. This viewing geometry alternates every 60 days due to 180° yaw maneuvers required for the TIMED satellite. Thus, we only use background multi-year (i.e., from 2002-2008) monthly mean temperatures and geopotential heights calculated SABER measurements between ±50°, where a continuous temperature measurements were made for all months. The SABER background temperatures polewards of ±50° latitude are extended (i.e., via extrapolation) from ±50° to the poles using temperatures from the Naval Research Laboratory Mass Spectrometer Incoherent Scatter Radar Extended (NRLMSISE-00) model (Picone et al., [95]). The background geopotential heights polewards of ±50° latitude are calculated self-consistently from the background temperature field using the following:

$$Z_{g_2} = Z_{g_1} - \frac{R}{g}\langle T\rangle \int_{p_1}^{p_2} \frac{dp}{p}, \tag{2.1}$$

where

$$\langle T\rangle = \frac{1}{\ln\frac{p_1}{p_2}} \int_{p_2}^{p_1} \frac{T}{p} dp$$

$\langle T\rangle$ is the zonally- and diurnally-averaged temperature between pressure level p_1 and p_2. Both the background temperature and geopotential heights are smoothed using a box-car average to eliminate any large latitudinal gradients, which can cause the TIE-GCM to give unrealistically large wind speeds close to the dynamo region.

The observationally-based background winds utilized at the TIE-GCM lower boundary are from combined Wind Imaging Interferometer (WINDII; Shepherd et al., [113]) – High-Resolution Doppler Imager (HRDI; Hays et al., [50]) measurements made onboard UARS at 95 km, which are computed by Forbes et al. [34]. The UARS satellite was in a 585 km and 57° inclination orbit, resulting in a viewing geometry for the WINDII (HRDI) instrument that covered between ∼42° latitude in one hemisphere to ∼72° latitude in the other hemisphere (±70° latitude) on a given day. By combining WINDII and HRDI measurements into one dataset, background multi-year (i.e., 1992-1994) monthly mean horizontal wind fields between ±70° latitude at 95 km were computed, which lies in the height regime where both WINDII and HRDI take overlapping measurements.

For more information on the WINDII-HRDI data processing methodology the reader is referred to Forbes et al. [34]. Similar to the observationally-based background temperatures and geopotential heights, the WINDII-HRDI background winds polewards of ±70° latitude are extended to the poles via smoothed extrapolation of wind patterns from the Horizontal Wind Model 2007 (HWM07; Drob et al., [15]). Thus, from above ±70° to the poles we use HWM07 wind patterns. We must note that since tidal effects on the zonal-mean IT system are mainly limited to low and middle latitudes (i.e., above ±60° magnetospheric effects dominate), we do not expect the background lower boundary conditions at high latitudes (i.e., latitudes where HWM07 and NRLMSISE-00 are used) to greatly affect our TIE-GCM results shown in the following sections and chapters.

Figure 2.1 shows the observationally-based TIE-GCM background lower boundary conditions used in our simulations from WINDII-HRDI at 95 km and SABER at pressure level 5.483×10^{-4} mbar (left column) and compares them with background fields computed from HWM07 at 95 km and NRLMSISE-00 at 5.483×10^{-4} mbar (right column) as a function of month and latitude. Equatorward of the dashed white lines only data from the WINDII-HRDI or SABER is plotted, whereas poleward of the dashed white lines the WINDII-HRDI or SABER measurements were extrapolated using HWM07 and NRLMSISE-00. The background zonal winds computed from WINDII-HRDI (Figure 2.1a) and HWM07 (Figure 2.1b) show great agreement at all latitudes with westward (eastward) winds at low (middle) latitudes throughout the entire year. There are noticeable differences between the background meridional wind fields computed from WINDII-HRDI (Figure 2.1c) and HWM07 (Figure 2.1d), although at higher latitudes (i.e., above ±70°) the two compare favorably, which should be expected given our data processing technique. Further investigation as to why there are noticeable differences between the WINDII-HRDI and HWM07 zonally- and diurnally-averaged meridional winds is outside the scope of this dissertation work. The seasonal and latitudinal structure of the background temperatures computed from SABER (Figure 2.1e) and NRLMSISE-00 (Figure 2.1f) show good comparison above ±50° as expected; although at low latitudes, NRLMSISE-00 shows a semiannual temperature minimum structure, whereas SABER temperatures remain relatively constant throughout the entire year. The NRLMSISE-00

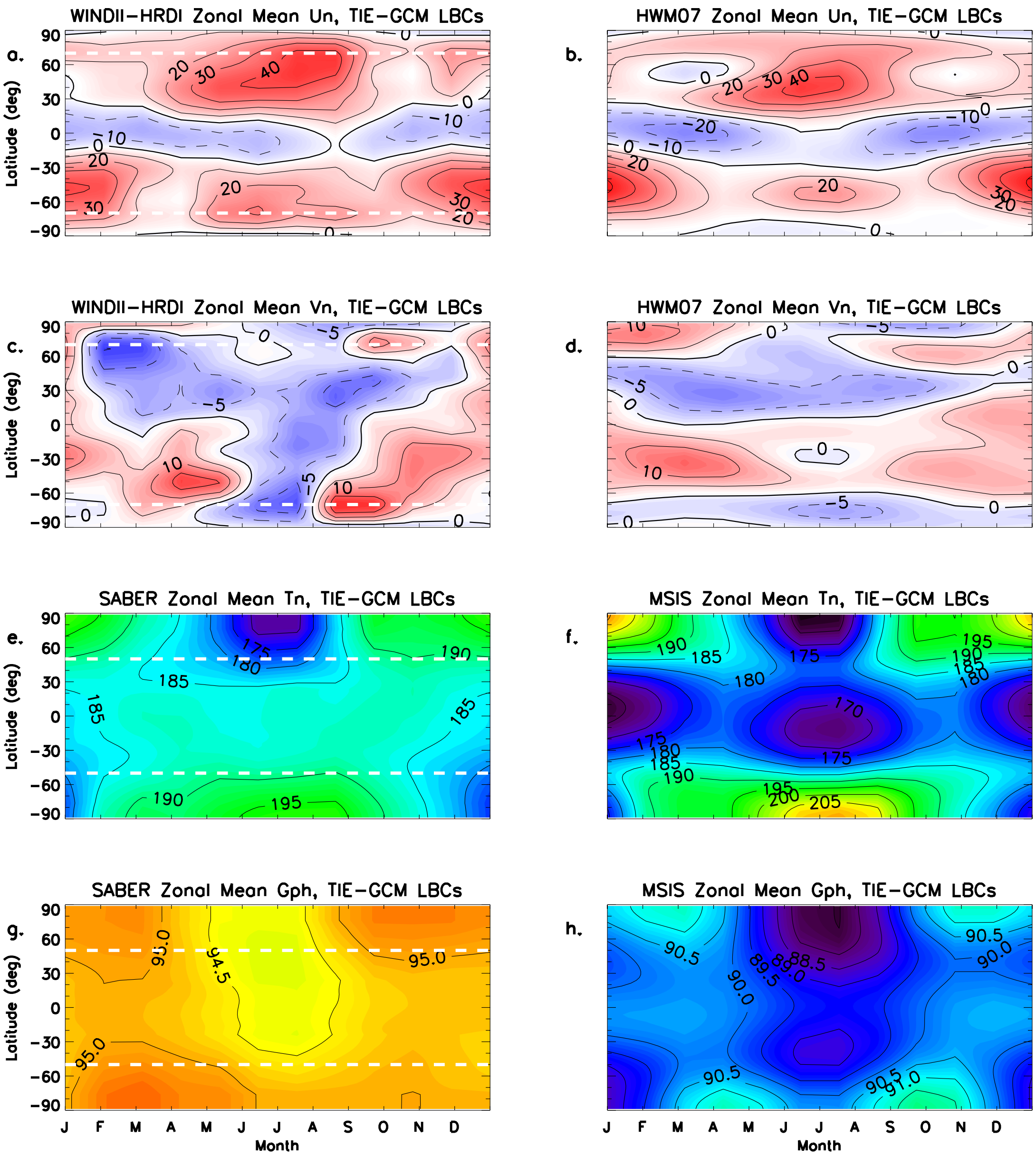

Figure 2.1: Background TIE-GCM lower boundary horizontal winds (a-d), temperatures (e and f), and geopotential heights (g and h) from WINDII-HRDI at 95 km and SABER at pressure level 5.483×10^{-4} mbar (left column) and from HWM07 at 95 km and NRLMSISE-00 at pressure level 5.483×10^{-4} mbar (right column) as a function of month and latitude. The zonal (meridional) wind fields are contoured every ±10 m s^{-1} (± 5 m s^{-1}), the temperatures every 5° K, and geopotential heights every 0.5 km. The dashed white lines signify the latitudes poleward of which the WINDII-HRDI and SABER measurements are extrapolated using HWM07 and NRLMSISE-00 results.

temperatures also show much stronger latitudinal gradients than do the SABER temperatures. The background geopotential height fields from SABER (Figure 2.1g) and NRLMSISE-00 (Figure

2.1h) have a similar latitudinal and seasonal structure to that of the temperature field. This is expected since the geopotential height fields are calculated from the temperature via equation 2.1. SABER geopotential heights have significantly weaker latitudinal gradients than those calculated from NRLMSISE-00 because of the TIE-GCM sensitivity to large latitudinal gradients at the lower boundary (i.e., can result in fictitious wind results). Please note that the SABER temperatures and geopotential heights are not internally consistent with the WINDII-HRDI wind fields (i.e., the WINDII-HRDI wind fields were not calculated from the SABER temperatures and geopotential heights, instead they are two independent data sources). Unfortunately, the geostrophic approximation breaks down in the mesopause region as gravity wave breaking generates turbulence, and so self-consistent winds derived from SABER geopotential heights would result in spurious mean winds. Therefore the subsequent subsection evaluates the sensitivity of the TIE-GCM zonal-mean solutions for specific IT fields given a different set of background lower boundary conditions from observations or empirical models.

2.1.2.2 Tidal Lower Boundary Conditions

The TIE-GCM inherently accounts for tidal perturbations excited in situ due to the absorption of EUV and FUV in the thermosphere. Atmospheric tides whose source regions lie in the troposphere, stratosphere, or lower mesosphere must be introduced at the TIE-GCM lower boundary. Previous tidal studies (e.g., Pedatella et al., [92]; Chang et al., [4]) using the TIE-GCM have represented tides of lower atmospheric origin by perturbing the model lower boundary with GSWM-02 migrating and non-migrating tides, which are what comes with a standard download of the TIE-GCM code. Wu et al. [126] replaced the GSWM-02 tidal lower boundary conditions in the TIE-GCM with observed tidal perturbations from the TIMED spacecraft (i.e., SABER temperatures and TIDI winds) at 97 km and demonstrated that inputting the TIMED tidal lower boundary conditions improved the TIE-GCM capability of reproducing realistic non-migrating tidal effects in thermospheric winds and temperatures, and ionospheric electron densities at low and middle latitudes. Similar to Wu et al. [126], we also force the TIE-GCM lower boundary with a set of observationally-based tidal perturbations from the CTMT at 97 km.

As previously discussed in Section 1.2.3., Hough modes represent solutions to Laplace's tidal equation for an individual tidal component in the absence of mean winds and dissipation. HMEs are numerical solutions (i.e., in the case of CTMT from pole-to-pole and 0-400 km) to the linearized tidal equations taking into account dissipation and a height dependent background temperature. The HMEs used in CTMT are calculated from a simplified version of GSWM-02 which includes tidal dissipation (i.e., gravity wave drag, eddy and molecular diffusivity, thermal conductivity, and ion drag) and an arbitrary tropospheric heat source equivalent to the classical Hough Mode, but neglects background winds and spatial gradients in temperature. These HMEs for diurnal (semidiurnal) tidal components with zonal wavenumbers ranging from -3 to $+2$ (-3 to $+4$) are then least-square fitted to TIMED SABER tidal temperatures and TIDI tidal winds averaged over 2002-2008 for each month of the year within the MLT region, providing a means to reconstruct tidal amplitudes and phases in winds, temperature, and density that are all self-consistent in terms of relative amplitudes and phases. For the TIE-GCM simulations discussed herein we use migrating and non-migrating diurnal and semidiurnal (i.e., DE3 to DW2 and SE3 to SW4) from CTMT as model tidal lower boundary conditions. The aforementioned observationally-based background winds, temperatures, and geopotential heights are added to CTMT tidal perturbations to comprise the total wind, temperature, geopotential height fields that are input at the TIE-GCM lower boundary. We must note that although, background winds are neglected in the calculation of the HMEs their effects are not neglected when fitting to the observed tidal structures in the MLT region, as the measured tides will have propagated through some background wind field. Svoboda et al. [118] showed that the distortion of the tidal structures from their classical forms can be viewed as mode coupling (see Lindzen and Hong, [68]), i.e., the excitation of higher-order modes, which linearly superimpose to approximate this distortion. Therefore, a few HMEs for a specific tidal component can be fit to the observed tidal fields in such a way that the weighted superposition of HMEs replicates the observed distortion (Svoboda et al. [118]). For a more detailed description of the CTMT the reader is referred to Oberheide et al. [87].

Figure 2.2 compares the typical diurnal (top) and semidiurnal (bottom) migrating and non-migrating zonal wind tidal lower boundary conditions input into the TIE-GCM from GSWM-02 (left column) and the CTMT tidal lower boundary conditions (right column) utilized herein. The most noticeable differences lie in the migrating tidal components (i.e., DW1 and SW2). Although the latitudinal shape of DW1 compares favorably between GSWM-02 and CTMT, the maximum amplitude of DW1 in GSWM-02 (i.e., ∼45 m s^{-1}) is more than a factor of 2 larger than the DW1 tidal component calculated in CTMT (i.e., ∼20 m s^{-1}). As for SW2, the amplitude peak in the northern hemisphere compares quite well between GSWM-02 and CTMT (on the order of 20 m s^{-1}), even though SW2 in GSWM-02 has a 2-peak type of structure. In the southern hemisphere, SW2 calculated by the GSWM-02 is about a factor of 2 larger than SW2 from CTMT. The latitudinal structure and maximum amplitude of DE3 from GSWM-02 and CTMT compare favorably with one another. Other smaller amplitude diurnal components including DE2, D0, and DW2 are captured by both GSWM-02 and CTMT, whereas smaller amplitude semidiurnal components including SE2, SW1, SW3, and SW4 are only accounted for in CTMT. The DW4 is only accounted for in GSWM-02, as CTMT does not include DW4 in the model. Figure 2.2 clearly shows differences between our CTMT TIE-GCM tidal lower boundary conditions and the GSWM-02 tidal lower boundary conditions typically used by the community to drive the TIE-GCM. Therefore, we can expect differences in the zonal-mean IT simulated by the TIE-GCM, especially close to the model lower boundary (i.e., dynamo region) depending on which set of tidal lower boundary conditions are used.

2.2 Validation of the TIE-GCM Solutions Near its Lower Boundary

Since the TIE-GCM lower boundary conditions are applied at 97 km (as opposed to 30 km in the TIME-GCM), and molecular dissipation of the tides occurs just above this boundary, it is important that we establish the veracity of the TIE-GCM in terms of properly simulating tidal structures, and the effects of tidal dissipation on the mean state, in and above this region. Although many prior studies have been performed over the past 20 or more years that are interpreted in terms of the tidal fields applied at the lower boundary of the TIE-GCM, no such assessment has been

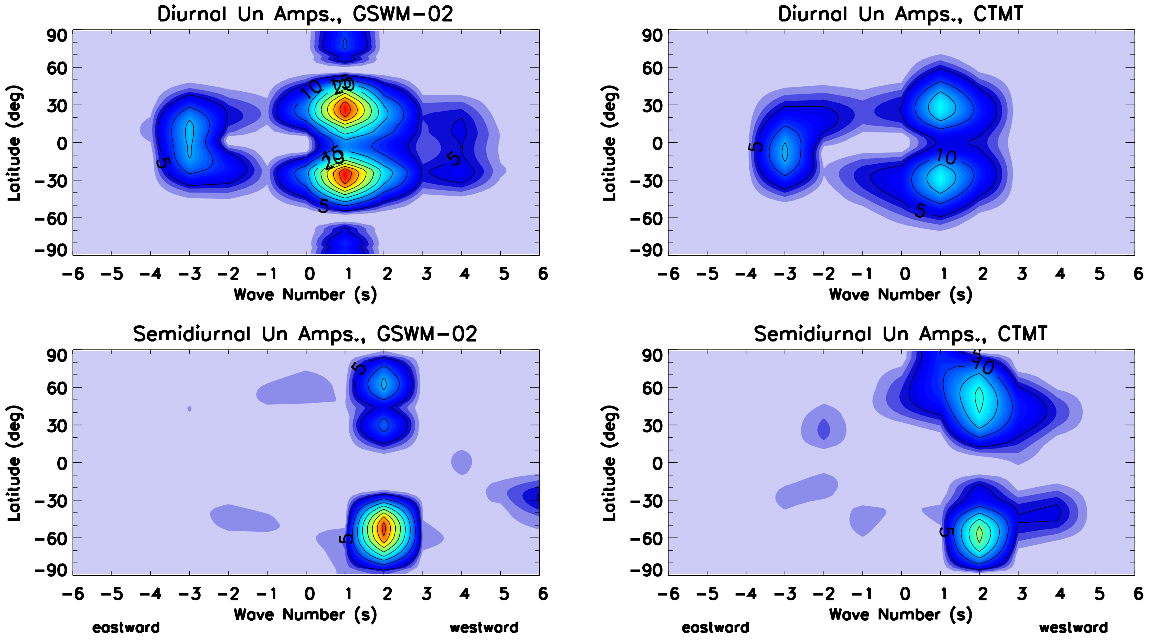

Figure 2.2: GSWM-02 (left column) and CTMT (right column) diurnal (top) and semidiurnal (bottom) zonal wind tidal amplitudes input at $\ln \frac{p_0}{p} = -7$. Tidal amplitudes are contoured every 5 m s^{-1}.

made as far as we know. Our approach is as follows. A TIME-GCM simulation is performed with lower boundary tidal specifications from the GSWM-09. The zonal-mean and tidal output fields (in the zonal and meridional winds, temperatures, and geopotential fields) from the simulation are then input at the lower boundary of the TIE-GCM, forcing the dynamical fields from the two models to be identical at this altitude. We then compare the outputs from the two models above 97 km; the degree of agreement between the two measures the capability of the TIE-GCM to provide a realistic tidal propagation and dissipation. The TIME-GCM serves as a useful tool for assessing the capability of the TIE-GCM to produce realistic results in the IT, and specifically realistic tidal results in the IT because both the GSMW-09 (i.e., the tidal perturbations specified at the TIME-GCM lower boundary) and TIME-GCM tidal results have previously been validated against satellite measurements in the IT (Liu et al., [71]; Häusler et al., [49]; Zhang et al. [128],[129]). One caveat is that some of the model physics specific only to the TIME-GCM (discussed above) extends above 97 km, so we cannot expect the two model results to be completely identical even under the best of conditions. Nevertheless, we believe that near self-consistency is achieved in this numerical experiment.

Figure 2.3 shows TIME-GCM and TIE-GCM results for the zonally- and diurnally-averaged zonal winds, DE3, and SW2 zonal wind amplitudes as a function of latitude and log-pressure level (i.e., altitude). Results from the TIME-GCM simulation (Figures 2.3a, 2.3e, and 2.3i) were forced at the model lower by a climatological background atmosphere (i.e., from *zatmos*) and tidal perturbations from the GSWM-09, while TIE-GCM results presented in the second column of Figure 2.3 (Figures 2.3b, 2.3f, and 2.3j) were forced at the model lower boundary by background and tidal perturbation winds, temperatures, and geopotential heights at $\ln \frac{p_0}{p} = -7$ from the same TIME-GCM solutions presented in Figures 2.3a, 2.3e, and 2.3i. All the results presented in Figures 2.3 and 2.4 are from model simulations under September conditions because this is when the lower atmospheric forcing of vertically-propagating tides is at or near its maximum (Forbes et al., [36]; Pedatella et al., [93]). Also, DE3 and SW2 zonal wind amplitude are illustrated Figure 2.3 because these are the largest amplitude components in the tidal spectrum at these IT altitudes during the month of September. The remain panels in Figure 2.3 (i.e., shown in third and fourth columns) will be discussed later.

Comparison between Figures 2.3a and 2.3b shows that the TIE-GCM replicates the overall latitudinal and vertical structure in the zonal wind field at low and middle latitudes. The most notable differences are seen in the westward jet feature near log-pressure level -3 (i.e., mean altitude of 136 km), where TIME-GCM results show a bifurcated westward jet structure with maximum wind speeds on the order of -50 m s^{-1}, while TIE-GCM shows more of a single-cell westward jet structure with maximum winds on the order of -60 m s^{-1}. Comparing the tidal amplitudes in Figures 2.3e and 2.3i with those in Figures 2.3f and 2.3j shows that the TIE-GCM is capable of replicating the latitudinal and vertical structure of DE3 and SW2 tidal components, although the TIME-GCM DE3 and SW2 maximum amplitudes are greater than the TIE-GCM DE3 and SW2 maximum amplitudes by ∼5 m s^{-1} and ∼10 m s^{-1}, respectively. The favorable comparison between TIME-GCM and TIE-GCM zonal wind results depicted in Figure 2.3 are representative of the TIE-

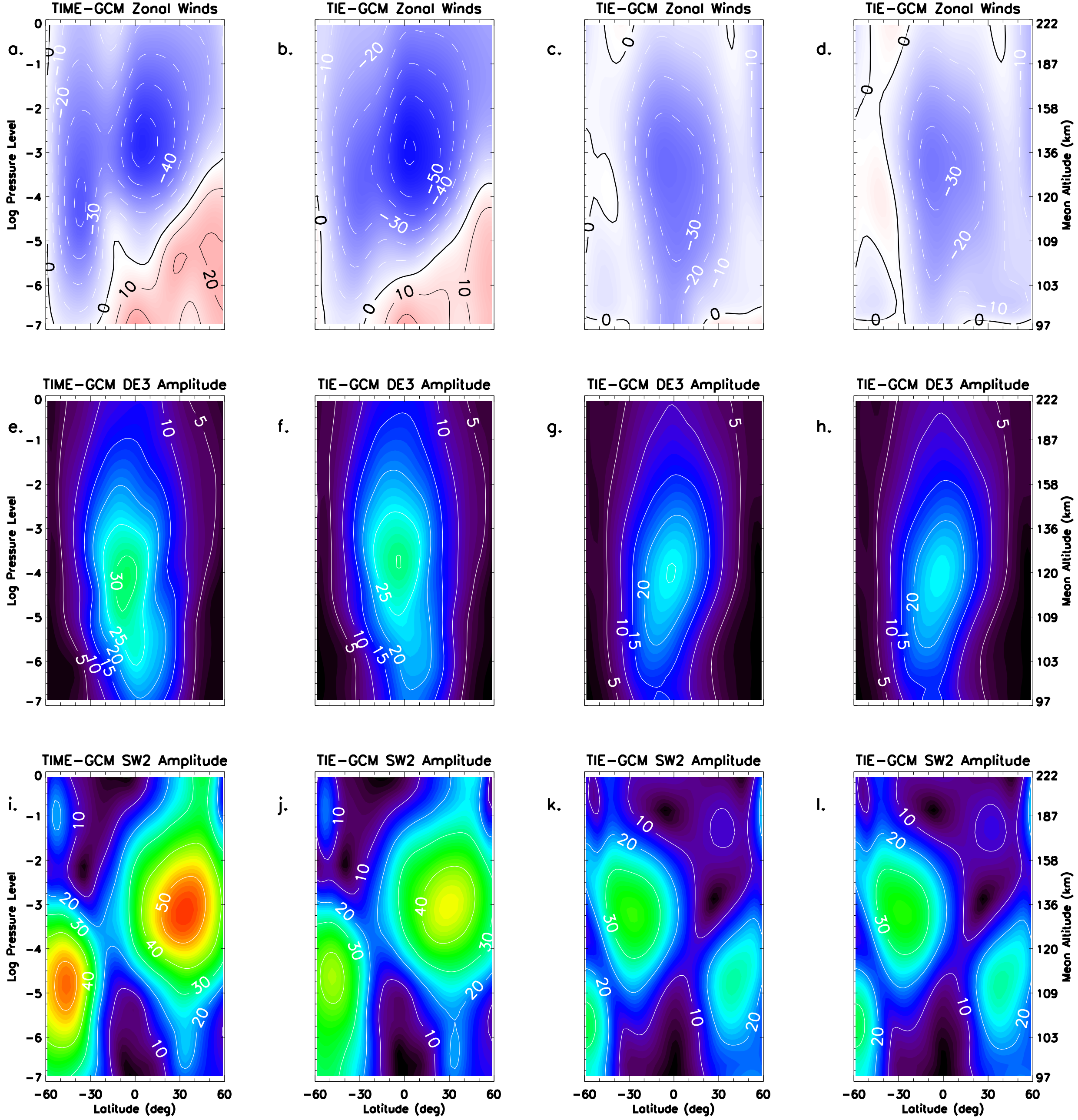

Figure 2.3: TIME-GCM and TIE-GCM zonally- and diurnally-averaged zonal winds (a-d), DE3 (e-h), and SW2 zonal wind amplitudes (i-l) during September from simulations with different combinations of background and tidal lower boundary conditions described in the supporting text. Zonally- and diurnally-averaged wind speeds and SW2 (DE3) zonal wind amplitudes are contoured every 10 (5) m s^{-1}.

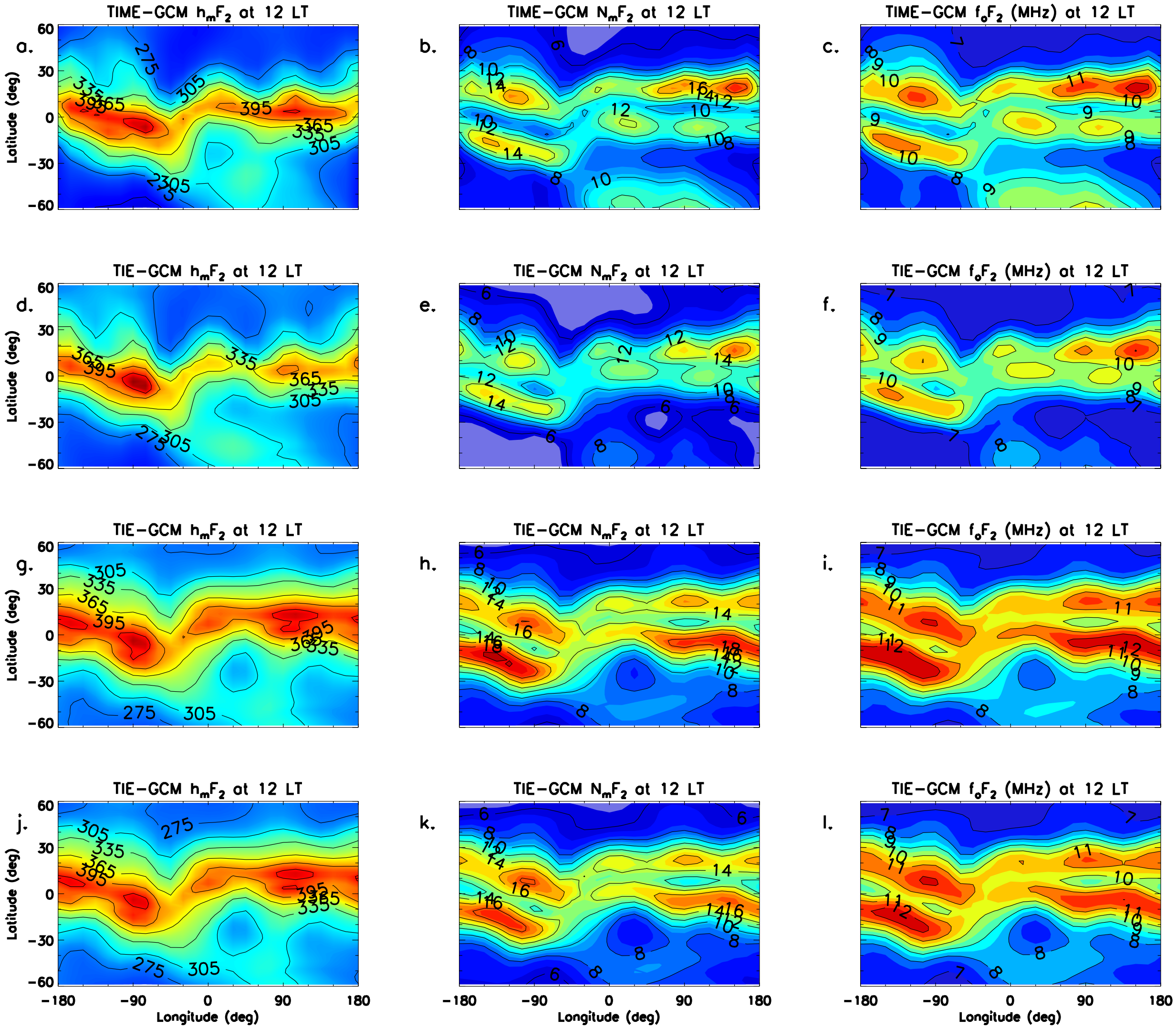

Figure 2.4: TIME-GCM and TIE-GCM h_mF_2 (a, d, g, j), N_mF_2 (b, e, h, k), and f_oF_2 (c, f, i, l) during September at 12 LT from simulations with different combinations of background and tidal lower boundary conditions described in the supporting text. h_mF_2 fields are contoured every 30 km, N_mF_2 fields are contoured every 2×10^5 cm^{-3}, and f_oF_2 fields are contoured every 1 MHz.

GCM capability of replicating latitudinal and vertical structure of other quantities in the IT (e.g., temperature and density). To reiterate, the solar fluxes in the 8–70 Å range in the TIME-GCM simulation used to produce the results shown in the first column of Figure 2.3 (and that were used to drive the lower boundary of the TIE-GCM simulations depicted in the second column of Figure 2.3) were not multiplied by the 4.4 factor presented in Fang et al. [21]. This could, at least in part explain some of the zonal-mean zonal wind and zonal wind tidal amplitude differences depicted in the first and second columns of Figure 2.3, although we suspect other differences between the NCAR TGCMs (e.g., gravity wave dissipation and chemistry differences) to be playing a larger role.

Figure 2.4 shows TIME-GCM and TIE-GCM results in h_mF_2, N_mF_2, and f_oF_2 as a function of longitude and latitude at 12 local time (LT) during the month of September in order to assess the TIE-GCM capability of replicating the spatial structure of the ionosphere when compared to TIME-GCM. The TIME- and TIE-GCM results shown in the top two rows of Figure 2.4 are from the same simulation used to produce the left two columns of Figure 2.3. Figures 2.4a and 2.4d compare favorably as spectral analysis of the h_mF_2 field calculated in the TIME-GCM (Figure 2.4a) and TIE-GCM (Figure 2.4d) revealed a dominant 4-peaked longitude structure at equatorial latitudes. Further comparison between Figures 2.4b and 2.4c with Figures 2.4e and 2.4f reveal similar spatial structures with spectral analyses of both TIME-GCM and TIE-GCM N_mF_2 and f_oF_2 fields having a dominant wave-4 structure in longitude. It is of note that the TIME-GCM is biased towards greater maximum values of h_mF_2, N_mF_2, and f_oF_2 when compared with the TIE-GCM by up to $\sim$30 km, 2×10^5 cm^{-3}, and 1 MHz respectively, especially in the Asian and Pacific sectors at tropical latitudes. Nonetheless, Figures 2.3 and 2.4 clearly display that the TIE-GCM is adept in producing comparable results to the TIME-GCM in zonal winds, major vertically propagating tidal components, and ionospheric F_2 fields when the TIE-GCM is forced consistently with the TIME-GCM. The model comparisons conducted above increase our confidence in obtaining reasonable solutions just above the TIE-GCM lower boundary (i.e., in the dynamo region) where the tides act to modulate the electric fields generated by the E-region wind-dynamo mechanism, leading to many of the features seen in Figure 2.4.

The TIE-GCM results presented in the third column (row) of Figure 2.3 (2.4) are from simulations was performed using HWM07 background winds, NRLMSISE-00 background temperatures and geopotential heights, while the TIE-GCM results depicted in the fourth column (row) of Figure 2.3 (2.4) are from simulations performed using the observationally-based background lower bound-

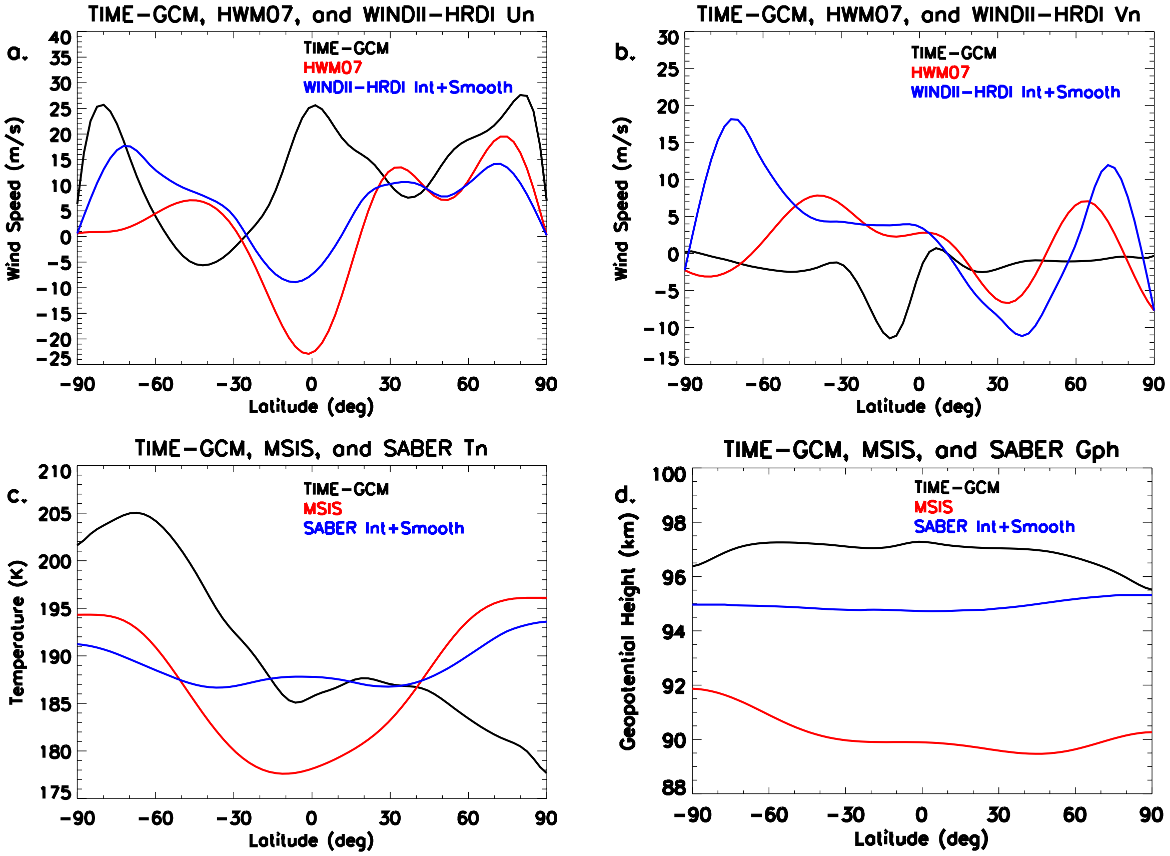

Figure 2.5: Background zonal (a) and meridional (b) winds, temperatures (c), and geopotential heights from TIME-GCM (black), HWM07/NRLMSISE00 (red), and WINDII-HRDI/SABER (blue) input at the TIE-GCM lower boundary during September as a function of latitude.

ary conditions discussed in Sections 2.1.2.1 and 2.1.2.2. Both TIE-GCM simulations were performed using CTMT tidal lower boundary conditions. First, a comparison between the zonal-mean zonal winds shown in Figure 2.3b (i.e., from our TIE-GCM simulation forced with the TIME-GCM results at the model lower boundary) with those shown in Figures 2.3c and 2.3d reveal clear differences in the latitudinal and vertical structure of the zonal-mean zonal winds, as westward winds persist through almost the entire low to mid latitude dynamo region with maximum wind speeds of about -35 m s^{-1}. A similar reduction in the zonal-mean zonal winds was also shown in Siskind et al. [116]. Comparison of DE3 and SW2 zonal wind amplitudes from the TIME-GCM driven TIE-GCM simulations (Figures 2.3f and 2.3j) versus those from our empirical model driven (Figures 2.3g and

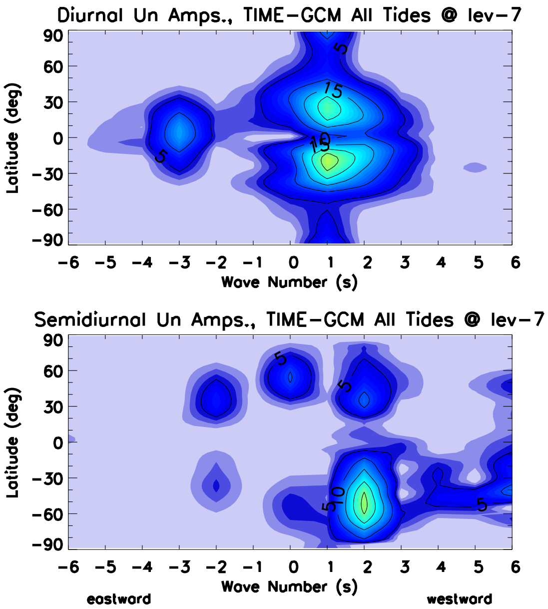

Figure 2.6: Same as Figure 2.2, except for the diurnal (top) and semidiurnal (bottom) tides from the TIME-GCM at $\ln \frac{p_0}{p} = -7$ during September from simulations forced with GSWM-09 tides at the lower boundary. Tidal amplitudes are contoured every 5 m s^{-1}.

2.3k) and observationally driven (Figures 2.3h and 2.3l) TIE-GCM simulations including CTMT tidal forcing, show a reduction in their maximum amplitudes by some 5 to 15 m s^{-1}, and a clear change in latitudinal structure of SW2. Noticeable changes also appear in the ionospheric quantities where increases of h_mF_2, N_mF_2, and f_oF_2 by ∼30 km, $\sim 6 \times 10^5$ cm^{-3}, and ∼1 MHz, respectively (i.e., comparison of row two with rows three and four in Figure 2.4) when the TIE-GCM is forced with boundary conditions from either empirical models or observations. These distinct changes in the zonal-mean IT within the TIE-GCM are due in part to differences in the background lower boundary conditions, which are depicted in Figure 2.5 from the TIME-GCM (black), empirical models (red), or observations (blue) during September. Differences of approximately 30 m s^{-1}, 15° K, and 2 km can persist in the background winds, temperature, and geopotential height fields that are input at the TIE-GCM lower boundary. Furthermore, the TIME-GCM DW1, DW2, S0, and SE2 zonal wind amplitudes depicted in Figure 2.6 are at least 5 m s^{-1} larger than those derived in CTMT (Figure 2.2, right column), which could also lead to changes in the TIE-GCM simulated zonal-mean IT. It is clear from the above discussion that the TIE-GCM is quite sensitive to changes in the total fields (i.e., background plus perturbations) at its lower boundary.

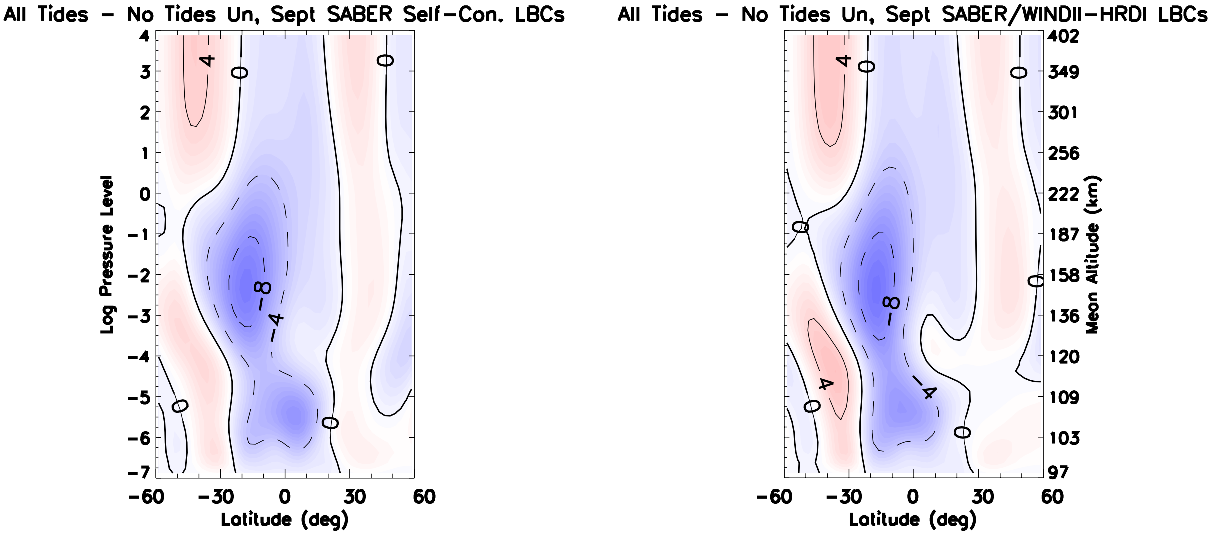
All Tides – No Tides Un, Sept SABER Self–Con. LBCs

All Tides – No Tides Un, Sept SABER/WINDII–HRDI LBCs

Figure 2.7: TIE-GCM zonally- and diurnally-averaged zonal wind differences as a function of latitude and log-pressure level during the month of September. Differences are calculated between TIE-GCM simulations including and excluding CTMT tidal forcing at the model lower boundary; differences calculated using background winds, temperatures, and geopotential heights from SABER are shown in the left panel; differences calculated using background winds from WINDII-HRDI and background temperatures and geopotential heights from SABER are shown in the right right. Zonal wind differences are contoured every 4 m s^{-1}.

To elucidate the effects that changes in the background lower boundary conditions can have on quantifying the role tides play in determining the zonal-mean state of the IT system in the TIE-GCM, we performed a set of numerical experiments in which the only differences between multiple TIE-GCM simulations are the background winds, temperatures, and geopotential heights. Figure 2.7 depicts zonal-mean zonal wind differences from TIE-GCM simulations including and excluding CTMT tidal perturbations at the TIE-GCM lower boundary during the month of September as a function of latitude and log pressure level. The differences calculated in the left panel of Figure 2.7 employed self-consistent background lower boundary conditions from SABER (i.e., the zonal and meridional background winds were calculated from SABER geopotential heights using geostrophic balance). For differences calculated in the right panel of Figure 2.7 background winds from WINDII-

HRDI, in addition to SABER temperatures and geopotential heights were utilized to force the TIE-GCM lower boundary. The latitudinal and vertical structure of the zonal wind differences shown in the left and right panels of Figure 2.7 are almost identical, with maximum differences of -10 m s^{-1} due to tidal dissipation at ~150 km. Similarities in difference fields also extend to include O number density ([O]) and O_2 number density [O_2], as well as TIE-GCM simulations performed under June conditions (not shown), further proving the robustness of the results presented in Figure 2.7. Therefore, the same tidal effects on the zonal-mean IT can be achieved in the TIE-GCM whether or not the background lower boundary conditions are internally consistent, and are not relevant to the results or conclusions offered in subsequent chapters of this dissertation.

2.3 Zonally- and Diurnally-Averaged Equations in the IT from the NCAR TGCMs

This subsection derives the zonally-averaged (i.e., zonally- and diurnally-averaged) equations in the IT using the conservation equations invoked in the NCAR TGCMs, while also discussing these in the context of linear tidal theory. This is done in order to frame the results discussed in Chapters 4, 5, and 6, which aim to answer science questions (2a), (2b), and (2c), respectively. The effects that atmospheric tides have on the mean IT dynamics, temperature, and composition are best understood by writing out the continuity equation, the horizontal momentum equations, the thermodynamic energy equation, and the hydrostatic approximation in log-pressure pressure and spherical coordinates following Dickinson et al. [10] and Holton [53], which can be expressed as:

$$\frac{1}{a\cos\theta}\frac{\partial u}{\partial \lambda} + \frac{1}{a\cos\theta}\frac{\partial}{\partial \theta}(v\cos\theta) + \frac{\partial w}{\partial z} - \frac{w}{H} = 0, \tag{2.2}$$

$$\begin{aligned}\frac{\partial u}{\partial t} + \frac{u}{a\cos\theta}\frac{\partial u}{\partial \lambda} + \frac{v}{a\cos\theta}\frac{\partial}{\partial \theta}(u\cos\theta) + w\frac{\partial u}{\partial z} - \frac{uv\tan\theta}{a} = \\ -\frac{1}{a\cos\theta}\frac{\partial \Phi}{\partial \lambda} + 2\Omega v\sin\theta - \lambda_{xy}(v - v_i) - \lambda_{xx}(u - u_i) + \frac{1}{\rho_0}\frac{\partial}{\partial z}\Big(\mu\frac{\partial u}{\partial z}\Big),\end{aligned} \tag{2.3}$$

$$\begin{aligned}\frac{\partial v}{\partial t} + \frac{u}{a\cos\theta}\frac{\partial v}{\partial \lambda} + \frac{v}{a}\frac{\partial v}{\partial \theta} + w\frac{\partial v}{\partial z} + \frac{u^2\tan\theta}{a} = \\ -\frac{1}{a}\frac{\partial \Phi}{\partial \theta} - 2\Omega u\sin\theta + \lambda_{yx}(u - u_i) - \lambda_{yy}(v - v_i) + \frac{1}{\rho_0}\frac{\partial}{\partial z}\Big(\mu\frac{\partial v}{\partial z}\Big),\end{aligned} \tag{2.4}$$

$$\frac{\partial T}{\partial t} + \frac{u}{a\cos\theta}\frac{\partial T}{\partial \lambda} + \frac{v}{a}\frac{\partial T}{\partial \theta} + w\left(\frac{\partial T}{\partial z} + \frac{\kappa T}{H}\right) = \frac{J}{c_p} + \frac{1}{\rho_0 c_p}\frac{\partial}{\partial z}\left[K_T\frac{\partial T}{\partial z} + K_E c_p \rho_0\left(\frac{g}{c_p} + \frac{\partial T}{\partial z}\right)\right], \quad (2.5)$$

$$\frac{\partial \Phi}{\partial z} = \frac{RT}{H}, \quad (2.6)$$

where the geopotential (Φ) is used in 2.3 and 2.4 instead of pressure because $\nabla\Phi = \frac{1}{\rho}\nabla p$, and the ideal gas law takes the same form as equation 1.4. The infrared (IR) radiative cooling due to nitric oxide (NO), carbon dioxide (CO_2), and $O(^3P)$ are considered within the diabatic heating term (J) in 2.5. Equations 2.2 and 2.6 are the continuity equation and the hydrostatic approximation, respectively. Equations 2.3 and 2.4 are the east-west and north-south components of the vector horizontal momentum equation 1.5, where $\mathbf{OF}_{\mathbf{V_h}}$ is now expanded to include the dissipative forces in the TGCMs (i.e., ion drag and vertical viscosity). Specifically, the dynamic viscosity (μ) in 2.3 and 2.4, encompasses both molecular and eddy diffusion, where $\mu \equiv (\mu_0 + \rho_0\nu_{eddy})$. Equation 2.5 is the full thermodynamic energy equation, which expands the advective derivative and $\mathbf{OF}_T$ shown in equation 1.7 to include molecular and eddy heat conduction. Please note that equations 2.3 - 2.5 include dissipative terms (i.e., the last terms on the right hand side of 2.3 - 2.5) specifically related to IT processes accounted for in the NCAR TGCMs, which is different from Holton [53] wherein he neglects dissipative processes in the stratosphere and mesosphere. One must also note that the form of the dissipative forces in equations 2.3 - 2.5 are consistent with the log-pressure vertical coordinate used by Holton [53]; thus these terms take a slightly different form in the NCAR TGCMs due to the use of a dimensionless log-pressure vertical coordinate (Dickinson et al. [10]). The thermodynamic energy equation (2.4) takes a slightly different form than that shown in Holton [53], as we assume that the temperature and geopotential fields take their full form (i.e., dependent on the spatial coordinates, altitude, and time). Lastly, the ion drag coefficients (i.e., the λ_s terms) are given by:

$$\lambda_{xx} = \frac{\sigma_P B^2}{\rho}(1 - \sin^2\delta\cos^2 I),$$

$$\lambda_{yy} = \frac{\sigma_P B^2}{\rho}(1 - \sin^2\delta\cos^2 I),$$

$$\lambda_{yx} = \frac{\sigma_P B^2}{\rho}(\sin\delta\cos\delta\cos^2 I) + \frac{\sigma_H B^2}{\rho}(\sin I),$$

$$\lambda_{xy} = -\frac{\sigma_P B^2}{\rho}(\sin\delta\cos\delta\cos^2 I) + \frac{\sigma_H B^2}{\rho}(\sin I).$$

where δ is the magnetic declination angle, I is the magnetic inclination or dip angle, B is the magnetic field strength, and σ_P (σ_H) is the Pedersen (Hall) conductivity.

In the context of classical tidal theory the assumptions (1) - (5) outlined in section 1.2.2 are made to arrive at equations 2.2 - 2.6. The last step before reaching the zonally-averaged conservation equations that govern neutral motions, temperature, and mass in the IT system is rewriting the conservation laws in flux form. Assuming density follows the barometric law the vertical derivative term in the continuity equation (2.2) can be re-written as:

$$\frac{1}{a\cos\theta}\frac{\partial u}{\partial\lambda} + \frac{1}{a\cos\theta}\frac{\partial}{\partial\theta}(v\cos\theta) + \frac{1}{\rho_0}\frac{\partial}{\partial z}(\rho_0 w) = 0. \tag{2.7}$$

Equation 2.7 represents the flux form of the continuity equation in log-pressure and spherical coordinates. By multiplying equation 2.7 by u, v, and T, adding those expressions to equations 2.3, 2.4, and 2.5, respectively, and using the product rule results in the following:

$$\begin{aligned}\frac{\partial u}{\partial t} + \frac{1}{a\cos\theta}\frac{\partial u^2}{\partial\lambda} + \frac{1}{a\cos^2\theta}\frac{\partial}{\partial\theta}(uv\cos^2\theta) + \frac{1}{\rho_0}\frac{\partial}{\partial z}(\rho_0 uw) =& \\ -\frac{1}{a\cos\theta}\frac{\partial\Phi}{\partial\lambda} + 2\Omega v\sin\theta - \lambda_{xy}(v-v_i) - \lambda_{xx}(u-u_i) + \frac{1}{\rho_0}\frac{\partial}{\partial z}\Big(\mu\frac{\partial u}{\partial z}\Big),&\end{aligned} \tag{2.8}$$

$$\begin{aligned}\frac{\partial v}{\partial t} + \frac{1}{a\cos\theta}\frac{\partial}{\partial\lambda}(uv) + \frac{1}{a\cos\theta}\frac{\partial}{\partial\theta}(v^2\cos\theta) + \frac{1}{\rho_0}\frac{\partial}{\partial z}(\rho_0 vw) + \frac{u^2\tan\theta}{a} =& \\ -\frac{1}{a}\frac{\partial\Phi}{\partial\theta} - 2\Omega u\sin\theta + \lambda_{yx}(u-u_i) - \lambda_{yy}(v-v_i) + \frac{1}{\rho_0}\frac{\partial}{\partial z}\Big(\mu\frac{\partial v}{\partial z}\Big),&\end{aligned} \tag{2.9}$$

$$\begin{aligned}\frac{\partial T}{\partial t} + \frac{1}{a\cos\theta}\frac{\partial}{\partial\lambda}(uT) + \frac{1}{a\cos\theta}\frac{\partial}{\partial\theta}(vT\cos\theta) + \frac{1}{\rho_0}\frac{\partial}{\partial z}(\rho_0 wT) + w\frac{\kappa T}{H} =& \\ \frac{J}{c_p} + \frac{1}{\rho_0 c_p}\frac{\partial}{\partial z}\Big[K_T\frac{\partial T}{\partial z} + K_E c_p\rho_0\Big(\frac{g}{c_p} + \frac{\partial T}{\partial z}\Big)\Big].&\end{aligned} \tag{2.10}$$

Equations 2.8, 2.9, and 2.10 are the zonal momentum, meridional momentum, and thermodynamic energy equations in flux form and in log-pressure and spherical coordinates.

From the linear tidal theory perspective we derive the zonal-mean equations by employing assumptions (7) and (8) outlined in section 1.2.2, i.e., decomposing our dependent variables into a zonal-mean quantity varying only in latitude and altitude, and a perturbation quantity depending on all three spatial coordinates and time. One can take the full conservation equations in flux form 2.7 - 2.10, plug in for the dependent variables, take the longitudinal and time average, and arrive at the zonal-mean equations in component form in log-pressure and spherical coordinates, after Holton [53] and Dickinson et al. [10]:

$$\frac{1}{a\cos\theta}\frac{\partial}{\partial\theta}(\overline{v}\cos\theta)+\frac{1}{\rho_0}\frac{\partial}{\partial z}(\rho_0\overline{w})=0, \tag{2.11}$$

$$\begin{aligned}\frac{\overline{v}}{a}\frac{\partial\overline{u}}{\partial\theta}+\overline{w}\frac{\partial\overline{u}}{\partial z}-2\Omega\overline{v}\sin\theta-\frac{\overline{u}\,\overline{v}\tan\theta}{a}+\overline{\lambda_{xy}}\overline{v}=&\\ -\overline{F}_x+\overline{\lambda_{xy}}\overline{v_i}-\overline{\lambda_{xx}}\overline{u}+\overline{\lambda_{xx}}\overline{u_i}-\overline{\lambda'_{xy}v'}+\overline{\lambda'_{xy}v'_i}-\overline{\lambda'_{xx}u'}+\overline{\lambda'_{xx}u'_i}+\frac{1}{\rho_0}\frac{\partial}{\partial z}\Big(\overline{\mu}\frac{\partial\overline{u}}{\partial z}\Big),&\end{aligned} \tag{2.12}$$

$$\begin{aligned}\frac{\overline{v}}{a}\frac{\partial\overline{v}}{\partial\theta}+\overline{w}\frac{\partial\overline{v}}{\partial z}+2\Omega\overline{u}\sin\theta+\frac{\overline{u}^2\tan\theta}{a}-\overline{\lambda_{yx}}\overline{u}=&\\ -\frac{1}{a}\frac{\partial\overline{\Phi}}{\partial\theta}-\overline{F}_y-\overline{\lambda_{yx}}\overline{u_i}-\overline{\lambda_{yy}}\overline{v}+\overline{\lambda_{yy}}\overline{v_i}+\overline{\lambda'_{yx}u'}-\overline{\lambda'_{yx}u'_i}-\overline{\lambda'_{yy}v'}+\overline{\lambda'_{yy}v'_i}+\frac{1}{\rho_0}\frac{\partial}{\partial z}\Big(\overline{\mu}\frac{\partial\overline{v}}{\partial z}\Big),&\end{aligned} \tag{2.13}$$

$$\frac{\overline{v}}{a}\frac{\partial\overline{T}}{\partial\theta}+\overline{w}\overline{S}=\frac{\overline{J}}{c_{p0}}-\overline{G}+\frac{1}{\rho_0 c_{p0}}\frac{\partial}{\partial z}\Big[\overline{K_T}\frac{\partial\overline{T}}{\partial z}+\overline{K_E}\rho_0 c_{p0}\Big(\frac{g}{c_{p0}}+\frac{\partial\overline{T}}{\partial z}\Big)\Big], \tag{2.14}$$

where $\overline{S}=(\frac{\partial\overline{T}}{\partial z}+\frac{\kappa\overline{T}}{H})$ is the static stability, and $\overline{F}_x$, $\overline{F}_y$, and $\overline{G}$ are zonal and time averages of the products of the perturbations (tides). $\overline{F}_x$, $\overline{F}_y$, and $\overline{G}$ are the so-called *eddy momentum and eddy heat source* terms (*eddy flux* terms in Holton [53]) and are defined as follows:

$$\overline{F}_x\equiv\frac{1}{a\cos^2\theta}\frac{\partial}{\partial\theta}(\overline{u'v'}\cos^2\theta)+\frac{1}{\rho_0}\frac{\partial}{\partial z}(\rho_0\overline{u'w'}),$$

$$\overline{F}_y\equiv\frac{1}{a\cos\theta}\frac{\partial}{\partial\theta}(\overline{v'^2}\cos\theta)+\frac{1}{\rho_0}\frac{\partial}{\partial z}(\rho_0\overline{v'w'})+\frac{\overline{u'^2}\tan\theta}{a},$$

$$\overline{G}\equiv\frac{1}{a\cos\theta}\frac{\partial}{\partial\theta}(\overline{v'T'}\cos\theta)+\frac{1}{\rho_0}\frac{\partial}{\partial z}(\rho_0\overline{w'T'})+\frac{\kappa}{H}\overline{w'T'}.$$

Equations 2.11, 2.12, 2.13, and 2.14 are the zonal-mean continuity, zonal momentum, meridional momentum, and thermodynamic energy equation. $\overline{F}_x$, $\overline{F}_y$, and $\overline{G}$ or the eddy momentum and eddy heat source terms represents the deposition of momentum and energy into the zonal-mean IT due to the dissipating tides. The individual forcing terms in these equations will be defined in Chapters 4, 5, and 6.

2.4 Analysis Methodology

2.4.1 Spectral Analysis

Spectral analysis is used extensively in this study. Remember from equation 1.18 that a tidal or planetary wave perturbation in Earth's atmosphere is periodic in time and longitude, and thus can be represented by a linear combination of sinusoidal basis functions. Therefore, tidal and planetary wave amplitudes and phases are extracted from TIE- and TIME-GCM data using Fourier Analysis and the discrete 2-dimensional Fast Fourier Transform (FFT) Function in Interactive Data Language (IDL). Any model field f at particular latitude and altitude is a function of time and longitude only, and a discrete Fourier transform of $f(t, \lambda)$ from physical space into frequency (m) and zonal wavenumber (s) space is given by

$$F(m, s) = \frac{1}{M_t N_\lambda} \sum_{t_i=0}^{M_t-1} \sum_{\lambda_i=0}^{N_\lambda-1} f(t_i, \lambda_i) \exp\left[-2\pi i\left(\frac{t_i m}{M_t} + \frac{\lambda_i s}{N_\lambda}\right)\right], \tag{2.15}$$

where $f(t, \lambda)$ is some arbitrary model field, $F(m, s)$ is the complex amplitude resulting from the FFT of a specific tidal or planetary wave component with frequency m and zonal wavenumber s, M_t (N_λ) is the total number of points in the time (longitude) domain, and t_i (λ_i) is the time (longitude) index, running from 0 to $t_i - 1$ $(\lambda_i - 1)$. The amplitude $A_{m,s}$ and phase $\phi_{m,s}$ of a particular tidal or planetary wave component as a function of latitude and altitude is then given by

$$A_{m,s}(\theta, z) = |F(m, s)| = \sqrt{Re[F(m, s)]^2 + Im[F(m, s)]^2}, \tag{2.16}$$

and

$$\phi_{m,s}(\theta, z) = \tan^{-1}\left[\frac{Im[F(m, s)]}{Re[F(m, s)]}\right]. \tag{2.17}$$

Any full model field can also be reconstructed from the amplitudes and phases of the tides or planetary waves solved for in 2.14 and 2.15 following:

$$f(\lambda, \theta, z, t) = \sum_{s=-k}^{s=+k} \sum_{m=0}^{m=N_m} A_{m,s}(\theta, z) \cos(m\Omega t + s\lambda - \phi_{m,s}(\theta, z)), \tag{2.18}$$

where $f(\lambda, \theta, z, t)$ is a linear superposition of a spectrum of tides and planetary waves with zonal wavenumbers of ±k and frequencies ranging from 0 to N_m. Equation 2.18 allows one to evaluate the contribution of an individual or a small subset of waves to the total IT system variable in question.

2.4.2 Difference Fields

The calculation of difference fields between two different numerical experiments performed with the TIE- or TIME-GCM allows one to isolate the essential physical processes that lead changes in the IT system. Figure 1.2 in Chapter 1 and Figure 2.7 above in Chapter 2 provide two examples of difference fields calculated between TIME- and TIE-GCM simulations including and excluding lower boundary tidal forcing, which provide a means to quantify the effects upward propagating tides can on the zonal-mean IT system. Taking differences in numerous IT variables and individual forcing terms in equations 2.11-2.14 from NCAR TGCMs simulations that have different magnetic field configurations, lower boundary background and tidal conditions, solar cycle and seasonal conditions is widely used throughout the remainder of this study.

Chapter 3

Non-migrating Tides in the IT: In situ versus Tropospheric Sources

As was discussed in Section 1.3.1, diurnal and semidiurnal non-migrating tides in the upper IT have been observed by instruments onboard the SETA, GRACE, and CHAMP satellites. Prior studies (e.g., Oberheide et al., [87]; Forbes et al., [35]) propose that plasma-neutral interactions vary longitudinally and could be responsible for the in-situ generation of non-migrating tides in the upper IT. In this chapter, science question (1) is addressed, by demonstrating how magnetic control of ion-neutral interactions in the IT system effectively produces source terms for non-migrating tides in the neutral momentum equations for the thermosphere. The TIME-GCM is utilized to quantify these tides, and to assess their importance relative to those that propagate upward from lower atmospheric regions. A detailed discussion on the numerical experiments performed with the TIME-GCM, methodology, and hydromagnetic coupling process is offered. Additionally, an analysis of the aggregate effects of these in-situ generated non-migrating tides in the IT system is presented. This chapter is the expanded version of a previously published Journal of Geophysical Research (JGR): Space Physics journal article by Jones Jr. et al. [59].

Supplemental figures for this chapter are located in Appendix B.

3.1 Introduction and Motivation

During the past decade, and more specifically during the most recent solar minimum period, there has been an upsurge of interest in meteorological influences on IT variability or space weather. Due to the restrictions imposed by space-based observing platforms, most of the emphasis has been on the longitudinal, seasonal, and interannual variability, which is mainly attributed to atmospheric tides. In the context of classical tidal theory (Chapman and Lindzen, [5]), solar thermal tides in Earth's atmosphere require that they be *directly* forced by the Sun. Other dynamical features that project onto tidal periods and their longitudinal variations, or that vary over intervals shorter than the five to fifteen day set-up time for tides (Vial et al., [122]) are known as "pseudo-tides" (e.g., Walterscheid et al., [123]). Notably, analyses of observational data, or self-consistent atmosphere-ionosphere general circulation simulations (i.e., the NCAR TGCMs), cannot distinguish tides from pseudo-tides. Therefore, in this chapter we broadly characterize all Fourier components that project onto tidal periods as "tides". In addition to tides excited by thermal sources, our definition encompasses tidal components created by stationary planetary wave-tide (e.g., Angelats i Coll and Forbes, [54]) and tide-tide interactions (Hagan et al., [45]), along with in-situ thermospheric wind-ion drag interactions that give rise to a spectrum of tidal components. The latter are the foci of this chapter.

Previous studies aimed at understanding the effects of upward propagating tides on the dynamics and structure of the ionosphere set the stage for the present investigation, in which interactions between the ionospheric plasma and the neutral atmosphere are considered. For instance, Sagawa et al. [109] first observed the wave-4 longitudinal structure in the F-region ionosphere and its seasonal variability that Immel et al. [56] later proposed was driven by upward propagating tides modulating E-region dynamo driven electric fields. Numerical experiments later confirmed that non-migrating tides generated by the latent heat release associated with convective clouds in the tropical troposphere modulate dynamo region electric fields producing wave-4 longitude variations in the F-region (Hagan et al., [46]). Direct penetration of upward propagating tides (e.g., England et al., [19] and England et al., [17]), in addition to an in situ non-linear interaction between DE3 and DW1 (producing SPW4 and SE2) contribute to the wave-4 longitude structure observed in the IT system (Hagan et al., [45]). The production of secondary waves due to non-linear tide-tide interactions also act to alter the four-peaked structure in the F-region (Obeheride et al., [86]).

As was previously discussed, migrating tides generated in the troposphere, stratosphere, and mesosphere have been extensively studied since the 1970s (Chapman and Lindzen, [5]; Forbes and Garrett, [28], Forbes, [24];[23]; Hagan, [40] and references therein). Migrating tides can also be generated in-situ in the thermosphere due to EUV absorption. Latent heat release from deep tropical convection in the upper troposphere produces non-migrating tides which propagate vertically into the thermosphere. Specifically, Oberheide et al. [85] found that DE3 attains its maximum amplitude in the upper thermosphere during solar minimum conditions due to reduced molecular dissipation above 120 km. Non-migrating tides are also produced in situ through non-linear tide-tide and tide-planetary wave interactions (Teitelbaum et al., [120]; McLandress, [74]; Angelats i Coll and Forbes, [54]; Forbes et al., [36]; Hagan et al., [45] and references therein). However, the question still remains, does a longitude-dependent ionosphere provide a means for in-situ generation of non-migrating tides through ion-neutral coupling, as suggested by Oberheide et al. [87] and Forbes et al. [35]?

This chapter aims to understand how, and to what extent, longitude variations in the ionosphere, primarily imposed by a realistic magnetic field configuration, introduce complexities in ion-neutral coupling that project onto diurnal and semidiurnal non-migrating tidal components in the neutral atmosphere (i.e., science question (1) and all of its subquestions). For this purpose the TIME-GCM is employed to perform numerical experiments that isolate the essential physics. These include simulations that compare results based on the International Geomagnetic Reference Field 2010 (IGRF 2010) with those characterized by a longitude-independent dipole field aligned with Earth's rotation axis. In addition, we consider how tropospherically-generated tides compete with this in-situ source by including/excluding tidal forcing based on the GSWM-09 at the lower boundary of the TIME-GCM. Spectral decomposition of steady-state September TIME-GCM simulations with the aforementioned magnetic field configurations, in accordance with the inclusion or exclusion of tidal forcing at the model lower boundary, provides a means to quantify the magnitude of the non-migrating tidal components generated in-situ due to ion-neutral interactions within the IT system. The relative importance of tidal components at different levels of solar activity is examined. The results presented in this chapter should prove insightful during the upcoming solar maximum period when space-based satellite observations of upper thermospheric longitudinal variability may be partially attributed to the in-situ generation of non-migrating tides through ion-neutral coupling processes, in addition to the vertical propagation of tides from below.

3.2 TIME-GCM Simulations and Methodology

A general description of the TIME-GCM and the TIME-GCM simulations performed as part of this work was offered in Chapter 2 including the model version and resolution, geomagnetic proxies, and background lower boundary conditions utilized herein. All six TIME-GCM simulations used to produce the results discussed below were run for the month of September (i.e., day of year 264) until the model reached a diurnally reproducible state. Simulations were performed for solar minimum (solar maximum) conditions using a F10.7 solar radio flux value of 75 sfu (10^{-22} W m^{-2} Hz^{-1}) (200 sfu). Migrating and non-migrating tides calculated from the GSWM-09 are input at the TIME-GCM lower boundary for our simulations performed to quantity potential tropospheric effects on the IT system. Please note that the GSWM-09 non-migrating tides introduced at the model lower boundary are the sole source of tropospheric non-migrating tides in the TIME-GCM.

In order to frame this work, an overview of characteristic thermospheric circulations is provided in Figure 3.1, and the following definitions are made. An “idealized” circulation is defined to be a flow that exists in the presence of a dipole magnetic field aligned with Earth’s rotation axis and without tidal forcing at the lower boundary. When the dipole magnetic field is replaced by the IGRF field (still without lower boundary tidal forcing), the corresponding thermospheric circulation is referred to as “modified”. And finally, when the additional effects of tidal forcing from the GSWM-09 are imposed at the TIME-GCM lower boundary, we arrive at what is referred as the “realistic” thermosphere circulation. Taking into account the historical works by Dickinson and Roble [13] and Roble and Dickinson [105], we hypothesize that ion-neutral interactions in the IT system are driven by ionization anomalies due to a longitudinal-dependent ion drag term in the horizontal momentum equations, thus leading to significant differences between the modified and idealized circulations defined above. Similarly, differences between the realistic and modified

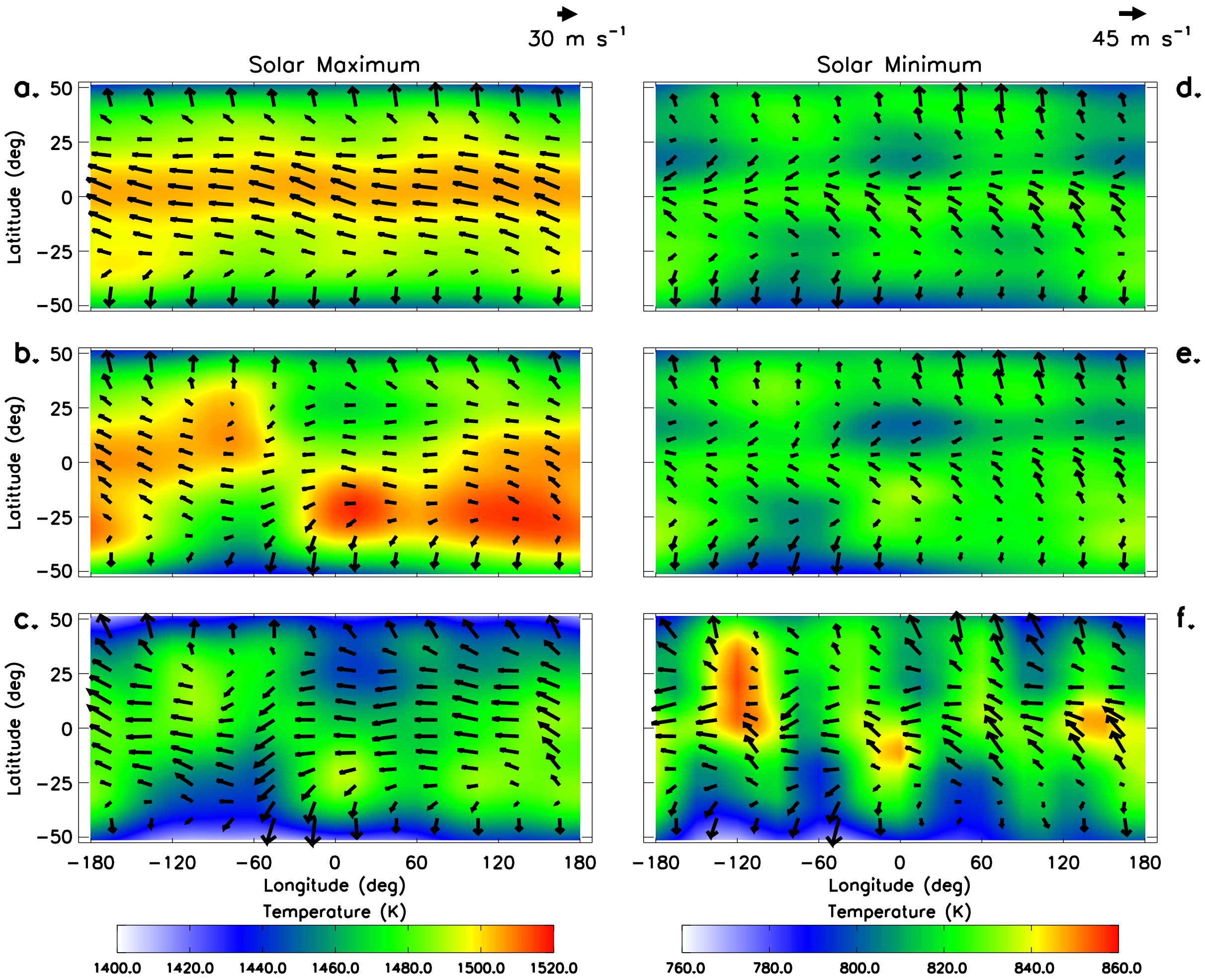

Figure 3.1: TIME-GCM winds and temperatures at log-pressure level 3.5 (∼500 km) at 15 LT during September for (a) idealized flow (aligned dipole magnetic field configuration and no GSWM-09 tidal forcing at the lower boundary) during solar maximum, (b) modified flow (realistic magnetic field configuration with no GSWM-09 tidal forcing at the lower boundary) during solar maximum, (c) realistic flow (realistic magnetic field configuration with GSWM-09 tidal forcing at the lower boundary) during solar maximum. (d), (e), and (f) are the same as (a), (b), and (c) except for solar minimum conditions at log-pressure level 3.5 (∼350 km).

circulations isolate the effects of tides entering the thermosphere from below.

Figures 3.1c and 3.1f show the TIME-GCM realistic flow overlaid on the corresponding temperature field on equivalent log-pressure levels (i.e. $\ln(\frac{p_0}{p}) = 3.5$) under solar maximum (∼500 km) and solar minimum conditions (∼350 km), respectively. Based on spectral analysis, the dominant zonal wavenumber for the structures in the temperature and wind fields in Figure 3.1f is wave-4 under solar minimum conditions, whereas a much smaller wave-4 occurs at solar maximum, and is not identifiable visually in Figure 3.1c. This is consistent with the differential dissipation that occurs between solar minimum and solar maximum for upward-propagating tides DE3 and SE2, which account for most of the wave-4 structure in the neutral atmosphere (Oberheide et al., [85]). Removing GSWM-09 tidal forcing at the TIME-GCM lower boundary (Figures 3.1b and 3.1e) causes a clear difference in the longitudinal variability in the temperature field. However, the resulting modified thermospheric circulation at solar maximum is similar in latitudinal structure and magnitude (Figure 3.1b) to the realistic circulation observed in Figure 3.1c, whereas notable differences are seen between these circulations at solar minimum (Figures 3.1e and 3.1f). Prescribing an idealized dipole magnetic field and removing tidal forcing at the lower boundary reveals the idealized neutral wind circulation and temperature fields for solar maximum and minimum shown in Figures 3.1a and 3.1d. Comparison between the thermospheric temperature and wind fields in Figure 3.1a with that of Figure 3.1b clearly show that significant spatial variability in the thermospheric temperature distribution and circulation is introduced in the presence of a longitude-dependent ionosphere at solar maximum. This modified circulation at solar maximum exists due to ion drag source terms in the horizontal momentum equations, which act to perturb the thermospheric circulation from its otherwise idealized motion. As we show below, this perturbation projects significantly onto D0 and DW2 non-migrating tides as suggested by Oberheide et al. [87].

The thermospheric temperature and wind fields displayed in Figures 3.1d and 3.1e show that under solar minimum conditions the idealized and modified temperature and winds are nearly identical. Please note that the longitudinal variability in the temperature and wind fields at middle latitudes seen in our idealized simulation during solar minimum (Figure 3.1d) and solar maximum (Figure 3.1a) is driven by the combination of longitudinal variability in the high latitude joule heating and the asymmetry of the auroral oval about the geomagnetic poles. This result is counterintuitive to what one would expect for a simulation that has an aligned dipole magnetic field without GSWM-09 tidal forcing at the model lower boundary, in which we would expect results to be longitudinally independent. However, this longitudinal variability does not have an affect on the remaining results presented herein. Supplementary figures for the joule heating, O, and electron density are shown in Figures B.1 - B.3.

3.3 Hydromagnetic Coupling

To aid in interpreting results presented in Chapter 3, it is useful to think about how the neutral gas is coupled to the ionospheric plasma above about 90 km in Earth's atmosphere. If collision frequencies are sufficiently large between the neutral gas and ionized plasma then momentum exchange amongst the neutrals and plasma is of potential importance (Forbes and Garrett, [28]). All of the assumptions and approximations used in the mathematical formulation of hydromagnetic coupling effects on the neutral gas horizontal momentum equations are discussed in this section following the works of Richmond [100], Forbes and Garrett [28], and references therein.

Hydromagnetic coupling processes affect tidal winds as a result of the Lorentz force (per unit mass) in the horizontal momentum equations, which is of the form

$$\frac{\mathbf{J} \times \mathbf{B}}{\rho_0}, \tag{3.1}$$

where the current density **J** is related to the electric field and winds by Ohm's law:

$$\mathbf{J} = \sigma_0 \mathbf{E}_{\|} + \sigma_1(\mathbf{E}_{\perp} + \mathbf{V} \times \mathbf{B}) + \sigma_2 \hat{b} \times (\mathbf{E}_{\perp} + \mathbf{V} \times \mathbf{B}). \tag{3.2}$$

Assuming a dipole magnetic field aligned with Earth's rotation axis, one can write the simplified form of the Lorentz terms following Richmond [100]:

$$\left[\frac{\mathbf{J} \times \mathbf{B}}{\rho_0}\right]_{\lambda} = -\epsilon_1(u - u_i) + \epsilon_2 \cos\theta_{co}(v - v_i), \tag{3.3}$$

$$\left[\frac{\mathbf{J} \times \mathbf{B}}{\rho_0}\right]_{\theta_{co}} = -\epsilon_1(v - v_i) - \epsilon_2 \cos\theta_{co}(u - u_i), \tag{3.4}$$

where θ_{co} is colatitude, ϵ_1, ϵ_2, and $\mathbf{V_i}$ (plasma drift vector) in 3.3 and 3.4 are given by

$$\epsilon_1 = \frac{\sigma_1 B^2(\theta_{co})}{\rho_0},$$

$$\epsilon_2 = \frac{\sigma_2 B(\theta_{co}) B_{pole}}{\rho_0},$$

$$\mathbf{V_i} = \frac{\mathbf{E} \times \mathbf{B}}{\mathbf{B^2}},$$

and σ_1 and σ_2 are the Pedersen and Hall conductivities, respectively. The Lorentz terms given by 3.3 and 3.4 are equivalent to the λ_s (e.g., $\lambda_{xx}(u - u_i)$) terms in equation 2.3 and 2.4, except that they are defined using colatitude which is positive southward. Additionally, assuming the masses of the neutrals and ions are equal ϵ_1 and ϵ_2 take the form

$$\epsilon_1 \approx \frac{N_i}{N} \frac{\nu_{in}}{1 + (\nu_{in}/\omega_i)^2} \tag{3.5}$$

$$\epsilon_2 \approx \frac{\nu_{in}}{\omega_i} \epsilon_1. \tag{3.6}$$

The terms in 3.3 and 3.4 proportional to ϵ_1 are called the “ion drag” force. In the low and middle latitude F-region the gyrofrequency is much greater than the ion-neutral collision frequency ($\omega_i \gg \nu_{in}$) meaning ions remain “bound” to magnetic field lines. Thus, the neutral gas experiences a loss of momentum when moving across magnetic field lines. This loss of momentum is mainly attributable to zonal momentum exchange due to ion-neutral coupling processes and because the terrestrial magnetic field is tilted in the meridional direction. Terms proportional to ϵ_2 in 3.3 and 3.4 are referred to as the “Hall force”. Through the collisions of neutrals and ions the Hall force acts to deflect the wind. Richmond [99] showed that under moderate sunspot conditions the diurnally averaged ion drag force greatly exceeds that of the Hall force above 130 km. Henceforth, only the hydromagnetic coupling effects due to the ion drag force are discussed.

Essentially, momentum source terms expressible in terms of non-migrating tidal components arise when considering the nonlinear hydromagnetic coupling terms of the form (ϵu) and (ϵv) in 3.3 and 3.4. Following the tidal oscillation formulation employed in 1.22, and expressing 1.22 in exponential form such that the idealized flow is defined as:

$$U_{m,s} \cos(m\Omega t + s\lambda - \phi_{m,s}) = U_{m,s} \frac{e^{i(m\Omega t + s\lambda - \phi_{m,s})} + e^{-i(m\Omega t + s\lambda - \phi_{m,s})}}{2}.$$

After manipulating the complex exponential form of the idealized flow defined above, and considering that the idealized flow is diurnally-varying but longitude-independent in the presence of a dipole magnetic field aligned with Earth's rotation axis,

$$u \approx u_0 + \sum_{s=m=1}^{2} [u^+_{m,s} e^{i(m\Omega t + s\lambda)} + u^-_{m,s} e^{-i(m\Omega t + s\lambda)}], \tag{3.7}$$

where $u^+_{m,s}$ and $u^-_{m,s}$ are the complex amplitudes of the idealized flow. $u^+_{m,s}$ and $u^-_{m,s}$ are given by

$$u^+_{m,s} = \frac{U_{m,s}}{2} e^{i\phi_{m,s}},$$

$$u^-_{m,s} = \frac{U_{m,s}}{2} e^{-i\phi_{m,s}}.$$

The first, second, and third terms in 3.7 represent the zonal-mean zonal wind (u_0), its migrating diurnal ($u_{1,1}$) and migrating semidiurnal ($u_{2,2}$) components, respectively. Latitude variations in all of the above coefficients are implicit. We then ask, what additional momentum source terms appear when a realistic magnetic field is introduced, i.e., when the idealized flow interacts with a longitude-dependent ionosphere ($\epsilon_{m,s}$)? $\epsilon_{m,s}$ takes the following form:

$$\epsilon \approx \epsilon_0 + \sum_{m=0}^{2} \sum_{s=-k}^{k} [\epsilon^+_{m,s} e^{i(m\Omega t + s\lambda)} + \epsilon^-_{m,s} e^{-i(m\Omega t + s\lambda)}] \tag{3.8}$$

where k is equal to the zonal wavenumbers of appreciable ion drag amplitude. For illustration purposes, assume that to first order the more realistic ionosphere now possesses an additional longitude dependence expressible as the zonal mean and SPW1 (i.e., $\epsilon_0 + \epsilon^+_{0,1} e^{i\lambda} + \epsilon^-_{0,1} e^{-i\lambda}$), in other words a wave-1 dependence in longitude. Specifically, this form for the realistic ionosphere is used because the geographic/geomagnetic offset is primarily a wave-1 longitude structure and so SPW1 is important. The product of this term with the zonal mean and DW1 (i.e., $u_0 + u^+_{1,1} e^{i(\Omega t + \lambda)} + u^-_{1,1} e^{-i(\Omega t + \lambda)}$) yields the following source terms in the momentum equation:

$$\begin{aligned} \epsilon u \quad \approx \quad & \epsilon^+_{0,1} u_0 e^{i\lambda} + \epsilon^-_{0,1} u_0 e^{-i\lambda} && \text{(SPW1 terms)} \\ & + \epsilon^+_{0,1} u^+_{1,1} e^{i(\Omega t + 0\lambda)} + \epsilon^-_{0,1} u^-_{1,1} e^{-i(\Omega t + 0\lambda)} && \text{(D0 terms)} \\ & + \epsilon^-_{0,1} u^+_{1,1} e^{i(\Omega t + 2\lambda)} + \epsilon^+_{0,1} u^-_{1,1} e^{-i(\Omega t + 2\lambda)} && \text{(DW2 terms)} \end{aligned}$$

Thus it is expected that the modified circulation will be strongly characterized by SPW1, D0, and DW2. Of course, additional terms in the expansions for u and ϵ will lead to source terms for

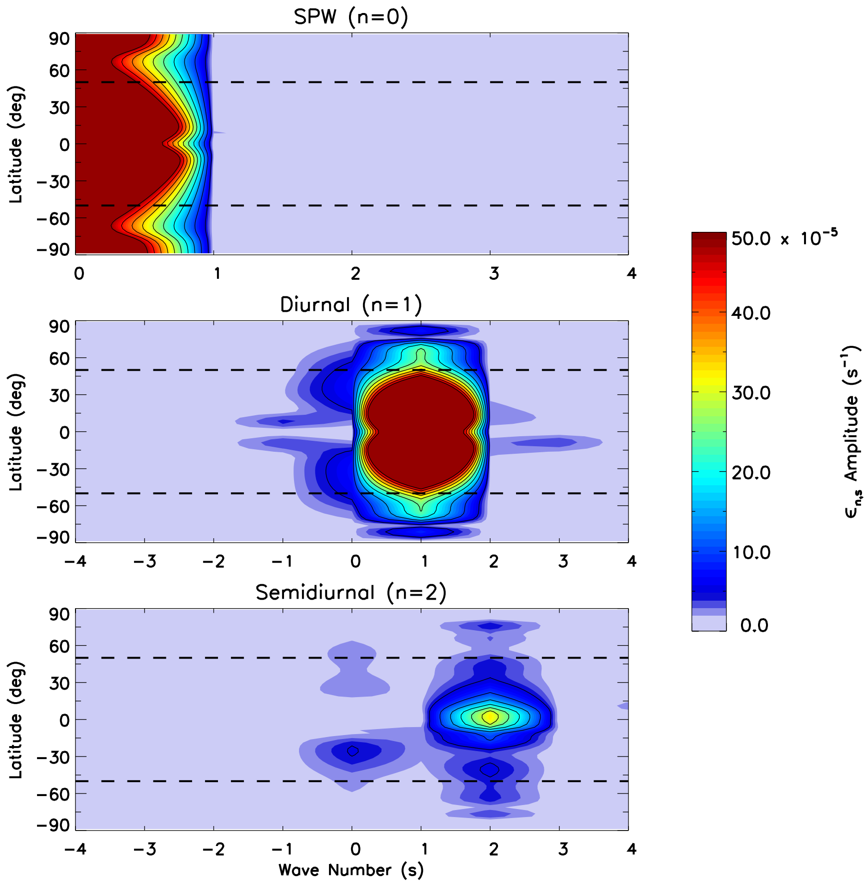

Figure 3.2: Ion drag components ($\epsilon_{m,s}$) calculated from the TIME-GCM at log-pressure level 3.5 (~500 km), during September under solar maximum conditions for the idealized flow regime. Components are contoured every 5×10^{-5} s^{-1}. The dashed lines are at 50° N and 50° S.

additional non-migrating tidal components that constitute the thermospheric circulation modified by the more realistic magnetic field.

Figure 3.2 shows the ion drag components at log-pressure level 3.5 (~500 km), during September under solar maximum conditions for the idealized simulation. The dominant ion drag components are the zonal mean (ϵ_0), DW1 ($\epsilon_{1,1}$), and to a lesser extent SW2 ($\epsilon_{2,2}$), which is what one would expect for a longitude independent ionosphere. Other smaller amplitude ion drag components including D0 ($\epsilon_{1,0}$) and S0 ($\epsilon_{2,0}$) are longitudinally dependent, and arise due to reasons described in Section 3.2. Please note that the widths of the spectra shown in Figure 3.2 are a plotting artifact and therefore do not have any physical meaning. Figure 3.3 is the same as Figure

3.2, but for the modified flow. Figure 3.3 shows that the largest amplitude components of the ion drag terms calculated at solar maximum for the modified ionosphere are SPW1 ($\epsilon_{0,1}$), SPW2 ($\epsilon_{0,2}$), D0, DW2 ($\epsilon_{1,2}$), DW3 ($\epsilon_{1,3}$), and SW2. All the non-migrating ion drag components discussed above and shown in Figure 3.3 have amplitudes that are at least $\sim 1.5 \times 10^{-4}$ s^{-1} greater than those shown for the idealized case (Figure 3.2). The zonal mean (ϵ_0) and DW1 ($\epsilon_{1,1}$) are an order of magnitude larger than the other ion drag terms shown in Figure 3.3, and are therefore set to zero in Figure 3.3 in order to highlight the other ion drag terms of importance in our hydromagnetic coupling expansion. The spectrum of ion drag components from the realistic simulation during solar maximum are shown in Figure B.4, and are similar in amplitude and latitudinal structure to those presented in Figure 3.3, although DE3 ($\epsilon_{1,-3}$) and SE2 ($\epsilon_{2,-2}$) are present.

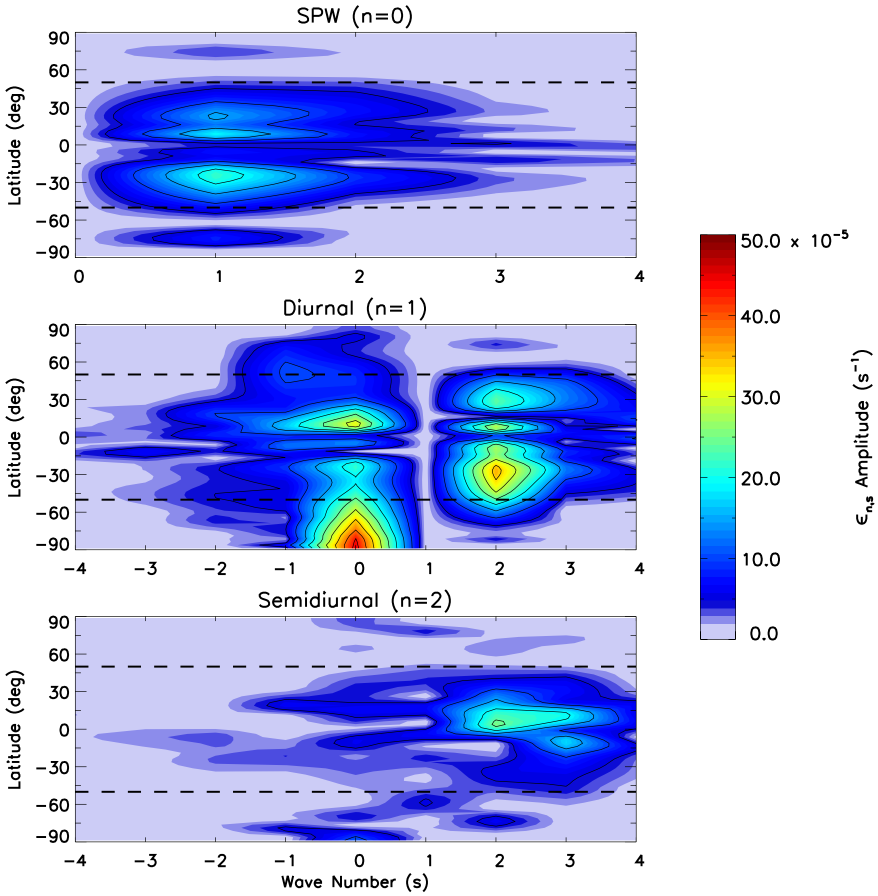

Figure 3.3: Same as Figure 3.2, except for the modified flow and with ϵ_0 (zonal mean) and $\epsilon_{1,1}$ (DW1) set to zero.

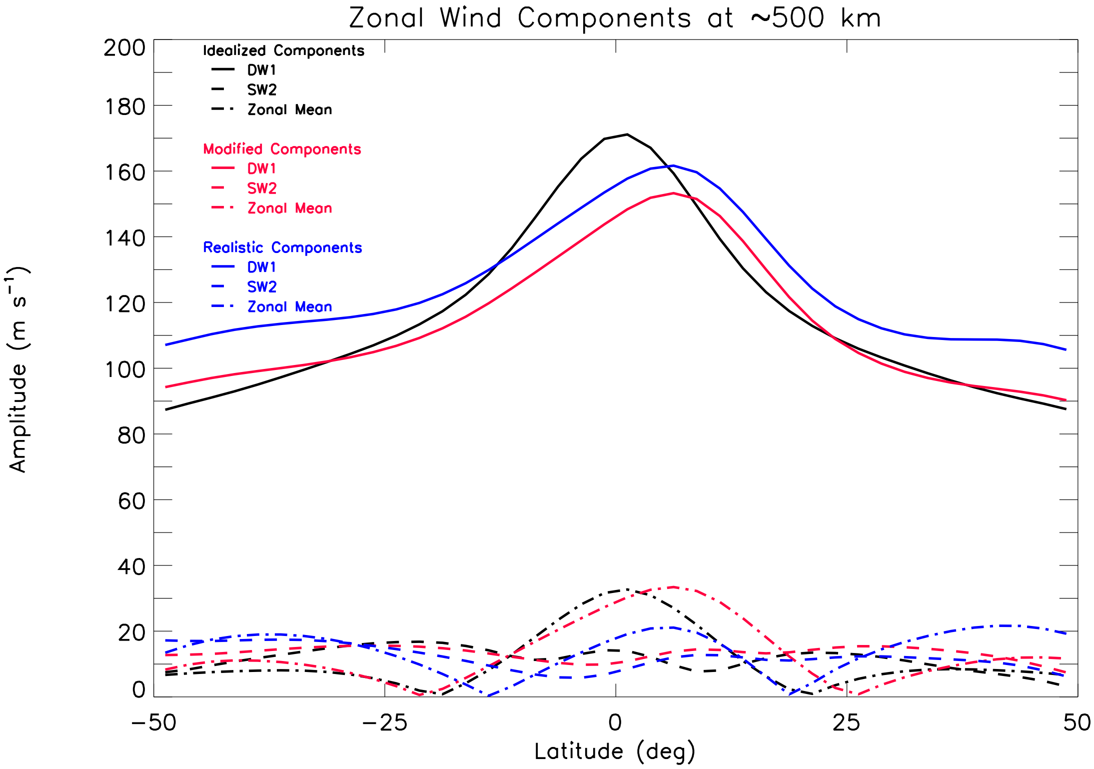

Figure 3.4: Idealized (black lines), modified (red lines), and realistic (blue lines) wind components calculated from the TIME-GCM at log-pressure level 3.5 (~500 km), during September under solar maximum conditions.

The zonal mean (u_0), DW1 ($u_{1,1}$), and SW2 ($u_{2,2}$) are the largest components from the idealized neutral wind circulation at solar maximum, and these are shown in Figure 3.4 (black lines). The more complete set of hydromagnetic coupling terms from above leads to a slight modification of the important idealized zonal wind components (Figure 3.4, red lines). Including GSWM-09 tides at the TIME-GCM lower boundary leads to small reductions (i.e., 10 m s^{-1}) in the zonal mean, DW1, and SW2 zonal wind components (Figure 3.4, blue lines), but the latitudinal structure remains unaltered compared to the modified case (Figure 3.4, red lines). Zonal momentum from DW1 is transferred into the zonal mean and SW2 components, leading to the creation of non-migrating tidal components (Figure 3.5b and 3.5e). Table 3.1 displays the results of a hydromagnetic coupling expansion that uses all the important terms (i.e. those $\epsilon_{m,s}$ values with amplitudes greater than or equal to 2×10^{-4} s^{-1}) from the modified ionosphere and idealized circulation listed above. For example, Table 3.1 shows that hydromagnetic coupling between the DW2 component of the

u,ϵ	ϵ_0	SPW1	SPW2	DE1	D0	DW1	DW2	DW3	SW2	SW3
u_0	mean term	SPW1*	SPW2*	DE1*	D0*	DW1*	DW2*	DW3*	SW2*	SW3*
DW1	DW1*	D0,DW2	DE1,DW3	SPW2,S0	SPW1,SW1	mean term,SW2	SPW1,SW3	SPW2,DW4	DW1,...	DW2,...
SW2	SW2*	SW1,SW3	S0,SW4	DW3,...	DW2,...	DW1,...	D0,...	DE1,...	mean term,...	SPW1,...

Table 3.1: Hydromagentic coupling momentum source terms due to the idealized wind circulation and modified ionosphere following the hydromagnetic coupling expansion given in 3.7 and 3.8. The top row lists the largest ion drag terms ($\epsilon_{m,s}$) from the modified ionosphere shown in Figure 3.3. The first column lists the largest zonal wind terms from the idealized wind circulation ($u_{m,s}$) shown in Figure 3.4 (black lines). The corresponding momentum source terms for the modified circulation consist of the sum and difference products of $\epsilon_{m,s}$ and $u_{m,s}$, which populate the table. Terms with asterisk represent terms that are modified by the zonal-mean quantities. Sum or difference products with $m \geq 3$ are represented by an ellipsis.

modified ion drag ($\epsilon_{1,2}$) and the DW1 ($u_{1,1}$) component of the idealized wind circulation results in a modified wind circulation characterized by SPW1 and SW3 momentum source terms.

Figure 3.5 depicts the zonal wind wave spectra at log-pressure level 3.5 (∼500 km) from the idealized (top), modified (middle), and realistic (bottom) simulations under solar maximum conditions at low and middle latitudes. The migrating tides in both Figures 3.5 and 3.6 are set to zero to accentuate the non-migrating diurnal and semidiurnal tides generally of smaller amplitude. Setting the migrating tides to zero leads no diurnal and small (2 to 3 m s^{-1}) semidiurnal zonal wind non-migrating tidal amplitudes in the idealized case (Figure 3.5, top panels). As expected, the largest diurnal components in the modified circulation are D0 and DW2 which attain amplitudes up to 20 m s^{-1} (Figure 3.5b). These two non-migrating tides come from the interaction between SPW1 and DW1 (as was shown in the initial simplified hydromagnetic coupling expansion). Therefore, D0 and DW2 are generated in-situ in the upper thermosphere due to the non-dipole nature of the geomagnetic field, supporting the conclusion made in Oberheide et al. [87]. Also, interaction between SPW2 and DW1 leads to a relatively large DE1 (∼15 m s^{-1}) zonal wind component at ∼500 km. Coupling between SPW1 and SW2 produces the largest semidiurnal zonal wind components (i.e., SW1 and SW3) in the modified circulation, shown in Figure 3.5e. Amplitudes of SW1 and SW3 range from 3 to 10 m s^{-1}. The smaller S0 and SE1 (amplitudes ranging from 1 to 7 m s^{-1}) components come from coupling between SPW2 with SW2 and SPW3 with SW2, respectively.

Figure 3.5 also shows that at log-pressure level 3.5 (∼500 km) the diurnal and semidiurnal

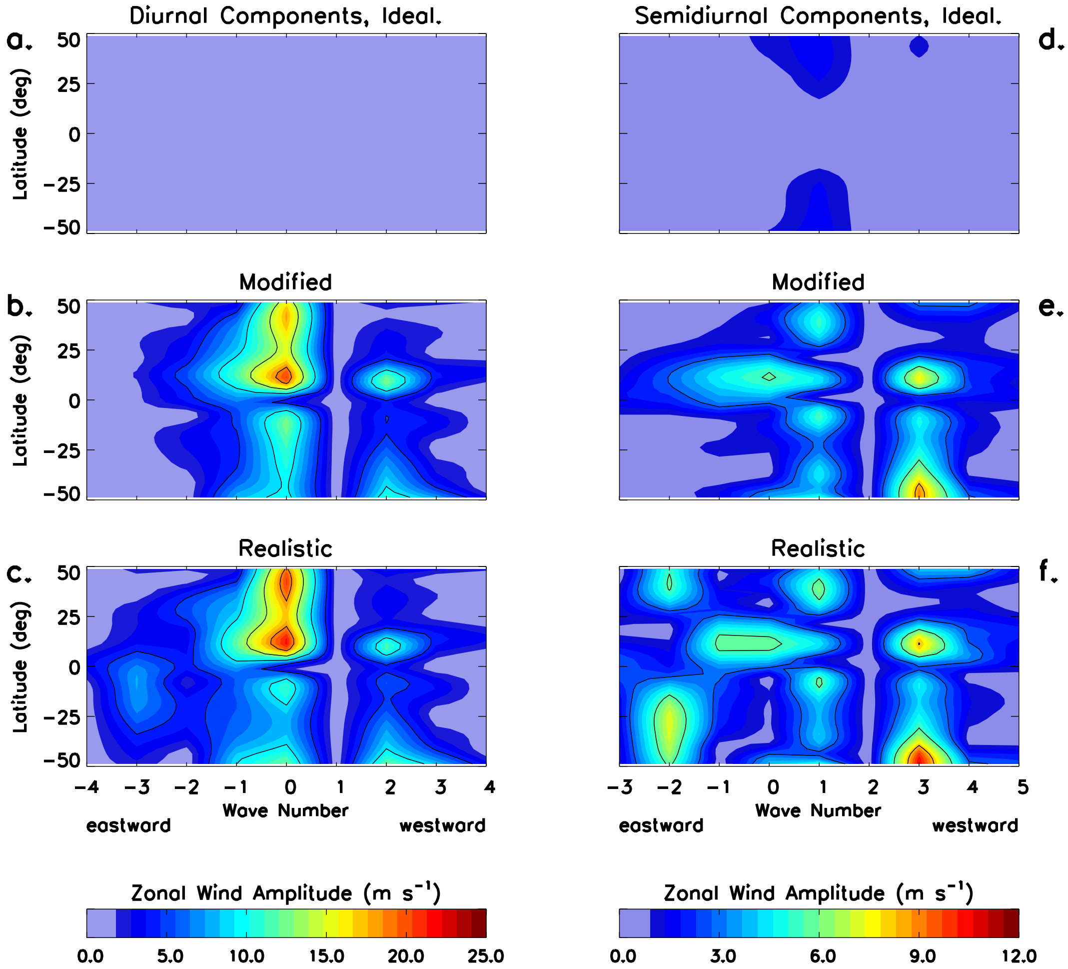

Figure 3.5: Zonal wind wave number spectra of the diurnal and semidiurnal non-migrating tidal components from the TIME-GCM at log-pressure level 3.5 (~500 km), during September solar maximum conditions; a and d correspond to the idealized flow regime, b and e correspond to the modified flow region, and c and f correspond to the realistic flow regime. Diurnal (Semidiurnal) components are contoured every 5 (3) m s^{-1}. The migrating tidal amplitudes have been set to zero.

non-migrating tides are mainly generated in-situ due to ion drag at solar maximum. This can be inferred from the evident similarities in latitudinal structure and amplitude between the above non-migrating tidal components calculated for the realistic (Figures 3.5c and 3.5f) and modified (Figures 3.5b and 3.5e) flows, respectively. Another interesting feature in Figure 3.5 is the latitudinal asymmetries of the non-migrating tides produced via ion-neutral interactions. These latitudinal differences in tidal amplitude are due to the hemispheric asymmetries in the modified ion drag term

(Figure 3.3), as the ionization anomalies that govern ion-neutral interactions are not only longitudinally dependent, but latitudinal dependent as well. Thus, the resulting momentum source terms shown in Figure 3.5 are latitudinally asymmetric because they are generated from the products of the modified (i.e. longitude/latitude dependent) ion drag terms with the idealized wind circulation (following Table 3.1). Other non-migrating tidal components shown in Figures 3.5c and 3.5f include DE3 and SE2, which also appear in the realistic ion drag terms (Figure B.4). Comparison between the realistic and modified circulations show that these tides are of tropospheric origin and are not generated in-situ due to ion-neutral interactions. During solar minimum at log-pressure level 3.5 (∼350 km; Figure 3.6), the dominant diurnal and semidiurnal non-migrating tides present are of tropospheric origin (i.e. DE3 and SE2) and there are few similarities in the modified (Figure 3.6b and 3.6e) and realistic (Figure 3.6c and 3.6f) flow regimes at low to mid-latitudes. This result is consistent with reduced amplitudes in the modified ion drag terms and idealized zonal wind components (i.e., specifically DW1) at solar minimum versus solar maximum (see Figures B.5 and B.6). The amplitude of the modified ion drag term (idealized DW1) was reduced by at least an order of magnitude (∼50 m s^{-1}) due to changes in solar cycle conditions. Therefore, the in-situ ion drag source of non-migrating tides in the upper thermosphere is of utmost importance during solar maximum and upward propagating non-migrating tides of tropospheric origin are dominant at low-latitudes at solar minimum, as was concluded in Oberheide et al. [85].

The results shown Figures 3.5 and 3.6 are also considered in light of tidal diagnostics from the CHAMP satellite presented in recent works by Häusler and Lühr [48] and Häusler et al. [49]. Häusler and Lühr [48] conclude that along the geomagnetic equator D0, DW2, SW1 and SW3 all significantly contribute to the observed wave-1 longitudinal structure at ∼400 km in the zonal wind field. Figure 3.5 shows that our TIME-GCM simulations under solar maximum conditions are largely consistent with the above conclusion as the largest amplitude non-migrating diurnal and semidiurnal tidal components in the zonal wind field are D0, DE1, DW2, SW1, and SW3 at ∼500 km and that these non-migrating tides are a result of using a realistic geomagnetic main field approximation. Further comparison between our TIME-GCM results with CHAMP data displayed

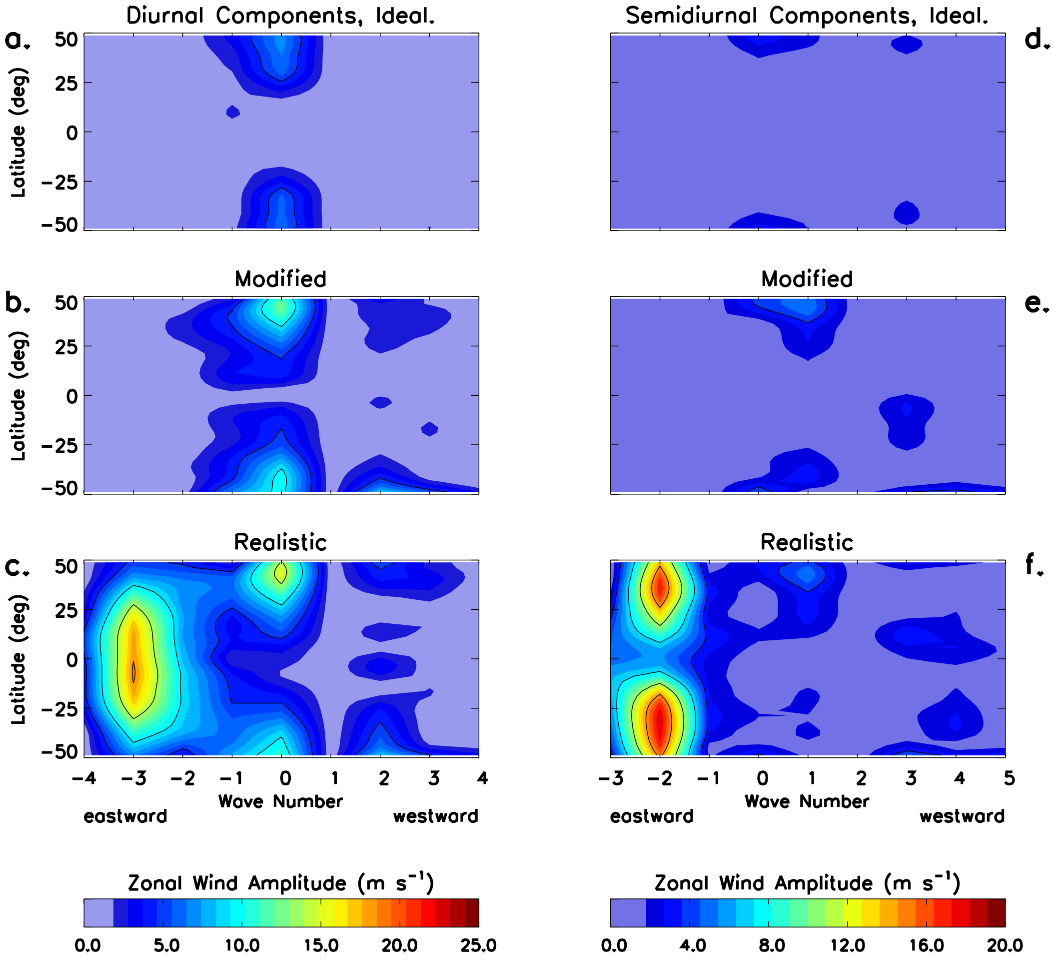

Figure 3.6: Same as Figure 3.5 at equivalent log-pressure level 3.5 (∼350 km) for solar minimum conditions. Diurnal (Semidiurnal) components are contoured every 5 (4) m s^{-1}.

in Häusler et al. [49] clearly shows that the TIME-GCM can correctly produce the solar cycle dependency observed in the tidal spectrum at ∼400 km. For example, at low and middle latitudes Figures 3.5 and 3.6 show an increase (a decrease) in D0 and DW2 (DE2 and DE3) amplitudes with increasing solar flux, which is consistent with CHAMP observations shown in Figure 3 of Häusler et al. [49]. The amplitudes of the above tidal components are of similar magnitude (e.g., 5 to 12 m s^{-1}) in the TIME-GCM and CHAMP observations.

3.4 Spatial Variability Introduced by a Realistic Magnetic Field

As was illustrated in Section 3.3 non-migrating tides in the horizontal wind fields are excited in the presence of a longitudinally-dependent ionosphere associated with a realistic magnetic field configuration (i.e., modified case). The combined effects of these non-migrating tides are substantial at low and middle latitudes, leading to significant spatial variability in horizontal winds. Figure 3.7 depicts the spatial differences in the zonal winds between the modified and idealized circulations under solar maximum conditions at log-pressure level 3.5 (∼500 km) at (a) 2 LT, (b) 8 LT, (c) 14 LT, and (d) 20 LT. The largest zonal wind differences between the modified and idealized circulations occur from 18 LT to 1 LT, and can be seen when comparing the differences shown in Figure 3.7d with Figures 3.7a, 3.7b, and 3.7c. Differences in zonal winds during these local times range from -110 to 140 m s^{-1} and are mainly attributed to differences in the ion drag term between the modified and idealized circulations. The sharp increase in the zonal wind difference at 18 LT coincides with the onset time of the pre-reversal enhancement (PRE), which is defined as a sharp increase in the vertical ion drift motion around sunset via an enhancement of the eastward electric field strength in the E-region. Since ion motions are organized relative to the Earth's magnetic field, a spatially variant ionosphere (i.e - modified case) will lead to spatially variant ion concentrations along these magnetic field lines. Thus, zonal wind differences between the modified and idealized circulations starting around dusk (∼18 LT) and persisting to around midnight (∼0 LT) are most likely driven by the PRE. Smaller zonal wind differences (-60 to 80 m s^{-1}) occur from 2 LT to 17 LT, and these smaller zonal wind differences are attributable to considerably smaller differences in both the ion drag and pressure gradient terms in the zonal momentum equation. Zonal wind differences at solar minimum (Figure B.7) from 18 LT to 1 LT (2 LT to 17 LT) are smaller by a factor of ∼8 (∼2) when compared to solar maximum results. Throughout the entire day meridional wind differences (Figures B.8 and B.9) are driven by a combination of the pressure gradient force differences and zonal momentum response differences. Between 18 LT to 1 LT at solar maximum, meridional wind differences are larger by a factor of ∼3 when compared with solar minimum meridional wind differences. However, from 2 LT to 17 LT meridional wind differences are comparable between the solar maximum and solar minimum.

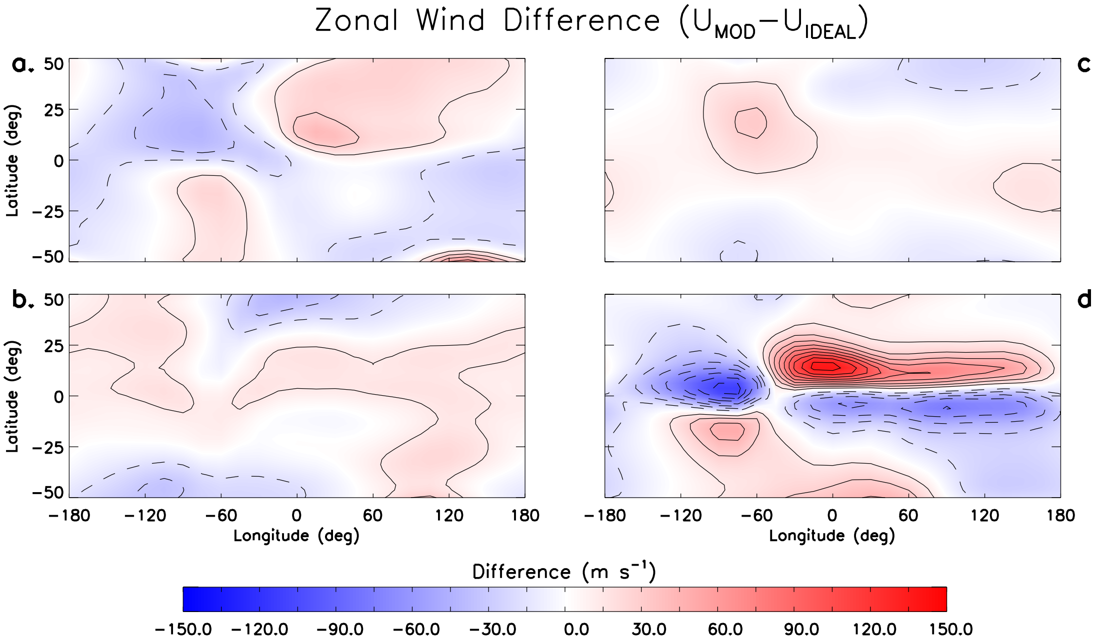

Figure 3.7: Zonal wind differences between the modified and idealized circulations at log-pressure level 3.5 (~500 km) during September under solar maximum conditions at (a) 2 LT, (b) 8 LT, (c) 14 LT, and (d) 20 LT contoured every ±15 m s^{-1}.

It is important to note that temperature differences between the modified and idealized cases also exist, due to adiabatic heating and cooling differences. Adiabatic heating and cooling differences are a result of vertical wind differences between the modified and idealized cases. This is best illustrated at night, in the absence of solar heating. For example, Figure 3.8 compares difference fields of two terms in the thermodynamic energy equation at 3 LT with the temperature differences between the modified and idealized cases at 5 LT and ~500 km at low and middle latitudes during solar maximum. Specifically, Figure 3.8a shows the adiabatic heating and cooling differences between the modified and idealized cases, while Figure 3.8b shows the differences of the time derivative of temperature between the modified and idealized cases. Similar spatial structures in the difference fields displayed in Figures 3.8a and 3.8b imply that the adiabatic heating and cooling term is the dominant term in the thermodynamic energy equation, thereby leading to the

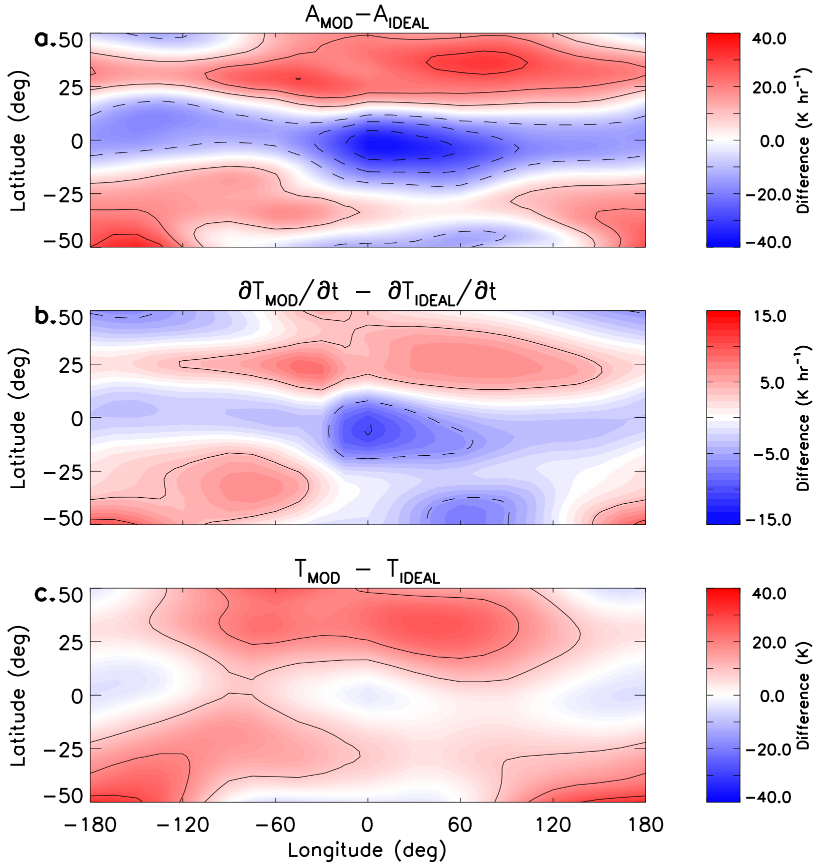

Figure 3.8: (a) Adiabatic heating differences between the modified and idealized circulations at log-pressure level 3.5 (~500 km) during September under solar maximum conditions at 3 LT contoured every 10 K° hr^{-1}. (b) same as (a) for time derivative of temperature derivative differences contour every 5° K hr^{-1}. (c) same as (a) for temperature differences at 5 LT contoured every 10° K.

greatest changes in temperature with time. Further comparison between the difference fields of $\frac{\partial T}{\partial t}$ (Figure 3.8b) at 3 LT and the overall temperature differences shown in Figure 3.8c at 5 LT, reveals similar spatial features. An analogous result is depicted in Figure 3.9 during solar minimum conditions, leading us to conclude that adiabatic heating and cooling differences are ultimately responsible for low and middle latitude temperature differences between the modified and idealized circulations at night, independent of solar cycle condition. However, it is of note that at solar maximum the temperature differences calculated are larger than those at solar minimum mainly due to larger ionization anomalies. Also, in order to completely replicate the time derivative of temperatures differences shown in Figures 3.8b and 3.9b the other terms from the thermodynamic energy equation, including heat transfer by molecular conduction, advection, and radiative cooling must be considered. At night these terms are comparatively small when compared to the adiabatic heating and cooling term. However, during the daytime these terms become non-negligible.

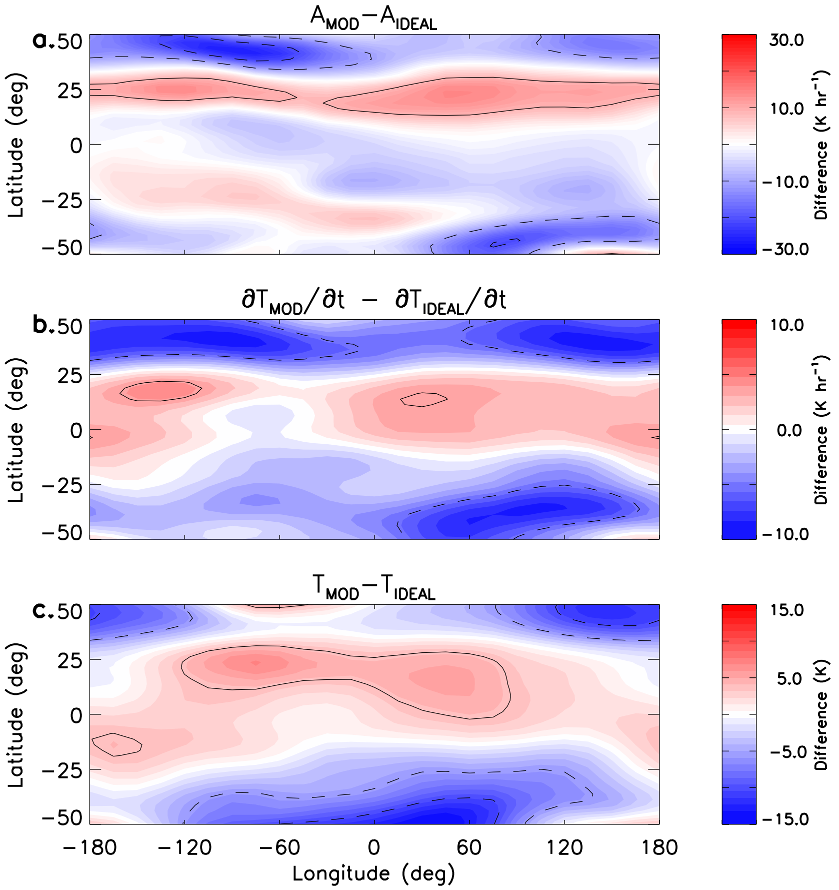

Figure 3.9: Same as Figure 3.8 at equivalent log-pressure level 3.5 (∼350 km) for solar minimum conditions. (a) is contoured every 10 K° hr^{-1}, (b) is contoured every 5 K° hr^{-1}, and (c) is contoured every 5° K.

Figure 3.10 depicts the aggregate effects that in-situ generated non-migrating tides have on the zonal-mean state of the thermosphere. Specifically, the top left (right) panel of Figure 3.10 depicts the zonal-mean zonal (meridional) wind differences for solar minimum and solar maximum. Differences in the zonal-mean zonal winds range from approximately ±10 m s^{-1} (−5 to +10 m s^{-1}) during solar minimum (maximum) in the tropics. There is a northward shift of the maximum zonal-mean zonal wind difference from ∼5° S at solar minimum to ∼15° N at solar maximum (Fig-

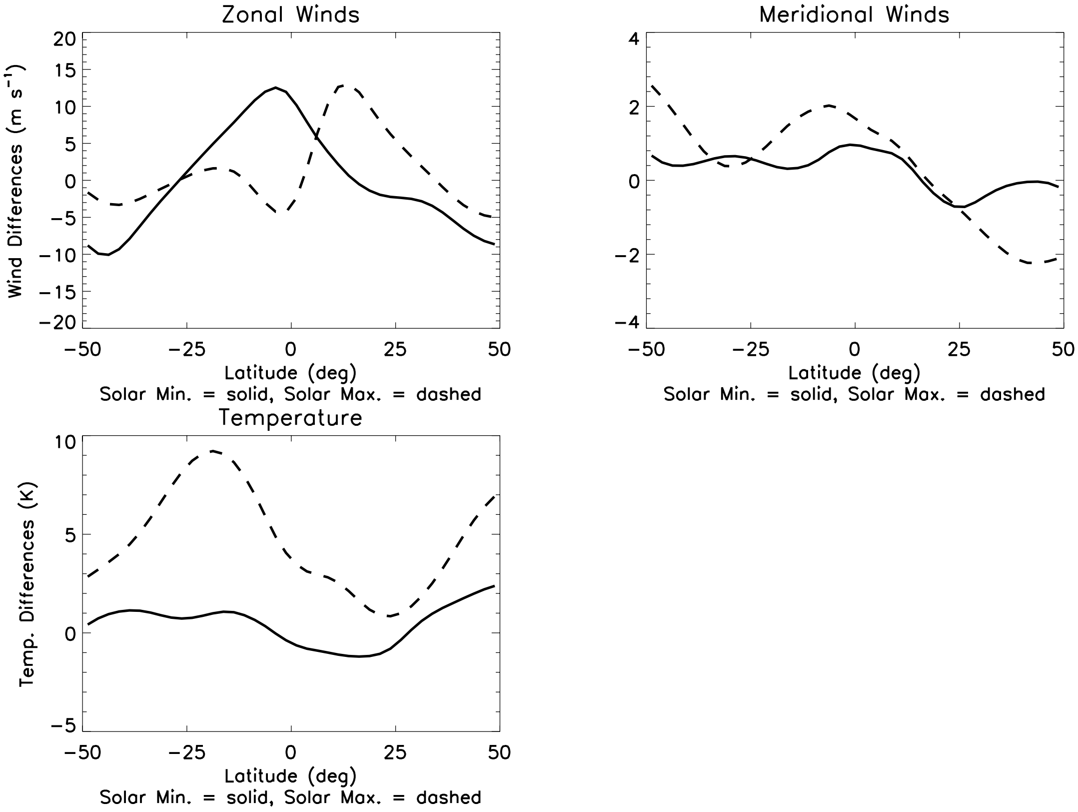

Figure 3.10: Zonal-mean zonal wind (top left), meridional wind (top right), and temperature (bottom left) differences between the modified and idealized circulations at log-pressure level 3.5 for solar minimum (solid lines) and solar maximum (dashed lines) conditions.

ure 3.5, top left). This northward shift corresponds to the latitudes where D0 and DW2 zonal wind amplitudes maximize in the modified circulation (Figure 3.5). Meridional wind differences between modified and idealized flow regime are quite small compared to the zonal wind differences only ranging from about ±2 m s^{-1}, regardless of solar cycle conditions (Figure 3.5, top right). Thus, it appears that in-situ generated non-migrating tides are of little consequence to the zonal-mean meridional winds. In-situ driven non-migrating tidal effects on the zonal-mean temperature are larger at solar maximum than solar minimum with differences between the modified and idealized simulations of up ∼10° K. However, the maximum temperature changes occur at ∼20° S, as opposed to ∼15° N for the zonal winds during solar maximum, further illustrating the latitudinal asymmetry in tidal amplitude that results from the latitudinal asymmetry in the ion drag term.

Larger non-migrating tidal effects on the zonal-mean temperatures at solar maximum compared to solar minimum are consistent with the results shown in Figures 3.8c and 3.9c, as large temperature differences between the modified and idealized circulations are calculated for at a constant local time as well.

3.5 In-Situ Generated Non-migrating Tides at High-Latitudes

At high-latitudes the momentum source terms for the modified neutral circulation now take their full form from 3.3 and 3.4, i.e, $\epsilon(u - u_i)$ and $\epsilon(v - v_i)$, which is a result of rotating the idealized circulation into the new magnetic frame. Therefore, the momentum source terms that drive the neutral modified circulation arise from two sources: (a) the modified ion drag terms times DW1 and SW2 of the idealized circulation (same as at low latitudes) and (b) the modified ion drag terms times the components of the plasma drift circulation in the new magnetic frame (i.e., not DW1 and SW2 from the idealized plasma circulation). As expected, Figures 3.11a and 3.11d show that the idealized circulation above 60° latitude in the northern hemisphere consist of DW1, SW2 and a zonal mean component (not shown), and from Figure 3.3 we see that the ion drag components at high latitudes primarily consist of the zonal mean, SPW1, DE1, D0, DW1, DW2, and SW2. Following the logic developed in Section 3.3, the corresponding momentum source terms for the modified circulation consist of the sum and difference products of ϵ and u. These include all of the components illustrated in Figures 3.11b and 3.11e (i.e., DW1, D0, DE1, S0, SW1) plus other smaller components including terdiurnal ones. Tides of tropospheric origin have a relatively small impact on the calculated migrating and non-migrating zonal wind tidal amplitudes, as evidenced by the similarity between Figures 3.11c and 3.11f with Figures 3.11b and 3.11e. Turning now to the spectra of zonal plasma drifts (u_i) in Figure 3.12, the modified plasma circulation mainly consists of DW1, D0, DE1, S0 and SW1. Since the zonal mean term of the ion drag is so large, the interaction between the modified ion drag and the plasma drift circulation in the new magnetic frame may be the dominant momentum source term for the high-latitude tidal components. However, we were unable to unambiguously separate the relative contributions of these forcing terms to the final modified circulation components depicted in Figures 3.11b and Figures 3.11e.

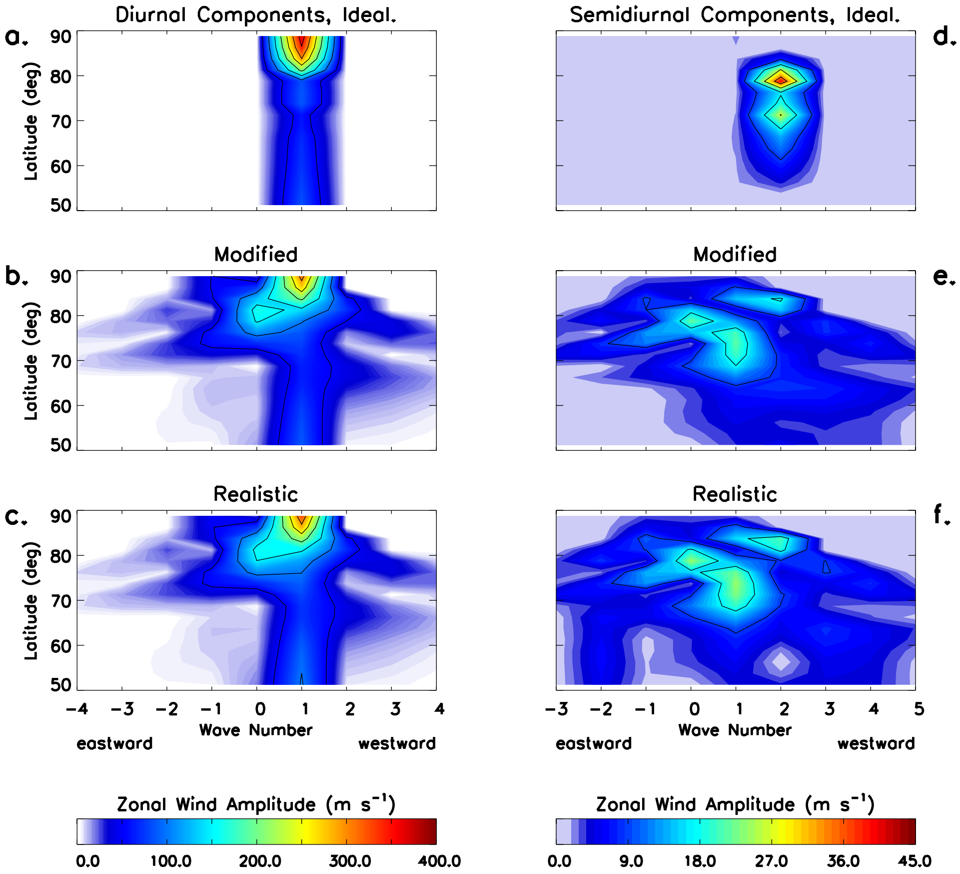

Figure 3.11: Zonal wind wave spectra of the diurnal and semidiurnal tidal components from the TIME-GCM at log-pressure level 3.5 (∼500 km), during September under solar maximum conditions; a and d are idealized flow results; b and e are modified flow results; c and f are from realistic flow results at high northern latitudes. Diurnal (Semidiurnal) components are contoured every 50 (9) m s^{-1}.

Further comparison between non-migrating tidal components generated in-situ at high southern latitudes (shown in Figures B.10 and B.11) with those at high northern latitudes reveals interhemispheric differences in both amplitude and latitudinal structure. The offset between the geomagnetic and geographic poles differs between hemispheres suggesting that the ion-neutral coupling processes and non-migrating tidal excitation, will differ in detail. Please also note that the wave spectra shown in Figure 3.11 for the modified circulation closely resembles wave spectra from the realistic circulation under both solar maximum (as stated above) and solar minimum conditions (shown in Figures B.12-B.15), thereby suggesting these non-migrating tidal components are generated in-situ, regardless of solar cycle.

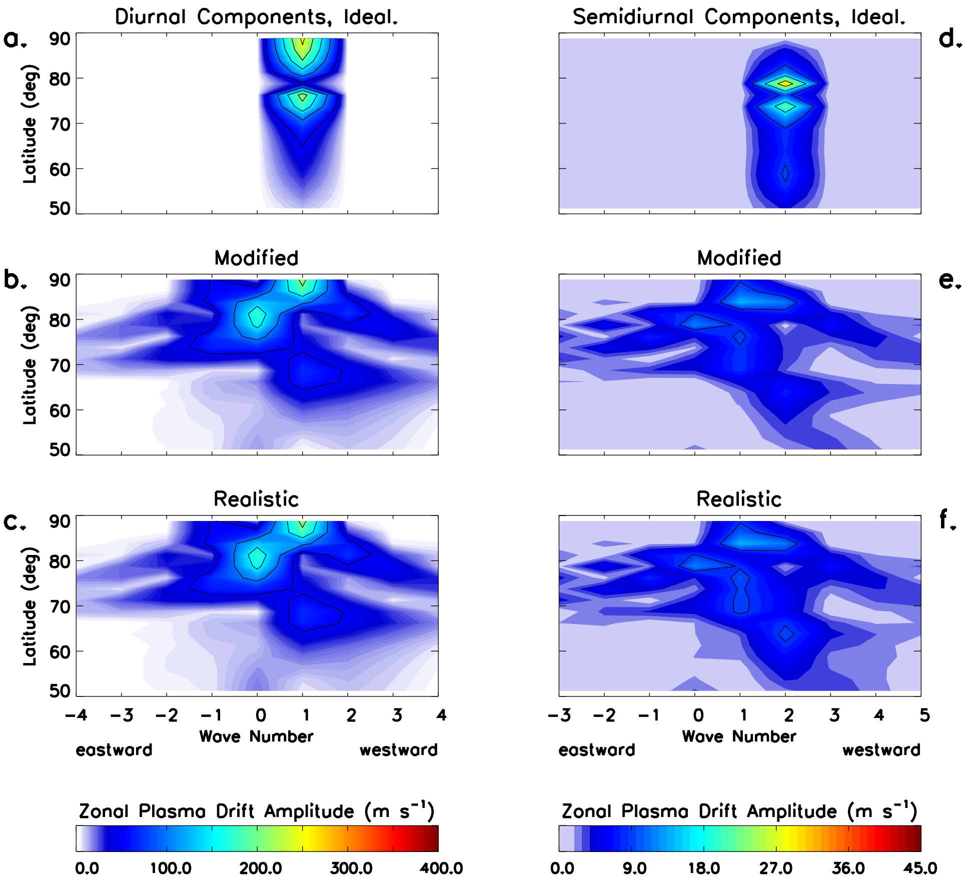

Figure 3.12: Same as Figure 3.11 except for the zonal plasma drift.

Similar to the analysis performed in Section 3.4, temperature differences between the modified and idealized cases also exist at high-latitudes (not shown). However, the origins of these temperature differences in relation to momentum source terms have not been pursued as part of this dissertation work, since other effects (i.e. joule and particle heating) can also produce high-latitude temperature differences.

3.6 Summary of Important Results

The importance of migrating and non-migrating tides to the dynamics and electrodynamics of the IT system is widely recognized. In many cases these tides propagate and electrodynamically couple into the IT from sources in the troposphere, but recent observational evidence suggests the existence of non-migrating tides excited in-situ as well. The results presented in this chapter demonstrate that non-migrating tidal components can be generated in-situ in the upper thermosphere due to ion-neutral coupling. Using six different TIME-GCM simulations one can distinguish between diurnal and semidiurnal migrating and non-migrating tidal components generated locally in the thermosphere from those that originate in the troposphere. The prominent results and conclusions are as follows:

1. At low and middle latitudes, migrating and non-migrating tides are generated in-situ through ion-neutral interactions due to the longitude-dependent ionosphere imposed by the realistic magnetic field configuration.

2. During solar maximum, non-migrating diurnal and semidiurnal tides forced by ion-neutral interactions are responsible for the majority of the longitude-dependent tidal structures seen in the low and middle latitude upper thermosphere. More specifically, non-migrating tidal components D0 and DW2 arising from hydromagnetic coupling between SPW1 (modified ionosphere) and DW1 (idealized wind circulation) reach amplitudes of up to 20 m s^{-1} at ∼500 km. Also, DE1 exists due to hydromagnetic coupling between SPW2 (modified ionosphere) and DW1 (idealized wind circulation), reaching amplitudes of up to ∼15 m s^{-1} at ∼500 km. Smaller amplitude (i.e - ranging from 1–10 m s^{-1}) semidiurnal non-migrating tidal components including SE1, S0, SW1, and SW3 are also present at ∼500 km. These tides are a result of hydromagnetic coupling between SW2 and SPW3, SPW2, and SPW1 respectively. The above results are in accord with the tidal observations from CHAMP shown in Häusler and Lühr [48] and Häusler et al. [49].

3. Since DE3 and SE2 are the two largest amplitude non-migrating tides at ∼350 km during solar minimum conditions and a wave-4 longitude variation in temperature and winds is prominent

in observations, we conclude that tropospherically forced tides dominate the tidal spectrum in the upper thermosphere at low and middle latitudes during solar minimum. The aforementioned wave-4 variation in temperature and winds at ~350 km under solar minimum conditions are consistent with the direct penetration of DE3 and SE2 into the F-region ionosphere, due to reduced dissipation in the IT during solar minimum as concluded by Oberheide et al. [85].

4. The aggregate effect of these non-migrating tides generated due to ion-neutral interactions at low and middle latitudes under solar maximum conditions is relatively large with extrema ranging from -110 to 140 m s^{-1} in latitude versus longitude local time snapshots. However, at solar minimum the aggregate effects at low and middle latitudes are much smaller with extrema ranging from 10 to 40 m s^{-1}.

5. Longitudinal temperature differences associated with the modified and idealized flows exist due to vertical winds accompanying the modified circulation which leads to adiabatic heating and cooling differences at night time. However, during the day, other terms in the thermodynamic energy equation become as important as adiabatic heating and cooling. Large ionization anomalies during solar maximum lead to larger temperature differences between the modified and idealized cases. These temperature differences can range from -40 to 50 K at low to middle latitudes during the late evening when viewed from a latitude versus longitude constant local time perspective (i.e., consistent with that of a near Sun-synchronous satellite). Additionally, zonal-mean zonal wind (temperature) differences of up to 10 m s^{-1} (~10 K) between the modified and idealized flows result from the presence of in-situ driven non-migrating tides.

6. High-latitude in-situ generated migrating and non-migrating tides driven by combined hydromagnetic coupling and convection electric field effects exhibit interhemispheric differences in both amplitude and latitude structure due to interhemispheric differences between the offset of the geographic and geomagnetic poles. Non-migrating tidal components include DE1, D0, DW2, SW1, S0, and SE1. These non-migrating tidal components are seen in both the modified and realistic circulations during both solar minimum and solar maximum leading to the conclusion that the majority of non-migrating tidal components observed at high-latitudes are generated locally in the

thermosphere.

Chapter 4

Tidal Impacts on the Mean State and Variability of the IT System: Momentum Equations

As was reviewed in Section 1.3.2., atmospheric tidal motions in Earth's atmosphere act to couple the lower atmosphere (i.e., troposphere and stratosphere) and the MLT, as well as the IT system through the vertical transport and deposition of energy and momentum, ultimately driving the effects of "meteorology" at these altitudes. Previous studies have shown that the dissipation of vertically propagating tides leads to momentum deposition within the "thermospheric gap" (Oberheide et al., [87]), in which lies the so-called dynamo region responsible for generating electric fields that can drive "space weather" at higher altitudes. However, prior numerical studies lacked the cutting-edge observations and the numerical modeling capabilities currently available to address some of the outstanding questions regarding non-linear tidal effects on the mean IT system. Consequently, this chapter aims to address science question (2a), i.e., what role do vertically-propagating tides play in determining the mean state, seasonal, and solar cycle variability of the mean circulation in the IT? Numerical experiments employing a new set of observationally-based lower boundary conditions input at the TIE-GCM lower boundary are used to investigate this question. The zonal-mean momentum equations in the TIE-GCM are reviewed, and difference fields between a number of different observationally-forced TIE-GCM simulations are discussed in order to isolate the essential physical mechanisms responsible for altering the zonal-mean circulation of the IT system. This chapter expands on results previously published in a JGR: Space Physics journal article by Jones Jr. et al. [60].

Supplemental figures for this chapter are located in Appendix C.

4.1 Introduction and Motivation

The propagation of atmospheric tides in planetary atmospheres results in a vertical flux of zonal and meridional momentum. Once vertically propagating tides reach MLT and IT altitudes they undergo dissipation via eddy and molecular diffusion, as well as ion drag, which alters their otherwise exponential growth, leading to the flux divergence of zonal and meridional momentum. These flux divergences (i.e., $\overline{F}_x$ and $\overline{F}_y$ in equations 2.12 and 2.13, respectively) represent a deposition of momentum that contributes to the acceleration and alteration of the zonal-mean circulation within the MLT and IT. Calculating the momentum flux divergences associated with tidal dissipation and quantifying their effects on the zonal-mean circulation in the MLT and IT has been the focus of many prior research efforts.

Miyahara [75]; [76] were two of the first publications to investigate zonal-mean motions induced by the dissipation of upward propagating tides numerically from first-principles. Specifically, Miyahara [75]; [76] found that the flux divergences driven by the diurnal tide induced easterlies of up to 60 m s^{-1} at 105 km near the equator and westerlies polewards of that on the order of 35 m s^{-1}. Also, Miyahara [75]; [76] reported that the momentum flux divergence attributable to the semidiurnal tide forced easterlies at low (middle) latitudes at 112 km of 15 m s^{-1} (17 m s^{-1}). Miyahara [78] followed the work of Miyahara [75]; [76] and calculated zonal momentum flux divergences on the order of 4×10^{-2} cm s^{-2}, which produced easterly winds at low latitudes and 100 km of at least 60 m s^{-1}. Teitelbaum and Vial [119] showed that the latitudinal distribution of zonal wind acceleration driven by momentum flux divergences ascribed to tidal dissipation was dependent on latitude, as well as the dissipative mechanism. During equinox, Groves and Forbes [39] were able to reproduce the result presented in Miyahara [78] for momentum flux divergences induced by the dissipating diurnal tide. Groves and Forbes [39] also showed that during equinox the $\overline{F}_x$ and $\overline{F}_y$ driven by the dissipating semidiurnal tide were comparable to the $\overline{F}_x$ and $\overline{F}_y$ generated by the diurnal tide (i.e., of order $\pm 1 \times 10^{-4}$ m s^{-2}) at low latitudes. For December solstice conditions, Groves and Forbes [39] stated that $\overline{F}_x$ and $\overline{F}_y$ were symmetric (asymmetric) between the summer and winter hemispheres below (above) 130 km for the diurnal tides, suggesting that seasonal variability in the thermosphere can be driven by a seasonal dependence in the momentum flux divergence due to the diurnal tide. Although all of the aforementioned studies, as well as references discussed therein, focused on the momentum flux divergences generated by the dissipation tides, equations 2.12 and 2.13 indicate that there are other forces that could change the zonal-mean winds, such as pressure gradient, ion drag, and momentum advection.

Others including Forbes et al. [31], and more recently Hagan et al. [45] have used the NCAR TGCMs and found that dissipation of the migrating and non-migrating tides acts to change the zonal-mean winds in the 100 to 170 km range by 10 to 30 m s^{-1}. This altitude range coincides with the dynamo region in which electric fields are generated via the wind-dynamo mechanism and strongly affect the upper IT. As Oberheide et al. [87] pointed out there is a lack of global IT observations in this height regime as a result of the orbital limitations experienced by low-earth orbiting satellites. Therefore, Oberheide et al. [87] dervied the observationally based CTMT from TIMED observations (see Section 2.1.2.2) to mitigate this issue. CTMT coupled with the TIE-GCM provide the opportunity to force a commonly utilized physics-based numerical model of the IT system with observationally-derived tidal perturbations and to quantify the tidal effects on the mean IT within and above the dynamo region.

The goal of this chapter is to better understand how the dissipation of upward propagating tides affect the zonal-mean winds of the IT, especially the seasonal, latitudinal, and solar cycle variability. Consequently, we report on a set of numerical experiments performed with the NCAR TIE-GCM that explore science question (2a) using observationally-based background (i.e., from the UARS and TIMED spacecraft) and tidal (i.e., from CTMT) lower boundary conditions near 97 km in order to best replicate the mean zonal state of the IT. We quantify the extent to which the dissipation of upward propagating tides alters the zonal-mean winds in the IT by comparing simulations including and excluding CTMT lower boundary tidal forcing. In addition, numerical experiments with the TIE-GCM are performed for all twelve months of the year and under different

F10.7 solar radio flux conditions to assess how tidal effects on the zonal-mean winds differ between seasons and solar cycle conditions. The individual terms in equations 2.12 and 2.13 for the zonal-mean zonal and meridional momentum, respectively are calculated in order to understand the mechanisms by which the dissipating tides act to change the zonal-mean circulation of the IT system. All the results presented herein are considered and discussed in light of the aforementioned efforts that have been conducted in this research area.

4.2 TIE-GCM Simulations and Methodology

A general description of the TIE-GCM and outline of the TIE-GCM simulations performed as part of this study was offered in Chapter 2 including the model version and resolution, geomagnetic proxies, changes to the solar fluxes and eddy diffusion coefficient, and the observationally-based background and tidal lower boundary condtions utilized herein. In order to more realistically resolve and assess the tidal effects on the zonal-mean IT, migrating and non-migrating tides from the CTMT and background winds, temperatures, and geopotential heights from WINDII-HRDI and SABER measurements are input at the TIE-GCM lower boundary. Differences between simulations that include CTMT tidal forcing with those that either include a combination of tidal components or exclude CTMT tidal forcing all together, not only provide a means to quantify the effect that upward propagating tides have on the zonal-mean circulation of the IT, but also elucidate which particular tidal components are most responsible for altering the zonal-mean circulation of the IT. All the TIE-GCM simulations discussed throughout the remainder of this dissertation represent a set of monthly climatologies where the model was run for the 15th day of every month until the TIE-GCM reached a diurnally-reproducible state, from which we examine the seasonal variability in the zonal-mean wind circulation of the IT brought about by the dissipating tides. Simulations were also performed for solar minimum, solar medium, and solar maximum conditions using F10.7 solar radio flux values of 75 sfu, 120 sfu, and 200 sfu, respectively, which allows us to evaluate whether or not the tidal impacts on the zonal-mean winds of IT system vary with solar cycle.

4.3 Tidal Impacts on the Zonal-Mean Zonal Winds

Figure 4.1 illustrates the monthly variability TIE-GCM zonal-mean (i.e., zonally- and diurnally-averaged) zonal wind fields generated with and without CTMT lower boundary tidal forcing at 140 km under solar medium conditions. The 140 km altitude was chosen because it is the altitude at which the strongest vertically propagating wave, SW2, attains its maximum in our TIE-GCM simulations. The zonal wind jet structures in Figures 4.1a and 4.1b are approximately in geostrophic balance (other forces such as ion drag and viscous dissipation are of secondary importance at this altitude). In the absence of tidal forcing at the TIE-GCM lower boundary, an eastward (westward) jet with wind speeds on the order of +40 m s^{-1} (-30 m s^{-1}) at northern mid-latitudes persists throughout the fall and winter (spring and summer) months (Figure 4.1b). The identical seasonal behavior in the zonal winds is seen in the southern mid-latitudes with winds speeds on the order of ± 40 m s^{-1} (Figure 4.1b). Additionally, Figure 4.1b shows a westward jet with wind speeds around -30 m s^{-1} at equatorial latitudes during the March-August timeframe. When CTMT lower boundary tidal forcing is included at the TIE-GCM lower boundary there is a clear strengthening of the equatorial westward jet during the first half of the year (Figure 4.1a). Most of the mid-latitude zonal jet features are enhanced as well, with the exception of eastward jet at middle southern latitudes during the winter months, whose maximum wind speeds at latitudinal extent has been somewhat reduced. Please also note that since geostrophic balance is the dominant force balance below 140 km, the zonal wind results presented in Figures 4.1a and 4.1b are representative of the zonal wind structure (i.e., latitudinal and seasonal structure) in the lower IT; however, above 140 km the structure of the zonal winds will change due to the influences of ion drag and viscous forces, which will be illustrated in a subsequent subsection.

Figures 4.2a and 4.2b display zonal wind difference fields at 115 and 140 km between TIE-GCM simulations with and without CTMT tidal lower boundary forcing under solar medium conditions. The 115 and 140 km altitude levels were chosen because it is where DE3 and SW2 reach maximum amplitudes in our TIE-GCM simulations, and could thereby lead to quantifiable changes

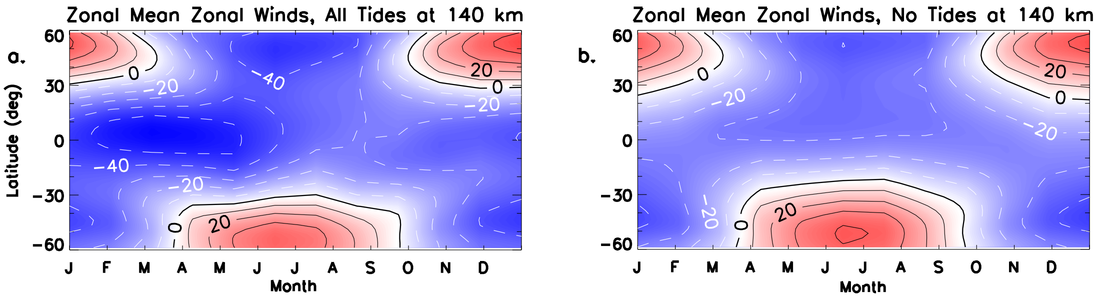

Figure 4.1: TIE-GCM zonal-mean zonal winds at 140 km as a function of month and latitude from simulations using WINDII-HRDI/HWM07 background winds, SABER/NRLMSISE-00 background temperatures and geopotential heights under solar medium conditions. (a) zonal winds from a TIE-GCM simulation including CTMT tidal forcing at the model lower boundary; (b) zonal winds from a TIE-GCM simulation excluding CTMT tidal forcing at the model lower boundary. Zonal winds are contoured every ±10 m s^{-1}.

in the zonal-mean circulation of the IT. We deduce from Figures 4.2a and 4.2b that the net effect of the upward-propagating tidal spectrum is to deposit westward momentum into the background zonal flow. Vertically propagating tides have their largest effects on the mean zonal winds at equatorial latitudes during the boreal winter and spring months, as they act to enhance these equatorial westward jet features by some -30 m s^{-1} at both 115 and 140 km. To a lesser extent the dissipation of upward propagating tides alters the mean zonal winds at mid-latitudes, but with differences only ranging from -10 to 5 m s^{-1}.

Figures 4.2c-4.2h all show zonal wind difference fields at 115 and 140 km between TIE-GCM simulations including CTMT lower boundary tidal forcing with TIE-GCM simulations that include combinations of specific tidal components from CTMT. Figures 4.2c and 4.2d show the differences between simulations that include all of the CTMT tidal components forced at the model lower boundary and simulations that only include tidal forcing from SW2 at 115 and 140 km. By including just SW2, the seasonal and latitudinal distribution of the mean zonal wind differences are reduced by up to 30 m s^{-1}. Particularly, the differences in the westward jet feature at low latitudes during boreal winter and spring months in Figures 4.2c and 4.2d are reduced by 20-30 m s^{-1} at 115 and 140 km. Results depicted in Figure 4.3, which shows the latitudinal and seasonal distribution of the zonal wind amplitude of SW2, DE3, and DW1 at 115 and 140 km, provide a means to assess if the spatial and temporal structure of the tidal amplitudes are related to changes in the zonal-mean zonal winds. Specifically, Figures 4.3a and 4.3b clearly show that the latitudinal and seasonal distribution of SW2 zonal wind amplitude corresponds quite well with its maximum influence on the zonal-mean zonal winds in the dynamo region, with amplitudes ranging from 10–45 m s^{-1} at low and middle latitudes. Due to the reduction in the zonal wind differences (i.e., up to -30 m s^{-1}) and its large zonal wind amplitude (Figures 4.3a and 4.3b), SW2 appears to be the main driver of the mean zonal winds within the dynamo region in the TIE-GCM. While SW2 above $\sim$100 km is partially attributable to an in-situ component generated by the absorption of EUV radiation, Figure C.1 shows that this component only contributes up to 8 (14) m s^{-1} to the total SW2 zonal wind amplitude depicted in Figure 4.3a (Figure 4.3b). Thus the presence of this comparatively small SW2 lower thermospheric component does not detract from our primary conclusion that the dissipation of the vertically propagating SW2 is important for maintaining the mean zonal winds within the dynamo region in the TIE-GCM.

Another striking feature from Figures 4.2c and 4.2d is that inclusion of SW2 leads to an increase in the positive zonal wind differences of $\sim$15 m s^{-1} at low latitudes during boreal summer. However, once DE3 is included with SW2 at the TIE-GCM lower boundary, these positive zonal wind differences are gone (Figures 4.2e and Figure 4.2f). This results from the dissipation of DE3, which is responsible for depositing eastward momentum into the low-latitude westward jet (Figure 4.1a), and thereby reducing the westward zonal wind speeds at low latitudes during boreal summer relative to a TIE-GCM simulation that does not include lower boundary tidal forcing (Figure 4.1b). Figures 4.3c and 4.3d show that DE3 attains its maximum amplitude during the boreal summer months, which corresponds to its maximum influence on the zonal-mean zonal winds in the dynamo region. Additionally, the effect of DE3 on the mean zonal winds is slightly greater at lower IT altitudes (i.e., slightly larger positive zonal wind differences in Figure 4.2c than in Figure 4.2d), as it reaches its maximum amplitude in the TIE-GCM at $\sim$115 km (Figure 4.3c).

Including SW2 and DE3 at the TIE-GCM lower boundary explains the majority of the zonal

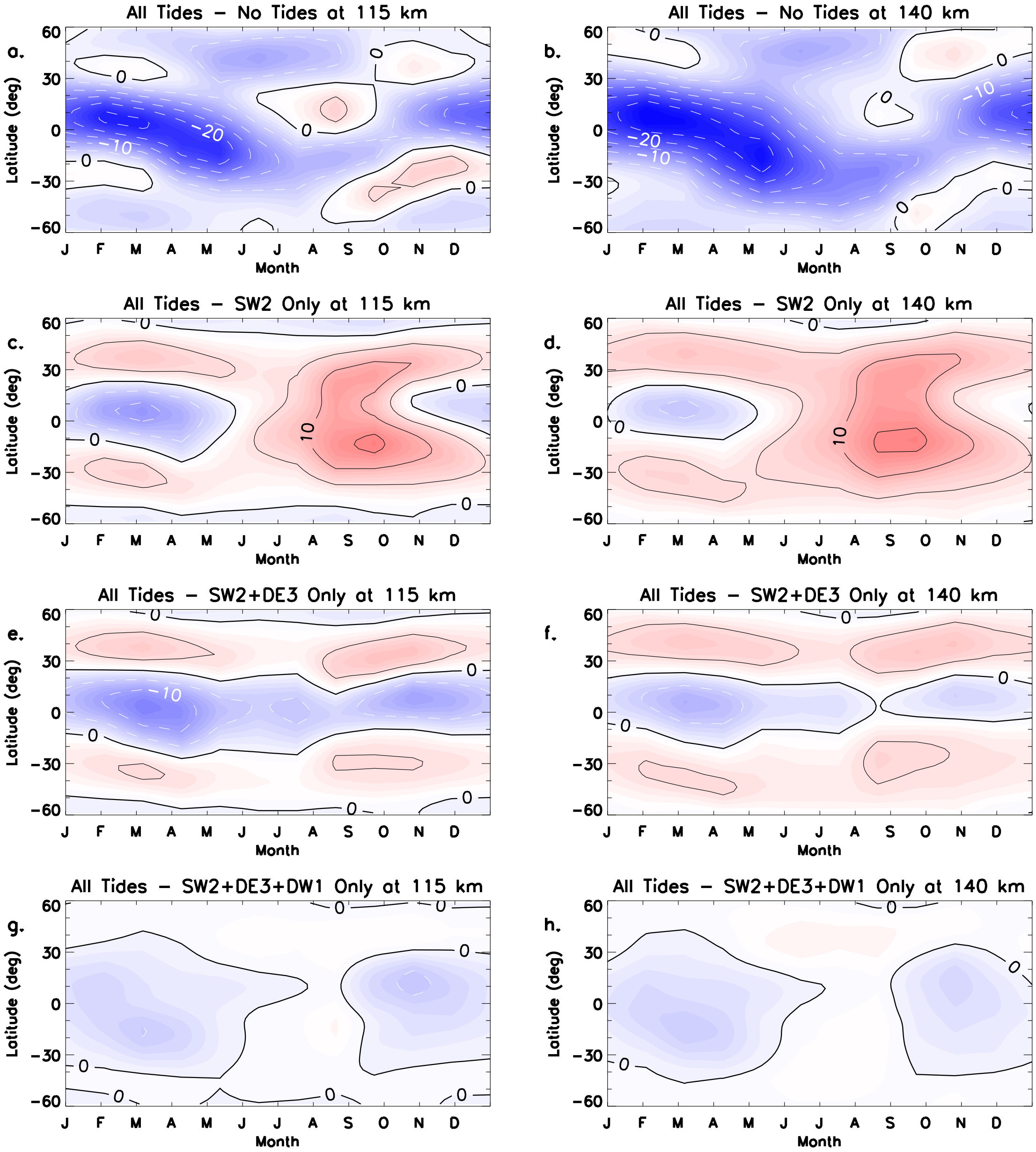

Figure 4.2: TIE-GCM zonally- and diurnally-averaged zonal wind differences as function of month and latitude at 115 km (Right Column) and 140 km (Left Column). Differences between TIE-GCM simulations including and excluding CTMT tidal forcing at the model lower boundary are shown in (a) and (b); differences between TIE-GCM simulations including all tidal components and only SW2 from CTMT at the model lower boundary are shown in (c) and (d); differences between TIE-GCM simulations including all tidal components and only SW2 and DE3 from CTMT at the model lower boundary are shown in (e) and (f); differences between TIE-GCM simulations including all tidal components and only SW2, DE3, and DW1 from CTMT at the model lower boundary are shown in (g) and (h). Zonal wind differences are contoured every ±5 m s^{-1}.

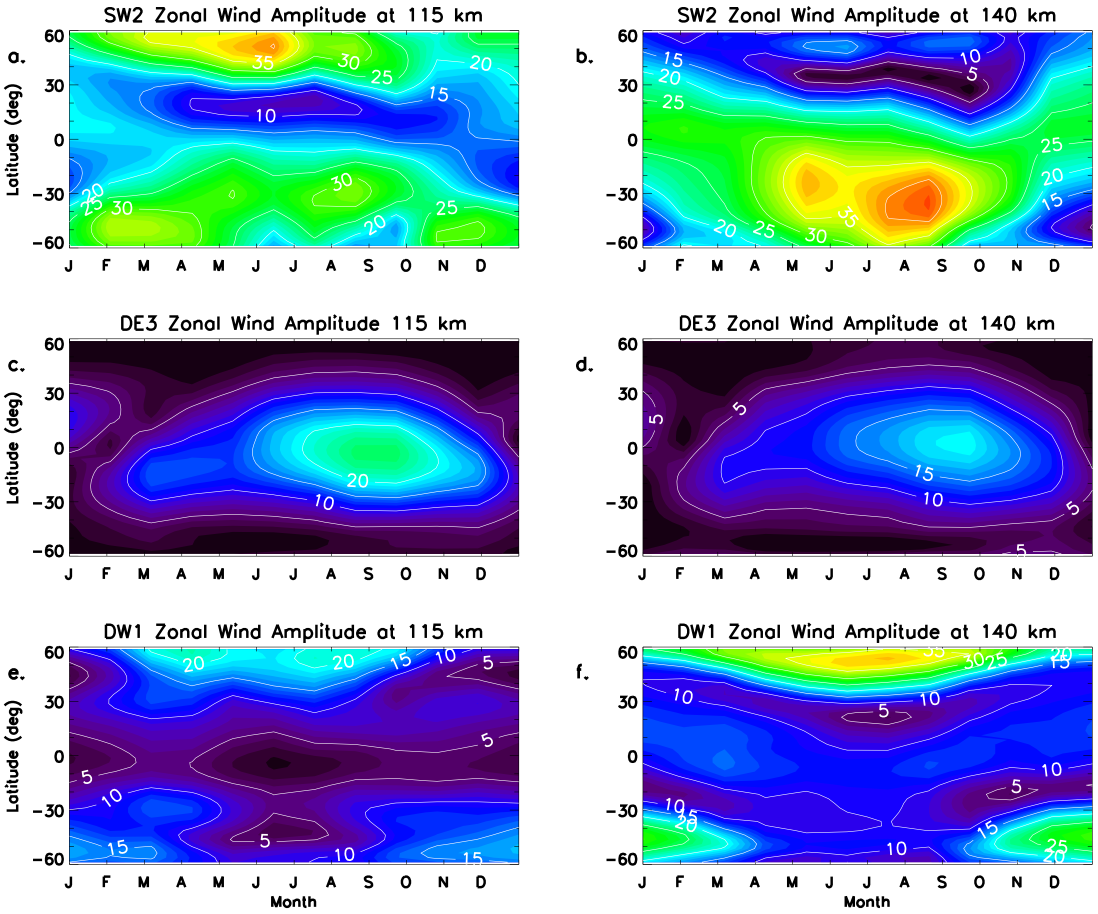

Figure 4.3: TIE-GCM zonal wind tidal amplitudes at 115 km (Left Column) and 140 km (Right Column). The SW2 is shown in (a) and (b); DE3 in (c) and (d); DW1 in (e) and (f). Zonal wind amplitudes contoured every 5 m s^{-1}.

wind features in the dynamo region, but zonal wind differences of up to 10 m s^{-1} still exist relative to the simulations forced with the complete CTMT tidal spectrum at the model lower boundary. The remainder of these zonal wind differences can almost be completely explained by adding DW1 to SW2 and DE3. Figures 4.2g and 4.2h show that when DW1 is included with SW2 and DE3, the mean zonal winds in the dynamo region can be almost completely replicated. Similar to SW2, above ∼100 km DW1 is mainly generated by in-situ absorption of EUV radiation, and is not vertically propagating (see Figure C.1). However, the in-situ forced DW1 is present in both simulations (i.e., the All Tides and No Tides Cases), and thus the difference fields illustrate the vertically propagating DW1 contribution. The results presented in Figures 4.2g and 4.2h show that DW1 is one of the most important tidal components at 115 km and to a lesser degree at 140 km. Therefore, DW1 must be included in the TIE-GCM simulations to better replicate the mean circulation within the dynamo region.

4.3.1 Interpreting the Zonal Wind Differences, Seasonal and Solar Cycle Variability

Understanding how the dissipating tides act to change the zonal-mean zonal winds in the IT system is best done by evaluating the changes in the forcing terms of the zonal-mean meridional momentum equation (i.e., equation 2.13). To facilitate description of the individual forcing terms in equation 2.13 it is shown again below,

$$\frac{\overline{v}}{a}\frac{\partial \overline{v}}{\partial \theta} + \overline{w}\frac{\partial \overline{v}}{\partial z} + 2\Omega \overline{u}\sin\theta + \frac{\overline{u}^2\tan\theta}{a} - \overline{\lambda_{yx}}\,\overline{u} = -\frac{1}{a}\frac{\partial \overline{\Phi}}{\partial \theta} - \overline{F}_y \\ - \overline{\lambda_{yx}}\,\overline{u_i} - \overline{\lambda_{yy}}\,\overline{v} + \overline{\lambda_{yy}}\,\overline{v_i} + \overline{\lambda'_{yx}u'} - \overline{\lambda'_{yx}u'_i} - \overline{\lambda'_{yy}v'} + \overline{\lambda'_{yy}v'_i} + \frac{1}{\rho_0}\frac{\partial}{\partial z}\left(\overline{\mu}\frac{\partial \overline{v}}{\partial z}\right). \quad \text{(2.13 revisited)}$$

The first two terms on the left hand side of 2.13 represent the advective terms, which result from the total or material derivative and shows that momentum transport occurs due to the mass movement of the fluid (i.e., changes in wind speeds can occur by the meridional and vertical winds transporting or redistributing momentum). Also note that the advective terms in 2.13 represent the change relative to a reference frame that is attached to an air parcel and moving with it, which is commonly referred to as the *Lagrangian* derivative and is abbreviated by *Adv.* in the figures below. The third term on the left hand side of 2.13 is the Coriolis force representing the fictitious deflection force an air parcel experiences in a rotating reference frame and is abbreviated by *Cor.* in the figures presented below. The fourth term on the left hand side of equation 2.13 is the curvature term which results from expressing the momentum equations in spherical coordinates. *Curv.* is the abbreviation used below in the subsequent figures to represent the curvature term. The fifth term on the left hand side of equation 2.13 is one of what we term the plasma neutral zonal-mean momentum source terms, which arises from the ion drag terms. This term is abbreviated by *P/N LHS* in the figures shown below and is shown on the left hand side of equation 2.13 in order to solve for $\overline{u}$.

The first term on the right hand side of 2.13 is the pressure gradient force and is represented by the abbreviation *PGF* in the figures below. $\overline{F}_y$ is the eddy momentum source term in the meridional direction, which represents the momentum deposition by the tides and is abbreviated as *Eddy* in the following plots. Terms three, four, and five on the right hand side of equation 2.13 are also zonal-mean ion drag terms, but since these do not include any product of $\overline{u}$ they are left on the right hand side of the equation and are abbreviated using *P/N ZM.* Terms six through nine represent what we term the plasma neutral eddy momentum source terms that result from the product of two perturbation quantities in the ion drag force. These terms have been evaluated before in the TGCM by Dickinson et al. [10], although they neglected the product of perturbations in the plasma drift velocities. Essentially, terms six through nine on the right hand side of 2.13 are the zonally- and diurnally-averaged analogs to the hydromagnetic coupling terms derived and discussed in Chapter 3, and are shown to be a source of momentum which arises from the correlation between perturbations in the horizontal wind and plasma drift fields with perturbations in ion drag (Figure 3.10). These terms are abbreviated as *P/N Eddy* in the plots shown below. The final term on the right hand side of 2.13 is the vertical viscosity term, which is due to friction on molecular scales that tries to eliminate vertical gradients in momentum by transferring momentum vertically. *Vis.* abbreviates the vertical viscosity term in the figures presented below. Please note that the meridional viscous stress term is neglected in the TIE-GCM due to scale arguments, i.e., the scale of meridional variations in the wind fields tend to be much greater than vertical variations, especially for the zonally- and diurnally-averaged IT system discussed herein.

Figure 4.4 shows all the terms of equation 2.13 along with the zonal-mean zonal wind field calculated from a TIE-GCM simulation that includes CTMT lower boundary tidal forcing under March and solar medium conditions as a function of latitude and altitude. The month of March was chosen because it is one of the months where the largest zonal-mean zonal wind differences occur in the dynamo region due to the dissipating tides (Figures 4.2a and 4.2b). Figure 4.4 clearly illustrates that the advective terms are almost negligible during the month of March. Including the PGF term

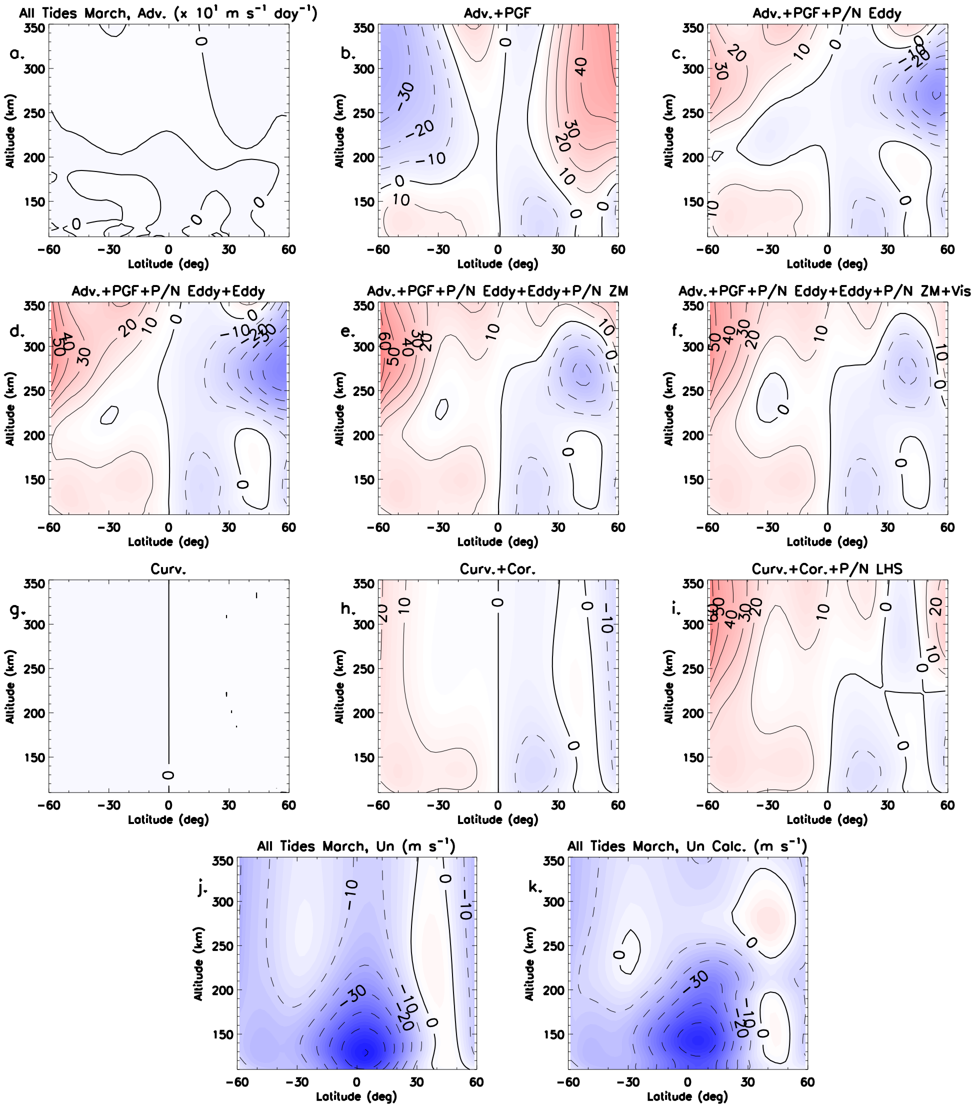

Figure 4.4: TIE-GCM zonally- and diurnally-averaged forcing terms from the meridional momentum equation including CTMT lower boundary tidal forcing under March and solar medium conditions as a function of latitude and altitude. The advection term is shown in (a); advection + pressure gradient terms in (b); advection + pressure gradient + plasma neutral eddy momentum source terms in (c); advection + pressure gradient + plasma neutral eddy momentum source + eddy momentum source terms in (d); advection + pressure gradient + plasma neutral eddy momentum source + eddy momentum source + plasma neutral zonal-mean momentum source terms (e); advection + pressure gradient + plasma neutral eddy momentum source + eddy momentum source + plasma neutral zonal-mean momentum source + viscosity terms (f); the curvature term in (g); curvature + Coriolis terms in (h); curvature + Coriolis + plasma neutral zonal-mean momentum source term on the left hand side of equation 2.13 (i); the zonally-averaged zonal winds are shown in (j); the calculated zonally-averaged zonal winds from equation 4.2 are shown in (k). Forcing terms from the meridional momentum equation are contoured every ±10 × 10^1 m s^{-1} day^{-1}, while the zonally-averaged zonal winds are contoured every ±10 m s^{-1}.

reveals forcing maxima and minima below (above) 200 km of ±100 m s^{-1} day^{-1} (±400 m s^{-1} day^{-1}) during March (Figure 4.4b). When the P/N Eddy term is added to the Adv. and PGF terms below ~160 km Figures 4.4b and 4.4c look very similar. Above ~160 km the P/N Eddy term dominates and acts to reverse the latitudes at which the maximum and minimum forcing of the zonal-mean zonal winds is experienced. A maximum (minimum) forcing of the zonal-mean zonal winds on the order of +300 m s^{-1} day^{-1} (−500 m s^{-1} day^{-1}) is shown in Figure 4.4c near 275 km in the southern (northern) mid-latitudes as a result of the P/N Eddy term. The importance of the P/N Eddy term at higher altitudes is not surprising as the ion drag force is proportional to the electron density that is increasing with altitude. Including the eddy momentum source term does very little to change the forcing of the zonal-mean zonal winds in both the lower and upper thermosphere (Figure 4.4d). This finding contradicts the results presented by Miyahara [75]; [76]; [78], Groves and Forbes [39], Miyahara and Wu [80], Miyahara et al. [79], and references therein, in which these authors claim that the eddy momentum source terms due to the dissipating diurnal and semidiurnal tides drive zonal-mean zonal wind differences. Figure 4.4d suggests that the momentum deposition via the eddy momentum source terms into the IT system due to the dissipating tides is small and is only of secondary importance when compared to the other forcing terms in the zonal-mean meridional momentum equation. Including the P/N ZM term to the Adv., PGF, P/N Eddy, and Eddy terms acts to reinforce (oppose) the P/N Eddy in the southern (northern) hemisphere by increasing the maximum (minimum) calculated at middle southern (northern) latitudes between 250 and 300 km (Figure 4.4e). Lastly, including the vertical viscosity term to the other forcing terms does very little to alter the forcing of the zonal-mean zonal winds, as is evidenced by the similarity between Figures 4.4e and 4.4f.

The third row of Figure 4.4 shows the terms in equation 2.13 that are products of $\overline{u}$. Figure 4.4g depicts the a small curvature term throughout the IT system, which is expected because this term is scaled by the Earth's radius. Including the Cor. term to the Curv. term shows a negative forcing of −100 m s^{-1} day^{-1} centered around 15° N latitude between 110 and 150 km, with positive and negative forcing also on the order of ±100 m s^{-1} day^{-1} above ±50° in the southern and northern hemispheres, respectively (Figure 4.4h). Above ∼200 km the P/N LHS term changes the latitudinal structure of the zonal-mean zonal wind forcing, such that Figures 4.4i and 4.4f are almost identical. Thus, we can conclude that below (above) ∼200 km the zonal-mean zonal winds are driven by a balance of Coriolis and pressure gradient forces (Coriolis, pressure gradient, and ion drag forces).

To assess how good of an agreement is obtained between the forcing terms calculated in the Figure 4.4, we calculate the zonal-mean zonal winds and compare them to what is directly output from the TIE-GCM. By putting the terms depicted in Figure 4.4i, neglecting the curvature term on the left hand side of equation 2.13, and leaving the terms illustrated in Figure 4.4f on the right hand side of equation 2.13, we can then write the following,

$$\begin{aligned} 2\Omega\overline{u}\sin\theta - \overline{\lambda_{yx}}\overline{u} = {} & -\frac{\overline{v}}{a}\frac{\partial\overline{v}}{\partial\theta} - \overline{w}\frac{\partial\overline{v}}{\partial z} - \frac{1}{a}\frac{\partial\overline{\Phi}}{\partial\theta} - \overline{F}_y \\ & - \overline{\lambda_{yx}}\overline{u_i} - \overline{\lambda_{yy}}\overline{v} + \overline{\lambda_{yy}}\overline{v_i} + \overline{\lambda'_{yx}u'} - \overline{\lambda'_{yx}u'_i} - \overline{\lambda'_{yy}v'} + \overline{\lambda'_{yy}v'_i} + \frac{1}{\rho_0}\frac{\partial}{\partial z}\left(\overline{\mu}\frac{\partial\overline{v}}{\partial z}\right), \end{aligned} \tag{4.1}$$

which then can be solved for $\overline{u}$ by the following procedure

$$\begin{aligned} (2\Omega\sin\theta - \overline{\lambda_{yx}})\overline{u} &= (RHS), \\ (LHS)\overline{u} &= (RHS), \\ \overline{u}_{calc} &= \frac{(RHS)}{(LHS)}. \end{aligned} \tag{4.2}$$

The calculated zonal-mean zonal winds following the above procedure are depicted in Figure 4.4k, while the zonal-mean zonal winds directly output from the model are shown in Figure 4.4j. Figures 4.4j and 4.4k are in fairly good agreement with one another showing a westward jet centered just north of the equator with zonal wind speeds on the order of -60 m s^{-1}. Differences between 5 to 10 m s^{-1} do exist between Figures 4.4j and 4.4k, especially near low latitudes and around 250 km in the northern hemisphere. These differences are caused by singularities in our solution at low latitudes and 250 km as f and $f - \overline{\lambda_{yx}}$ approach zero (see Figure C.2). Therefore, between ±16.25° latitude and log-pressure level -0.625 - 1.375 (i.e, between a mean altitude of ∼200-260 km) $\overline{u}_{calc}$ values are interpolated to avoid this singularity. It must be noted that differences of up 20 m s^{-1} can occur depending on month and TIE-GCM simulation, as is depicted for the analog of Figure

4.4 that excludes CTMT tidal forcing at the lower boundary (Figure C.3). These large eastward winds are purely an artifact of interpolating over the aforementioned latitude and altitude regions. Nonetheless, the favorable comparison in the latitude, altitude, and magnitude structure of the zonal-mean zonal winds presented Figures 4.4j and 4.4k provide further evidence that the forcing terms from the model are calculated correctly.

To elucidate how the dissipating tides act to change the zonal-mean zonal winds, differences in the forcing terms between TIE-GCM simulations including and excluding CTMT lower boundary tidal forcing under March and solar medium conditions are presented in Figure 4.5. Please note that the dashed line shown in every individual panel of Figure 4.5 at 200 km is used to separate the altitude range at which certain forcing terms become dominant. Figure 4.5a shows that the PGF below 200 km is altered by up to -60 m s^{-1} day^{-1} at low northern latitudes due to dissipating tides. Specifically, the PGF is modified mainly via the eddy heat source term in the thermodynamic energy equation (with other terms including the adiabatic and diabatic heating and cooling terms playing smaller roles), through which the dissipating tides act to deposit heat in the zonal-mean IT system, thereby leading to a change in the meridional gradient of geopotential through the ideal gas law (i.e., equation 1.4), and ultimately because $\nabla\Phi = \frac{1}{\rho}\nabla p$. This minimum in the PGF difference extends to above 200 km at low northern latitudes and then is accompanied by a maximum on the order of $+50$ m s^{-1} day^{-1} at low southern latitudes centered around 15° N. Similar to the results presented in Figure 4.4, adding the differences in the eddy momentum source term to the PGF differences does not alter the latitudinal, altitudinal, or magnitude structures of the force term differences already explained by the PGF (Figure 4.5b). Figure 4.5b provides further evidence that the eddy momentum source terms are of secondary importance in altering the zonal-mean zonal winds of the IT system. Additionally, including the advective and viscous difference terms with the PGF and eddy momentum source difference terms does little change to the forcing differences already accounted for by the PGF (Figure 4.5c), except as we approach 350 km where viscous dissipation differences are starting to become important.

Above $\sim$200 km the changes in the zonal-mean zonal winds are mainly driven by the ion

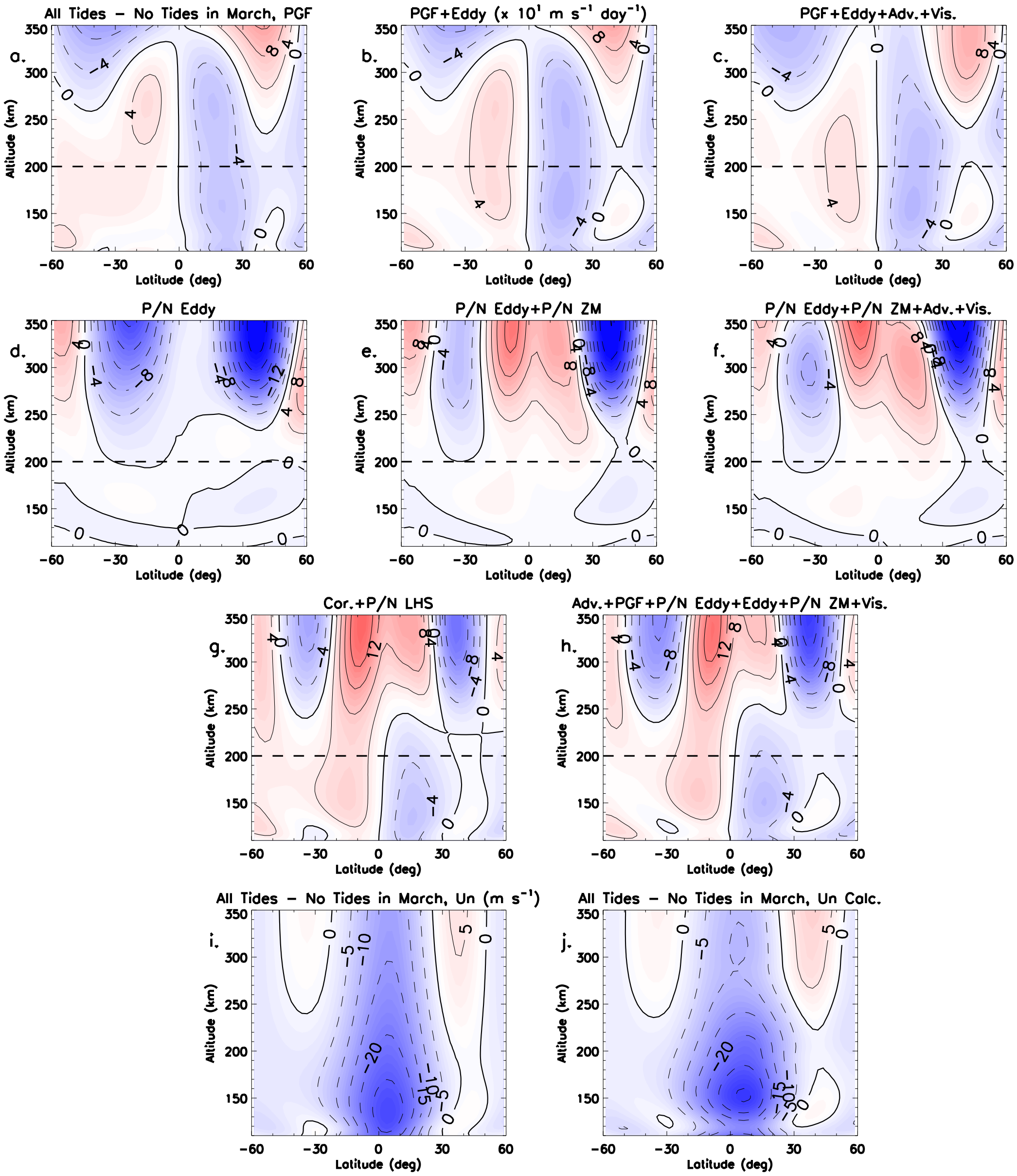

Figure 4.5: TIE-GCM forcing term differences between TIE-GCM simulations including and excluding CTMT tidal lower boundary forcing under March and solar medium conditions as a function of latitude and altitude. The PGF term is shown in (a); PGF + Eddy terms in (b); PGF + Eddy + Adv. + Vis. terms in (c); the P/N Eddy term in (d); P/N Eddy + P/N ZM terms in (e); P/N Eddy + P/N ZM + Adv. + Vis. terms in (f); the Cor. + P/N LHS terms in (g); the Adv. + PGF + P/N Eddy + Eddy + P/N ZM + Vis. terms in (h); the zonally-averaged zonal wind differences are shown in (i); the calculated zonally-averaged zonal winds calculated following equation 4.2 are shown in (j). Forcing terms from the meridional momentum equation are contoured every ±4 × 10^1 m s^{-1} day^{-1}, while the zonally-averaged zonal wind differences are contoured every ±5 m s^{-1}.

drag terms (see Figures 4.5d and 4.5e). Particularly, the differences in the P/N Eddy term between TIE-GCM simulations that include and exclude CTMT lower boundary tidal forcing increase with increasing altitude, showing two minima of order -200 m s^{-1} day^{-1} centered around ±30° latitude (Figure 4.5d). Including the P/N ZM differences with the P/N Eddy differences reduces (enhances) the magnitude of the P/N Eddy forcing minimum at 30° S (30° N) by ∼120 m s^{-1} day^{-1} (40 m s^{-1} day^{-1}) shown in Figure 4.5e above 200 km. Figure 4.5e also shows the low-latitude maximum in the forcing difference fields imposed by the P/N ZM term above 200 km reaching values of up 160 m s^{-1} day^{-1}. Similar to what was shown in Figure 4.5c, Figure 4.5f adds the Adv. and Vis. terms to the P/N Eddy and P/N ZM terms, and depicts no noticeable changes in the latitudinal, altitudinal, or magnitude structure of the zonal-mean zonal wind forcing term differences already explained by the P/N Eddy and P/N ZM terms. Comparison of Figures 4.5a-c with Figures 4.5d-f clearly shows that the dominant driver of the zonal-mean zonal wind differences calculated below (above) 200 km is due to changes in the PGF (ion drag force) terms in the zonal-mean meridional momentum equations.

The sum of all the terms on the left (right) hand side of equation 4.1 is illustrated in Figure 4.5g (Figure 4.5h). Below 200 km the Cor. term and PGF term balance one another and depict a forcing difference minimum similar to the one presented in Figures 4.5a-c. The altitudinal and latitudinal extent of this difference minimum is mainly attributable to changes in the PGF, which corresponds nicely with the maximum (from a magnitude standpoint) differences in the zonal-mean zonal winds depicted in Figures 4.5i and 4.5j. Particularly, the dissipating tides act to increase the westward winds at low latitudes and between ∼115-160 km by some -25 to -30 m s^{-1} (Figure 4.5i and Figures 4.2a and 4.2b). Above 200 km in Figures 4.5g and 4.5h the different ion drag terms balance (i.e., P/N LHS differences balance with P/N Eddy + P/N ZM terms), through which zonal-mean zonal wind differences around -10 m s^{-1} are carried to higher altitudes at equatorial latitudes (Figure 4.5i). The calculated zonal-mean zonal wind differences from the calculated forcing term differences depicted in Figures 4.5a-f using equation 4.2 are shown in Figure 4.5j, which compare reasonably well with the differences in the zonal-mean zonal winds calculated directly from the

TIE-GCM and shown in Figure 4.5i. The favorable comparison between Figures 4.5i and 4.5j suggests that we are not only calculating the forcing terms correctly, but also their differences between different TIE-GCM simulations. This validation step is presented only for the zonal-mean meridional momentum equation, as the other conservation laws would either require the use of numerical methods to compute their solutions or the magnitude of the forcing terms are so small such that small errors would result in noticeable differences between fields directly output from the TIE-GCM and those that are post-processed. Nonetheless, the validation process performed and discussed above for the zonal-mean zonal winds demonstrates that we properly account for the individual forcing terms in the TIE-GCM.

In order to understand how the dissipating tides drive the seasonal variability in the zonal-mean zonal wind differences within the dynamo region (Figure 4.2), a difference term analysis is performed for the months of July (Figure 4.6) and September (Figure 4.7), and then compared with the results presented in Figure 4.5 for the month of March. Figure 4.6a (Figure 4.7a) illustrates the differences in the PGF term from TIE-GCM simulations including and excluding CTMT lower boundary tidal forcing during July (September) as a function of latitude and altitude. In July, maximum (minimum) PGF differences occur between ∼160 and 240 km (∼110 and 150 km) with values of up to +130 m s^{-1} day^{-1} (−70 m s^{-1} day^{-1}). Below 200 km during September, maximum (minimum) PGF differences are calculated between ∼110 and 140 km (∼110 and 120 km) at low latitudes with values of up to +70 m s^{-1} day^{-1} (−40 m s^{-1} day^{-1}). Similar to March, PGF differences in the July and September below 200 km are driven by differences in the eddy heat source terms due to the dissipation of the vertically-propagating tides (with the adiabatic and diabatic heating and cooling terms playing smaller roles). The differences in the PGF term during September reach their largest magnitudes in the upper thermosphere at 350 km in Figure 4.7a, displaying the same latitudinal structure as those shown in Figure 4.5 during the month of March. As was shown for March (Figure 4.5c), including the Eddy, Adv., and Vis. term differences does not lead to drastic changes in the latitudinal, altitudinal, and magnitude structure of the forcing differences already imposed on the IT by the PGF during July (Figure 4.6b) and September (Figure 4.7b). Please note

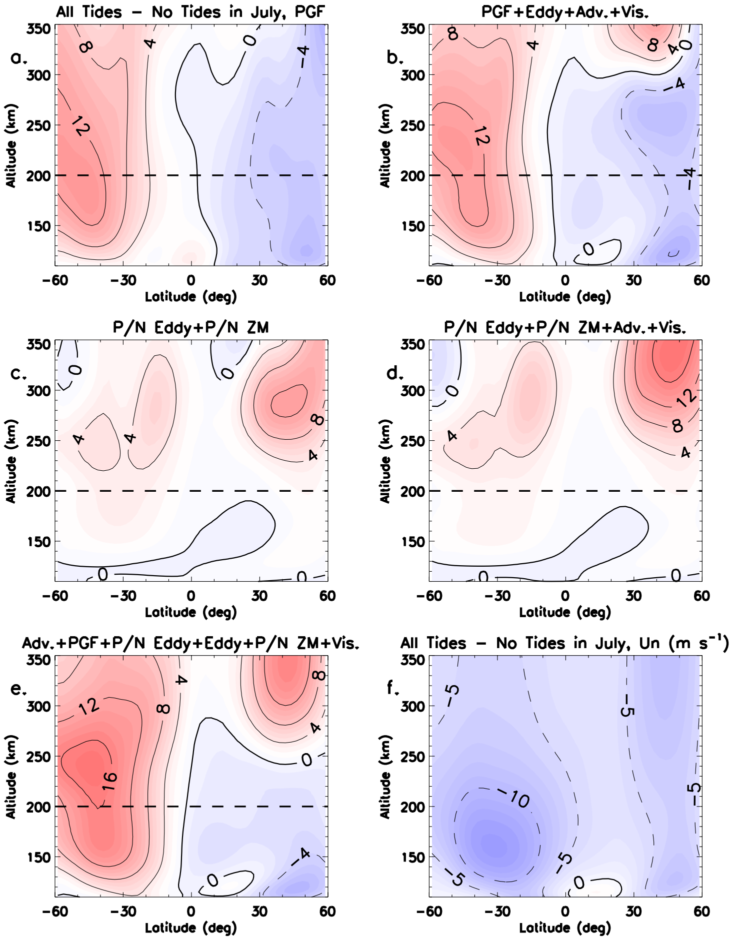

Figure 4.6: TIE-GCM forcing term differences between TIE-GCM simulations including and excluding CTMT tidal lower boundary forcing under July and solar medium conditions as a function of latitude and altitude. The PGF term is shown in (a); PGF + Eddy + Adv. + Vis. terms in (b); the P/N Eddy + P/N ZM terms in (c); P/N Eddy + P/N ZM + Adv. + Vis. terms in (d); the Adv. + PGF + P/N Eddy + Eddy + P/N ZM + Vis. terms in (e); the zonally-averaged zonal wind differences are shown in (f). Forcing terms from the meridional momentum equation are contoured every $\pm 4 \times 10^1$ m s^{-1} day^{-1}, while the zonally-averaged zonal wind differences are contoured every ± 5 m s^{-1}.

that it appears the Eddy term does have its maximum influence during the month of September, as the two-cell PGF difference structure at low latitudes and altitudes discussed above disappears once the Eddy difference term is included. This effect is approximately equal and opposite to the PGF differences.

Above 200 km, differences in the ion drag terms (i.e., P/N Eddy and P/N ZM) dominant

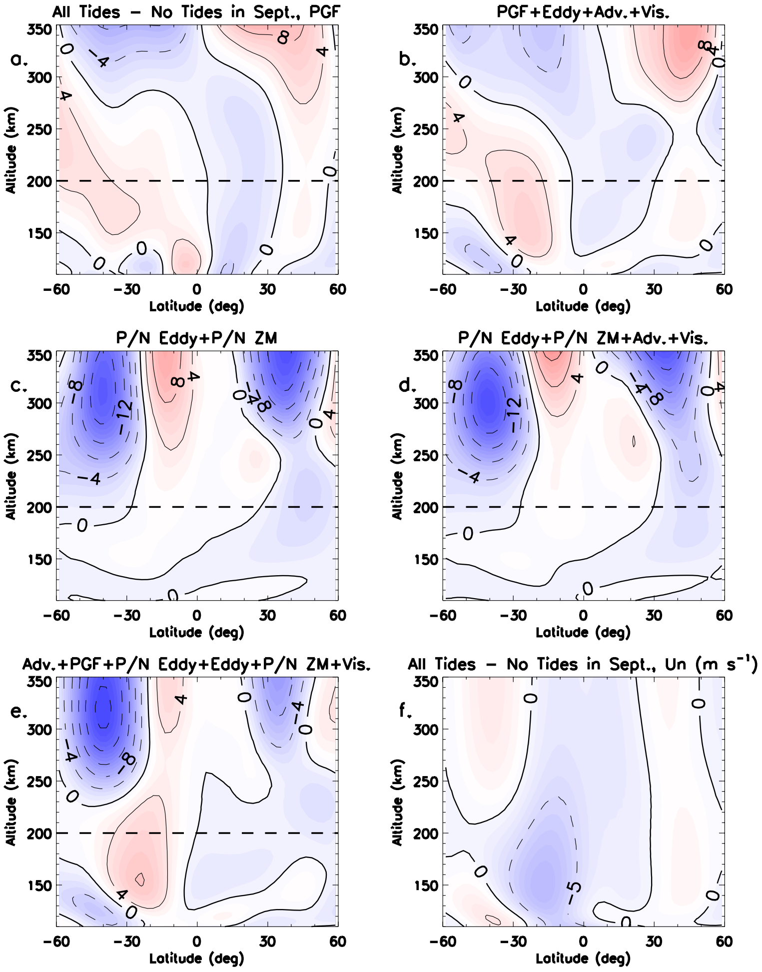

Figure 4.7: Same as Figure 4.6, except during the month of September.

the force differences during September (Figure 4.7c), while the Adv. and Vis. terms are of secondary importance (Figure 4.7d). This result is consistent with what was shown for the month of March (Figures 4.5d-f). Above 200 km during the month July P/N Eddy and P/N ZM maximum differences of +120 m s^{-1} day^{-1} (+70 m s^{-1} day^{-1}) are calculated in the northern (southern) hemisphere at mid-latitudes (Figure 4.6c). By comparing Figure 4.6a with Figure 4.6c, we see that the differences in the ion drag terms are of similar magnitude to those calculated for the PGF in the southern hemisphere. This seasonal variation in the tidally driven differences in the ion drag terms could be attributable to the seasonal asymmetry in solar forcing, which would more preferably heat and ionize the northern hemisphere ionosphere between April through September, thereby generating migrating and non-migrating tides in situ in the upper IT that act to change the ion drag term. However, further investigation is required to substantiate this mechanism. Once again including the Adv. and Vis. force term differences to the ion drag differences does very little to change the forcing differences already imposed by P/N Eddy and P/N ZM during July (Figure 4.6d) and September (Figure 4.7d), although Vis. forces tend to play more significant role during July. Supplemental contour plots showing the individual forcing terms during July and September from their respective TIE-GCM simulations that both include and exclude CTMT lower boundary tidal forcing are shown in Figures C.4-C.7.

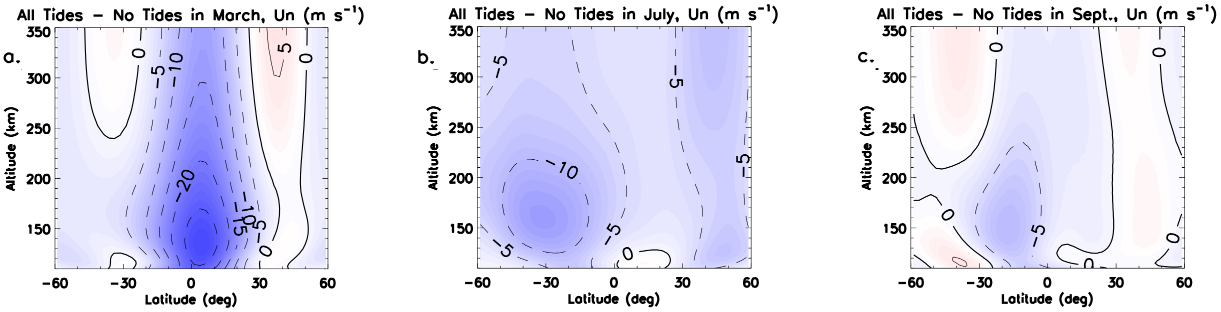

Figure 4.8: TIE-GCM zonal-mean zonal wind differences as function of latitude and altitude during March (a), July (b), and September (c), under solar medium conditions. Zonal mean zonal wind differences are contoured every ±5 m s^{-1}.

To facilitate a discussion on how the forcing terms contribute to the seasonal variability in the zonal-mean zonal winds, difference fields from March (Figure 4.5i), July (Figure 4.6f), and September (Figure 4.7f) are combined into one summary plot, Figure 4.8. Similar to the results is shown in Figure 4.2, the largest zonal wind differences occur during March within the dynamo region at equatorial latitudes (Figure 4.8a). These zonal wind differences are reduced to −14 m s^{-1} as we move to July (Figure 4.8b), and eventually reach their minimum differences of −9 m s^{-1} in September (Figure 4.8c). These reduced zonal-mean zonal wind differences are driven by the relative importance and magnitude of the forcing term differences attributable to tidal dissipation, as well as the latitudes and altitudes at which they occur. For example, if the PGF differences from March, July, and September all were of the same order of magnitude and occurred at the same latitude and altitude then the zonal wind differences would not vary with season. However, if (1) there is stronger forcing during one month versus another then larger zonal wind differences would occur, and similarly if (2) the latitude and altitude region of the largest force differences are seasonally dependent then the zonal wind differences will be seasonally dependent due to the terms in the denominator of 4.2. Applying the above logic to the zonal-mean zonal wind differences shown in Figures 4.2 and 4.8, one can easily understand how the dissipating tides drive seasonal variations in the zonal-mean zonal winds. Although, the tides drive the largest changes in the PGF below 200 km during July (compare Figure 4.6b with Figures 4.5c and 4.7b), because this maximum difference occurs at mid-latitudes instead of the equatorial latitudes (i.e., as it does for March and September) the changes in the zonal-mean zonal winds are smaller in July than March due to the increased influence of the Cor. and P/N LHS terms (i.e., the denominator of 4.2). Using the explanation offered above for the month of July and noticing that the PGF differences during September are comparatively weaker and are restricted to a smaller altitude range (Figure 4.7a) than those shown for March (Figure 4.5c) and July (Figure 4.6b), we now see why the zonal-mean zonal wind differences are minimum during September. In summary, maximum zonal-mean zonal wind changes occur in March because the changes in the PGF mainly attributable to the eddy heat source term produced due to tidal dissipation are relatively big (i.e., between -70 and $+40$ m s^{-1} day^{-1}) and confined to equatorial latitudes. These large zonal-mean zonal wind differences during March are reduced during July due to the explanation offered in (2) above, and then are further reduced in September due to a combination of (1) and (2). Below 200 km, the relative importance of explanations (1) and (2) are what drives the zonal-mean zonal wind differences throughout the other months not described herein. Above 200 km, zonal-mean zonal wind differences are driven by tidally induced differences to the ion drag term, although it becomes more difficult to use explanations (1) an (2) at higher altitudes because of the increased role of vertical viscous forces (i.e., the molecular diffusion of momentum occurs over short time scales in the upper IT and its importance increases with decreasing density).

Figures 4.9a and 4.9b (Figures 4.9e and 4.9f) display zonal wind difference fields at 115 km

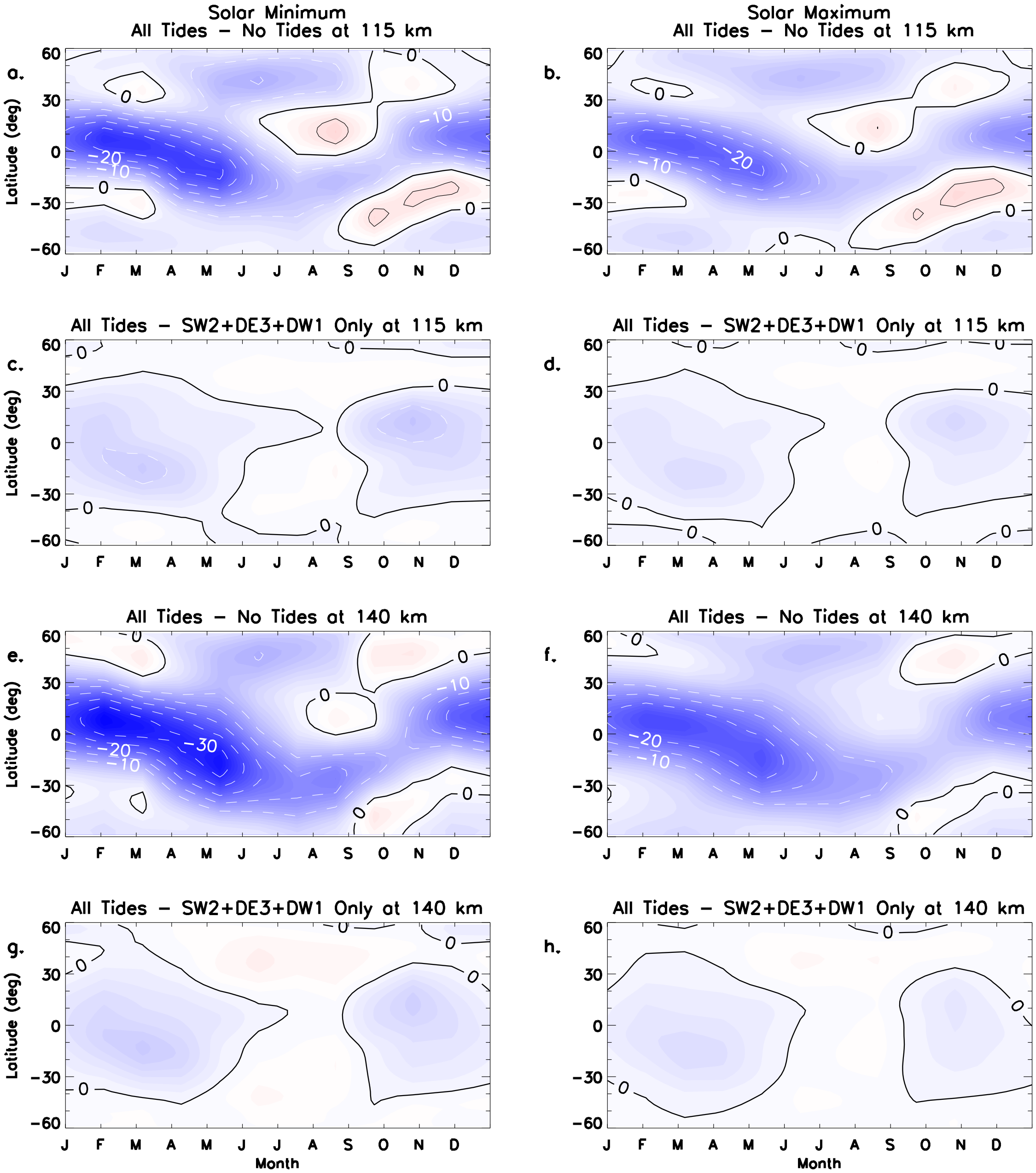

Figure 4.9: TIE-GCM zonal-mean zonal wind differences as function of month and latitude at 115 km (a-d) and 140 km (e-h) under solar minimum (Left Column) and solar maximum (Right Column) conditions. Differences between TIE-GCM simulations including and excluding CTMT tidal forcing at the model lower boundary are shown in (a), (b), (e), and (f); differences between TIE-GCM simulations including all tidal components and only SW2, DE3, and DW1 from CTMT at the model lower boundary are shown in (c), (d), (g), and (h). Zonal mean zonal wind differences are contoured every ±5 m s^{-1}.

(140 km) between TIE-GCM simulations with and without CTMT tidal lower boundary forcing under solar minimum and solar maximum conditions, respectively. A comparison between Figures 4.9a and 4.9b (Figures 4.9e and 4.9f) with Figure 4.2a (Figure 4.2b) shows that, regardless of solar cycle condition, the zonal-mean zonal wind differences induced by dissipating tides are mainly constrained to low latitudes (i.e., between ± 30° latitude). Maximum differences occur in the boreal winter and spring months, and eventually reach their minimum during the autumnal equinox. The largest zonal-mean zonal wind differences exhibit small solar cycle variations of 8 m s^{-1} (in an absolute sense) between solar minimum (largest difference of 32 m s^{-1} at 140 km in Figure 4.9e) and maximum (largest difference of 24 m s^{-1} at 140 km in Figure 4.9f). Also, consistent with the zonal-mean zonal wind difference fields calculated for at solar medium (shown in Figures 4.2g and 4.2h), zonal wind differences under solar minimum and maximum conditions can almost be completely explained by three tidal components: DW1, SW2, and DE3 (Figures 4.9c, 4.9d, 4.9g, and 4.9h). Small changes in the zonal wind differences and the important tidal components responsible for these differences as function of solar cycle result from small changes in DW1, SW2, and DE3 zonal wind tidal structures as a function of solar cycle (see Figure 4.3 and Figures C.8-C.9).

Small changes in the seasonal variability of the zonal-mean zonal wind differences is best explained by calculating the differences in the forcing terms of equation 2.13 as a function of solar cycle. Figure 4.10 illustrates the important forcing term and zonal-mean zonal wind difference fields from solar minimum (Left Column) and solar maximum (Right Column) as a function of latitude and altitude during the month March. Since the largest zonal wind differences occur below 200 km we restrict our discussion of Figure 4.10 to the dynamo region, recognizing that when all the terms on the right hand of 4.1 are included (i.e., Figures 4.10e and 4.10f) differences above 200 km are of similar or slightly smaller magnitudes. Once again, the largest differences in the forcing terms on the right side of 4.1 result from changes in the PGF (Figures 4.10a and Figures 4.10b) via the eddy heat source term. The latitudinal and altitudinal structure below 200 km of the forcing term differences driven by the PGF are extremely similar between solar minimum (Figures 4.10a and 4.10e), medium (Figures 4.5a and 4.5h), and maximum (Figures 4.10b and Figures 4.10f), depicting

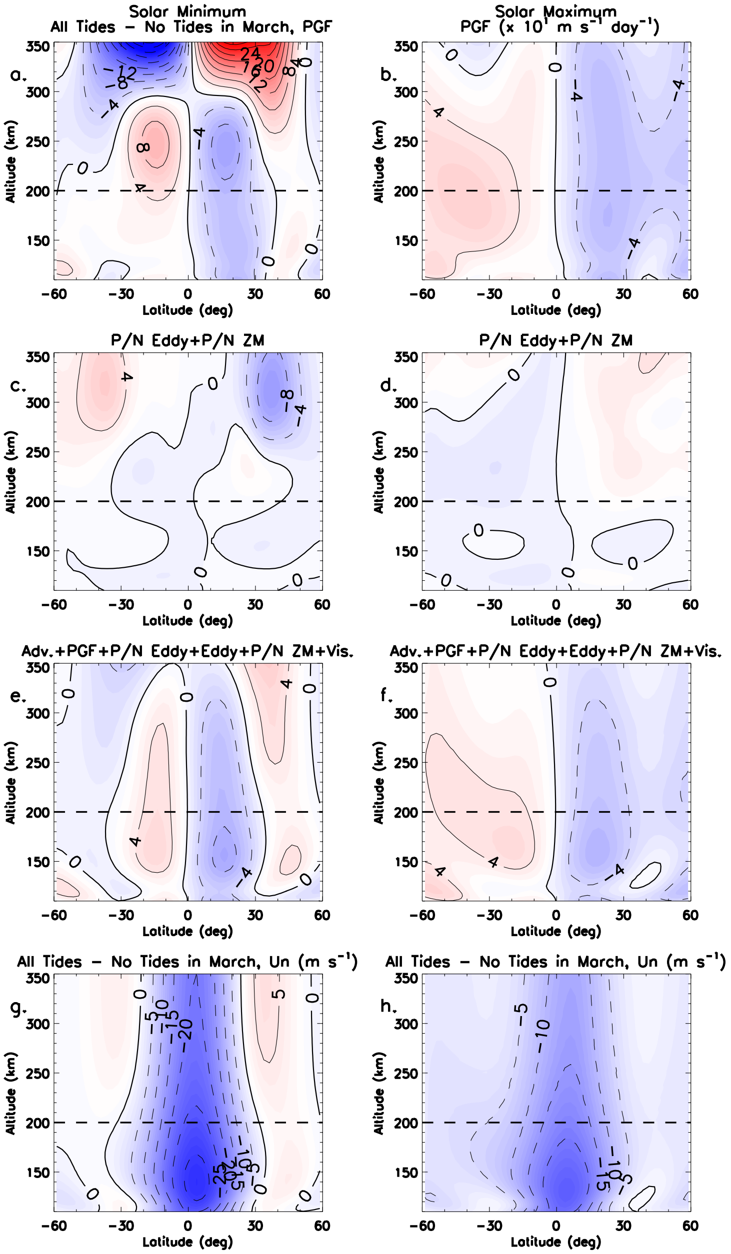

Figure 4.10: TIE-GCM forcing term differences between TIE-GCM simulations including and excluding CTMT tidal lower boundary forcing during March under solar minimum (Left Column) and solar maximum (Right Column) conditions as a function of latitude and altitude. The PGF term is shown in (a) and (b); the P/N Eddy + P/N ZM terms in (c) and (d); the Adv. + PGF + P/N Eddy + Eddy + P/N ZM + Vis. terms in (e) and (f); the zonally-averaged zonal wind differences are shown in (g) and (h). Forcing terms from the meridional momentum equation are contoured every $\pm 4 \times 10^1$ m s^{-1} day^{-1}, while the zonally-averaged zonal wind differences are contoured every ± 5 m s^{-1}.

the differences ranging from -70 to $+60$ m s^{-1} day^{-1} at low-latitudes and $\sim$150 km. The lack of solar cycle variability in the forcing term differences, and especially in the PGF differences provides the explanation as to why the zonal-mean zonal wind differences do not vary much with solar cycle. The rationale given above for the lack of solar cycle variability associated with the zonal-mean zonal winds induced by the dissipating tides applies to the other months as well, including July and September (see Figures C.10 and C.11). It must also be noted that the relative importance of the secondary terms does vary with solar cycle; however, their contributions are still not large enough to greatly affect the overall lack of solar cycle variability in the zonal-mean zonal winds (e.g., the eddy momentum source term contributes more in solar minimum than solar maximum as evidenced by the comparison of Figures 4.10a and 4.10e, which illustrates the extension of the positive force differences at low latitudes when the Eddy term is considered in addition to the PGF and other forces).

4.4 Tidal Impacts on the Zonal-Mean Meridional Winds

Figure 4.11 depicts TIE-GCM zonally- and diurnally-averaged meridional winds generated with and without CTMT lower boundary tidal forcing at 140 km over a climatological year. Again, the 140 km altitude was chosen because it is the altitude at which the strongest vertically propagating wave, SW2, attains its maximum in our TIE-GCM simulations. In the absence of tidal forcing at the TIE-GCM lower boundary, summer to winter flow persists throughout the entire year with meridional wind speeds ranging between ±7 m s^{-1} (Figure 4.11b). When tidal forcing is included at the TIE-GCM lower boundary the meridional wind structure still shows summer to winter flow persisting throughout the year, although the latitudinal structure is altered slightly and meridional wind speeds have increased by up to 2 m s^{-1} (Figure 4.11a). The structure (i.e., latitudinal and seasonal structure) of the meridional winds depicted in Figures 4.11a and 4.11b is representative of meridional structure at other altitudes as the meridional winds do not vary much with altitude in the IT.

Figure 4.12a illustrates the meridional wind difference fields at 140 km between TIE-GCM

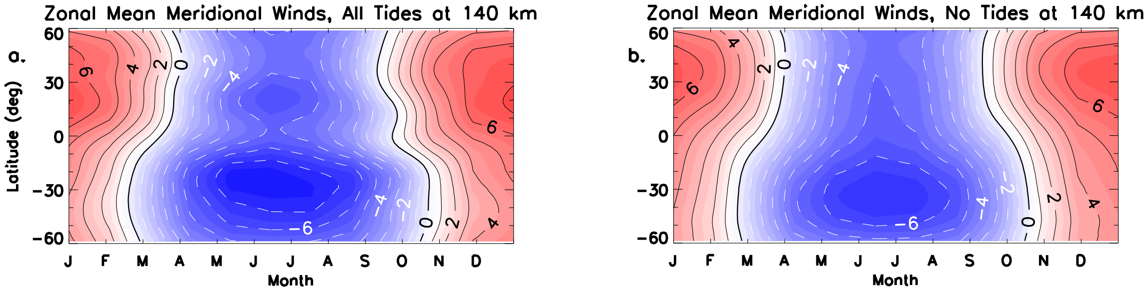

Figure 4.11: Same as Figure 4.1, except for the zonal-mean meridional winds. Meridional winds are contoured every ±1 m s^{-1}.

simulations with and without CTMT tidal lower boundary forcing under solar medium conditions. We deduce from Figure 4.12a that the net effect of the upward-propagating tidal spectrum is relatively small with respect to changes in the zonal-mean meridional winds in the IT, as differences between -2.5 and 2 m s^{-1} are attributable to the dissipating tides. Although, these tidal induced differences in the zonal-mean meridional winds are small in an absolute sense, they are on the order of ∼30 to 40% of their zonal-mean values and therefore are investigated in the same level of detail as the zonal-mean zonal wind differences presented in section 4.3. Vertical propagating tides have their largest effects on the zonal-mean meridional winds at low latitudes during boreal spring and summer months, as they act to accelerate (decelerate) the southward winds shown in Figure 4.11 by up to -2.5 m s^{-1} (2 m s^{-1}) at southern (northern) low latitudes and 140 km.

Figures 4.12b and 4.12c show meridional wind difference fields at 140 km between TIE-GCM simulations including CTMT lower boundary tidal forcing with TIE-GCM simulations that include only migrating tidal components from the CTMT. Specifically, Figure 4.12b shows the differences between simulations that include all of the CTMT tidal components forced at the TIE-GCM lower boundary and simulations that only include tidal forcing from DW1 at 140 km. By including just DW1 (Figure 4.12b), the seasonal and latitudinal distribution of the zonal-mean meridional winds remain unchanged from what is shown in Figure 4.12a. However, at altitudes close to the TIE-GCM lower boundary (i.e., between 100-110 km) DW1 has relatively large effect on the zonal-mean meridional wind changes (not shown), but we tend to disregard TIE-GCM results within the first

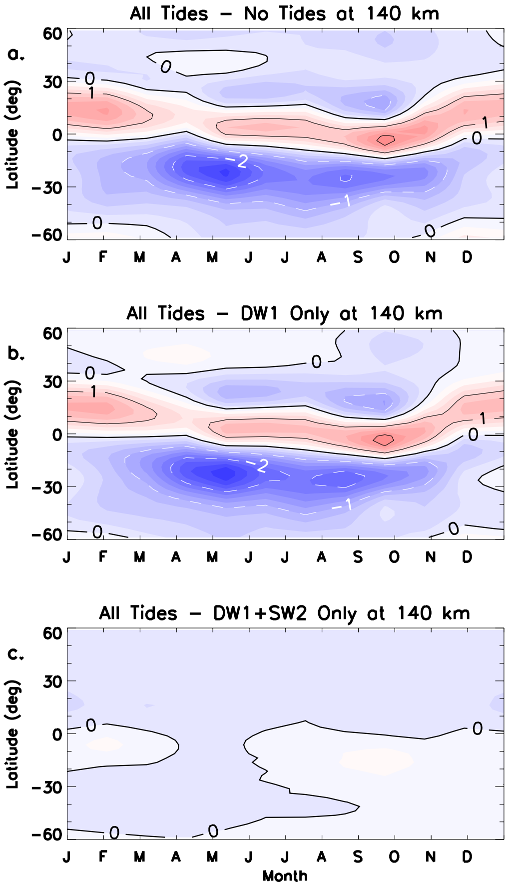

All Tides – No Tides at 140 km

All Tides – DW1 Only at 140 km

All Tides – DW1+SW2 Only at 140 km

Figure 4.12: TIE-GCM zonal-mean meridonal wind differences as function of month and latitude at 140 km. Differences between TIE-GCM simulations including and excluding CTMT tidal forcing at the model lower boundary are shown in (a); differences between TIE-GCM simulations including all tidal components and only DW1 from the CTMT at the model lower boundary are shown in (b); differences between TIE-GCM simulations including all tidal components and only DW1 and SW2 from the CTMT at the model lower boundary are shown in (c). Meridional wind differences are contoured every ±1 m s^{-1}.

couple of scale heights in the model because of the influence of the fixed chemical lower boundary conditions. These fixed chemical lower boundary conditions alter the solar radiation absorption and thus the pressure gradients used to calculate the meridional winds. Therefore, we limit our discussion to zonal-mean meridional wind fields above 110 km, although we do acknowledge that meridional winds in the lower thermosphere will be affected by DW1 and that will be discussed further in Chapter 6, when discussing tidal impacts on constituent distributions in the IT.

By including both migrating tidal components (i.e., DW1 and SW2), we see that the majority

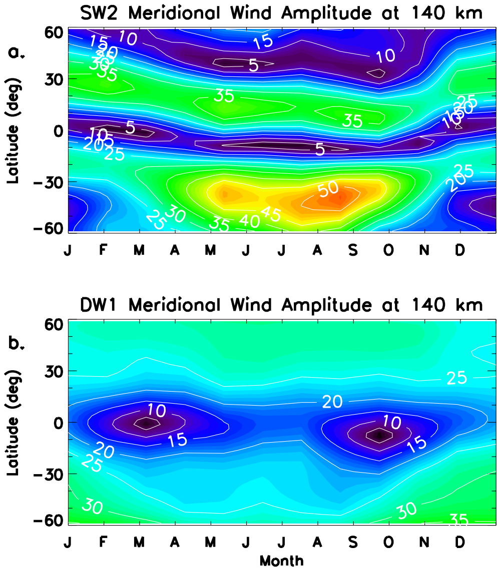

Figure 4.13: TIE-GCM meridional wind tidal amplitudes at 140 km. The SW2 is shown in (a) and DW1 is shown in (b). Tidal wind amplitudes contoured every 5 m s^{-1}.

of the zonal-mean meridional wind differences are gone, implying that SW2 is the dominant driver of the zonal-mean meridional wind differences at 140 km (Figure 4.12c). Results illustrated in Figure 4.13, which show the seasonal and latitudinal distribution of the meridional wind amplitude of SW2 and DW1, and provide a means to determine if the latitudinal and seasonal structure of the tidal amplitudes are related to changes in the zonal-mean meridional winds. Figure 4.13a clearly shows that the latitudinal and seasonal distribution of SW2 meridional wind amplitude corresponds extremely well with its maximum influence on the zonal-mean meridional winds in the dynamo region, with a strong bifurcated amplitude structure about the equator revealing maximum amplitudes on the order of 50 m s^{-1} (35 m s^{-1}) in April, May, August and September at southern (northern) latitudes. Please note that above ~100 km SW2 is partially generated in-situ by EUV absorption, however, this in-situ component (Figure C.12a) only contributes between 10 to 15 m s^{-1} to the total SW2 meridional wind amplitude depicted in Figure 4.13b. Therefore, we can draw the same conclusion as was drawn for the zonal-mean zonal winds, i.e., the dissipation of the vertically propagating SW2 is the dominant driver of the zonal-mean meridional wind changes within the dynamo region.

Comparing Figure 4.13b with Figure C.12b shows that at 140 km DW1 is forced in-situ in the meridional wind field. This in-situ forced DW1 will appear in all of the TIE-GCM simulations discussed above and thus explains its small contribution to the zonal-mean meridional wind differences shown in Figure 4.12b. Additionally, unlike the zonal-mean zonal winds DE3 does not play a role in changing the zonal-mean meridional winds. This is most probably due to the fact that typically the strongest amplitude Hough mode of DE3 is its first symmetric mode, which is a Kelvin wave that has small amplitudes in the meridional direction.

4.4.1 Interpreting the Meridional Wind Differences, Seasonal and Solar Cycle Variability

In order to assess the dissipating tidal impacts on the zonal-mean meridional winds in the IT system, we follow the procedure utilized in section 4.3.1, except now forcing terms from the zonal-mean zonal momentum equation (i.e., equation 2.12) are analyzed. Shown again below is equation 2.12,

$$\frac{\overline{v}}{a}\frac{\partial \overline{u}}{\partial \theta} + \overline{w}\frac{\partial \overline{u}}{\partial z} - 2\Omega\overline{v}\sin\theta - \frac{\overline{u}\,\overline{v}\tan\theta}{a} + \overline{\lambda_{xy}}\,\overline{v} =$$

$$-\overline{F}_x + \overline{\lambda_{xy}}\,\overline{v_i} - \overline{\lambda_{xx}}\,\overline{u} + \overline{\lambda_{xx}}\,\overline{u_i} - \overline{\lambda'_{xy}v'} + \overline{\lambda'_{xy}v'_i} - \overline{\lambda'_{xx}u'} + \overline{\lambda'_{xx}u'_i} + \frac{1}{\rho_0}\frac{\partial}{\partial z}\left(\overline{\mu}\frac{\partial \overline{u}}{\partial z}\right). \qquad \text{(2.12 revisited)}$$

The zonal-mean zonal momentum equation includes all of the same forces and processes as those discussed in section 4.3.1 for the zonal-mean meridional momentum equation, with the exception of the pressure gradient force in the zonal direction (i.e., disappears because our zonal-mean variables do not depend on longitude). Briefly from left to right in equation 2.12 the first two terms are the Adv., term three is the Cor. term, term four is the Curv. term, term five is the P/N LHS term, term six is the Eddy term, terms seven through nine are the P/N ZM terms, terms ten through thirteen are the P/N Eddy terms, and term fourteen is the Vis. term.

Figure 4.14 (Figure C.13) shows all of the terms in equation 2.12 along with the zonal-mean meridional wind field from the TIE-GCM forced with (without) CTMT tidal forcing at the model lower boundary under September and solar medium conditions as a function of latitude and

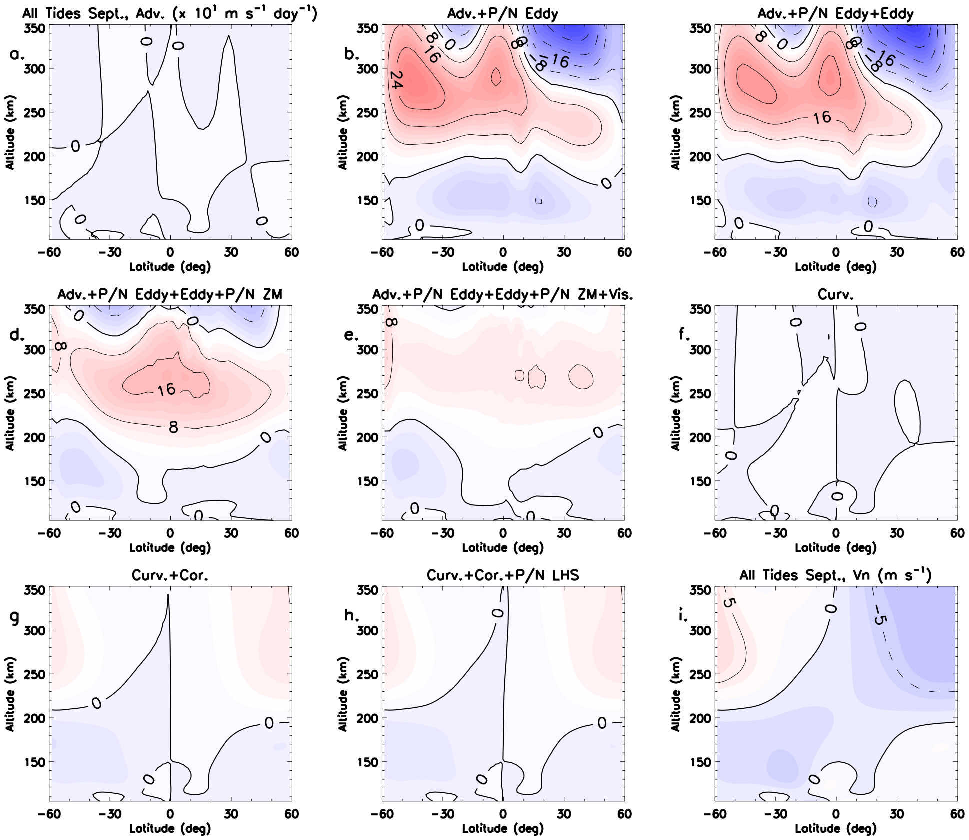

Figure 4.14: TIE-GCM zonal-mean forcing terms from the zonal-mean zonal momentum equation including CTMT lower boundary tidal forcing under September and solar medium conditions as a function of latitude and altitude. The Adv. term is shown in (a); Adv. + P/N Eddy terms in (b); Adv. + P/N Eddy + Eddy terms in (c); Adv. + P/N Eddy + Eddy + P/N ZM terms in (d); Adv. + P/N Eddy + Eddy + P/N ZM + Vis. terms in (e); the Curv. term in (f); Curv. + Cor. terms in (g); Curv. + Cor. + P/N LHS in (h); the zonally-averaged meridional winds are shown in (i). Forcing terms from the zonal-mean zonal momentum equation are contoured every $\pm 8 \times 10^1$ m s^{-1} day^{-1}, while the zonally-averaged meridional winds are contoured every ± 5 m s^{-1}.

altitude. The month of September was chosen because it is one of the months where the largest zonal-mean meridional wind differences occur in the dynamo region (Figure 4.12a). During equinox the advective terms in the zonal-mean zonal momentum equation are quite small (Figure 4.14a). The P/N Eddy term is one of the largest forcing terms in equation 2.12 showing acceleration values of -80 m s^{-1} day^{-1} at low latitudes near 150 km during September (Figure 4.14b). Figure 4.14b also shows large P/N Eddy values above 200 km ranging from -350 to $+300$ m s^{-1} day^{-1} over low and middle latitudes. The eddy momentum source term in the zonal direction does little to alter the P/N Eddy imposed forcing structure in the month of September (Figure 4.14c). Once the P/N ZM and Vis. terms are included with the Adv., P/N Eddy, and Eddy terms we see a large reduction in the forcing terms on the right hand side of equation 2.12 (Figure 4.14e). The P/N ZM and Vis. terms act to reduce the strong zonal-mean meridional wind accelerations due to the P/N Eddy term by ∼200 m s^{-1} day^{-1} (∼50 m s^{-1} day^{-1}) in the upper (lower) IT (compare Figure 4.14e with Figure 4.14c).

Figures 4.14f-g show the terms in equation 2.12 that are products of $\overline{v}$. Clearly, the most important term is the Cor. term driving zonal-mean meridional wind accelerations on the order ±40 m s^{-1} day^{-1} in the IT (Figures 4.14g and 4.14h). The Cor. term is roughly balanced by the combination of mostly the P/N Eddy, P/N ZM, and Vis. forces in the zonal-mean zonal momentum equation. The author does acknowledge here that the balance between Figures 4.14e and 4.14h is not as good as that depicted for the forcing terms shown for zonal-mean meridional momentum equation (e.g., Figure 4.4). However, forcing terms in equation 2.12 (Figure 4.14) are generally an order of magnitude smaller than the forcing terms in equation 2.13 (Figure 4.4), and so discrepancies between these smaller terms become more apparent, even though the errors between the calculated forcing terms are of the same order of magnitude.

Understanding of how the dissipating tides act to change the zonal-mean meridional winds is gained by analyzing the differences in the forcing term between TIE-GCM simulations including and excluding CTMT lower boundary tidal forcing under September and solar medium conditions presented in Figure 4.15. Due to the dominance of the ion drag terms at higher altitudes, Figure 4.15 only shows the 110 to 150 km height regime in order to better understand the tidal impacts in the dynamo region. Figure 4.15a clearly shows that differences in the zonal-mean meridional winds below 150 km are not driven by differences in the curvature term. Differences in the Cor. term between TIE-GCM simulations with and without CTMT lower boundary forcing show differences ranging from -10 to $+5$ m s^{-1} day^{-1} between 110 and 150 km, with the largest differences seen mainly polewards of ±30° latitude (Figure 4.15b). Adding in the P/N LHS and Adv. forcing term differences does not noticeably alter the forcing differences already imposed by the Coriolis force

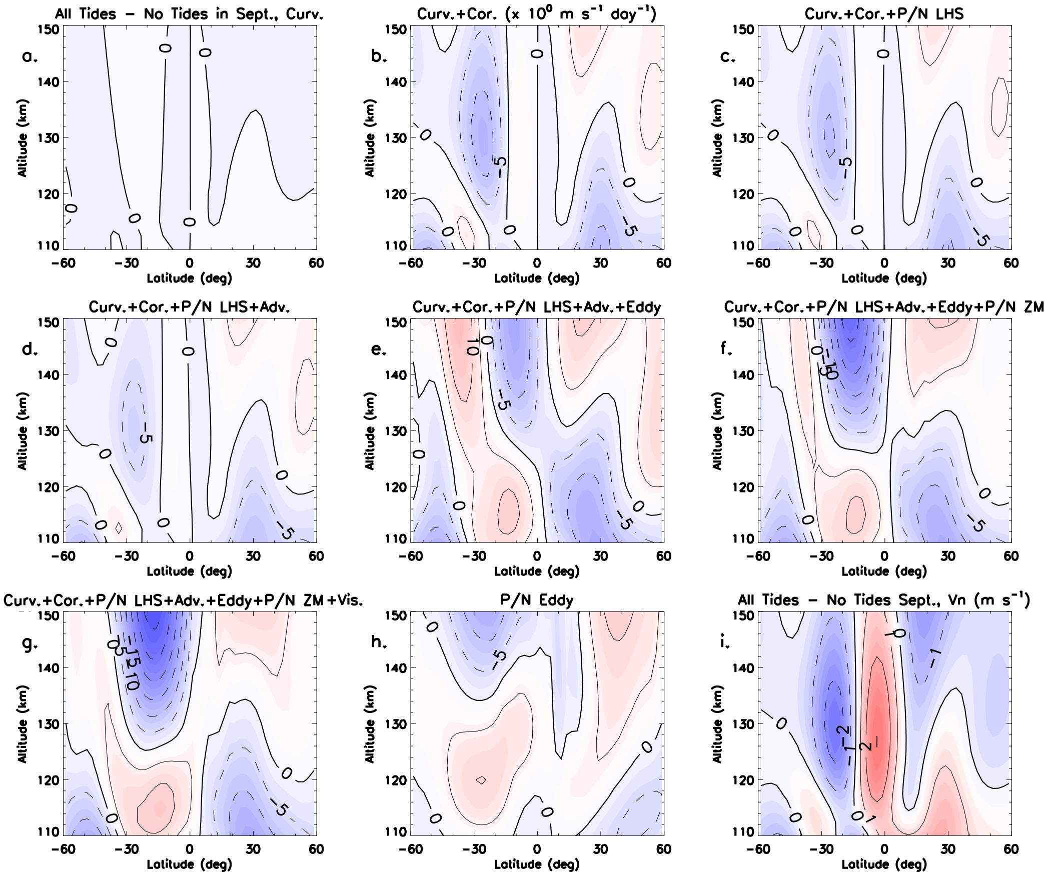

All Tides – No Tides in Sept., Curv.

Curv.+Cor. (x 10^0 m s^{-1} day^{-1})

Curv.+Cor.+P/N LHS

Curv.+Cor.+P/N LHS+Adv.

Curv.+Cor.+P/N LHS+Adv.+Eddy

Curv.+Cor.+P/N LHS+Adv.+Eddy+P/N ZM

Curv.+Cor.+P/N LHS+Adv.+Eddy+P/N ZM+Vis.

P/N Eddy

All Tides – No Tides Sept., Vn (m s^{-1})

Figure 4.15: TIE-GCM forcing term differences between simulations including and excluding CTMT tidal lower boundary forcing under September and solar medium conditions as a function of latitude and between 110 and 150 km. The Curv. term is shown in (a); Curv. + Cor. terms in (b); Curv. + Cor. + P/N LHS terms in (c); Curv. + Cor. + P/N LHS + Adv. terms in (d); Curv. + Cor. + P/N LHS + Adv. + Eddy terms in (e); Curv. + Cor. + P/N LHS + Adv. + Eddy + P/N ZM terms in (f); Curv. + Cor. + P/N LHS + Adv. + Eddy + P/N ZM + Vis. terms in (g); the P/N Eddy term in (h); the zonally-averaged meridional wind differences are shown in (i). Forcing terms from the zonal-mean zonal momentum equation are contoured every ±5 m s^{-1} day^{-1}, while the zonally-averaged meridional wind differences are contoured every ±1 m s^{-1}.

(Figures 4.15 and 4.15d). Tidal dissipation enhances the differences in the forcing terms of the zonal-mean zonal momentum equation by up to 10 m s^{-1} day^{-1} at low latitudes throughout the entire 110 to 150 km height regime during September (Figure 4.15e). P/N ZM and Vis. effects occur above ~130 km mainly acting to enhance the region of negative forcing differences to −30 m s^{-1} day^{-1} at low latitudes (Figure 4.15g). Differences in the P/N Eddy term (Figure 4.15h) show good balance with those calculated from the sum of all the other forces including, Curv. + Cor.

+ P/N LHS + Adv. + Eddy + P/N ZM + Vis. terms. Since the largest zonal-mean meridional wind differences occur during September and are constrained to ±30° latitude in Figure 4.15i, one can conclude that the forcing terms most responsible for driving the tidal-induced differences are a combination of the Eddy, P/N ZM, and P/N Eddy terms with the others being of secondary importance.

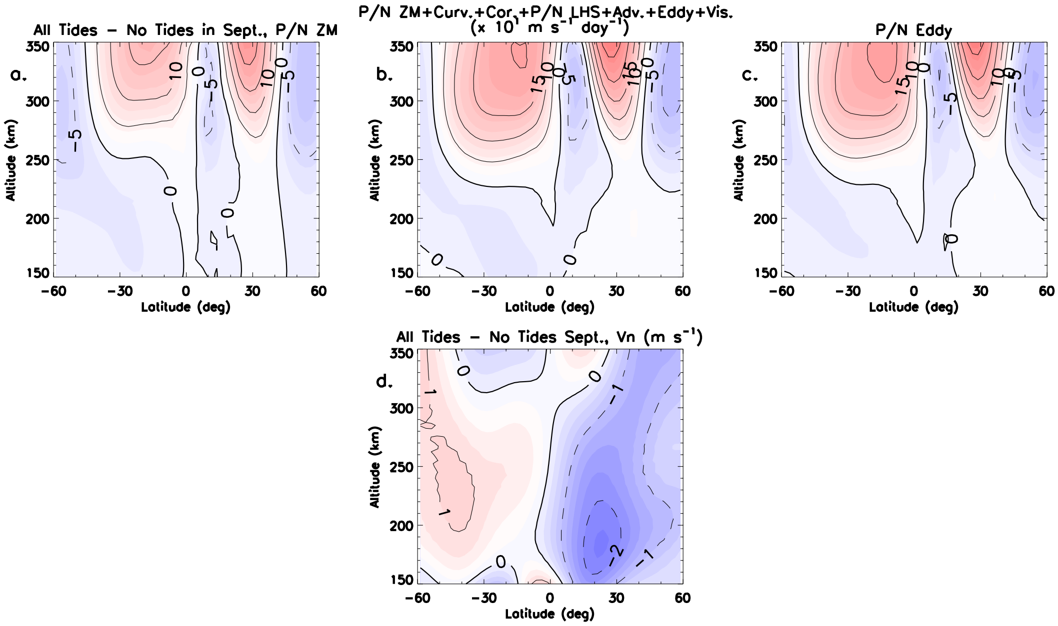

Figure 4.16: TIE-GCM forcing term differences between simulations including and excluding CTMT tidal lower boundary forcing under September and solar medium conditions as a function of latitude and between 150 and 350 km. The P/N ZM term is shown in (a); P/N ZM + Curv. + Cor. + P/N LHS + Adv. + Eddy + Vis. terms in (b); the P/N Eddy term in (c); the zonally-averaged meridional wind differences are shown in (d). Forcing terms from the zonal-mean zonal momentum equation are contoured every ±5 × 10^1 m s^{-1} day^{-1}, while the zonally-averaged meridional wind differences are contoured every ±1 m s^{-1}.

As was shown in the Figure 4.14 the largest magnitude forcing terms in equation 2.12 were the ion drag terms. Figure 4.16 shows the differences in the forcing terms of equation 2.12 in the upper IT from TIE-GCM simulations with and without CTMT lower boundary tidal forcing under September and solar medium conditions, in order to better understand how tidal dissipation drives changes in the zonal-mean meridional winds in the upper IT. Figures 4.16a and 4.16c clearly shows that the dissipating tides have their largest effect on P/N ZM and P/N Eddy terms with all of the other forcing terms being of much less importance. Tidal dissipation acts to alter the P/N ZM and P/N Eddy terms by up to 200 m s^{-1} day^{-1} around 350 km at low and middle latitudes (Figures 4.16a-c). Although, the tidal effects on the ion drag terms in the upper IT are an order of magnitude larger than the tidal effects on the forcing terms in the lower IT zonal-mean meridional wind differences only change by 1 or 2 m s^{-1} (Figure 4.16d). This is a result of the increased influence of molecular diffusion of momentum in the upper IT, as the role of dissipation increases as $\sim\frac{1}{\rho}$ and is trying to eliminate the vertical gradients in the zonal-mean wind fields.

There is not a great deal of seasonal variability in the zonal-mean meridional wind differences attributable to tidal dissipation in the dynamo region (see Figure 4.12a). Meridional winds differences on the order of ±1-2 m s^{-1} persist over low latitudes throughout most of the year. This is due to the lack of seasonal variability in the dominant forcing term differences, as well as the small magnitudes of the forcing term differences. For example, Eddy, P/N ZM, and P/N Eddy terms are the dominant drivers of the zonal-mean meridional wind differences in the lower IT in both March and July (Figures C.14 and C.15), which is the same as September. The same can be said for the dominant forcing terms in the upper IT (i.e., the P/N ZM and P/N Eddy terms) in both March and July (Figures C.16 and C.17), although in July differences in the Vis. terms are also important.

There is also not a great deal of solar cycle variability in the zonal-mean meridional wind differences induced by tidal dissipation in the dynamo region, as is evidenced by the similarities of the zonal-mean meridional wind differences at 140 km shown in Figures 4.17a and 4.17b. During all three solar cycle conditions examined herein (i.e., solar minimum, medium, and maximum) the differences in the zonal-mean meridional wind field has the same seasonal and latitudinal structure with largest differences constrained to low latitudes. Furthermore, the magnitude of the differences only changes by at most ∼0.5 to 1 m s^{-1} at low latitudes (Figures 4.17a and 4.17b). Regardless of solar cycle DW1 has little affect on the zonal-mean meridional winds at 140 km (Figures 4.17c and 4.17d). Since SW2 is the largest amplitude tidal component in the dynamo region during all three solar cycle conditions (see Figure C.18), it drives the mean meridional wind differences throughout

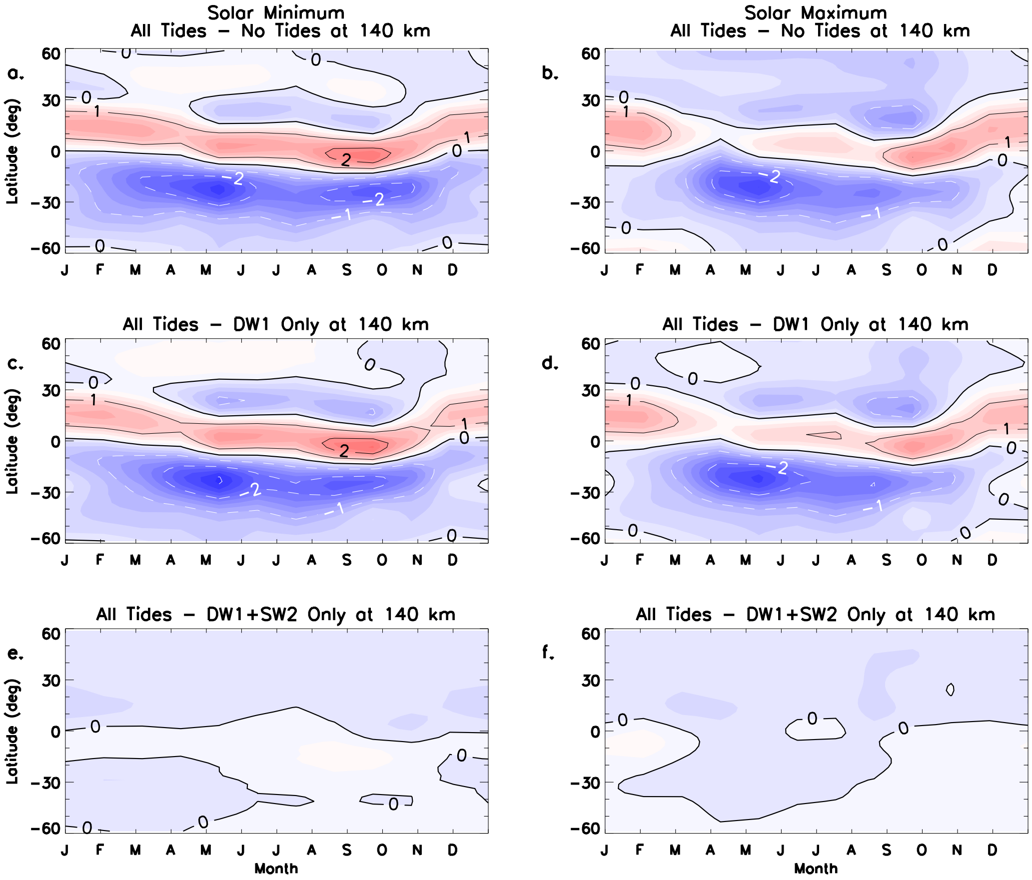

Figure 4.17: Same as Figure 4.12, except for zonal-mean meridional wind differences under both solar minimum (Left Column) and solar maximum (Right Column) conditions.

the solar cycle within the dynamo region (Figures 4.17e and 4.17f). Due to these small changes in the zonal-mean meridional wind differences and the tides responsible for their changes, a forcing term analysis of equation 2.12 for the different solar cycle conditions was not considered as part of this work; although, one could surmise that given the forcing term analysis for the zonal-mean zonal winds, the same forcing terms would be dominant with only very small changes in their magnitudes relative to different solar cycle conditions.

4.4.2 Tidal Induced Meridional Wind Effects on h_mF_2

Figure 4.18 depicts difference fields in the height of the F_2-layer peak, h_mF_2, meridional winds, and the field-aligned plasma motions at 330 km (i.e., approximately the globally averaged

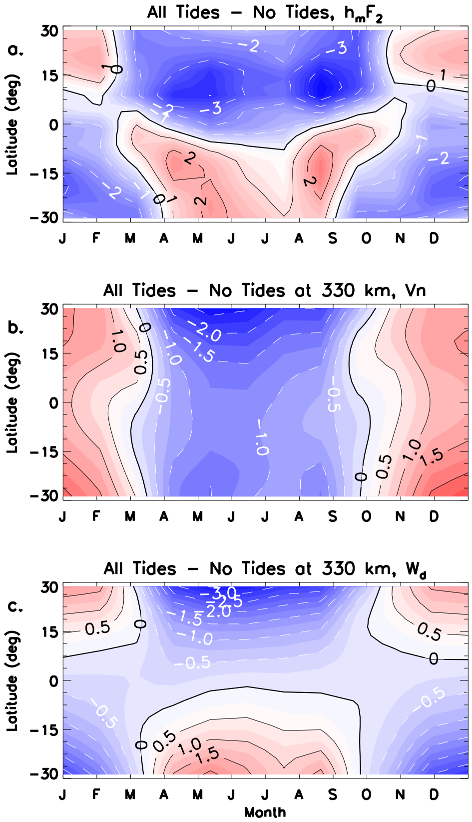

Figure 4.18: Difference fields between TIE-GCM simulations including and excluding CTMT lower boundary tidal forcing in h_mF_2 (a), meridional wind (b), and calculated parallel field-aligned plasma motion (c) at 330 km as a function of month and latitude. h_mF_2 differences are contoured every 1 km, while meridional wind and vertical plasma motion differences are contoured every ± 0.5 m s^{-1}.

h_mF_2 height in our TIE-GCM simulations), for TIE-GCM simulations with and without CTMT lower boundary tidal forcing. Changes in h_mF_2 due to vertically-propagating tides range from -4 to $+2$ km, with the biggest differences centered right around ±15° latitude during May and August (Figure 4.18a), which is when the largest differences in the zonal-mean meridional winds are experienced (Figure 4.12a). These differences in h_mF_2 mainly result from the changes in the meridional winds (Figure 4.18b), which induce changes in the field-aligned plasma motions (Figure 4.18c). Differences in the field-aligned plasma motions (Figure 4.18c) range from -3.5 to 2 m s^{-1} and have a seasonal variation that correlate well with the h_mF_2 differences shown in Figure 4.18a. Field-aligned plasma motions are induced by meridional winds blowing along inclined magnetic field lines in the F-region ionosphere. The velocity parallel to the magnetic field (what we term W_d) induced by an incident meridional wind due to ion drag is given by,

$$W_d = \frac{v}{\cot I}. \tag{4.3}$$

For example, a northward (southward) wind encountering a magnetic field line north of the magnetic equator would result in plasma being pushed up (down) a magnetic field line, thus lifting (lowering) the h_mF_2. This is what is occurring during the boreal winter (summer) months north of the magnetic equator in Figure 4.18. The opposite effect (i.e., a southward (northward) wind blowing south of the magnetic equator would result in plasma being pushed up (down) the magnetic field line, thus lifting (lowering) the h_mF_2) is occurring south of the magnetic equator during the austral summer (winter) months in Figure 4.18. The effects of tidally-induced meridional winds on the h_mF_2 maximizes/minimizes at fairly low geographic latitudes (e.g., Arecibo, 18.35° N) where the magnetic dip angle equals ±45°. Additionally, the tidal-induced h_mF_2 differences do not vary much with solar cycle (i.e., see Figure C.19) since the meridional wind differences, and thus the field-aligned plasma motion, do not vary much with solar cycle.

4.5 Summary of Important Results

The effects of tidal dissipation on the zonal-mean wind fields in the MLT and IT system have been extensively studied since the 1970s. This chapter expands on these prior research efforts by quantifying and elucidating the seasonal, latitudinal, and solar cycle variations in the zonal-mean wind fields attributable to the dissipation of vertically propagating tides. To accomplish this we invoked differences between TIE-GCM simulations with and without CTMT lower boundary tidal forcing at the ~97 km model lower boundary. Also imposed were background lower boundary winds, temperatures, and geopotential heights from WINDII-HRDI and SABER measurements. The major results and conclusions from numerical experiments described in this chapter are as follows:

1. An enhancement on the order of 20-35 m s^{-1} in an equatorial westward jet structure is

induced by the dissipation of vertically propagating tides during boreal winter and spring months under solar minimum, medium, and maximum conditions. The dissipation of the vertically propagating SW2 is the primary tidal component responsible for this enhancement.

2. The differences in the zonal-mean zonal winds at low and middle latitudes within the dynamo region attributable to CTMT tidal lower boundary forcing in TIE-GCM can be almost completely replicated by including just three tidal components (i.e., DW1, DE3, and SW2) throughout the entire year and under all solar conditions. The migrating tides contribute significantly to the mean zonal circulation at all times of the year, whereas the largest DE3 contributions are limited to July, August, and September.

3. Unlike the results presented in Miyahara [75]; [76]; [78], Groves and Forbes [39], Miyahara and Wu [80], Miyahara et al. [79], and references therein, we show that throughout the year the zonal-mean zonal wind differences in the dynamo region are mainly generated by changes in the pressure gradient force through the tidally-driven eddy heat source terms in the thermodynamic energy equation (with other terms including the adiabatic and diabatic heating and cooling terms playing smaller roles). Below 200 km all the other terms in the zonal-mean meridional momentum equation are of secondary importance to the PGF, including the eddy momentum source terms. Changes of ±120 m s^{-1} day^{-1} in the PGF term due to tidal dissipation vary in latitude, altitude, and season leading to the seasonal variations in the zonal-mean zonal winds within the dynamo region. Above 200 km the zonal-mean zonal wind differences generated by tidal motions are mainly driven by differences in the ion drag terms. Although differences in the ion drag forcing terms (i.e., ±200 m s^{-1} day^{-1}) are larger than the PGF differences in the lower IT, they only act to change the zonal-mean zonal winds by up to 10 m s^{-1} due to the increased role of vertical viscosity in the upper IT. Only small (i.e., between 5 and 8 m s^{-1}) solar cycle variations in the zonal-mean zonal winds exist due to the small solar cycle variations in the PGF.

4. Changes in the zonal-mean meridional winds of order ± 3 m s^{-1} are limited to low latitudes throughout the entire year, maximizing in the boreal spring and summer months within the dynamo region. These changes do not vary with solar cycle. As was the case for the zonal-mean

zonal winds, the dissipation of SW2 is the primary tidal component responsible for changing the zonal-mean meridional winds.

5. Zonal mean meridional wind changes in the dynamo region are mainly attributable to tidally-driven effects on the eddy momentum source and ion drag terms of the zonal-mean zonal momentum equation. However, these differences are an order of magnitude smaller (i.e., ± 10 m s^{-1} day^{-1}) than those shown for the zonal-mean meridional momentum equation. Above 200 km meridional wind differences are only $\pm$ 1.5 m s^{-1}, and are driven by tidal effects on the ion drag terms of up to 200 m s^{-1} day^{-1}. These large ion drag forcing differences do little to change the zonal-mean meridional winds in the upper IT due to the short time constant of molecular diffusion.

6. h_mF_2 differences ranging from -4 to $+2$ km at low latitudes are a result of variations in the field-aligned plasma motion driven by meridional wind differences when vertically propagating tides are included at the TIE-GCM lower boundary. Tidally-driven h_mF_2 differences do not vary much with solar cycle due to small solar cycle variations in the tidally-driven meridional wind differences.

Chapter 5

Tidal Impacts on the Mean State and Variability of the IT System: Thermodynamic Energy Equation

In section 1.3.2., a brief review of the prior research efforts focused on quantifying the effects that vertically propagating tides have on the temperature structure of the IT was offered. Although numerous studies have been focused on understanding and quantifying tidal effects on the zonal-mean winds in the IT, one can very easily conclude from the literature review provided in section 1.3.2. that comparatively less work has been done on understanding and quantifying tidal effects on the zonal-mean temperature structure of the IT. Therefore, this chapter addresses this issue by answering science question (2b), i.e., how do the dissipating tides affect the zonal-mean thermal balance and temperature structure of IT system, and do these tidal effects vary seasonally or with solar cycle? This chapter follows the procedure and makes use of the same TIE-GCM simulations discussed in Chapters 2 and 4, except now applied to the thermodynamic energy equation. For this reason Chapter 5 is a results-oriented chapter, only offering a very short introduction, motivation, and description of the methodology below.

Supplemental figures for this chapter are located in Appendix D.

5.1 Introduction, Motivation, TIE-GCM Simulations, and Methodology

The majority of the energy input into the IT system comes from above, i.e., the absorption of EUV and UV solar radiation by Earth's atmosphere. However, solar radiation absorption in the lower atmosphere produces atmospheric tides, which acts a secondary energy source through the upward transport of energy associated with these waves, ultimately coupling the lower atmosphere to the IT. Since atmospheric tides are subharmonics of a solar day, this dynamical upward flow of energy is a regular and repeatable energy source within the IT, yet the net heating caused by these waves and their effects on the thermal balance of the IT system have only been examined by a select few over the last 50 years.

Prior studies including Hines [52], Lindzen [65], and Lindzen and Blake [67] showed that the dissipation of internal gravity waves and atmospheric tides transport energy vertically from the lower atmosphere into the IT, and affect the energy budget of the IT via the eddy heat source term $(\overline{G})$ in equation 2.14. Specifically, Hines [52] reported heating rates of $\sim$100° K day^{-1} at E-region altitudes due to the dissipation of internal gravity waves, which ultimately results in an energy flux exceeding 10^{-4} W m^{-2} at higher altitudes in IT. Lindzen [65] calculated an upward energy flux of 7 ergs cm^{-2} s^{-1} in the lower thermosphere near the equator as a result of the dissipation of the diurnal tide, which they reported to be 2.5 times greater than the absorbed downward flux of solar radiation at lower thermospheric altitudes. Groves and Forbes [38]; [39] also showed that diurnal and semidiurnal tidal dissipation can lead to globally averaged energy inputs comparable to the daily-averaged EUV absorption in the lower thermosphere. Lindzen and Blake [67] stated that the heat transport that arose due to the dissipation of the semidiurnal tide is extremely important in maintaining exospheric temperatures. Forbes et al. [31] utilized the TIGCM and concluded that the dissipation of the migrating tides alters the zonal-mean temperatures by -5 to $+8$ K in the IT.

All the studies discussed above highlight the important role that atmospheric tides play in maintaining the thermal balance of the IT system. In this chapter, we look to build on these prior research efforts by reassessing to what extent the dissipation of atmospheric tides contribute to the thermal energy budget of the IT system by performing numerical experiments with the state-of-the-art TIE-GCM forced with observationally-based background and tidal lower boundary conditions from WINDII-HRDI, SABER, and CTMT. Following the methodology outline in Chapter 4, upward propagating tidal effects on the zonal-mean temperature structure of the IT are analyzed by comparing TIE-GCM simulations with and without CTMT lower boundary tidal forcing. Also following the procedure presented in Chapter 4, seasonal and solar cycle dependencies associated with these tidal impacts on the zonal-mean temperatures of the IT system are evaluated from TIE-GCM simulations covering all twelve months of the year and under solar minimum, medium, and maximum conditions. Please note that all of the TIE-GCM results discussed below are from simulations that have been described thoroughly in Chapters 2 and 4.

5.2 Tidal Impacts on the Zonal-Mean Temperature

Figure 5.1 displays zonal-mean temperature difference fields as a function of month and latitude at 130 km (Figures 5.1a, 5.1c, 5.1e), and as function of latitude and altitude during March (Figure 5.1b), July, (Figure 5.1d), and September (Figure 5.1f) under solar medium conditions. The 130 km altitude level was chosen because it is where SW2 reaches its maximum amplitude in the TIE-GCM simulations discussed herein. Zonal mean temperature differences between TIE-GCM simulations with and without CTMT lower boundary tidal forcing range from ±4° K and persist throughout most of the year at low and middle latitudes (Figure 5.1a). Vertically propagating tides have their largest affect at middle (low and middle) southern (northern) latitudes with maximum (minimum) differences of +4° K (−4° K) extending May through August (August through September). Figures 5.1c and 5.1e show temperature differences between TIE-GCM simulations including CTMT lower boundary tidal forcing with TIE-GCM simulations that include only a combination of the migrating tidal components from CTMT. Figure 5.1c shows differences between simulations that include all of the CTMT tidal components forced at the model lower boundary and simulations that only include tidal forcing from DW1. Including just DW1 reduces the narrow band of positive zonal-mean temperature differences located between ±30° latitude (Figure 5.1)c. Tidal temperature amplitudes depicted in Figure 5.2 show that the of DW1 maximizes (i.e., ∼12 K) during the equinoxes at low latitudes (Figure 5.2c), and its latitudinal and seasonal variability correspond well with its maximum influence on the zonal-mean temperatures. Please note that it is the vertically-propagating component of DW1 that mainly contributes to the zonal-mean temperature differences, as Figure 5.2d depicts small DW1 amplitudes (i.e., ∼5 K) at

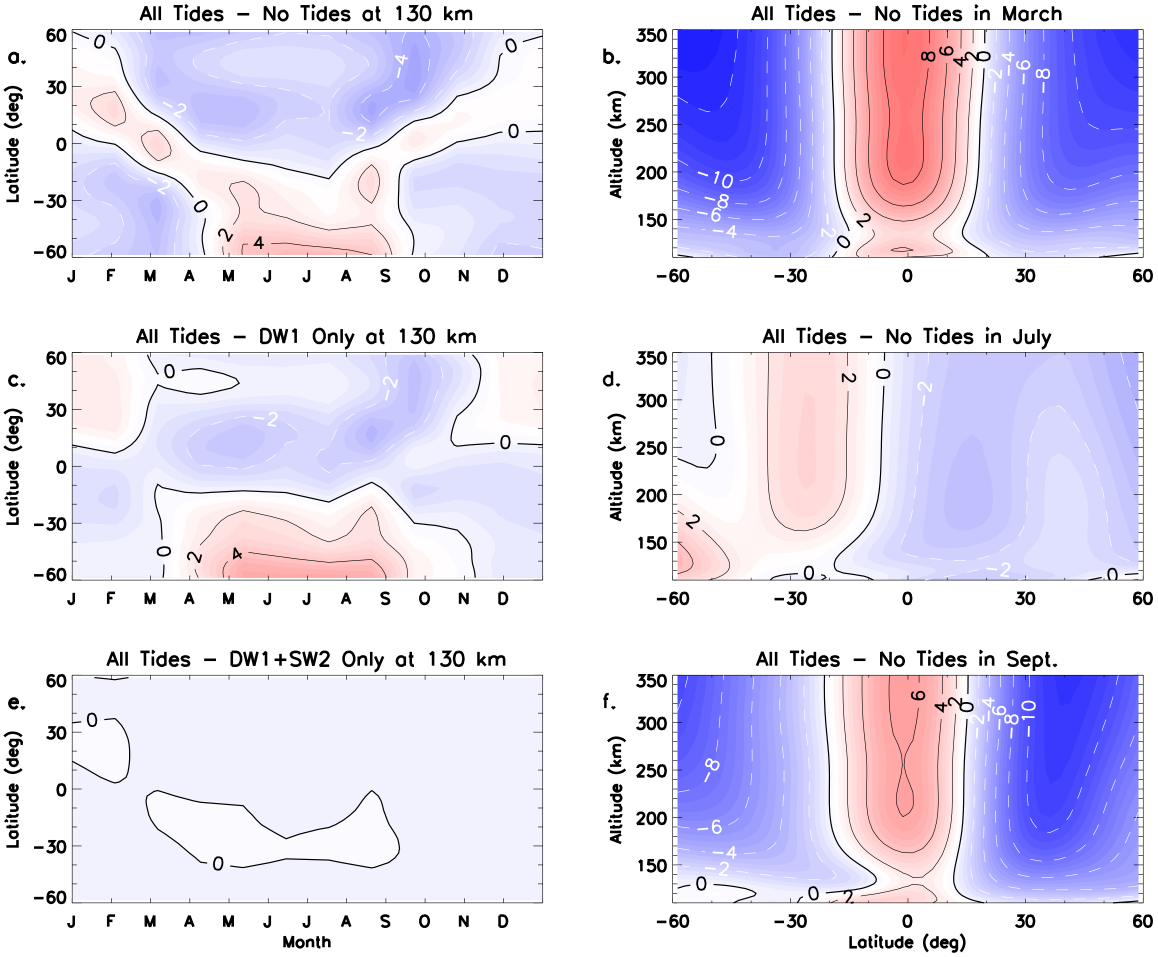

Figure 5.1: TIE-GCM zonal-mean temperature differences as a function of month and latitude at 130 km (Left Column) and as a function of latitude and altitude (Right Column). Differences between TIE-GCM simulations including and excluding CTMT tidal forcing at the model lower boundary are shown in (a); differences between TIE-GCM simulations including all tidal components and only DW1 from CTMT at the model lower boundary are shown in (c); differences between TIE-GCM simulations including all tidal components and only DW1 and SW2 from CTMT at the model lower boundary are shown in (e). Differences between TIE-GCM simulations with and without CTMT lower boundary tidal forcing are shown for March (b); July (d); September (f). Zonal mean temperature differences are contoured every ±2 K.

low latitudes when CTMT tidal forcing is excluded from the TIE-GCM. Including both migrating tidal components at the TIE-GCM lower boundary explains almost all the zonal-mean temperature differences in the dynamo region (Figure 5.1e). Specifically, maximum (minimum) differences located at southern (northern) middle (low and middle) latitudes shown in Figure 5.1a appear to be explained by the presence of SW2. SW2 reaches maximum amplitudes (~45 K) during boreal spring and summer months at low latitudes (Figure 5.2a), with the in-situ forced component only contributing about 10° K (Figure 5.2b). Similar to DW1, the seasonal and latitudinal distribution of SW2 corresponds well with its maximum influence on the zonal-mean temperatures, although the maximum temperature differences that occur at southern middle latitudes is offset from the maximum SW2 amplitudes calculated for in Figure 5.1e.

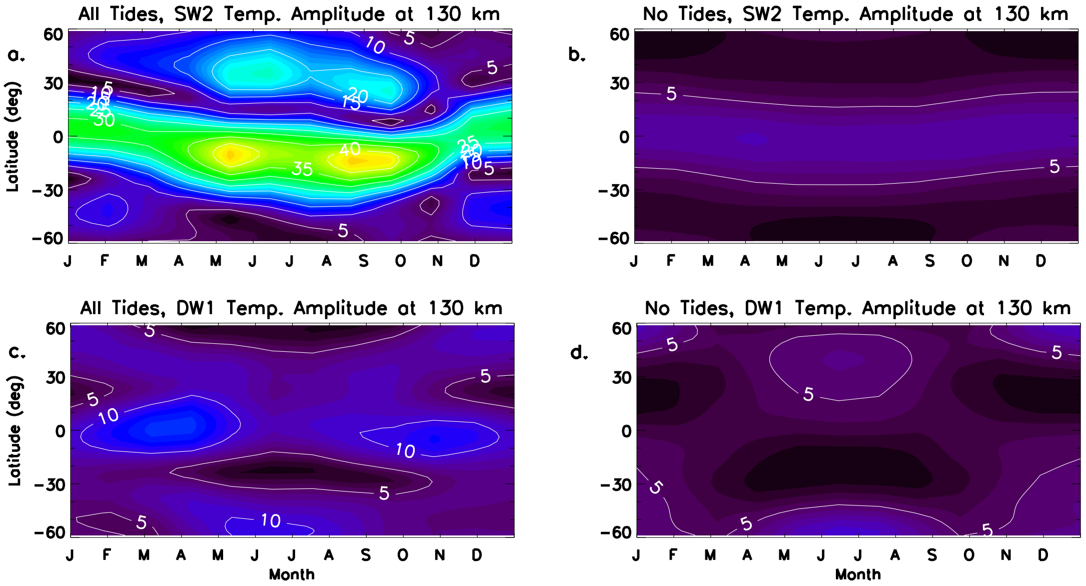

Figure 5.2: TIE-GCM temperature tidal amplitudes at 130 km from simulations including (Right Column) and excluding (Left Column) CTMT tidal forcing at the model lower boundary. The SW2 is shown in (a) and (c); DW1 in (b) and (d). Tidal temperature amplitudes are contoured every 5 K.

For zonal-mean temperature differences as a function of latitude and altitude during a specific month, there appear to be noticeable differences between those shown at equinox (i.e., Figures 5.1b and 5.1f) to those shown at other times of year (i.e., Figure 5.1d). Both March and September show extremely similar zonal-mean temperature differences attributable to the presence of vertically-propagating tides with maximum (minimum) temperature differences illustrated at low (middle) latitudes (Figures 5.1b and 5.1f). Temperature differences of +2° K (−2° K) near 125 km increase (decrease) with altitude during March and September up to ~200 km, where they reach +6° to +8° K (−10° to −12° K), and then remain relatively constant with altitude above ~200 km (Figures 5.1b and 5.1f). The 6 to 8° K increase in the zonal-mean temperature at low-latitudes depicted in Figures 5.1b and 5.1f is consistent with what Forbes et al. [31] calculated due to the migrating tides alone in the TIGCM. This further validates our prior conclusion that DW1 and SW2 are the dominant drivers of the zonal-mean temperature differences in the thermosphere. During June, zonal-mean temperature differences are generally smaller than those shown for March and September with differences ranging from $-3°$ to $+4°$ K (Figure 5.1d). Temperature differences in July also show a different latitudinal distribution than those calculated under March and September conditions, with positive (negative) temperature differences located mainly in the southern (northern) hemisphere. Please also note that the latitudes at which the largest positive zonal-mean temperature differences occur in Figures 5.1b, 5.1d, and 5.1f correspond with the latitudes at which the largest pressure gradient force differences occur in zonal-mean meridional momentum equation, which are shown in Figures 4.5a, 4.6a, and 4.7c, respectively. The previous statement offers additional support to the conclusion presented in Chapter 4 that tidally-induced changes in the pressure gradient force drive zonal-mean zonal wind differences in the dynamo region, and that these zonal-mean zonal wind differences vary with season.

5.2.1 Diagnosing the Temperature Differences and associated Seasonal Variability

Diagnosing the mechanisms by which the tides act to change the zonal-mean temperatures is facilitated by calculating each individual term of the thermodynamic energy equation and quantifying the changes in these forcing terms due to the presence of the tides in the TIE-GCM. The zonal-mean temperature equation was first presented in Chapter 2 and is shown again below

$$\frac{\overline{v}}{a}\frac{\partial \overline{T}}{\partial \theta} + \overline{w}\overline{S} = \frac{\overline{J}}{c_{p0}} - \overline{G} + \frac{1}{\rho_0 c_{p0}}\frac{\partial}{\partial z}\left[\overline{K_T}\frac{\partial \overline{T}}{\partial z} + \overline{K_E}\rho_0 c_{p0}\left(\frac{g}{c_{p0}} + \frac{\partial \overline{T}}{\partial z}\right)\right]. \tag{2.14 revisited}$$

The first term on the left hand side of equation 2.14 is the meridional temperature advection term, representing the transport of temperature (or energy) due to the mass movement of the fluid. It is abbreviated in the subsequent figures by *Adv.* (i.e., the same abbreviation used for momentum advection in Chapter 4). The second term on the left hand side of equation 2.14 is the adiabatic heating and cooling term, which describes changes in temperature as an air parcel is moved vertically. The adiabatic heating and cooling term is abbreviated as *Adia H/C* in the figures shown below. The first term on the right hand side of 2.14 is the diabatic heating and cooling term. The diabatic heating rate (J) represents the differences in the diabatic heating sources (Q) and sinks (L). Diabatic heating sources in the TIE-GCM include radiative heating, joule heating, heating due to O recombination, heating due to molecular diffusion, and heating due to numerical diffusion. Diabatic heating loss terms in the TIE-GCM result from NO, CO_2, and $O(^3P)$ IR radiative cooling. The diabatic heating and cooling term is abbreviated as *Dia. H/C* in the plots below. Term number two on the right hand side of 2.14 is the eddy heat source term, which represents the heat (energy) deposition by the tides and is abbreviated *Eddy Heat or Eddy* in the figures shown below. The final term on the right hand side of 2.14 is the dissipative term that includes both vertical molecular heat conduction (thermal conductivity) and eddy diffusion of heat. Since the lower boundary of the TIE-GCM is situated at ∼97 km the thermal conductivity term is the dominant dissipative term in the TIE-GCM. The full dissipative term is abbreviated as *Diss.* in the subsequent figures presented below.

Figure 5.3 shows all the terms of equation 2.14 calculated from a TIE-GCM simulation that includes CTMT lower boundary tidal forcing under September and solar medium conditions. The month of September was chosen because it is one of the months where the largest zonal-mean temperature differences occurs in the dynamo region due to the dissipating tides (Figure 5.1a). Figure 5.3a clearly illustrates that the advection of temperature due to meridional motions is quite small during the month of September. In the dynamo region adiabatic heating and cooling rates are largest at low latitudes and below 160 km, ranging from -15 to $+30$ K day^{-1} (Figure 5.3b). Above 160 km adiabatic heating and cooling rates increase dramatically with values ranging from -60 to $+80$ K day^{-1}. Although, the adiabatic heating and cooling term is quite large at higher altitudes they do very little to affect the zonal-mean temperature structure of the thermosphere due to the fast time scales of molecular heat conduction as a result of the exponential decrease in density with height. The previous statement is true for all of the other terms in thermodynamic energy equation that are presented in Figure 5.3. Summing the terms on the left hand side of equation 2.14 shows that adiabatic heating and cooling is one of the important drivers of the zonal-mean temperature structure in the IT, as can be inferred from the similarities between Figures 5.3b and 5.3c.

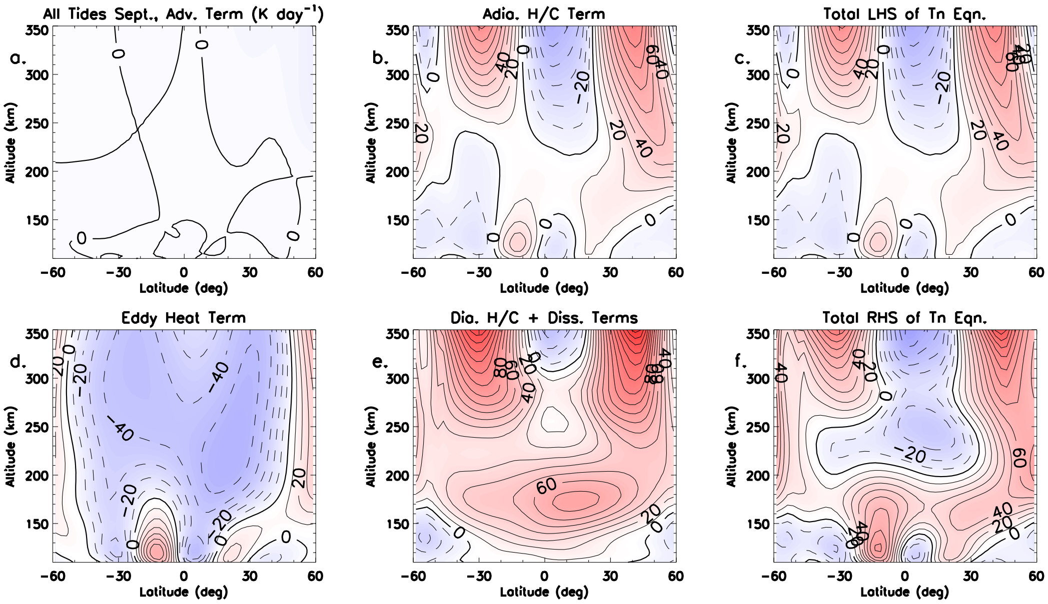

Figure 5.3: TIE-GCM zonally- and diurnally-averaged forcing terms from the thermodynamic energy equation including CTMT lower boundary tidal forcing under September and solar medium conditions as a function of latitude and altitude. The Adv. term is shown in (a); the Adia. H/C term is shown in (b); the sum of the Adv. and Adia H/C terms on the left hand side of equation 2.14 are shown in (c); the Eddy Heat term is shown in (d); the sum of the Dia. H/C and Diss. terms are shown in (e); the sum of the Eddy Heat, Dia. H/C, and Diss. terms are shown in (f). Forcing terms from the thermodynamic energy equation are contoured every ±10 K day^{-1}.

The eddy heat source term induced by the dissipating tides drives the largest heating rates at low latitudes in the dynamo region below 150 km during the month of September (Figure 5.3d). Heating rates ranging from -40 to $+60$ K day^{-1} are calculated at equatorial latitudes within the dynamo region as a result of the eddy heat source term with mainly negative heating rates above 175 km of -40 K day^{-1}. Combining the diabatic heating and cooling and the dissipative terms depict maximum heating rates of $+70$ K day^{-1} in the upper portion of the dynamo region around 175 km over low latitudes, with the largest heating rates calculated at higher altitudes (Figure 5.3e). Summing all the terms in the bottom row of Figure 5.3 (i.e., all the terms on the right hand right of equation 2.14) shows the heating rates driven the Eddy Heat, Dia. H/C, and Diss. terms balance the heating rates produced by adiabatic motions (Figure 5.3c). Specifically, the eddy heat source term (diabatic heating and cooling and the dissipative terms) tends to balance the adiabatic heating and cooling term below (above) 150 km in the TIE-GCM. We do acknowledge that the balance of terms presented on the left and right hand sides of equation 2.14, and shown in Figures 5.3c and 5.3f do have some differences and should be treated with some caution. For instance, the diabatic cooling terms are split into two parts (i.e., an implicit and explicit part) that are then multiplied by some numerical factors in order to provide a numerically stable solution to the neutral temperature equation. For the chemical cooling terms that represent part of the Dia. H/C term shown in Figure 5.3e, we calculate the chemical cooling rates using the same equations employed in the TIE-GCM source code, neglecting these numerical factors, which could be one source of error. Another source of error could arise from the calculation of the dissipative term. Specifically, the TIE-GCM is a model that assumes hydrostatic equilibrium and uses a constant gravitational acceleration. For the calculated dissipative term shown in Figure 5.3e, we found that the best balance of forcing terms in equation 2.14 is achieved by using a gravitational acceleration that is height dependent. Nonetheless, we are interested in understanding the tidal effects on the zonal-mean temperature differences, which result from differences in the forcing terms of equation 2.14 when CTMT lower boundary tidal forcing is included or excluded from the TIE-GCM lower boundary. Better balance is achieved in the difference fields of the forcing terms on the left and right hand side of equation 2.14 (see Figure D.1), and represents the typical level of balance one has typically achieved when performing the exercise of balancing the individual terms in the thermodynamic energy equation from the TIE-GCM (*A. Burns, personal communication*). We therefore conclude that the individual forcing term difference fields will not exactly balance in practice, and that this does not detract from the conclusions to be presented later in Chapter 5.

Because the zonal-mean temperature differences depicted in the left column of Figure 5.1 do not change much with altitude above ~200 km due to molecular conduction, Figure 5.4 illustrates the Adia. H/C, Eddy Heat (shortened to just Eddy in the Figure 5.4), and the Dia. H/C difference

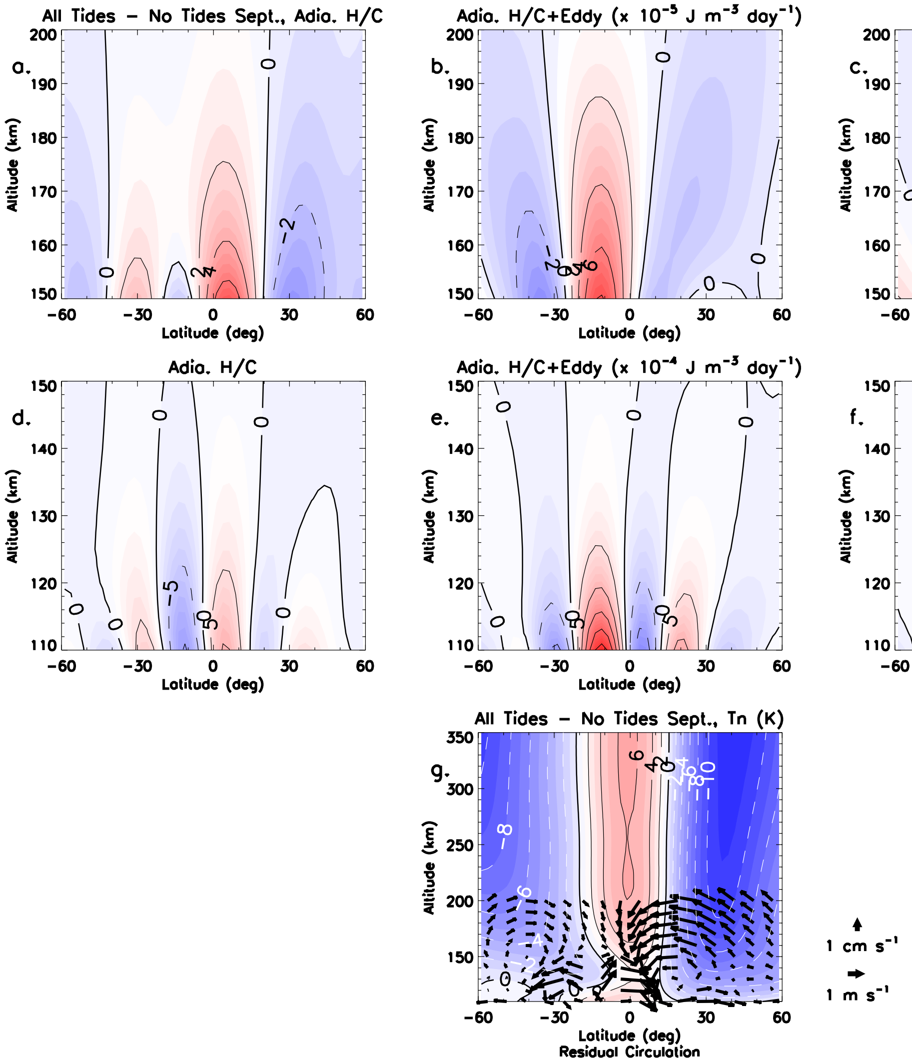

Figure 5.4: Forcing term difference fields from the thermodynamic energy equation between TIE-GCM simulations performed with and without CTMT tidal lower boundary forcing under September and solar medium conditions as a function of latitude and altitude between 110-150 km (Second Row) and between 150-200 km (First Row). The Adia. H/C term is shown in (a) and (d); the Adia. H/C + Eddy terms in (b) and (e); the Adia. H/C term + Eddy + Dia. H/C terms in (c) and (f). (g) depicts the same zonal-mean temperature differences shown Figure 5.1f, except with the zonal-mean residual meridional circulation induced by the dissipating tides between 100-200 km overlaid. Forcing term differences between 110-150 km (150-200 km) are contoured every ±5 × 10^{-4} J m^{-3} day^{-1} (±2 × 10^{-5} J m^{-3} day^{-1}), while zonal-mean temperature differences are contoured every ±2 K.

fields under September and solar medium conditions between 110 and 200 km. The differences fields for the Adia. H/C, Eddy Heat, and the Dia. H/C terms depicted in Figure D.1 were converted to energy density units (i.e., heating rate per unit volume) in Figure 5.4 to account for the exponential decrease in density with altitude, recognizing that differences in the zonal-mean temperatures mainly occur at lower thermospheric altitudes where the neutral density is at its maximum. In addition to the differences fields in the forcing terms, Figure 5.4g also displays the zonal-mean residual meridional circulation induced by tidal dissipation between 110 and 200 km overlaid on the zonal-mean temperatures differences that were previously shown in Figure 5.1f. Please note that the difference fields calculated in the first row of Figure 5.4 are an order of magnitude smaller than those shown in the second row. The Adia H/C term differences shown in Figures 5.4a and 5.4d were calculated as if this term was moved to the right hand side of equation 2.14 to facilitate the interpretation of the differences, as the temperature changes that result from vertical motions are anti-correlated (i.e., downward (upward) motions lead to adiabatic heating (cooling)). Figure 5.4d (Figure 5.4a) shows adiabatic heating and cooling differences of $\pm 10 \times 10^{-4}$ J m^{-3} day^{-1} ($\pm 4 \times 10^{-5}$ J m^{-3} day^{-1}) between 110 and 150 km (150 and 200 km) that maximize at low-latitudes and can extend into the mid-latitudes. Including the eddy heat source term reinforces the differences already imposed by the Adia. H/C term (Figures 5.4b and 5.4e). The largest forcing term differences are concentrated at low-latitudes with differences now ranging from -10 to $+25 \times 10^{-4}$ J m^{-3} day^{-1} (-3.5 to $+8 \times 10^{-5}$ J m^{-3} day^{-1}) in Figure 5.4e (Figure 5.4b). Averaging the differences attributable to the Adia. H/C and Eddy Heat terms over low- (mid-) latitudes results in a net heating (cooling), which is mainly driven by the Eddy Heat (Adia. H/C and Eddy Heat) terms between 110 and 150 km (150 and 200 km). This is consistent with the residual mean circulation that shows downwelling (upwelling) at low- (mid-) latitudes resulting in increases (decreases) in the zonal-mean temperature differences in Figure 5.4g between 130 and 200 km.

Between 110 and 150 km forcing term differences remain relatively unaffected by the diabatic heating and cooling term differences, but between 150 and 200 km the diabatic heating and cooling term differences clearly affect the forcing term differences already imposed the by Adia. H/C and Eddy Heat terms, especially at low-latitudes (Figures 5.4c and 5.4f). Tidally-induced zonal-mean temperature differences at low-latitudes are limited due to an increase in NO cooling, which is

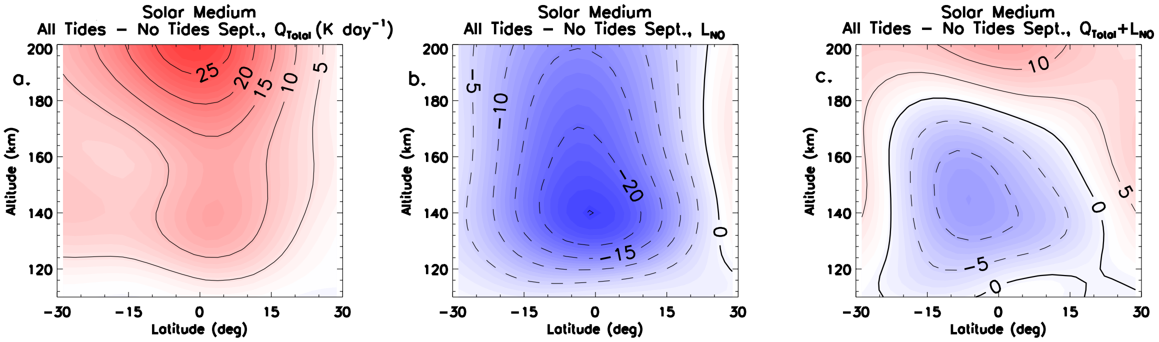

Figure 5.5: Diabatic heating term differences fields between TIE-GCM simulations performed with and without CTMT tidal lower boundary forcing under September and solar medium conditions as a function of latitude and altitude. The total solar heating term is shown in (a), the NO cooling term in (b), and the sum of the total solar heating term and NO cooling term differences is shown in (c). Diabatic heating term differences are contoured every ±5 K day^{-1}.

accounted for in the Dia. H/C term. Figure 5.5 illustrates the tidally-induced changes in the radiative heating (Q_{Total}) and NO cooling (L_{NO}), as well as the sum of the two at low-latitudes during September. NO cooling differences on the order of -20 K day^{-1} are stronger than the increases in radiative heating (+10 to +15 K day^{-1}) from ∼120-180 km due to tidally-induced constituent changes, which will be discussed further in Chapter 6. This increase in NO cooling leads to a reduction in the net heating and increase in the zonal-mean temperatures induced by the dissipating tides through the Adia. H/C and Eddy Heat terms. This increase in NO cooling due to tides also occurs in March (Figure D.2), reducing the zonal-mean temperature increases between 120 and 150 km shown in Figure 5.1b.

In Figure 5.1 we showed that the zonal-mean temperature differences in the IT varied seasonally, with the largest differences occuring during the equinoxes and smaller differences throughout the rest of the year. This seasonal variability in the tidal-induced zonal-mean temperature differences is better understood by comparing the thermodynamic energy equation forcing term differences shown in Figure 5.6 for the month of July, with the forcing term differences shown in Figure 5.4. Between 110 and 200 km tidally-driven forcing term differences in the TIE-GCM are at least a factor of 2 weaker during July (Figure 5.6) than in September (Figure 5.4). Similar to the forcing term differences in September, during July tidal-induced differences in the Eddy Heat term are the dominate driver of zonal-mean temperature differences between 110 and 150 km, with differences ranging from -5 to $+10 \times 10^{-4}$ J m^{-3} day^{-1} (Figures 5.6e and 5.6f). Between 150 and 200 km the latitudinal structure of the Adia. H/C and Eddy Heat forcing term differences shown in Figure 5.6b are similar to those shown in Figure 5.4b, but their magnitudes are 50% smaller. Differences in the Dia. H/C term act to oppose the differences imposed by the Adia. H/C and Eddy Heat, resulting in mainly positive differences of up to $+4 \times 10^{-5}$ J m^{-3} day^{-1} situated south of equator (Figure 5.6c).

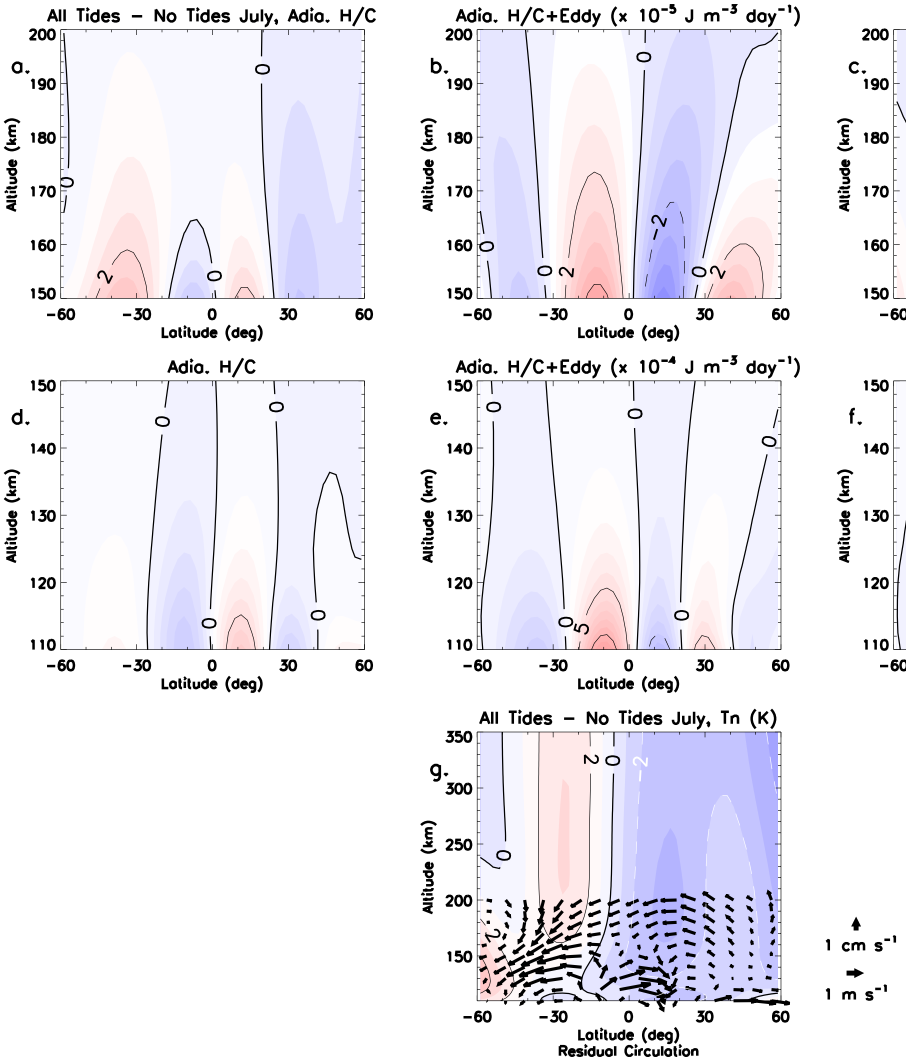

Figure 5.6: Same as Figure 5.4, except during the month of July.

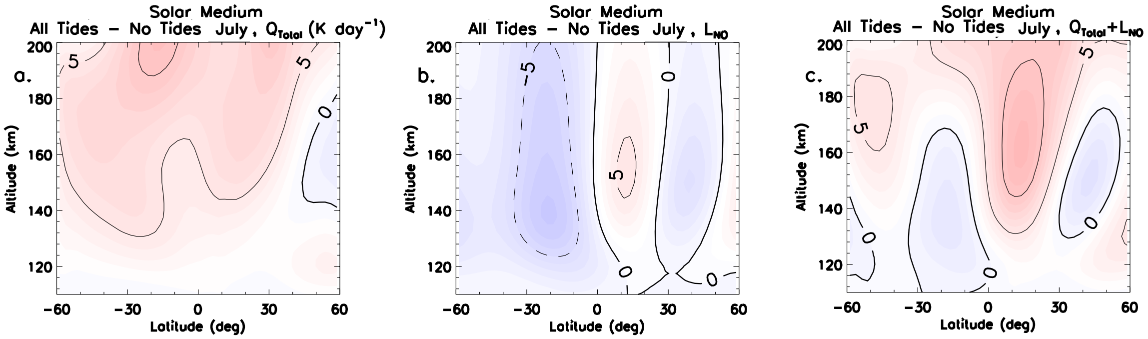

Figure 5.7: Same as Figure 5.5, except during the month of July.

Once again the Dia. H/C differences between 150 and 200 km are driven by the differences in the radiative heating and NO cooling, which are shown in Figure 5.7. Radiative heating and NO cooling differences range between ±5 K day^{-1} in the dynamo region (Figures 5.7a and 5.7b). The aggregate affect of the radiative heating and NO cooling differences result in mainly positive changes between +5-10 K day^{-1} above 160 km (Figure 5.7c), which act to oppose the negative differences calculated for the Eddy Heat term in Figure 5.5b. As was the case for the month of September, tidal-induced zonal-mean temperature changes in July can be explained by the relative importance of the Adia. H/C, Eddy Heat, and Dia. H/C terms. Specifically, increases (decreases) in the zonal-mean temperature during July are initially driven by the Eddy Heat term between 110 to 150 km, which result in a net heating (cooling) when averaged over low and middle southern (northern) latitudes (Figure 5.6e). These increases in the zonal-mean temperature in the southern hemisphere are supplemented by downwelling in the residual meridional circulation (Figure 5.6g) and increased radiative heating (Figure 5.7c) due to constituent changes between 150 and 200 km. Decreases in the zonal-mean temperatures in the northern hemisphere are reinforced by upwelling in the residual meridional circulation (Figure 5.6g) and negative differences in the Eddy Heat term (Figure 5.6b). In summary, the seasonal variability in the zonal-mean temperature differences shown in Figure 5.1 are driven by the aggregate effects of the tidal-induced adiabatic heating and cooling, eddy heat source, and diabatic heating and cooling terms (which are driven by changes in radiative heating and NO cooling) in equation 2.14.

5.3 Solar Cycle Variability

Figure 5.8 displays zonal-mean temperature differences as a function of month and latitude under solar minimum and solar maximum conditions. Comparing Figures 5.8a, 5.8b, and 5.1a reveals a clear solar cycle dependency in the zonal-mean temperature difference fields induced by the dissipation of the vertically-propagating tides. The zonal-mean temperature generally increases (decreases) when CTMT tides are included at the TIE-GCM lower boundary at low and middle latitudes in the dynamo region with maximum (minimum) temperature differences of $+9°$ K ($-7°$ K) calculated in Figure 5.8a (Figure 5.8b). As was the case during solar medium, the zonal-mean temperature differences during solar minimum and maximum can be almost completely explained by the including just the migrating tides (i.e., DW1 and SW2) at the TIE-GCM lower boundary (Figures 5.8c and 5.8d). Please note that the $+2$ K zonal-mean temperature difference during August shown in Figure 5.8c can be explained by including DE3, in addition to the migrating tidal components during solar minimum. This results is consistent with the solar cycle variability in DE3, which has its maximum influence during solar minimum due to reduced dissipation (Oberheide et al., [85]). The seasonal variability in the zonal-mean temperature differences during solar minimum and maximum are extremely similar to that of the seasonal variability during solar medium, with the largest (positive or negative) zonal-mean temperature differences calculated in the months of March and September. This seasonal variability in the zonal-mean temperature differences corresponds well with the maximum amplitudes of SW2 and DW1 shown in Figure 5.9, which attain their maximum amplitudes of 42 K and 12 K (45 K and 17 K), respectively under solar minimum (solar maximum) conditions during the equinoxes. Please note that the maximum amplitudes in SW2 and DW1 are larger at solar maximum and solar minimum, which is due a larger in-situ forced component of 9 K and 6 K, respectively as a result of increased solar radiation absorption in the IT (Figure D.3). Therefore, we conclude that it is the vertically-propagating components of the migrating tides that are mainly responsible for driving the zonal-mean temperature differences in the dynamo region.

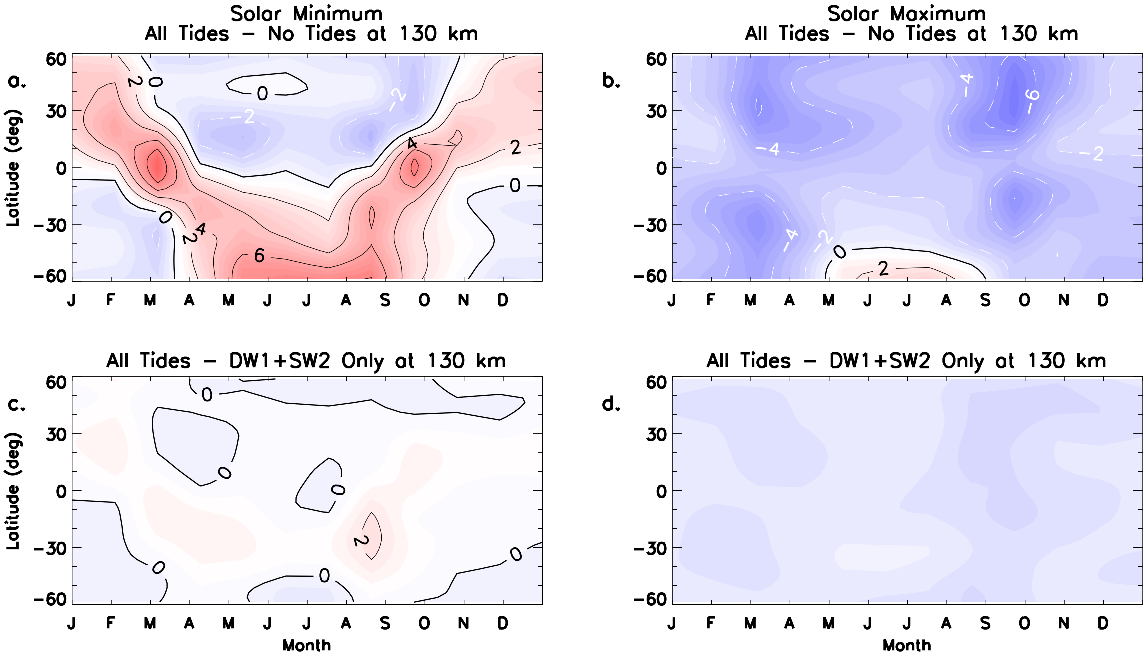

Figure 5.8: TIE-GCM zonal-mean temperature differences as a function of month and latitude at 130 km under solar minimum (Left Column) and solar maximum (Right Column) conditions. Differences between TIE-GCM simulations including and excluding CTMT tidal forcing at the model lower boundary are shown in (a) and (b); differences between TIE-GCM simulations including all tidal components and only DW1 and SW2 from CTMT at the model lower boundary are shown in (c) and (d). Zonal mean temperature differences are contoured every ±2 K.

Zonal mean temperature differences as a function of latitude and altitude during the months of September and July are depicted in Figure 5.10. Similar to Figure 5.8, there is pronounced solar cycle variability associated with the tidal-induced zonal-mean temperature differences, especially during September (Figures 5.10a and 5.10b). Temperature differences in the dynamo region vary by ∼30 K between solar minimum and maximum during September, with increases of up to +18 K depicted for solar minimum (Figure 5.10a) and a decrease of −8 K depicted for solar maximum (Figure 5.10b) at low-latitudes that extend into the upper IT. Negative temperature differences calculated for at mid-latitudes also show a noticeable change depending on solar cycle reaching values of ∼15 K and ∼4 K in TIE-GCM under solar maximum and minimum conditions, respectively (Figures 5.10a and 5.10b). Zonal mean temperature differences calculated during the month of July show the same solar cycle variability as September, i.e., the large positive temperature differences

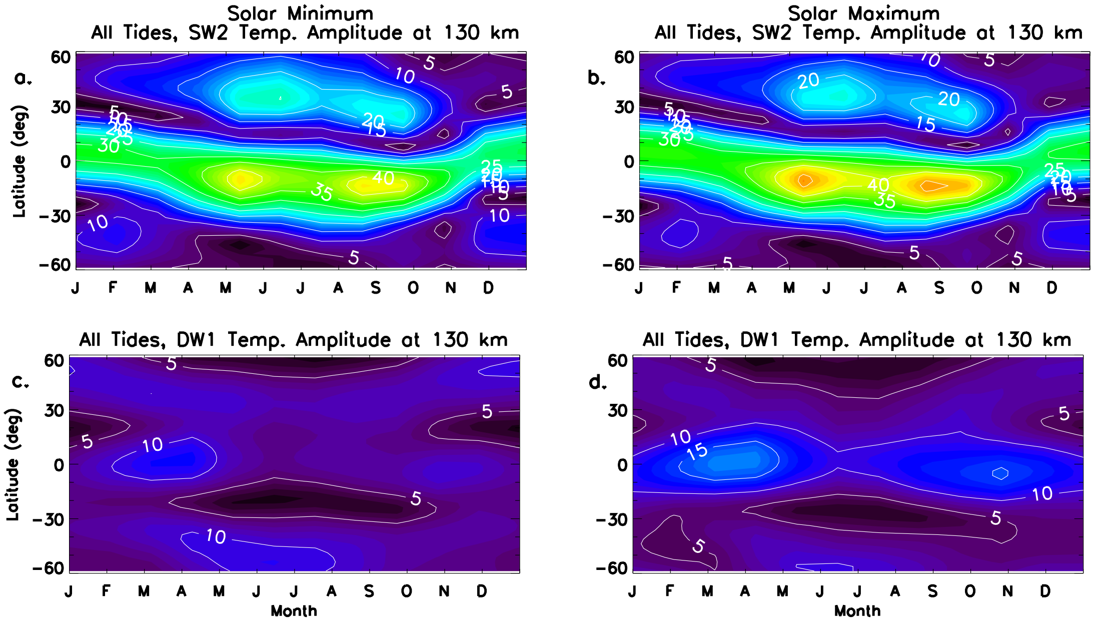

Figure 5.9: TIE-GCM temperature tidal amplitudes at 130 km including CTMT tidal forcing at the model lower boundary as a function of month and latitude under solar minimum (Left Column) and solar maximum (Right Column) conditions. The SW2 is shown in (a) and (b); DW1 in (c) and (d). Tidal temperature amplitudes are contoured every 5 K.

in solar minimum are reduced with increased solar flux, ultimately leading to negative temperature differences in solar maximum. Similar to solar medium, zonal-mean temperature differences in July under solar minimum and maximum conditions are smaller in magnitude compared to those in September with differences ranging from −2 K and +6 K solar minimum, and −5 K to +2 K in the dynamo region (Figures 5.10c and 5.10d). The latitudinal structure of the zonal-mean temperature differences in both September and July are also very similar over all three solar cycle conditions in the TIE-GCM. Since solar cycle variations in the zonal-mean temperature differences attributable to the dissipation of the upward-propagating tides is strongest during September, we restrict our subsequent analysis of the forcing term differences to September.

In order to understand the solar cycle variability in the zonal-mean temperature difference fields attributable to atmospheric tides, a comparison between the forcing term difference fields from equation 2.14 under different solar cycle conditions is required. Therefore, Figure 5.11 and Figure 5.12 are identical to Figure 5.4, except that the forcing term difference fields in energy density

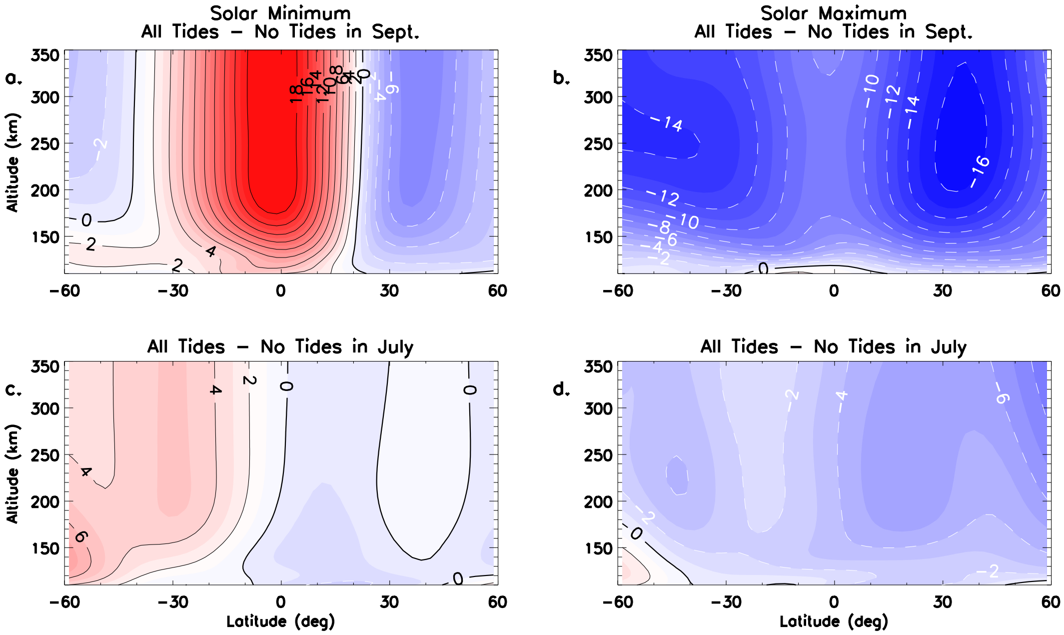

Figure 5.10: TIE-GCM zonal-mean temperature differences as function of latitude and altitude under solar minimum (Left Column) and solar maximum (Right Column) conditions during the month of September (a and b) and July (c and d). Zonal mean temperature differences are contoured every ±2 K.

units are depicted under solar minimum and solar maximum conditions in September. Changes in the zonal-mean temperatures mainly occur below 200 km and then are transmitted to the upper IT via molecular heat conduction, thus Figures 5.11 and 5.12 are only considered below 200 km. The adiabatic heating and cooling differences shown in the left column of Figures 5.11 and 5.12 do not vary much with solar cycle, showing differences on the order of approximately $\pm 10 \times 10^{-4}$ J m^{-3} day^{-1} ($\pm 4 \times 10^{-5}$ J m^{-3} day^{-1}) between 110 and 150 km (150 and 200 km). Similar magnitudes are calculated for the Adia. H/C differences during solar medium shown in the left column of Figure 5.4. Therefore, we conclude that the zonal-mean meridional circulation induced by the dissipating tides is not solar cycle dependent, which is consistent with the zonal-mean meridional wind differences presented in Chapter 4 (i.e., very little solar cycle variability in the zonal-mean meridional wind differences). This conclusion is further supported by the similarities in the latitudinal and vertical structure of the wind vectors depicted in Figures 5.11g, 5.12g, and 5.4g.

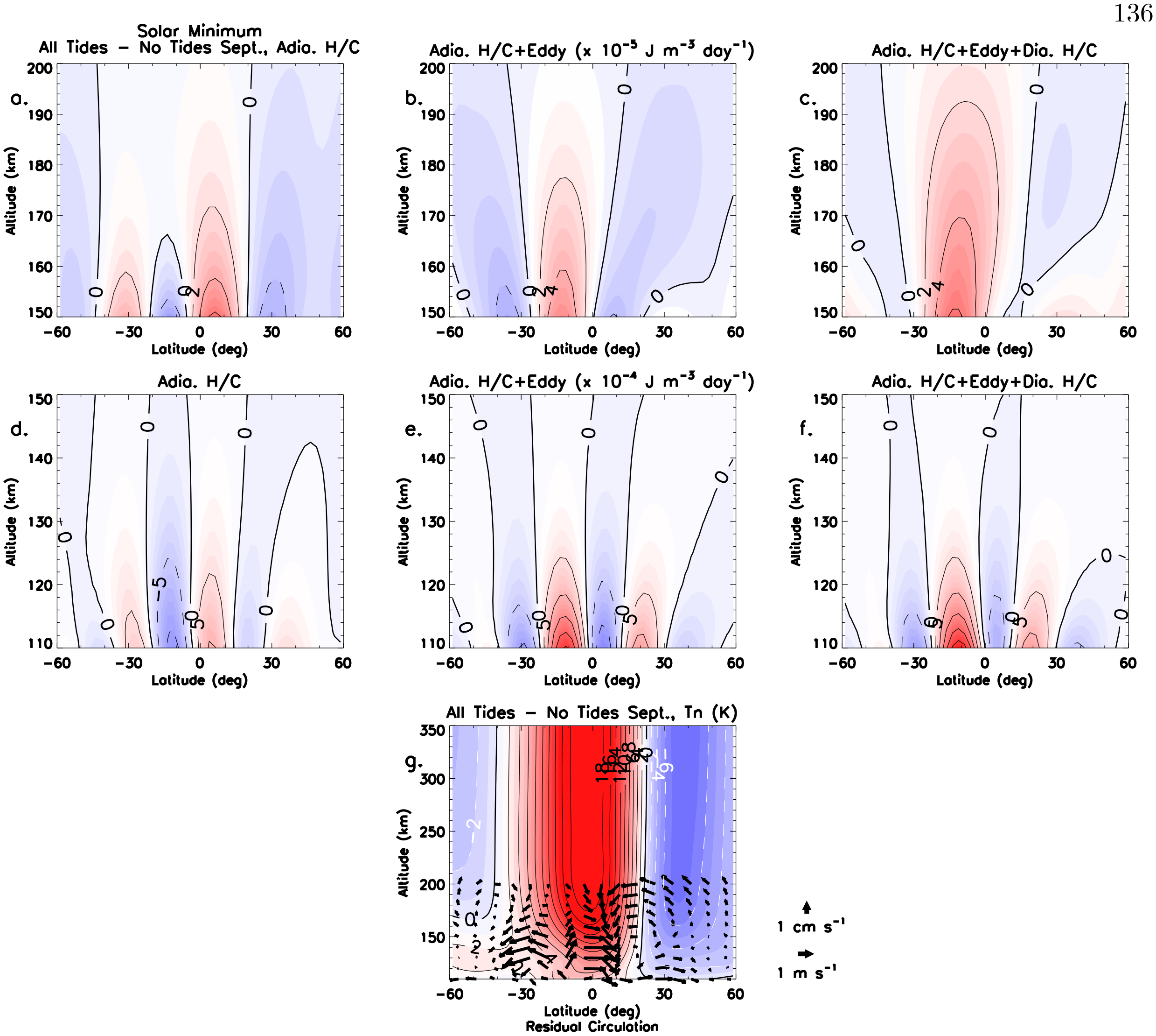

Figure 5.11: Same as Figure 5.4, except for a TIE-GCM simulation under solar minimum conditions.

The eddy heat source term between 110 and 150 km also does not vary much with solar cycle showing a similar latitudinal structure under solar minimum, medium, and maximum conditions with differences ranging from −10 to +25 × 10^{-4} J m^{-3} day^{-1} over low and middle latitudes (Figures 5.11e, 5.12e, and 5.4e). Comparing Figure 5.11b with Figure 5.12b shows that differences in the Eddy Heat term are stronger during solar maximum than at solar minimum and extend higher into the IT with positive (negative) differences of +4 × 10^{-5} J m^{-3} day^{-1} (−4 × 10^{-5} J m^{-3} day^{-1}) extending to 180 km (175 km) in Figure 5.12b, as opposed to 160 km (155 km) in

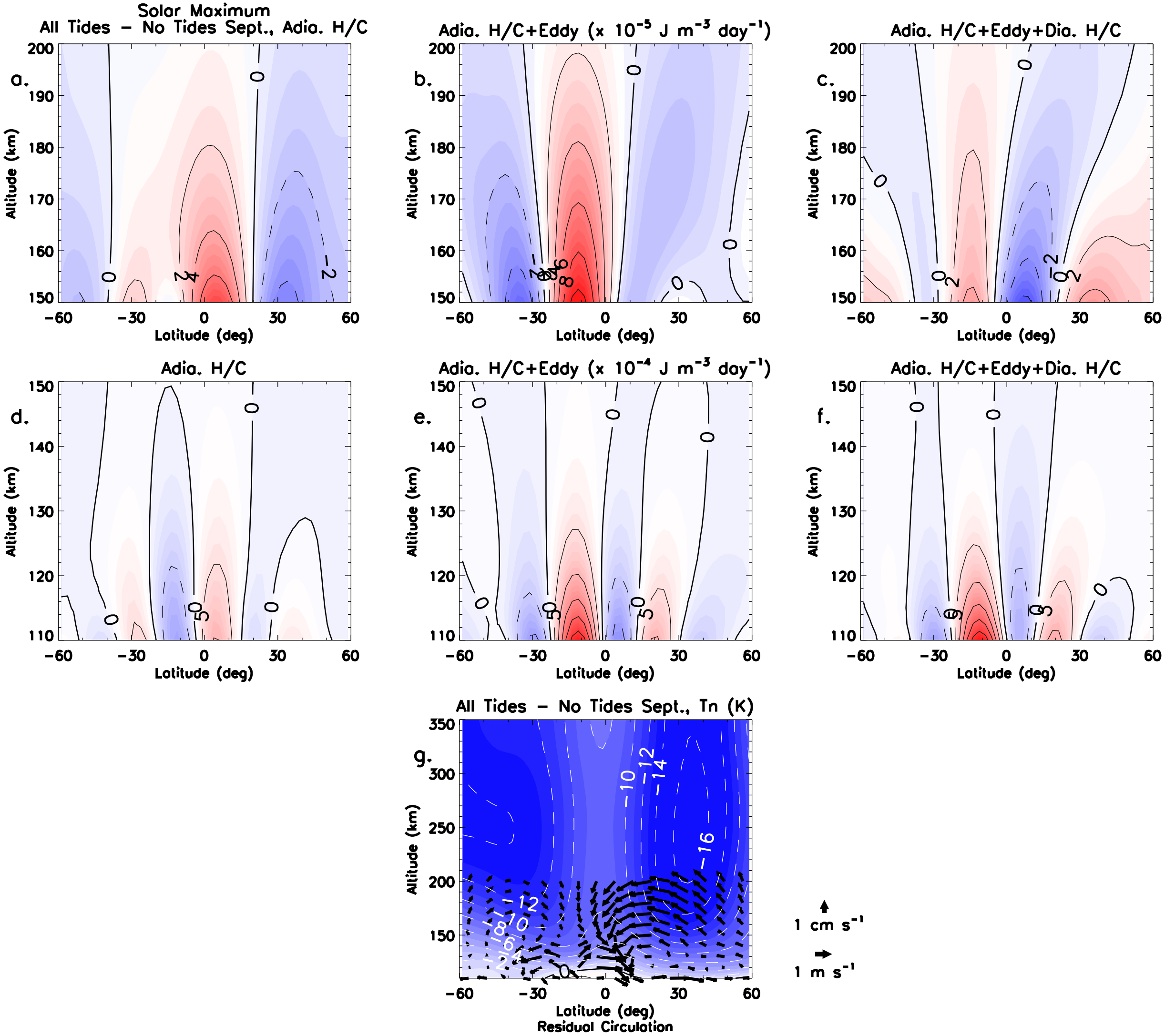

Figure 5.12: Same as Figure 5.4, except for a TIE-GCM simulation under solar maximum conditions.

Figure 5.11. This increase in the Eddy Heat term in solar maximum would lead one to believe that the maximum temperature differences should occur at solar maximum, which is the opposite of what is shown Figures 5.11g and 5.12g. However, including the diabatic heating and cooling differences to the Adia. H/C and Eddy Heat term differences above 150 km shows a clear solar cycle variation. Specifically, including the Dia. H/C term under solar minimum conditions actually reinforces (opposes) the already positive (negative) differences imposed by the Adia. H/C and Eddy Heat terms, with differences of $+6 \times 10^{-5}$ J m^{-3} day^{-1} (-0.5×10^{-5} J m^{-3} day^{-1}) just

above 150 km near the equator (at low latitudes) in Figure 5.11c. Conversely, Figure 5.12c shows that the stronger (relative to solar minimum) positive differences driven by the Eddy Heat term at low-latitudes are reduced by 50% just south of the equator resulting in values of $+4 \times 10^{-5}$ J m^{-3} day^{-1}, which is slightly less than what is calculated for at solar minimum. Additionally, the negative differences imposed by the Eddy Heat term between the equator and 20° N are strengthened by Dia. H/C differences to values of -6×10^{-5} J m^{-3} day^{-1}.

Figure 5.13 shows the changes in the radiative heating, NO cooling, and the sum of these two due the tides under solar minimum and solar maximum conditions during the month of September. Comparing the differences in the left and right columns of Figure 5.13 makes it easy to see that the solar cycle variability in the zonal-mean temperature differences driven by the tides results from changes in the NO cooling via the diabatic heating and cooling term in the thermodynamic energy equation. Stronger (weaker) positive differences on the order of +20 K day^{-1} (+10 K day^{-1}) in the radiative heating are reduced by weaker (stronger) negative differences in NO cooling of −10 K day^{-1} (−30 K day^{-1}) in dynamo region. The aggregate of effect of this increased NO cooling during maximum is shown in Figure 5.13f and leads to a 20-25 K day^{-1} net reduction in the Dia. H/C. This ∼20 K day^{-1} decrease in the Dia. H/C term is at least 10 K day^{-1} (30 K day^{-1}) stronger than aggregate differences in the radiative heating and NO cooling illustrated in Figure 5.5c (Figure 5.13e) during solar medium (minimum). Therefore, the +18° K zonal-mean temperature differences at low-latitudes driven by the Adia. H/C and Eddy Heat during solar minimum (Figure 5.11g) are reduced by the increased NO cooling forced by the dissipating tides to +6 K at solar medium (Figure 5.4g), and ultimately to −8 K at solar maximum (Figure 5.12g). The mechanism by which the tides act to change NO in the IT is the subject of section 6 in Chapter 6. The stronger negative temperature differences of ∼15 K just polewards of ±30° latitudes during solar maximum (Figure 5.12g), compared to those of ∼8 K and ∼4 K at solar medium (Figure 5.4g) and solar minimum (Figure 5.11g), respectively are due to a combination of increased NO cooling, the negative heating rate differences resulting from the Eddy Heat terms, and the upwelling provided by the residual meridional circulation. However, further research is required to fully understand the solar cycle variability in zonal-mean temperatures that are calculated at mid-latitudes.

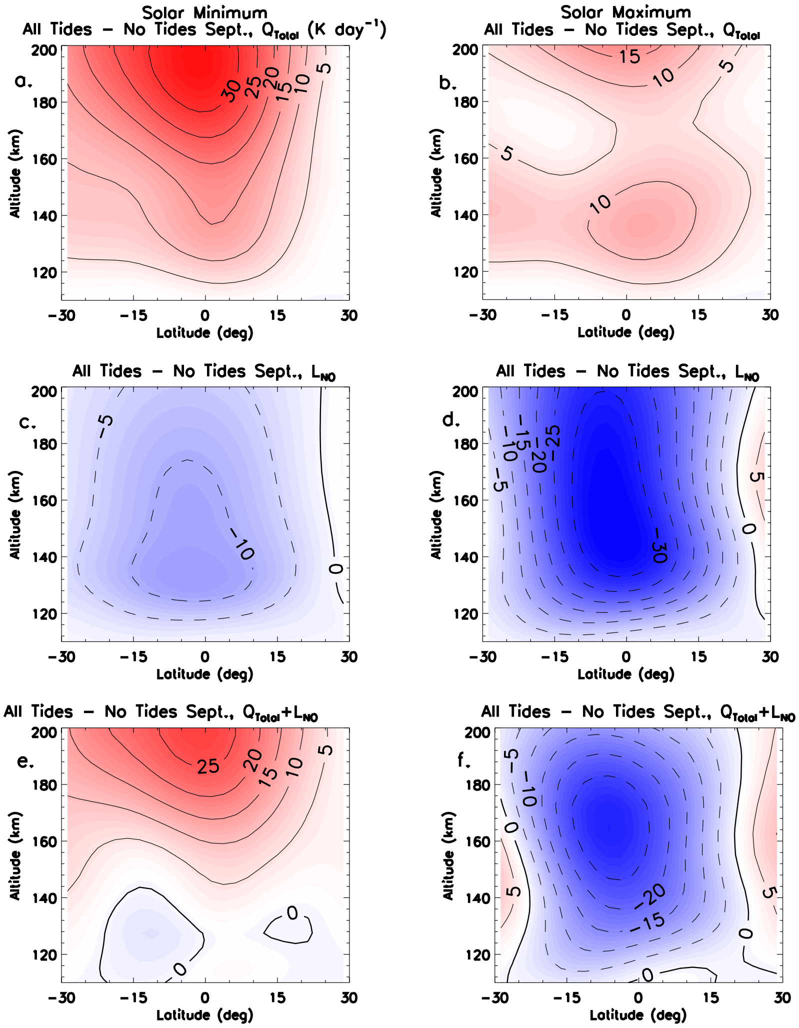

Figure 5.13: Diabatic heating term differences fields between TIE-GCM simulations performed with and without CTMT tidal lower boundary forcing during September under solar minimum (Left Column) and solar maximum (Right Column) conditions as a function of latitude and altitude. The total solar heating term is shown in (a) and (b), the NO cooling term in (c) and (d), and the sum of the total solar heating term and NO cooling term are shown in (e) and (f). Diabatic heating term differences are contoured every ±5 K day^{-1}.

5.4 Summary of Important Results

The impacts that the vertically-propagating tides have on the zonal-mean temperature structure and thermal balance of the IT system have garnered little attention over the past 50 years.

Therefore, this chapter addresses science question (2b), which focuses on better understanding and quantifying the role that atmospheric tides play in determining the seasonal, latitudinal, and solar cycle variability of the zonal-mean temperature structure in the IT. The ways by which the dissipating tides act to change the zonal-mean temperature of the IT were evaluated by calculating difference fields in the thermodynamic energy equation forcing terms between TIE-GCM simulations that included and excluded observationally-based tidal perturbations at the model lower boundary. The major results and conclusions are as follows:

1. The zonal-mean temperature differences are strongly dependent upon season and solar cycle. Maximum (minimum) zonal-mean temperature differences of up to approximately +20 K (−10 K) occur during the equinoxes under solar minimum (maximum) conditions. The zonal-mean temperature differences in the dynamo region can be almost completely explained due to dissipation of DW1 and SW2.

2. The latitudinal and seasonal variability associated with the tidal-driven changes in the zonal-mean temperatures corresponds quite well with the largest pressure gradient force differences calculated in the zonal-mean meridional momentum equation. Therefore, we conclude that the tidally-induced zonal-mean temperature changes introduce latitudinal and seasonal variability into the pressure gradient force, ultimately driving zonal-mean zonal wind differences in the dynamo region.

3. The tides have their largest effect on the zonal-mean temperature below 200 km where the neutral density is largest in the IT. Above 200 km the zonal-mean temperature differences remain relatively constant with altitude due to the increased importance of thermal conductivity, which quickly tries to remove any vertical gradients in temperature.

4. Diagnosis of the individual terms in the thermodynamic energy equation revealed that the dissipating tides act to alter the zonal-mean temperature structure of the IT system through the adiabatic heating and cooling, eddy heat source, and diabatic heating and cooling terms. The relative importance of these three forcing mechanisms are dependent upon season and solar cycle, and are ultimately responsible for driving the seasonal and solar cycle variability of the zonal-mean

temperatures in the TIE-GCM.

5. A 30° K change between zonal-mean temperature differences calculated at low latitudes between solar minimum and maximum is forced by tidally-induced changes in the diabatic heating and cooling. Specifically, tidally-induced changes in the major neutral constituents of the IT system result in a strengthening of the thermosphere's "natural thermostat" or NO infrared cooling (Mlynczak et al., [81]), thereby reducing the $+18°$ K zonal-mean temperature difference calculated at solar minimum to a $-10°$ K zonal-mean temperature difference at solar maximum.

Chapter 6

Tidal Impacts on the Mean State and Variability of the IT System: Contiunity Equation and Composition

As Chapters 4 and 5 clearly illustrated, the dissipation of vertically-propagating tides affect the zonal-mean momentum and energy budgets of the IT, which implies that these waves can also impact the chemical constituents of Earth's upper atmosphere. Density variations in the IT are relevant for the prediction of satellite drag in cases of re-entry and aerobreaking measurements (see Leonard et al., [63]). However, section 1.3.2 only referred to one prior study (i.e., Forbes et al., [31]) that quantified the zonal mean changes in the chemical constituents of the IT due to the dissipating tides. Thus, there remain a number of outstanding questions regarding the effects that atmospheric tides can have on the compositional (and therefore density) structure of the IT. Chapter 6 aims to advance the current state of knowledge in this area by answering science question (2c) which is how does the dissipation of vertically-propagating tides affect the composition and densities of the IT system, and do these effects vary with season and solar cycle? Following the procedure and using the same NCAR TGCMs simulations discussed in Chapters 2, 4, and 5, we address science question (2c). This chapter expands on results previously published in JGR: Space Physics by Jones Jr. et al. [60], as well as Geophysical Research Letters by Jones Jr. et al. [58].

Supplemental figures for this chapter are located in Appendix E.

6.1 Introduction, Motivation, TIE-GCM Simulations, and Methodology

Understanding the physical mechanisms and processes that drive the compositional structure of Earth's upper atmosphere is essential to the field of aeronomy because it plays an important role in driving the dynamics and energetics of the IT system. Based on the magnitude of the dynamical perturbations induced by the dissipation of the vertically-propagating tides analyzed in Chapters 3-5, significant tidal effects on the neutral and charged constituent densities, as well as emissions associated with these compositional changes in the IT should be expected. Additionally, the seasonal and solar cycle variability associated with these expected tidal effects on the constituents should impact the IT in a number of ways, including photochemistry and plasma-neutral interactions. Several prior works have focused on measuring and modeling the different tidal components from the constituents and emissions of IT.

Forbes [22] was one of the first to theoretically model and discuss tidal perturbations and their associated solar cycle variability in the chemical constituents of the thermosphere, including O, O_2, N_2, Argon (Ar), Helium (He), and Hydrogen (H). Specifically, Forbes [22] showed that the solar cycle (latitudinal) variations in thermospheric composition associated with the diurnal (semidiurnal) tide were greater than the latitudinal (solar cycle) variations. Therefore, Forbes [22] concluded that the effects of the tides on the composition were dependent on solar cycle and latitude, as well as the specific constituent. Roble and Shepherd [107] performed numerical experiments with the TIME-GCM and showed that the local time variation in the equatorial $O(^1S)$ green line emission measured by WINDII could be explained by the presence of a strong diurnal tide. Satellite measurements of [NO], the NO 5.3 μm infrared emission, $O(^1S)$ green line emission, and O_3 all have revealed distinctive longitudinal and seasonal variability, which have been attributed to the propagation and dissipation of non-migrating in the MLT and IT (Oberheide and Forbes, [84]; Oberheide et al., [88]; Shepherd, [111]; Shepherd and Cho, [112]; Pancheva et al., [91]). Many of the previous research efforts described above have focused on identifying tidal perturbations in the chemical constituents and their emissions in the IT, whereas relatively less attention has been paid to quantifying the changes in the zonal-mean composition of the IT.

One of the only studies to investigate this issue was Forbes et al. [31] in which they reported on compositional differences from numerical experiments performed with the TIGCM forced with observationally-based migrating tides at the model lower boundary. These authors showed that dissipation of the vertically-propagating tides increased (decreased) the N_2 and O_2 (O and electron density) by 10-15% and 20-25% (30-50% and 5-15%), respectively in the IT. They also showed that dissipating tides caused changes in the minor constituent densities, including NO, $N(^4S)$, and $N(^2D)$ ranging from -30 to $+60\%$ in the IT. This chapter looks to extend the results presented in Forbes et al. [31], by re-examining the role atmospheric tides play in determining the zonal-mean compositional structure of IT, with specific attention to the seasonal and solar cycle variability associated with these tidal effects, as well as determining the different physical mechanisms responsible for driving the constituent changes. We quantify the constituent changes induced by the dissipating tides using results from the TIE-GCM forced with observationally-based background and tidal lower boundary conditions from WINDII-HRDI, SABER, and CTMT. Consistent with the methodology utilized throughout this study, tidal effects on the zonal-mean composition of the IT are evaluated by computing difference fields from TIE-GCM simulations that include or exclude CTMT tidal lower boundary forcing. Similar to what was done for the zonal-mean winds and temperatures, seasonal and solar cycle variations in the constituents of the IT are identified from TIE-GCM simulations covering all twelve months of the year and under solar minimum, medium, and maximum conditions. We also make use of the TIME-GCM in section 4 to discern the different tidally-induced mechanisms responsible for driving O constituent changes in the IT. Please note that all of the NCAR TGCMs results analyzed below are from simulations previously described in Chapters 2 and 4.

6.2 The Continuity Equation and Mass Flow Stream Function

Before diagnosing the tidal effects on the individual constituents in the IT, we first demonstrate that the two terms in the zonal-mean continuity, which are shown below

$$\frac{1}{a\cos\theta}\frac{\partial}{\partial\theta}(\overline{v}\cos\theta)+\frac{1}{\rho_0}\frac{\partial}{\partial z}(\rho_0\overline{w})=0, \qquad \text{(2.11 revisited)}$$

do in fact balance. This is an important validation step as equation 2.11 is derived starting with the general form of the continuity equation shown in Chapter 1 (equation 1.3), in which the total neutral density is related to the individual constituent number densities by the following:

$$[N_i]=\frac{\rho\zeta_i}{m_i},$$

where $[N_i]$ is the individual constituent number density, ζ_i and m_i are the mass mixing ratio and molecular mass of the individual constituent of interest, respectively. The first (second) term in equation 2.11 represents the meridional (vertical) component of the mass flux divergence, assuming the basic state density (ρ_0) only varies vertically following the hydrostatic law (or barometric law, both are used interchangeably throughout the remainder of the text).

Figure 6.1 depicts the individual terms of the zonal-mean continuity equation, as well as their differences from TIE-GCM simulations that include or exclude CTMT lower boundary tidal forcing under September and solar medium conditions. Once again the month of September is chosen because it is during this month that vertically-propagating tides are at or close to their maximum amplitudes. It is clear that the meridional (Figure 6.1, Left Column) and vertical (Figure 6.1, Right Column) terms in the zonal-mean continuity equation do balance, as well as their differences (Figure 6.1, Third Row). This type of balance is calculated over all months and all solar cycle conditions (see Figure E.1). Specifically, the largest differences in the mass flux divergence due to the presence of atmospheric tides occurs at low-latitudes and below ~200 km with values ranging from -30 to $+30 \times 10^{-2}$ day^{-1} (Figures 6.1e and 6.1f). Thus, we expect the dissipating tides to have their largest affects on constituents of IT system within the dynamo region which will then be carried to higher altitudes via molecular diffusion (similar to what was shown in Chapter 5 for the zonal-mean temperature differences). Please note that the vertical component of the mass flux divergences shown in Figures 6.1 and Figure E.1, were calculated using the mathematical formulation outlined in Dickinson et al. [10] as opposed to Holton [53], which uses a dimensionless vertical coordinate (see Chapter 2 for more details).

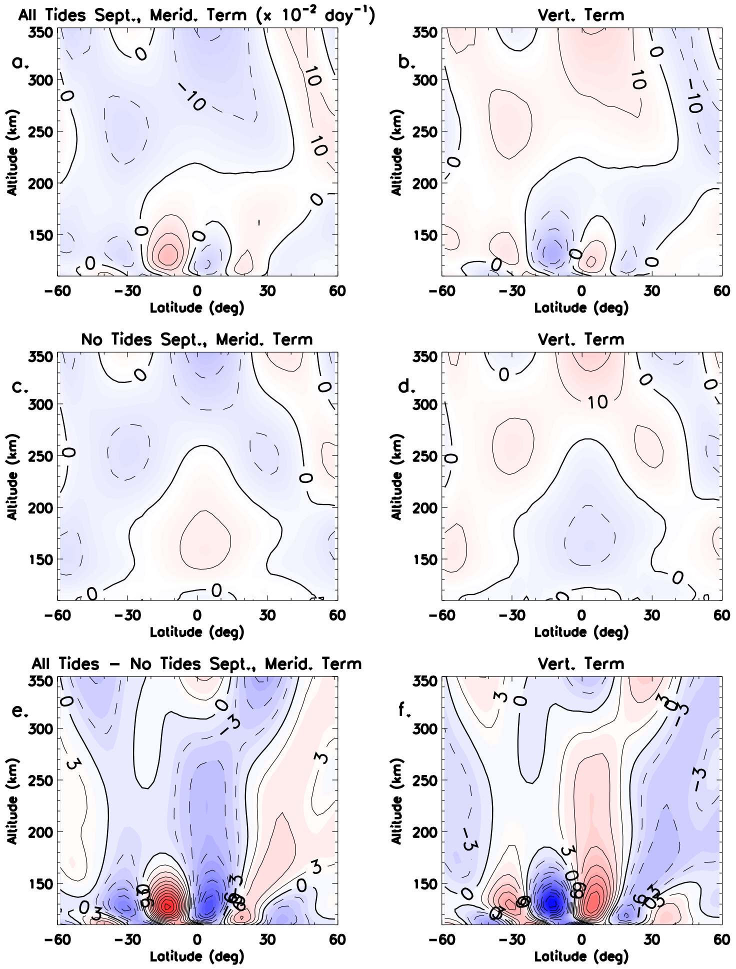

Figure 6.1: Forcing terms from TIE-GCM simulations including (First Row) and excluding (Second Row) CTMT tidal lower boundary forcing, as well as forcing term difference fields (Third Row) computed between TIE-GCM simulations with and without CTMT tidal lower boundary forcing as a function of latitude and altitude under September and solar medium conditions. The meridional (vertical) term is shown in the left (right) column in a, c, and e (b, d, and f). Forcing terms are contoured every $\pm 10 \times 10^{-2}$ day^{-1}, while forcing term differences are contoured every $\pm 3 \times 10^{-2}$ day^{-1}.

The zonal-mean continuity equation also states that if either the zonal-mean meridional or vertical wind is known then one can calculate the other by integrating equation 2.11 in either the meridional and vertical direction. Thus, it is advantageous to define the mass flow stream function (Ψ), which can fully describe the two-dimensional flow field in equation 2.11, while also providing a more physical representation of the two-dimensional flow field and its differences due to the dissipating tides. The mass flow stream function (Ψ) can defined as the vertically integrated northward mass flux at a given latitude from a given pressure level to the top of the atmosphere and can written following Cook [8]:

$$\Psi \equiv \frac{a\cos\theta}{g}\int_{p}^{p_T}\int_{0}^{2\pi}\overline{v}\,d\lambda\,dp. \tag{6.1}$$

Equation 6.1 can be rewritten for log-pressure coordinates using the barometric law, and performing the longitudinal integration results in

$$\Psi = -(2\pi\cos\theta)\frac{p_0}{gH}\int_{z}^{z_T}\overline{v}e^{-\frac{Z_g}{H}}\,dz. \tag{6.2}$$

Differentiating with respect to z results in an expression for $\overline{v}$, that can then be plugged into the zonal-mean continuity equation to obtain an expression for $\overline{w}$,

$$\overline{v} = -\frac{gH}{p_0 2\pi a\cos\theta}e^{\frac{Z_g}{H}}\frac{\partial\Psi}{\partial z} \quad \text{and} \quad \overline{w} = e^{\frac{Z_g}{H}}\left(\frac{gH}{p_0 2\pi a^2\cos\theta}\frac{\partial\Psi}{\partial\theta}\right). \tag{6.3}$$

Figure 6.2 illustrates the mass flow stream function calculated from TIE-GCM simulations including and excluding CTMT tidal lower boundary forcing, as well as the differences between these two during September under solar medium conditions. Whether or not CTMT tides are forced at the TIE-GCM lower boundary, a divergence in the mass flow stream function is located at low- and mid-latitudes between ~110 and 170 km during the month of September with values ranging from $\pm 10^9$ kg day^{-1} (Figures 6.2a and 6.2b). Between 30° S and the equator tidal dissipation induces a divergence in the mass flow stream function between 110 and 150 km (Figure 6.2c). However outside of this small region, tidal dissipation mainly acts to drive clockwise (counterclockwise) flow at low- and mid-latitudes in the southern (northern) hemisphere extending up to ~250 km. Thus, the dissipation of the vertically-propagating tides leads to mass flow stream function convergence centered over the equator (Figure 6.2c). This convergence implies a net increase in the constituent densities centered over the equator, as higher density N_2, O_2, and O is transported upward and equatorward averaged over low- and mid-latitudes. We therefore expect any increase or decrease in the major constituent densities of the thermosphere induced by the dissipating tides to be either further increased or counteracted by this mechanism. Please note that the magnitude of the differences in the mass flow stream function driven by tides does not vary much with solar cycle (see Figure E.1). This is not surprising since the differences in the mass flow stream function are driven by the zonal-mean residual meridional circulation, which did not show much solar cycle variability in Figures 5.11g, 5.12g, and 5.4g presented in Chapter 5.

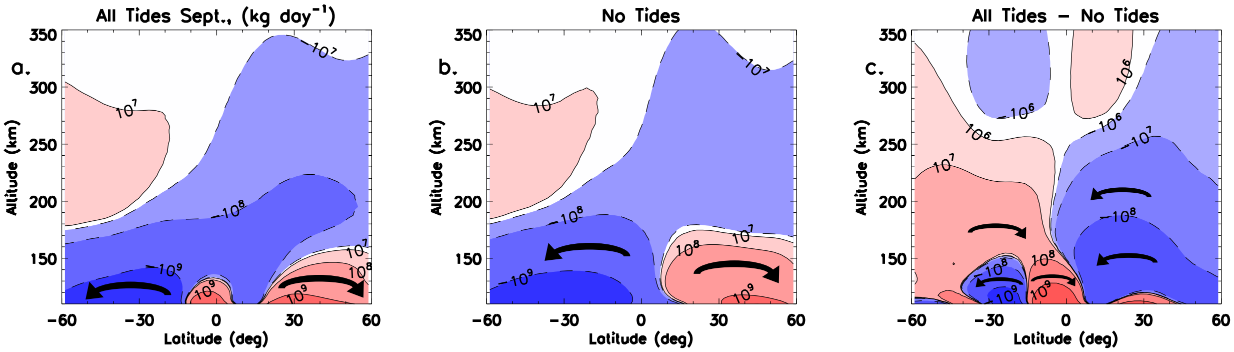

Figure 6.2: Mass flow stream function calculated for a TIE-GCM simulation including CTMT tidal lower boundary forcing (a), and excluding CTMT tidal lower boundary forcing (b), as well as the differences in the mass flow stream function computed between TIE-GCM simulations with and without CTMT tidal lower boundary forcing (c), as a function of latitude and altitude under September and solar medium conditions. Clockwise (counterclockwise) flow is represented by the red (blue) contours and denoted by the arrows (the size of the arrows holds no physical meaning). The mass flow stream function and its differences are contoured by positive or negative powers of 10 kg day^{-1}.

6.3 Tidal Impacts on the Major Constituents

Figure 6.3 illustrates difference fields of [O], [O_2], [O]/[N_2] ratio, and electron density ([N_e]) as a function of month and latitude at 130 and 200 km for TIE-GCM simulations with and without CTMT lower boundary tidal forcing. The 130 and 200 km altitudes were chosen to depict the results in Figure 6.3, as they provide a nice example of the typical latitudinal and seasonal variability associated with the percent changes in the major constituents due to vertically propagating tides in the TIE-GCM. Additionally, the largest percent differences calculated in the major constituents of Figure 6.3 occur around the equinoxes at 130 and 200 km, therefore we choose to illustrate difference fields in the major constituents from TIE-GCM simulations with and without CTMT lower boundary tidal forcing under September conditions (Figure 6.4) as a function of latitude and

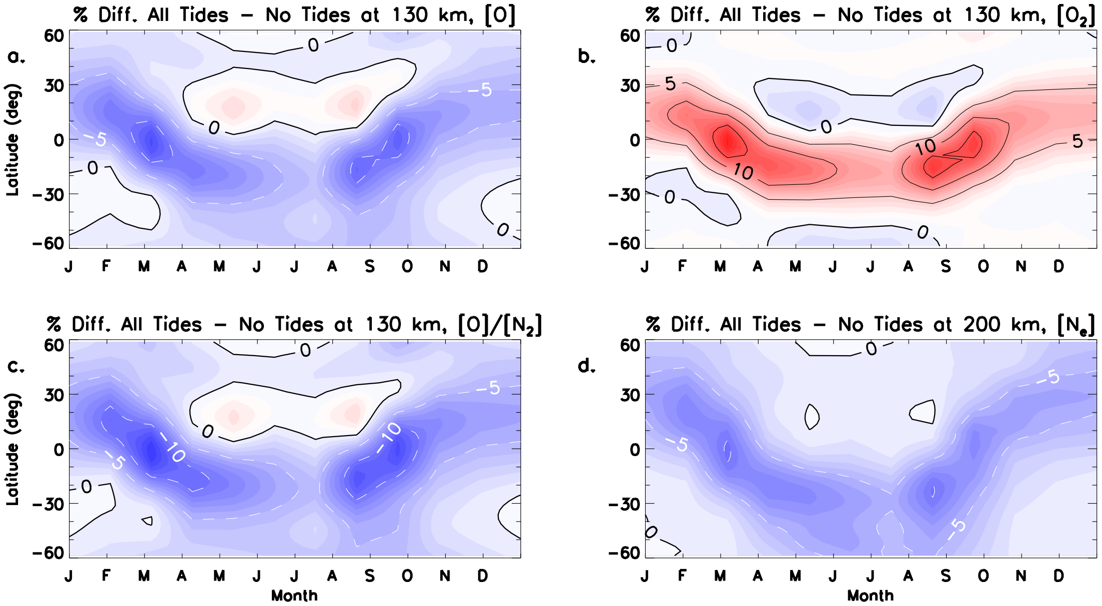

Figure 6.3: Percent differences between TIE-GCM simulations including and excluding CTMT tidal lower boundary forcing as a function of month and latitude at 130 and 200 km under solar medium conditions. [O] differences are shown in (a), [O$_2$] differences in (b), [O]/[N$_2$] differences in (c), and electron density differences in (d). Percent difference are contoured every ±5%.

altitude, in order to evaluate the maximum affect vertically propagating tides have on the chemical constituents in and beyond the dynamo region. When CTMT tidal lower boundary forcing is included, changes in [O] at 130 km (Figure 6.3a) ranging from −13 to +3% persist throughout the entire year at low and middle latitudes. The largest [O] differences do occur during the equinoxes near the equator and extend well into the F-region with differences on the order of −5% at 300 km (Figure E.3a). Comparison between the [O] differences calculated during March (Figure E.3a) and September (Figure 6.4a) shows similar spatial structures, and therefore we present mainly September results in the subsequent sections of Chapter 6, realizing that describing the changes in the IT constituents during September is also representative of March. We also chose September in order to facilitate our discussion of the different mechanisms by which the tides could act to change the constituent densities. The opposite is true for [O$_2$]; when CTMT lower boundary tidal forcing is included [O$_2$] generally increases at 130 km by up to 16% at low latitudes (Figure 6.3b). Similarly to [O], the maximum [O$_2$] differences occur during equinoxes near the equator, and these

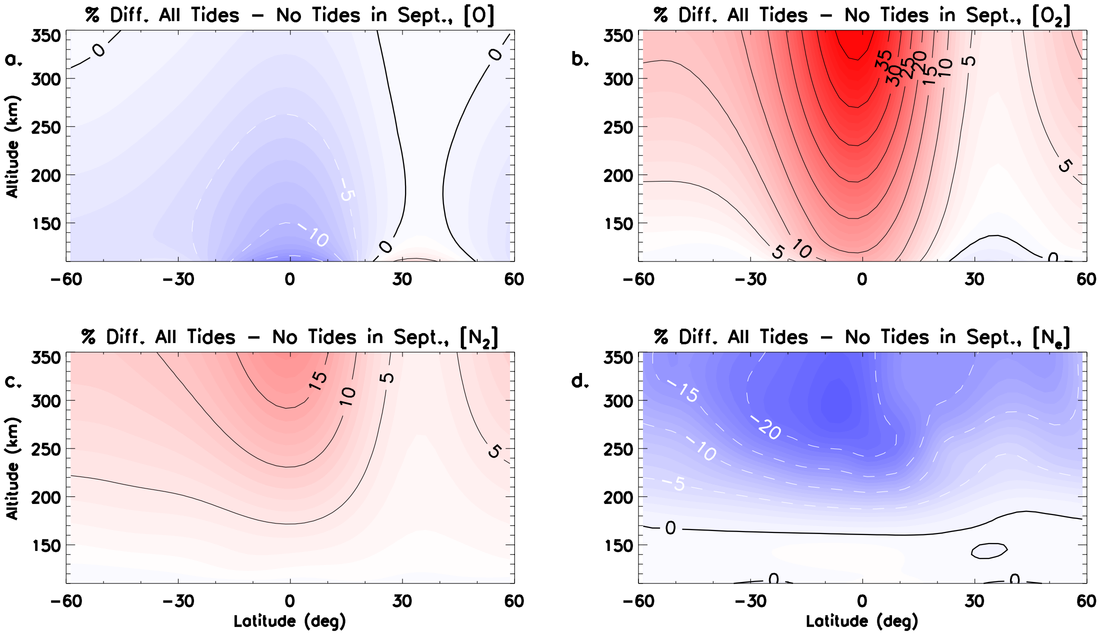

Figure 6.4: Percent differences between TIE-GCM simulations including and excluding CTMT tidal lower boundary forcing as a function of latitude and altitude under September and solar medium conditions. [O] differences are shown in (a), [O_2] differences in (b), [N_2] differences in (c), and electron density differences in (d). Percent differences are contoured every ±5%.

differences increase with altitude reaching a maximum of ~40% at 350 km (Figures 6.3b and E.3c). Differences in the [O]/[N_2] ratio presented in Figure 6.3c mainly follow the [O] depletion results discussed above, although differences of −14% at 130 km are slightly larger than those calculated for [O] only at 130 km, due to a slight increase (between 1 and 3%) in [N_2] number density when tides are included at the TIE-GCM lower boundary (Figure 6.4c). Differences in [N_e] at 200 km illustrated in Figure 6.3d range from −5 and −10% with the largest differences calculated around the equinoxes. This electron density depletion when CTMT tides are forced at the TIE-GCM lower boundary does increase with height up to −24% (Figure 6.4d), as a result of a decrease in electron density production (i.e., decrease in [O]) and increase in electron density loss (i.e., increase in [O_2] and [N_2]) at F-region altitudes. We must also note here that the percent changes in the IT constituents presented in Figure 6.4 show good agreement with those calculated in Forbes et al. [31].

Changes in the [O], [O_2], [O]/[N_2] ratio, and [N_e] show the same latitudinal structure and seasonal variability as the changes in the zonal-mean temperatures (Figure 5.1a). Specifically, the largest (smallest) differences in IT composition at low latitudes corresponds with maximum (minimum) changes in the zonal-mean temperature, as well as the zonal-mean meridional winds (Figure 4.12a) within the dynamo region. For example, the smallest increases in the zonal average temperatures at low latitudes due to the dissipating tides occur during the boreal summer months in Figure 5.1a, which is also when the smallest percent change in IT constituents occurs in Figure 6.3 and the right column of Figure E.3. A notable feature of Figures 6.3a and 6.3b are the similarly-located bands of [O] depletion and [O_2] enhancement, the latter about 1.5 times the former (i.e., this is when considering the percent change not absolute value), that occur as a result of upward-propagating tides. Another notable feature is that a similar enhancement does not occur in [N_2], which can also be inferred by the similarity between [O] and [O]/[N_2] in Figures 6.3a and 6.3c. Application of the hydrostatic law to zonally-averaged temperature profiles calculated from TIE-GCM simulations with and without lower boundary tidal forcing explains about 10% (i.e., between 3 and 6%) of the increases in [O_2] at low latitudes between 150 and 350 km (Figure E.4, red line). The 3 to 6% increase in [O_2] number densities driven by zonal-mean temperature changes (see Figure 5.1f) represents a pretty conservative estimate because the results presented in Figure E.4 are averaged between ±30° latitude. Thus, we suspect that at any one latitude this temperature effect (driven by eddy heat flux, adiabatic heating and cooling, and diabatic heating and cooling) to be larger, and to be further reinforced by the upward and equatorward transport of [O_2], as was shown in Figure 6.2c. The hydrostatic law also predicts increases in both [N_2] and [O] number densities ranging from 2-4.5% and 1-3%, respectively at low latitudes between 150 and 350 km (Figure E.4 black and blue lines); although this predicted increase in [O] number densities is reduced by a combination of both chemical and dynamical effects.

The decrease in [O] and increase in [O_2] is qualitatively consistent with an increase in eddy mixing in the lower thermosphere in the context of the classical picture of oxygen photochemistry: [O_2] is photo-dissociated to produce [O], which diffuses downward where it is converted to [O_2]

through 3-body recombination. In the steady-state, an equivalent flux of [O] atoms diffuses upward in the form of [O_2]. According to calculations by Akmaev and Shved [1], addition of vertical motions due to the diurnal tide in the above scenario produces effects in the same direction that one would ascribe to an increase in eddy mixing; they referred to this as tidal mixing. Their interpretation is that vertically-oscillating [O] parcels experience a net loss as a result of dipping into the 3-body recombination region. Thus, the diurnal tide produces the same net effect as an increase in eddy mixing. Through a series of numerical experiments involving DW1 specified at the lower boundary of the TIE-GCM, Yamazaki and Richmond [127] examined several possible mechanisms wherein the presence of a diurnal tidal oscillation could affect mean atomic oxygen densities in the thermosphere. They concluded that the Akmaev and Shved [1] mechanism was not very efficient, probably due to the slow time scale for recombination compared with the tidal period. They contended that the needed vertical transport is actually provided by a mean meridional circulation induced by the dissipating diurnal tide (DW1) flowing upward at the equator and poleward and downwards at higher latitudes. In this way, the two large-scale eddies act like large-scale turbulence (i.e., increasing eddy diffusion) in the mesosphere and lower thermosphere; thereby "mixing" the constituents of the lower thermosphere, leading to a net downward transport of [O] averaged over the low-latitude region. However, this does not explain why Akmaev and Shved [1] obtain the result that they do with a 1-dimensional model that does not allow for production of a mean circulation due to tidal dissipation.

Akmaev and Shved [1] also show that vertical motions due to the semidiurnal tide are not sufficient to produce a loss of [O] of the same magnitude as the diurnal tide, while Yamazaki and Richmond [127] only examine diurnal tidal effects on the meridional circulation. Our results differ from those of Akmaev and Shved [1] and Richmond [127] in that the role of SW2 is comparable to DW1 in producing neutral composition changes. This assertion is illustrated in Figure 6.5, which shows the percent changes in [O] and [O_2] as a function of month and height at 1.25° S between TIE-GCM simulations including CTMT lower boundary tidal forcing with TIE-GCM simulations including only a combination of the migrating tides from CTMT. We chose 1.25° S because it not

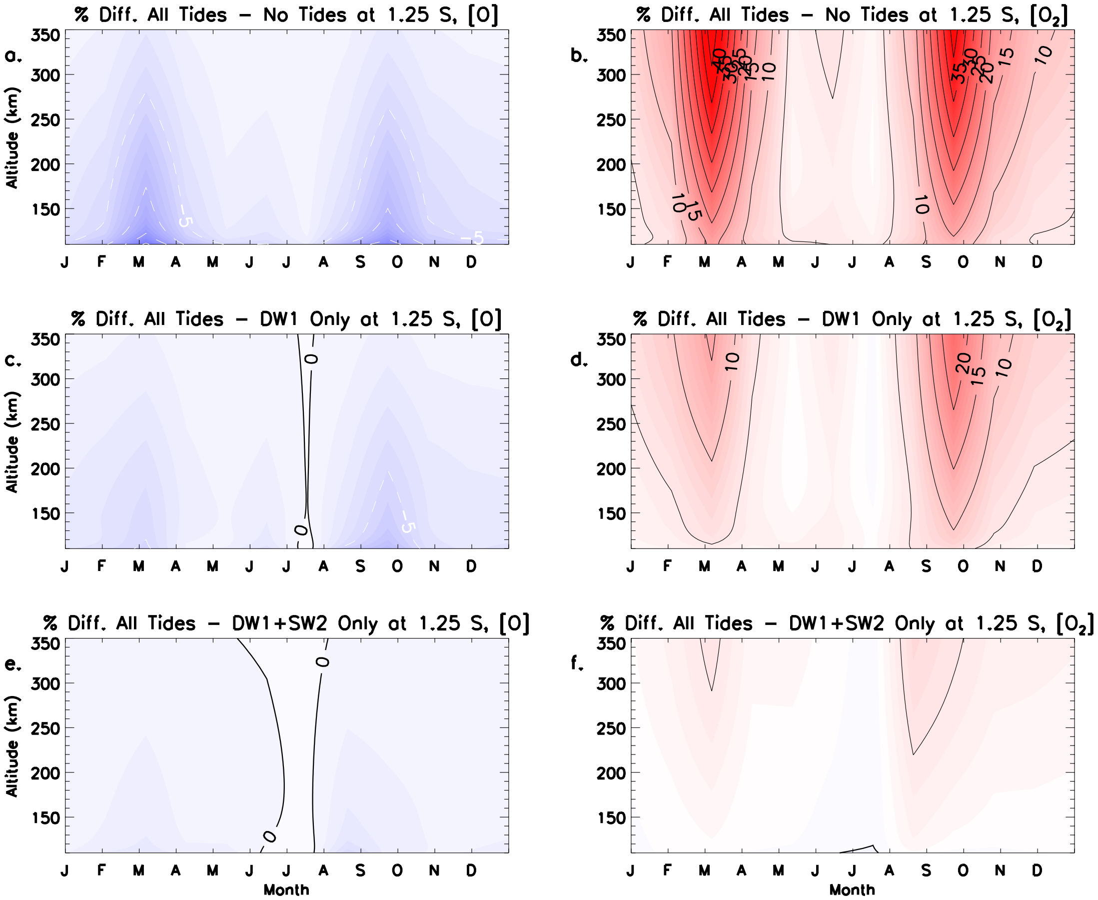

Figure 6.5: Percent differences in [O] (Left Column) and [O_2] (Right Column) as function of month and height at 1.25° S. Percent differences between TIE-GCM simulations including and excluding CTMT tidal forcing at the model lower boundary are shown in (a) and (b); percent differences between TIE-GCM simulations including all tidal components and only DW1 from CTMT at the model lower boundary are shown in (c) and (d); percent differences between TIE-GCM simulations including all tidal components and only DW1 and SW2 from CTMT at the model lower boundary are shown in (e) and (f). Percent differences are contour every ±5%.

only provides a representative depiction of the constituent response due to tidal propagation and dissipation at low-latitudes, but also it is the latitude at which the maximum percent differences occur in Figure 6.3. Including CTMT tides at the TIE-GCM lower boundary leads to a percent decrease (increase) in [O] ([O_2]) number density that decreases (increases) with altitude from about −20% to −2% (5% to 40%) between 110 and 350 km (Figures 6.5a and 6.5b). Similar to Figure 6.3, the largest percent changes in [O] and [O_2] occurs during the equinoxes (Figures 6.5a and 6.5b). Figure 6.5c (Figure 6.5d) shows that by including just DW1 at the TIE-GCM lower boundary percent changes in [O] ([O_2]) are reduced by a factor of $\sim$4 during the March equinox and by a factor of $\sim$2 during the September equinox. If we then include both migrating tides (i.e., DW1 and SW2) at the TIE-GCM lower boundary we see that the percent changes in [O] and [O_2] near the equator have been reduced to 5% or less (Figures 6.5e and 6.5f). The results presented in Figure 6.5 appear to be consistent with an initial enhancement in mixing associated with DW1, and a further enhancement in mixing that follows the dissipation of SW2 and its acceleration of the zonal flow in the thermosphere.

It appears there may be some other mechanism by which the tides can affect the net vertical transport of constituents in the thermosphere, perhaps similar to the type of wave-induced transport that is associated with shorter-period gravity waves (Gardner and Liu, [37]). In other words, the tides may induce net transport themselves, in addition to the effects of the mean circulation that is driven by dissipation of the tides. In the nomenclature reviewed in Gardner and Liu [37], the mechanism proposed by Akmaev and Shved [1] would be termed wave-induced *chemical transport*. This type of transport occurs when a wave-induced oscillation of a reactive species interacts with chemical processes to modify the concentration profile of that species in a manner similar to that of net vertical transport. In the context of oxygen photochemistry, tidal-driven chemical transport can produce effects similar to the "mixing" effects of eddy diffusion (Akmaev and Shved, [1]). Chemical transport can be driven either by dissipating or non-dissipating waves, but to be effective the chemical time constants must be much less than the period of the oscillation. Dissipating waves can also drive a mean meridional circulation that *advectively transports* constituents; this is the type of transport studied advocated by Yamazaki and Richmond [127] to be more effective in redistributing thermospheic atomic oxygen than the mixing mechanism proposed by Akmaev and Shved [1]. *Dynamical transport* refers to the net vertical flux of a constituent $\overline{w'n'_i}$ produced by a dissipating wave. This occurs because when a wave undergoes dissipation, w' and n' do not necessarily remain in quadrature (Liu and Gardner, [70]). It is this type of transport that we suggest may also be operative vis-à-vis tidal dissipation in the lower thermosphere, and contributing to our calculated [O] and [O_2] changes.

6.4 Tidal-Induced Net Transport Effects on the O Distribution in the Thermosphere

Atomic oxygen is fundamental to the aeronomy of the IT system and its distribution in the upper thermosphere is controlled by the transport, photochemical, and diffusion processes in the MLT region. As was discussed Chapters 4-6, the dissipation of atmospheric tides leads to a deposition of energy and momentum into the mean flow, thereby affecting the transport, photochemical, and diffusion processes that determine the distribution of O near and above the turbopause. Three different tidal-induced transport mechanisms that could be responsible for changes in O were outlined in the previous section. Hence, the purpose of this section is to verify the claim provided above, i.e., the tides induce a *net* transport of O themselves, as well as an *advective transport* of O via the mean meridional circulation generated by tidal dissipation. We test the above hypothesis using a set of numerical experiments from the TIME-GCM under September, solar medium, and geomagnetically quiet conditions that were described in detail in Chapters 2 and 3. Differences between TIME-GCM including and excluding GSWM-09 tides at the model lower boundary are calcualted in order to quantify the relative contributions of the different tidal-induced mechanisms which act to alter the [O] presented in Section 6.3.

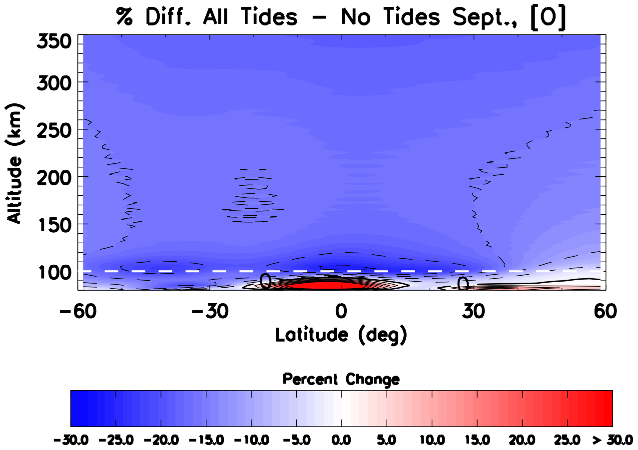

Figure 6.6: Percent differences in [O] between TIME-GCM with and without GSWM-09 lower boundary tidal forcing as a function of latitude and altitude during September and under solar medium conditions. Percent differences are contoured every ±5%.

Since the lower boundary of the TIE-GCM is near the turbopause (i.e., ∼97 km) and the constituent distributions within the first one or two scale heights are controlled by the fixed constituent lower boundary condition, it is difficult to assess the mechanisms responsible for altering the O distribution in the MLT. Furthermore, Figure 2.3 showed that the largest tidal components entering the thermosphere around 97 km were DW1, SW2, and DE3, and that the TIE-GCM was capable of producing comparable tidal amplitude structures to those produced in the TIME-GCM. Therefore, we utilize the TIME-GCM (i.e., model lower boundary ∼30 km) to further investigate the tidal-induced mechanisms that act to modify the O distribution in the height region around the TIE-GCM lower boundary. Figure 6.6 depicts the percent change in [O] from the TIME-GCM during the month of September extending from 80 to 350 km, with dashed line (at 100 km) approximately indicating the lower boundary of the TIE-GCM. Figure 6.6 clearly shows a reduction in [O] of ∼25% at 100 km, which extends to higher altitudes with percent decreases double that shown in Figure 6.4a from the TIE-GCM. The smaller percent changes in [O] above about 150 km shown in Figure 6.4a compared to Figure 6.6 are partially due to an increase in temperature when tides are included in the TIE-GCM, which causes an increase in O scale height (i.e., a less rapid decrease in O with altitude). Temperature decreases result in the opposite behavior in the TIME-GCM (Figure 6.6). The opposite behavior of the tidal-induced zonal-mean temperature changes in the TIE-GCM versus the TIME-GCM is outside the scope of this dissertation, and is left as future work. Also depicted in Figure 6.6 is a large increase in [O] (∼65%) between 85 and 95 km. Since the main source of SW2 excitation (insolation absorption by stratospheric ozone) is the same in both TIME-GCM simulations, the above variations in [O] can be explained mainly by the dissipation of DW1, with SW2 and DE3 playing secondary roles.

The largest [O] differences displayed in Figure 6.6 occur in the altitude range of 85 to 105 km, where transport, chemical, eddy, and molecular diffusion processes can be of equal importance. In order to diagnose which one of the above mechanisms is of utmost importance in this region one

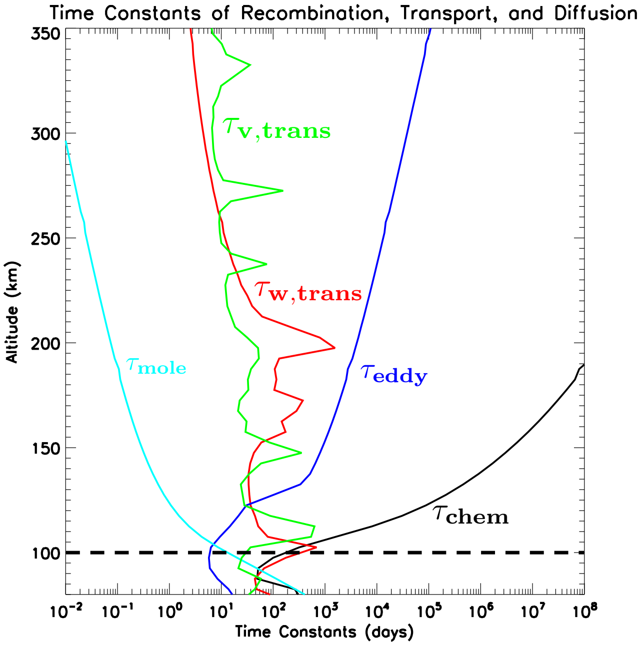

Figure 6.7: Time constants of O recombination, tidal transport, and molecular diffusion during September under solar medium conditions from the TIME-GCM as a function of altitude. $\tau_{v,trans}$ ($\tau_{w,trans}$) is shown in green (red), τ_{chem} is shown in black, τ_{eddy} is shown in blue, τ_{mole} is shown in cyan.

can refer to their respective time constants, which are calculated using the following:

$$\tau_{v,trans} = \frac{L}{v_{Tidal}}$$

$$\tau_{w,trans} = \frac{\overline{H}_O}{w_{Tidal}}$$

$$\tau_{chem} = \frac{1}{2k_r\overline{[O]}\,\overline{[N_2]}}$$

$$\tau_{eddy} = \frac{\overline{H}^2}{K_{zz}}$$

$$\tau_{mole} = \frac{\overline{H}_O^2}{\overline{D(O,N_2)}}$$

where L is the characteristic meridional length scale (we assumed it to be ∼10° in latitude or 1000 km which is about the latitudinal extent of the −15% [O] change in Figure 6.4a near 110 km), H_O is the diffusive-equilibrium scale height of O, v_{Tidal} (w_{Tidal}) are the *effective* meridional (vertical) *net tidal* transport velocities that are explicitly defined below, k_r is the rate constant of three-body recombination of O, $9.59 \times 10^{-34} \exp(\frac{480}{T})$ in $\mathrm{cm}^6\ \mathrm{s}^{-1}$ (after Allen et al., [2]), K_{zz} is the eddy diffusion coefficient from the TIME-GCM, and $D(O, N_2)$ is the mutual molecular diffusion coefficient from Colegrove et al. [7]. These time constants averaged over low latitudes are depicted in Figure 6.7. The lifetime of O due to meridional and vertical tidal transport ranges from ∼10 to 100 days near the [O] peak around 100 km and remains relative constant with increasing altitude (Figure 6.7, green and red lines). Both $\tau_{v,trans}$ and $\tau_{w,trans}$ are comparable to or faster than chemistry, which is near ∼100 days at 100 km and increases with altitude (Figure 6.7, black line). Due to the long chemical lifetime of O, compared to tidal period (hours) and the time scales of eddy (∼10 days at 100 km) and molecular diffusion (∼20 days at 100 km), the aforementioned Akmaev and Shved, [1] mechanism is not likely to cause the changes in [O] shown in Figures 6.3a, 6.4a and 6.6, as concluded by Yamazaki and Richmond [127]. Also near the [O] peak, the tidal transport and eddy diffusion time constants (e.g., ∼1 to 30 days) are of comparable importance and similar to the time constant of molecular diffusion in the TIME-GCM (Figure 6.7). Above an altitude of ∼125 km molecular diffusion dominates over tidal transport and eddy diffusion. Thus, the net effects of meridional and vertical transport associated with the dissipation of vertically-propagating tides in the altitude range of 80 to ∼125 km (see Figures 6.3a, 6.4a and 6.6) are playing a significant role in determining the vertical structure of [O], which in turn affect higher altitudes via molecular diffusion.

In order to separate the tidally induced *advective* and *net* transport of [O] in the MLT region we derive the continuity equation for [O], assuming that the dependent variables (i.e., meridional wind (v), vertical wind (w), and [O]) can be decomposed into a zonal mean and perturbation, following assumption (8) presented in Chapter 1. Substituting these zonal mean and perturbation quantities into the continuity equation (equation 1.3), neglecting chemical production and loss, and taking the zonal and diurnal average of that equation, we arrive at the following:

$$0 = \frac{\partial \overline{[O]}}{\partial t} = -\frac{1}{a}\frac{\partial}{\partial \theta}\overline{v}\,\overline{[O]} - \frac{1}{a}\frac{\partial}{\partial \theta}\overline{v'[O]'} - \frac{\partial}{\partial z}\overline{w}\,\overline{[O]} - \frac{\partial}{\partial z}\overline{w'[O]'}. \tag{6.4}$$

Please note that the continuity equation presented in equation 6.4 takes a slightly different form than equation 2.11 because the only simplifying assumption made to derive equation 6.4 was neglecting chemical production and loss. The first and third terms on the right hand side of (equation 6.4) represent the meridional and vertical [O] flux divergences due to the zonally- and diurnally-averaged meridional and vertical winds, respectively. The transport of [O] due to the tidally-induced mean winds is what we refer to as the *advective* transport of [O] or the prominent transport mechanism proposed byYamazaki and Richmond [127]. The remaining two terms on the right hand side of (equation 6.4) represent the divergences of the *net* transport fluxes of [O] due to the tides themselves, i.e., the mechanism proposed above in Section 6.3. Following the derivation of the effective dynamical transport velocity shown by Gardner and Liu, [37], we derive *effective* meridional and vertical *net tidal* transport velocities of [O], which are given by the following:

$$\overline{v'[O]'} \approx v_{Tidal}\overline{[O]} \quad \text{and} \quad \overline{w'[O]'} \approx w_{Tidal}\overline{[O]}. \tag{6.5}$$

Please note that dynamical transport velocity as defined by Gardner and Liu, [37] is the same for all species, which are assumed to be chemically inert. This is not the case for O, which is why the term *net tidal transport velocity* is used throughout the remainder of this dissertation. If v_{Tidal} and w_{Tidal} are of comparable magnitude to meridional and vertical advective velocities (v_{Adv} and w_{Adv}), we deduce that they are also playing an important role in transporting O in the MLT region.

Figure 6.8 (Figure 6.9) shows TIME-GCM September v_{Tidal} and v_{Adv} (w_{Tidal} and w_{Adv}) results with GSWM-09 tides at the lower boundary in the top row, and differences between TIME-GCM simulations with and without GSWM-09 tides introduced at the model lower boundary in the bottom row. Comparison between Figures 6.8a and 6.8b shows that v_{Tidal} is larger than v_{Adv} between 80 to 95 km with values ranging between ± 8 m s^{-1}, while v_{Adv} is larger than v_{Tidal} above 95 km with values ranging from -10 to $+6$ m s^{-1}. Further comparison between difference fields calculated in Figures 6.8c and 6.8d reveals a meridional structure of v_{Tidal} that is relatively unchanged, whereas there is a reduction in v_{Adv}. The similarity between Figures 6.8a and 6.8c implies that the *tidally* induced meridional wind is mainly coming from the tropospherically-forced DW1 with the strato-mesospherically forced DW1 and SW2, as well as the tropospherically-forced

DE3, playing secondary roles.

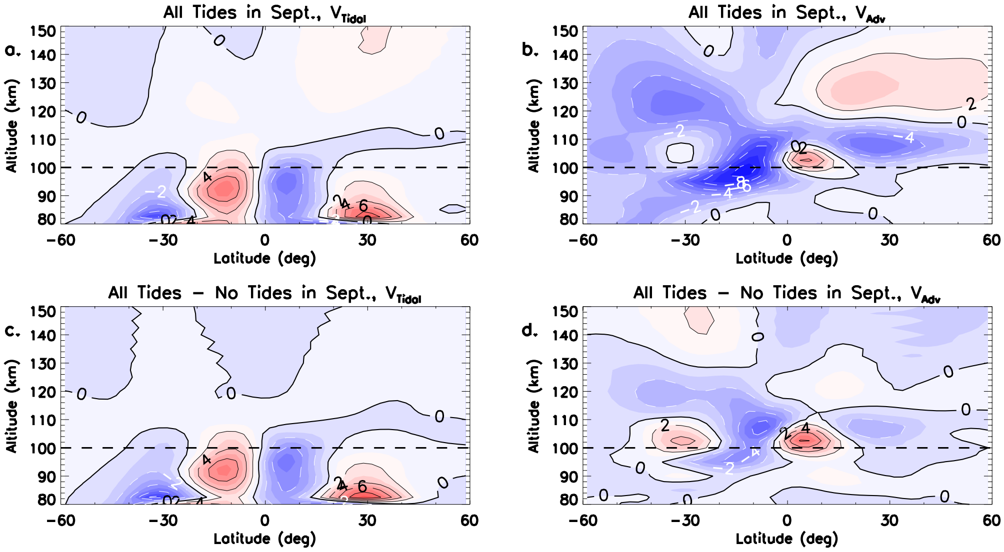

Figure 6.8: Meridional tidal and advective transport velocities as a function of latitude and altitude from TIME-GCM simulations during September. v_{Tidal} and v_{Adv} velocities from TIME-GCM simulations including GSWM-09 lower boundary tidal forcing are shown in (a) and (b), respectively. Differences in v_{Tidal} and v_{Adv} velocities from TIME-GCM simulations including and excluding GSWM-09 lower boundary tidal forcing are shown in (c) and (d), respectively. Velocities are contoured every 2 m s^{-1}.

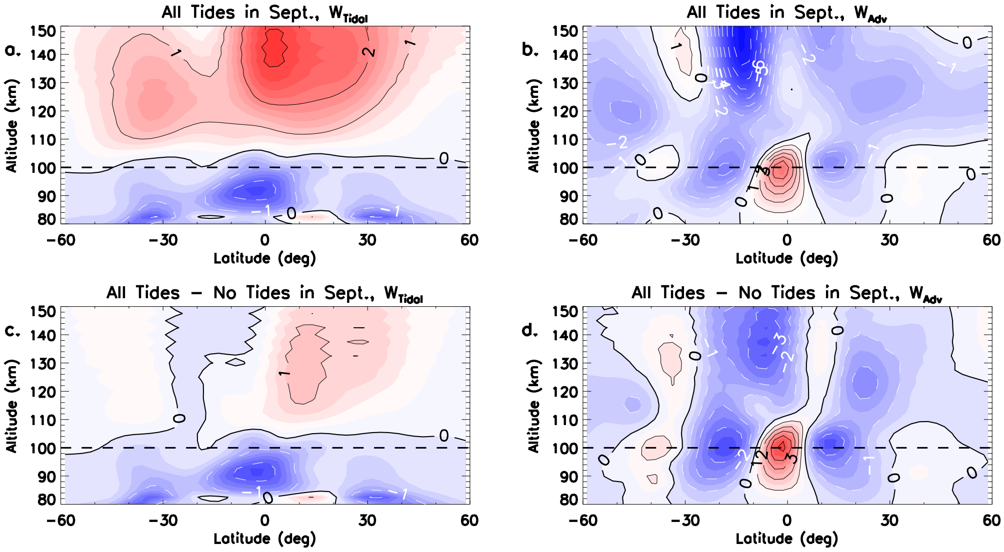

Figure 6.9: Same as Figure 6.8, except for vertical transport velocities w_{Tidal} and w_{Adv}. Velocities are contoured every 1 cm s^{-1}.

A discussion similar to the one above can be had for the vertical transport velocities, w_{Tidal} and w_{Adv} (Figure 6.9). Below 100 km w_{Tidal} is downward at low and middle latitudes with a maximum downward velocity of 2 cm s^{-1} near the equator (Figure 6.9a). Above 100 km w_{Tidal} is upward with maximum velocities of 3 cm s^{-1} centered about the equator. The differences between w_{Tidal} with and without GSWM-09 tides at the TIME-GCM lower boundary show that below (above) 100 km the downward (upward) w_{Tidal} velocities remain relatively unchanged (reduced) due to the dissipation of tides. w_{Adv} has a clear three-cell structure at low latitudes that is upward at the equator (5 cm s^{-1}) and downward just poleward of the equator (-4 cm s^{-1}) at 100 km (Figure 6.9b). This three-cell vertical circulation structure is evidently generated by the dissipation of the tides because it is present in Figure 6.9d.

It is clear from Figures 6.8 and 6.9 that the magnitudes of the net tidal transport velocities are comparable to the magnitudes of the advective transport velocities. We now consider the flux divergences due to each one of the different transport velocities and their respective difference fields in order to describe the [O] difference fields shown in Figure 6.6 (as well as Figures 6.3a and 6.4a). Equation 6.4 can be rewritten in terms of difference fields between TIME-GCM simulations with and without GSWM-09 tides at the model lower boundary, which results in the following equation:

$$0 \approx \frac{\partial}{\partial t}\Delta\overline{[O]} \approx -\frac{1}{a}\frac{\partial}{\partial \theta}(\overline{v}_1 - \overline{v}_0)\overline{[O]}_1 - \frac{\partial}{\partial z}(\overline{w}_1 - \overline{w}_0)\overline{[O]}_1 - \frac{1}{a}\frac{\partial}{\partial \theta}\overline{v_1'[O]_1'} - \frac{\partial}{\partial z}\overline{w_1'[O]_1'} \qquad (6.6)$$

where subscript zero (one) refers to TIME-GCM simulations excluding (including) GSWM-09 lower boundary tidal forcing, and $\Delta\overline{[O]} = \overline{[O]}_1 - \overline{[O]}_0$. Equation 6.6 also assumes $\overline{[O]}_1 \approx \overline{[O]}_0$ (i.e., only changing by 10-20% see Figure 6.6) and $\overline{w_0'[O]_0'} \ll \overline{w_1'[O]_1'}$.

Figure 6.10 illustrates both the individual terms on the right hand side of (equation 6.6) and the sum of these terms as function of latitude and height from the September TIME-GCM simulations in order to facilitate the interpretation of the [O] differences (Figure 6.10h). The panels in the first column of Figure 6.10 (a, c, and e) depict the [O] flux divergences due to tidally induced *net* transport, whereas the panels in the second column of Figure 6.10 (b, d, and f) portray the [O] flux divergences due to tidal induced *advective* transport. The meridional component of the [O]

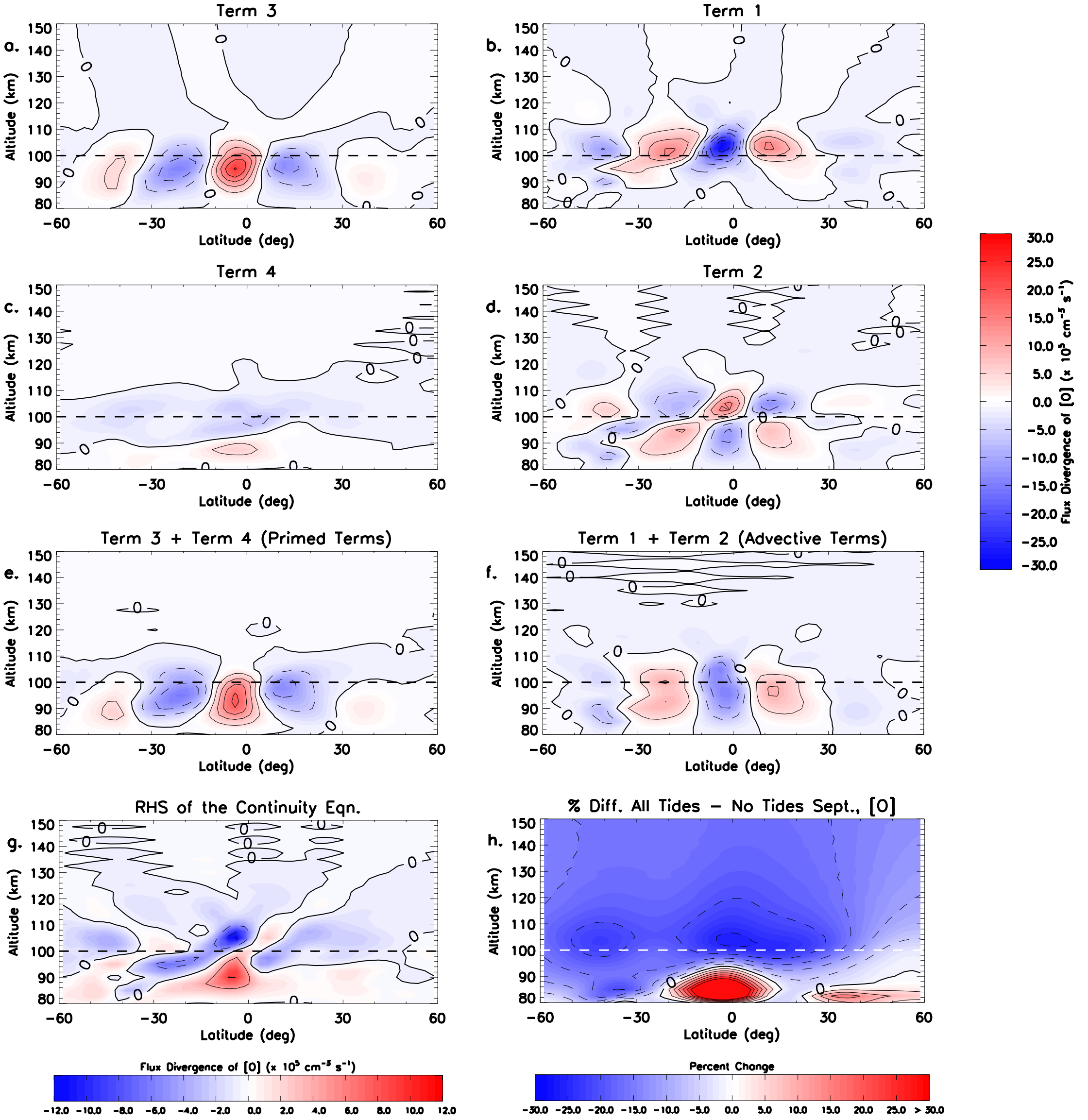

Figure 6.10: Meridional and vertical derivatives in the [O] fluxes from the continuity equation 6.6 calculated from TIME-GCM simulations during September. (a) Third term on the right hand side of 6.6; (b) First term on the right hand side of 6.6; (c) Fourth term on the right hand side of 6.6; (d) Second term on the right hand side of 6.6; (e) Total divergence due to tidal transport; (f) Total divergence due to advective transport; (g) The full right hand side of 6.6; (h) Same as Figure 6.6 except from 80 to 150 km.

flux divergence due to net (advective) tidal transport of [O] in Figure 6.10a (6.10b) results in a net source (sink) of [O] centered close to the equator near 100 km on the order of 25 × 10^5 cm^{-3} s^{-1} (−25 × 10^5 cm^{-3} s^{-1}). Also in Figure 6.10a (6.10b) are two net sink (source) regions of [O] just poleward of source (sink) regions near 100 km on the order of -10×10^5 cm^{-3} s^{-1} (15×10^5 cm^{-3} s^{-1}). The vertical component of the [O] flux divergences due to tidally induced net transport reveals a net sink in [O] between ∼90 and ∼105 km over the low and middle latitudes, while below ∼90 km there is a source region of [O] over the low and middle latitudes (Figure 6.10c). These source (sink) maxima (minima) are 6×10^5 cm^{-3} s^{-1} (-5×10^5 cm^{-3} s^{-1}), which are an order of magnitude smaller than the meridional [O] flux divergences. Vertical [O] flux divergences due to advective transport show antisymmetric source and sink regions centered about 100 km and between ±30° in latitude (Figure 6.10d). Below (above) 100 km there is a net sink (source) of [O] at equator flanked by two source (sink) regions with magnitudes on the order of $\pm 12 \times 10^5$ cm^{-3} s^{-1}. The sum of the meridional and vertical [O] flux divergences due to tidally induced net (advective) transport shown in Figure 6.10e (6.10f) reveals the same structure as the meridional flux divergences shown in Figure 6.10a (6.10b), with a source (sink) of [O] at the equator, flanked on each side by a sink (source) of [O] near 100 km. The sum of all of the flux divergence terms are shown in Figure 6.10g. The large percent increase (i.e., source) in [O] between 85 and 95 km and close to the equator shown in Figure 6.10h appears to be consistent with the *net* meridional divergence term due to the tides, which is then extended poleward in both hemispheres by the *advective* part of the meridional and vertical divergence terms. This percent increase in [O] and could possibly be connected with the effects of tides on the mesospheric odd-oxygen chemistry. Also depicted in Figure 6.10h is a percent decrease (i.e., sink) in [O] of ∼25% at 100 km and tropical latitudes that appears to be consistent with the *advective* meridional divergence term due to the tides, which is then extended downward and polewards in both hemispheres due to the *net* tidal portion of the meridional divergence term. Hence, both the tidally induced *net* and *advective* transport of [O] in the MLT region are equally contributing to the [O] distribution at these altitudes, with the meridional component playing the primary role and the vertical component playing a secondary role. Please note that the above analysis of the continuity equation (6.6) was done using Eulerian mean quantities, which is different than Lagrangian mean quantities (i.e., mean motion following an air parcel). A complementary Lagrangian analysis is beyond the purview of this dissertation.

We also consider the above results presented in Figure 6.10 in light of an observational study performed by Smith et al. [117], in which they state that the seasonal variations in SABER measured O at mesospheric altitudes is affected by the semiannual variation of DW1. Additionally, Smith et al. [117] conclude that the semiannual variation in the tidal amplitudes is responsible for driving the aforementioned seasonal variations in daily-averaged O via what they term "irreversible" transport induced by the tides. Specifically, they suggest two types of irreversible tidal transport including "chemical eddy transport", which can be thought of as the Akmaev and Shved [1] mechanism (i.e., wave-induced chemical transport), and a net transport of O induced by an Eliassen-Palm (EP) flux divergence generated by the dissipating DW1. Smith et al. [117] state that at 84 km (94 km) the chemical eddy transport (tidal-induced EP flux divergence) is the most likely mechanism responsible for the semiannual cycle in O. Thus, the SABER O results presented in Smith et al. [117] validate the results shown in Figure 6.10, as their tidal-induced EP flux divergence encompasses both the *net* and *advective* transport mechanisms analyzed and presented above. However, Smith et al. [117] do state that it is the vertical transport that is most important for the observed semiannual variation in O, whereas we find that the meridional transport is the dominant driver in the month of September.

The above analysis was only carried out for [O] only and not for the other major neutral constituents, including [O_2], and [N_2]. Additionally, the above analysis was only performed during the month of September and under solar medium conditions. We surmise that the relative importance of the different tidal transport mechanisms described above would vary with season and solar cycle condition. However, since the zonal-mean residual meridional circulation depicted in Figures 5.11g, 5.4g, 5.12g did not vary much with solar cycle during the month of September, most of the seasonal and solar cycle variability in the analysis presented above may reside in the *net* tidal transport of [O], as opposed to the *advective* tidal transport of [O]. Nonetheless, the seasonal and solar cycle variability associated with the different tidal-induced transport mechanisms of [O], as well as investigating the different tidal-induced transport mechanisms associated with [O_2], and [N_2] warrant further investigation and is left for future work.

6.5 Solar Cycle Variations in the Major Constituents of the IT

Figure 6.11 illustrates difference fields in the [O], [O_2], [O]/[N_2] ratio, and [N_e], as a function of month and latitude at 130 and 200 km from TIE-GCM simulations performed with and without CTMT lower boundary tidal forcing under solar minimum (left column) and maximum (right column) conditions. As was the case during solar medium (Figure 6.3), the largest percent differences calculated in the major constituents during solar minimum and maximum (Figure 6.11) occur around the equinoxes at 130 and 200 km. The solar cycle variations in the [O] differences during other months (e.g., July see Figure E.5) tend to be smaller, and therefore we focus the remainder of our discussion on the solar cycle variations associated with the constituent changes in the IT during the month of September. Differences fields in the major constituents from TIE-GCM simulations with and without CTMT lower boundary tidal forcing during September as a function of latitude and altitude under solar minimum (left column) and maximum (right column) conditions are shown in Figure 6.12. When CTMT tidal lower boundary forcing is included, Figure 6.11a (Figure 6.11b) depicts changes in [O] at 130 km ranging from -18 to $+7\%$ (-7 to 0%) that persist throughout the entire year at low and middle latitudes under solar minimum (maximum) conditions. Similar to the [O] differences calculated the solar medium conditions, the [O] differences during solar minimum and maximum are driven by DW1 and SW2 (see Figures E.9 and E.7). Near the equator, [O] percent differences extend into the F-region with negative differences of $\sim 5\%$ ($\sim 1\%$) at 300 km under solar minimum (maximum) conditions (see Figures 6.12a and 6.12b). Comparison between Figures 6.11a, 6.3a, and 6.11b shows a clear solar cycle variability associated with the tidally-induced [O] changes in the IT, with the largest (smallest) differences occurring at low latitudes under solar minimum (maximum) conditions (i.e., similar to what was shown for the zonal-mean zonal winds and zonal-mean temperatures in Chapters 4 and 5). Further comparison between 6.12a, 6.4a, and 6.12b shows that larger reductions in [O] extend higher into the IT during solar minimum and medium, than in solar maximum. The hydrostatic law predicts increases (decreases) in [O] during solar minimum (maximum) ranging from 3-9% (-1-0%), at low latitudes

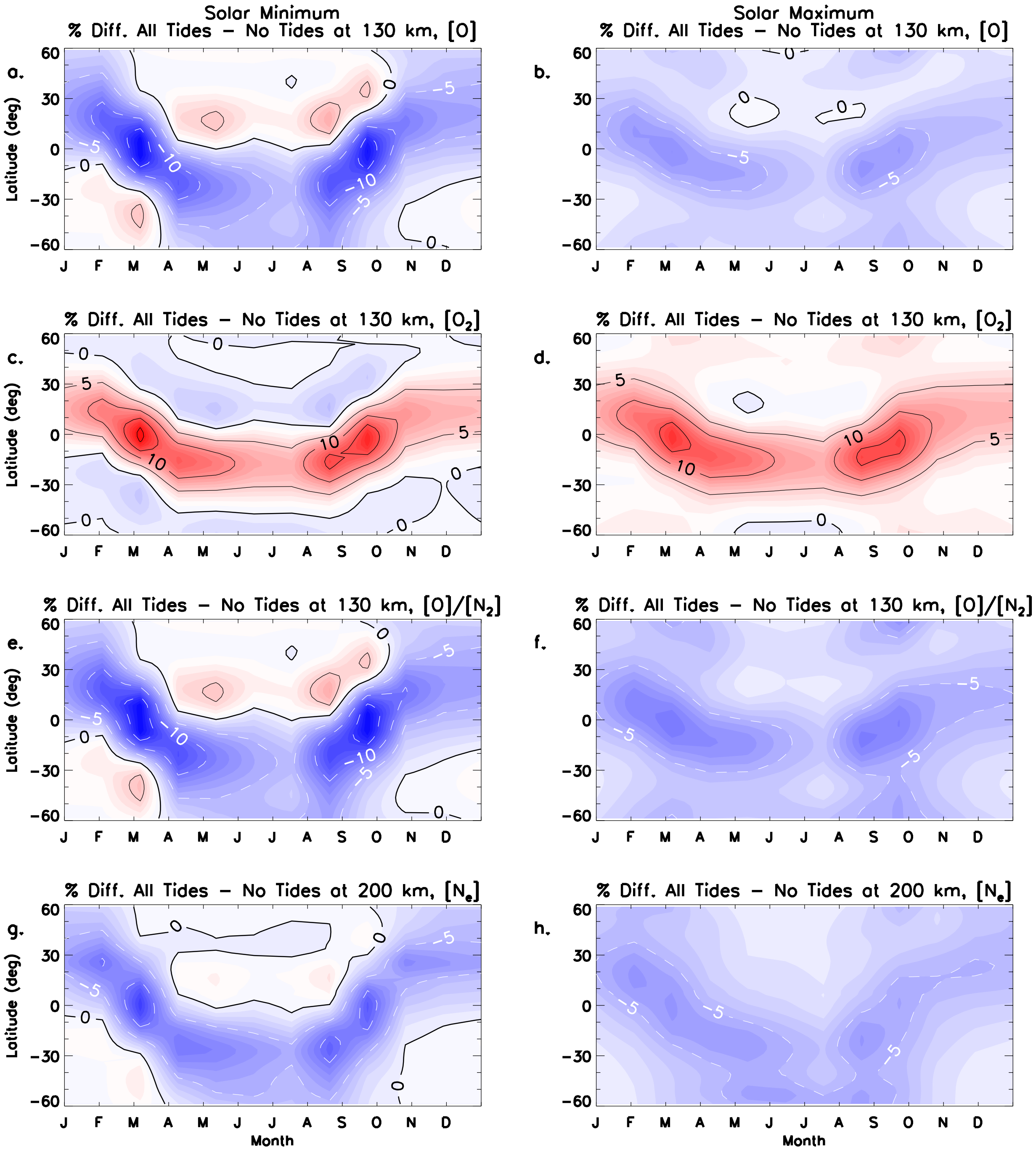

Figure 6.11: Percent differences between TIE-GCM simulations including and excluding CTMT tidal lower boundary forcing as a function of month and latitude at 130 and 200 km under solar minimum (Left Column) and maximum (Right Column) conditions. [O] differences are shown in (a) and (b), $[O_2]$ differences in (c) and (d), $[O]/[N_2]$ differences in (e) and (f), and electron density differences in (g) and (h). Percent differences are contoured every ±5%.

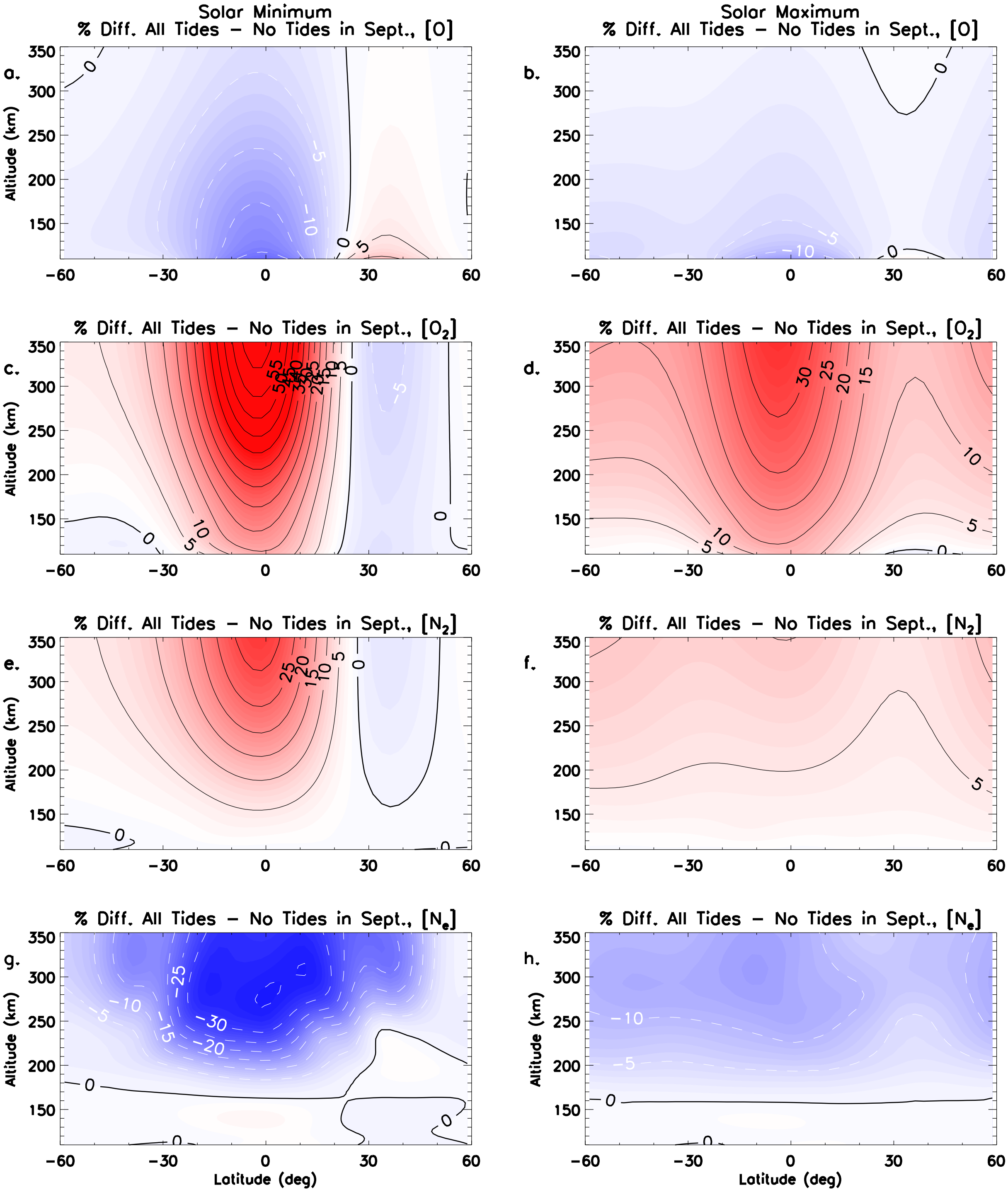

Figure 6.12: Percent differences between TIE-GCM simulations including and excluding CTMT tidal lower boundary forcing as a function of latitude and altitude during September and under solar minimum (Left Column) and maximum (Right Column) conditions. [O] differences are shown in (a) and (b), [O$_2$] differences in (c) and (d), [N$_2$] differences in (e) and (f), and electron density differences in (g) and (h). Percent differences are contoured every ±5%.

between 150 and 350 km (see Figure E.8, blue lines). Similar to the [O] differences calculated under solar medium conditions, changes in the zonal-mean temperatures induced by the dissipating tides cannot be the sole driver of the [O] differences under solar minimum and maximum conditions. We therefore hypothesize that the tidal induced *net* and *advective* transport of O in the MLT region is more efficient during solar minimum than solar maximum, and can also extend to higher altitudes due to reduced molecular dissipation. This increased tidal induced *net* and *advective* transport of O would result in a enhanced O sink, and thus would manifest in larger negative [O] differences that would then extend to higher altitudes in the IT. However, further research is required to validate the hypothesis offered above.

When CTMT lower boundary tidal forcing is included at the TIE-GCM lower boundary the seasonal and latitudinal structure of the [O_2] differences remains relatively unchanged under different solar cycle conditions at low and middle latitudes (see Figures 6.11c, 6.3b, and 6.11d). As was the case with [O], the largest (smallest) [O_2] differences occur under solar minimum (maximum) conditions with enhancements of ∼20% (∼15%) during the equinoxes at 130 km (Figures 6.11c and 6.11d), which are mainly driven by DW1 and SW2 (see Figures E.9 and E.7). Tidal-induced enhancements of [O_2] of ∼50% are calculated at upper IT altitudes maximizing under solar minimum conditions in September (Figure 6.12c). This ∼50% increase in [O_2] above 300 km during solar minimum is 10% (20%) more than what is calculated during solar medium (maximum) in Figure 6.4b (Figure 6.12d). The solar cycle variability associated with the tidally-induced [O_2] changes is in part explained by the solar cycle variability associated with tidally-induced zonal-mean temperature changes. Applying the hydrostatic law to the increases in the zonal-mean temperatures during solar minimum (Figure 5.10a) leads to a 6-24% increase in [O_2], between 150 and 350 km (Figure E.8, dotted red line). Applying the hydrostatic law to the decreases in the zonal-mean temperatures (Figure 5.10b) during solar maximum leads to the small decreases (i.e., ∼1%) in [O_2] at upper IT altitudes (Figure E.8, dashed red line). Therefore, this temperature affect is acting to enhance (reduce) the increases in [O_2] already imposed by the convergence of the mass flow stream function above 150 km near the equator (Figure E.2), leading to larger positive percent changes in [O_2] during solar minimum versus solar maximum (Figures 6.12c and 6.12d). Please note that above 300 km the zonal-mean residual meridional circulation is also acting to increase [O_2] via the minor species continuity equation, as upward winds (or vertical winds in the residual meridional circulation, see Figure E.9) act like a source for minor species whose molecular weight is greater than the mean molecular weight (Liu, [72]). Tidally-induced *net* transport of O_2 might also be acting to enhance [O_2] in the MLT region more during solar minimum as opposed solar maximum, although additional work is needed to substantiate this claim.

Differences in the [O]/[N_2] ratio presented in Figures 6.11e and 6.11f mainly follow the [O] depletion results discussed above, which is similar to what was shown for [O]/[N_2] ratio differences calculated under solar medium conditions (Figure 6.3c). By comparing Figures 6.12e, 6.4c, and 6.12f, we see that differences in [O]/[N_2] ratio show solar cycle variations similar to that of [O] differences, as larger positive differences in [N_2] occur at F-region altitudes during solar minimum (Figure 6.12e), as opposed to solar maximum (Figure 6.12f). Differences of 25% (8%) or more are calculated for in Figure 6.12e (Figure 6.12f) above 300 km at low-latitudes during solar minimum (maximum). Unlike the [O_2] increases due to the tides, zonal-mean temperature increases appear to account for the majority of [N_2] differences during solar minimum above 150 km, as Figure E.8 (black dotted line) shows a 5-20% increase in [N_2]. At solar maximum the hydrostatic law predicts very small and even negative changes in [N_2] (Figure E.8, black dashed line). Therefore, we conclude that in addition to the zonal-mean temperature affect the mass flow stream function convergence, residual vertical winds, and potentially tidally-induced *net* transport processes are acting to enhance [N_2] in the same way they are acting to enhance [O_2].

Tidally-driven differences in [N_e] at 200 km illustrated in Figures 6.11g and 6.11h range from -14 to $+2$% and -7 to -1% during solar minimum and maximum respectively, with the largest differences calculated around the equinoxes (i.e., similar to solar medium). As was the case for TIE-GCM simulations under solar medium conditions, electron density depletions occur when CTMT tides are forced at the TIE-GCM lower boundary, and these depletions increase with altitude reaching minimum values of -35% and -14% in the upper IT during solar minimum and solar maximum, respectively (Figures 6.12g and 6.12h). These solar cycle variations in the electron density result from a more pronounced decrease in electron production during solar minimum as compared to solar maximum (i.e., more of decrease in [O] during solar minimum than in solar maximum), as well as an enhanced increase in electron loss during solar minimum as compared to solar maximum (i.e., more of an increase in [O_2] and [N_2] during solar minimum than in solar maximum).

6.6 Solar Cycle Variations in NO

Vertically-propagating tides not only act to change the major constituents of the IT system, but also the minor constituents (Forbes et al., [31]; Oberheide and Forbes, [84]; Oberheide et al., [88]). For example, we showed in Chapter 5 that the disspating tides modulate the NO 5.3 μm IR cooling in the lower thermosphere, which acted to produce a more pronounced cooling during solar maximum as compared to solar minimum (Figure 5.13). This implies that the dissipating tides are acting to change the amount of NO in the IT, and that these changes depend on solar cycle. Therefore, this section focuses on investigating the mechanism by which the vertically-propagating tides are acting to alter NO in the lower IT, and the solar cycle variations associated with this mechanism. We also discuss how these changes in NO can lead to diabatic cooling term differences in the zonal-mean thermodynamic energy equation of the TIE-GCM, which ultimately results in solar cycle variations associated with the tidally-driven zonal-mean temperature differences. Please note that all the results presented in this section are from the TIE-GCM simulations described in Chapters 2 and 4 during the month of September and are averaged between ±30° because the largest changes in the major constituents and zonal-mean temperatures due to the vertically-propagating tides occur at the equinoxes and are situated at low latitudes.

At low and middle latitudes NO is formed in the thermosphere (and thus in the TIE-GCM) mainly by the following reactions (Sharma et al., [110]):

$$N(^4S) + O_2 \rightarrow NO + O \tag{R1}$$

$$N(^2D) + O_2 \rightarrow NO + O. \tag{R2}$$

R1 is temperature dependent, and thus is not very efficient in producing NO in the lower thermosphere. Therefore, it is R2 that is mostly responsible for producing NO at lower thermospheric altitudes in the TIE-GCM. One can deduce from R2 that increases in $N(^2D)$, O_2, or both induced by the tides would act to increase the amount of NO in thermosphere. Figure 6.13 shows the average mass mixing ratios of $N(^2D)$ and NO, as well as the percent differences in $N(^2D)$ and NO calculated between TIE-GCM simulations with and without CTMT tidal lower boundary forcing under solar minimum (dotted lines), solar medium (solid lines), and solar maximum (dashed lines) conditions. The mass mixing ratios of $N(^2D)$ and NO are larger during solar maximum than in solar medium, and solar minimum, which implies that their number densities are also larger (Figure 6.13). The type of solar cycle behavior in the $N(^2D)$ and NO mass mixing ratios are expected due to increased neutral density at solar maximum as compared to solar minimum (Qian et al., [97]). Evaluating the percent changes in the $N(^2D)$ and NO between TIE-GCM simulations that include and exclude CTMT lower boundary tidal forcing, but are performed under the same solar cycle conditions, allows us to eliminate the inherent increases in $N(^2D)$ and NO mass mixing ratios. Percent changes in $N(^2D)$ and NO mass mixing ratios range from -8 to $+5\%$ and $+12$ to $+45\%$, respectively depending on solar cycle (Figure 6.13, bottom panel). The tides induce between a 15-20% increase in the NO mass mixing ratio (and thus number density) during solar maximum (Figure 6.13, black dashed line). During solar minimum this percent increase in NO mass mixing ratio is between 20-45% (Figure 6.13, black dotted line). However, the mass mixing ratio of NO in solar maximum is ~3 times that of solar minimum and would thereby lead to a larger increase in NO during solar maximum.

Since the changes in $N(^2D)$ are relatively small, we conclude that the tides are not acting to appreciably change the NO via changes $N(^2D)$. This is probably related to the short chemical lifetime of $N(^2D)$ compared to tidal period at lower thermosphere altitudes. Figure 6.14 shows the [O], [O_2], and [N_2], as well as their percent differences calculated between TIE-GCM simulations

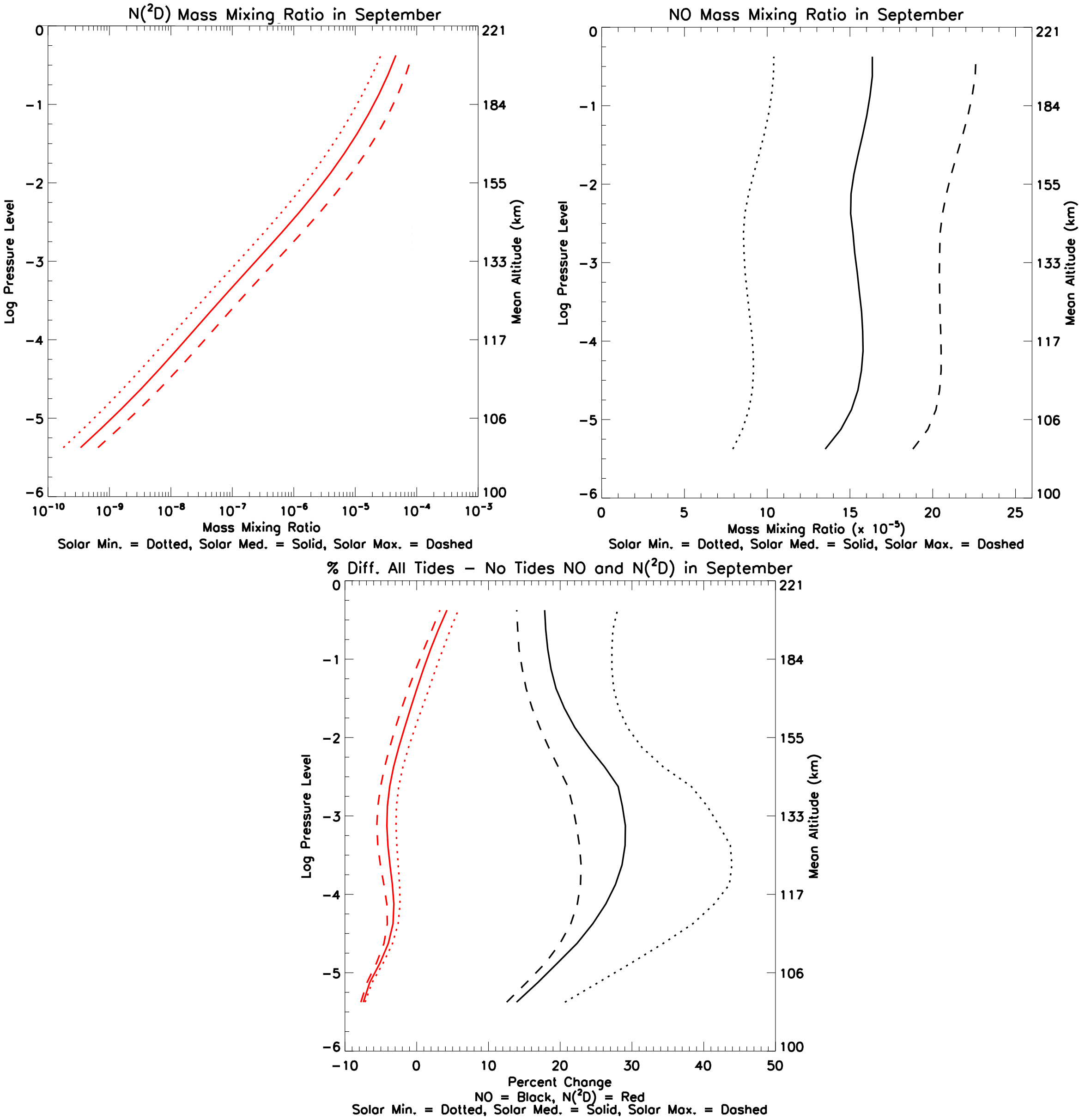

Figure 6.13: N(^{2}D) (top left) and NO (top right) mass mixing ratios in September averaged between ±30° as a function of altitude from TIE-GCM simulations including CTMT tidal lower boundary forcing. Percent differences between TIE-GCM simulations including and excluding CTMT tidal lower boundary forcing in N(^{2}D) (red) and NO (black) are shown in the bottom panel. Mass mixing ratios and percent differences from TIE-GCM simulations under solar minimum, medium, and maximum conditions are represented by the dotted, solid, and dashed lines, respectively.

including and excluding CTMT tidal lower boundary forcing. Similar to Figure 6.13, constituent densities and their differences in Figure 6.14 from TIE-GCM simulations performed under solar minimum, medium, and maximum conditions are represented by dotted, solid, and dashed lines, respectively. Please note that the [O_2] is larger during solar maximum as compared to solar minimum (Figure 6.14, red lines). Tidally-driven increases of 10-15% in the [O_2] during solar maximum is only ~5% less than the [O_2] increases during solar minimum, which results in a larger abundance of O_2 during solar maximum than in solar minimum (Figure 6.14, right panel). Thus, the tidal-induced changes in O_2 are responsible for driving the increases in NO.

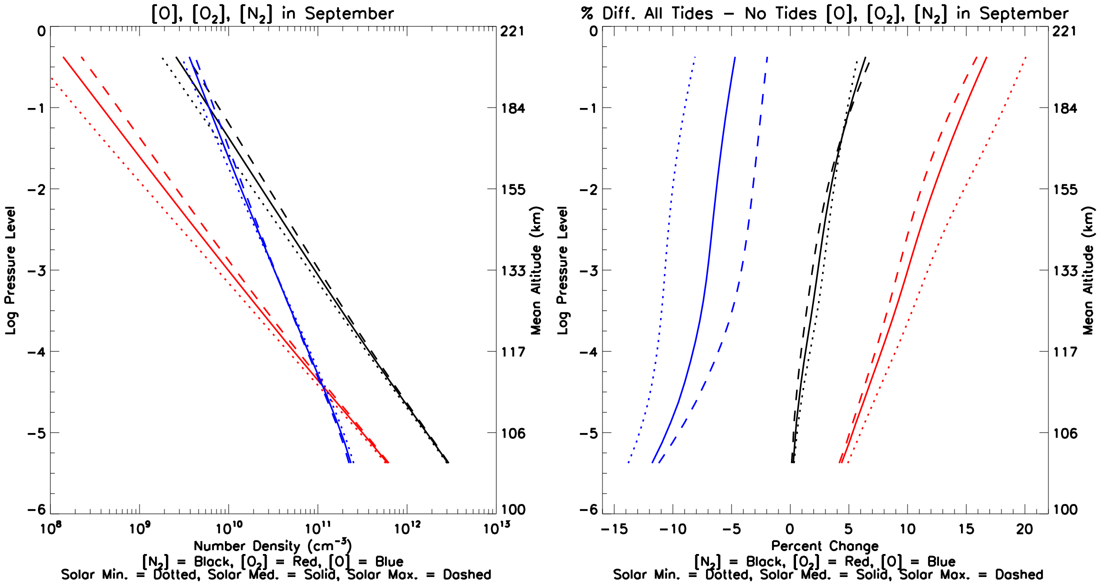

Figure 6.14: [O] (blue lines), [O_2] (red lines), and [N_2] (black lines) (left panel), as well as percent differences in [O], [O_2], and [N_2] between TIE-GCM simulations including and excluding CTMT tidal lower boundary (right panel), as a function of altitude during September and under solar minimum (dotted lines), medium (solid lines), and maximum (dashed lines) conditions.

In order to produce the NO 5.3 μm IR emission, NO must be excited to a higher energy state. The primary excitation mechanism of NO vibrations is through inelastic collision with O (Mlynczak et al., [81]). These collisions increase the internal energy of the NO molecule that is either radiated by spontaneous emission or is quenched via collisions (Kockarts, [61]). Mlynczak et al. [81] outlines the different processes that can act to increase the amount of IR radiation emitted by the NO molecule, including an increase in NO abundance which leads to more vibrationally excited NO via collisions with O, and an increase in O concentration which results in more collisions with NO. As was discussed above, there is an increase in NO abundance in our TIE-GCM simulations driven by tidal dissipation that is greater during solar maximum than in solar minimum. Furthermore, the percent decreases in [O] differs with solar cycle with the largest percent changes between −10 an −15% occurring during solar minimum, whereas percent decreases of only −2 to −10% occur during solar maximum (Figure 6.14, blue lines). Given that there is less O and more O depletion due to the tides during solar minimum than in solar maximum, it appears there will be more O available to inelastically collide with more NO molecules to produce more NO cooling, following the logic presented by Mlynczak et al. [81]. In this way the tides are acting to modulate the natural thermostat of the NO emission (Mlynczak et al., [81]) in the thermosphere.

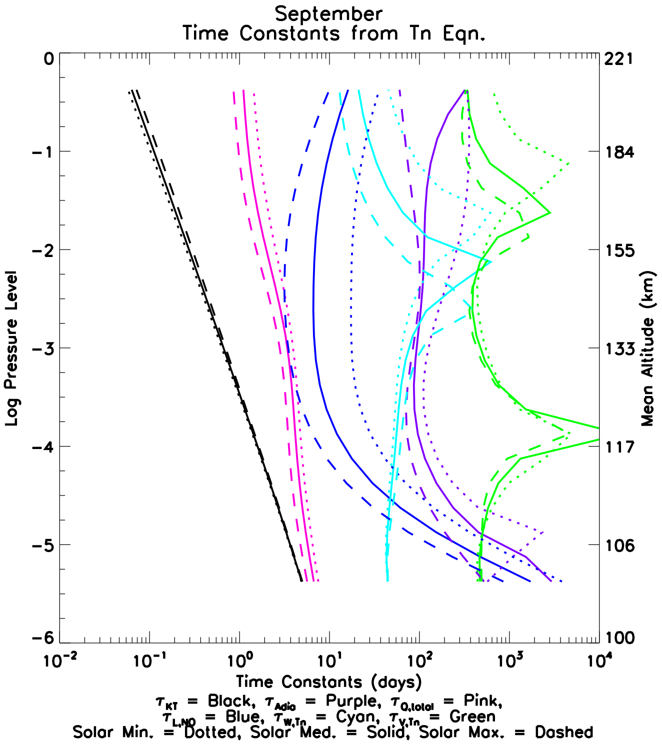

Figure 6.15: Time constants of the different forcing terms in the thermodynamic energy equation during September under solar minimum (dotted lines), medium (solid lines), and maximum (dashed lines) from a TIE-GCM simulations that included CTMT tidal lower boundary forcing as a function of altitude. τ_{K_T} is shown black, τ_{Adia} is shown in purple, $\tau_{v,TH}$ ($\tau_{w,TH}$) is shown in green (cyan), $\tau_{Q_{Total}}$ is shown in pink, and $\tau_{L_{NO}}$ is shown in blue.

Solar cycle variability in NO cooling differences induced by the dissipating tides affect the zonal-mean temperature differences in the IT via the diabatic heating and cooling terms (J) in the zonal-mean thermodynamic energy equation (equation 2.12). As was described in Chapter 5 the diabatic heating rate (J) represents the differences in the diabatic heating sources and sinks. The largest diabatic heating source (sink) in the TIE-GCM is radiative heating (NO IR radiative cooling). The largest (positive or negative) zonal-mean temperature differences depicted in Figures 5.11g, 5.4g, and 5.12g occur below 200 km where adiabatic heating and cooling, the eddy heat source terms, diabatic heating and cooling, and diffusion processes can be of equal importance. In order to diagnose which one of the above mechanisms is of utmost importance in the lower IT one can refer to their respective time constants, which are calculated using the following:

$$\tau_{K_T} = \frac{\rho_0 \overline{H} c_p}{K_T},$$

$$\tau_{Adia} = \frac{\overline{H}}{\overline{w}\kappa},$$

$$\tau_{v,TH} = \frac{L}{v_{TH}},$$

$$\tau_{w,TH} = \frac{\overline{H}}{w_{TH}(1-\kappa)},$$

$$\tau_{Q_{Total}} = \frac{c_p \overline{T}}{Q_{Total}},$$

$$\tau_{L_{NO}} = \frac{c_p \overline{T}}{L_{NO}},$$

where K_T is the thermal conductivity, L is the characteristic meridional length scale (we assumed it to be ~60° in latitude covering latitudinal extent of the low latitude changes in the zonal-mean temperature in Figures 5.11g, 5.4g, and 5.12g), Q_{Total} is the total heating term in the TIE-GCM including radiative heating, joule heating, heating due to O recombination, heating due to molecular diffusion, and heating due to numerical diffusion, L_{NO} is the NO IR cooling rate, and v_{TH} (w_{TH}) are the meridional (vertical) *tidal heat* transport velocities that are defined after Gardner and Liu [37],

$$\overline{v'T'} = v_{TH}\overline{T} \quad \text{and} \quad \overline{w'T'} = w_{TH}\overline{T}. \tag{6.7}$$

These time constants averaged over low latitudes are depicted in Figure 6.15. Above ∼120 km zonal-mean temperatures are mainly determined by molecular heat conduction and diabatic heating and cooling, as the time constants of thermal conductivity (black lines) and diabatic heating and cooling (pink and blue lines) are shorter than all the others in Figure 6.15. Specifically, $\tau_{L_{NO}}$ shifts from longer (i.e., ∼30 days) to shorter (∼5 days) time scales as solar activity increases (Figure 6.15, blue lines), whereas $\tau_{Q_{Total}}$ remains relatively constant over all solar cycle conditions in the lower IT (Figure 6.15, pink lines). Between ∼130 and 150 km $\tau_{L_{NO}}$ is comparable to molecular heat conduction during solar maximum, whereas it is at least an order of magnitude longer during solar minimum. So, not only are the tides generating a larger abundance of NO during solar maximum than in solar minimum, the time constant for NO cooling is also considerably shorter meaning the increased NO IR cooling during solar maximum is also more efficiently cooling the lower IT. This offers additional support to the conclusions drawn in Chapter 5 regarding the solar cycle variability associated with tidally-induced zonal-mean temperature differences that occurs at low latitudes in Figures 5.11g, 5.4g, and 5.12g, in which a +18° K zonal-mean temperature increase during solar minimum is reduced by increased NO cooling (which is also a more efficient cooling mechanism) to +6 K at solar medium, and ultimately to −8 K at solar maximum.

It is important to note that the zonal-mean residual circulation induced by the tides is creating downwelling over low-latitudes in Figures 5.11g, 5.4g, and 5.12g, which could also play a role in increasing the NO in the TIE-GCM discussed herein. Similar to the tidally induced *net* transport of O discussed in Section 6.4, tidally induced *net* transport of NO is another plausible mechanism by which the tides could be acting to enhance the NO in the lower IT. These other tidally-induced NO processes warrant additional investigation.

6.7 Tidal-Induced Constituent Effects on N_mF_2 and Their Associated Variability

Figure 6.16 illustrates difference fields in the peak concentration of the F_2-layer, N_mF_2, [O], [O_2], and [N_2], at 330 km, for TIE-GCM simulations with and without CTMT lower boundary tidal

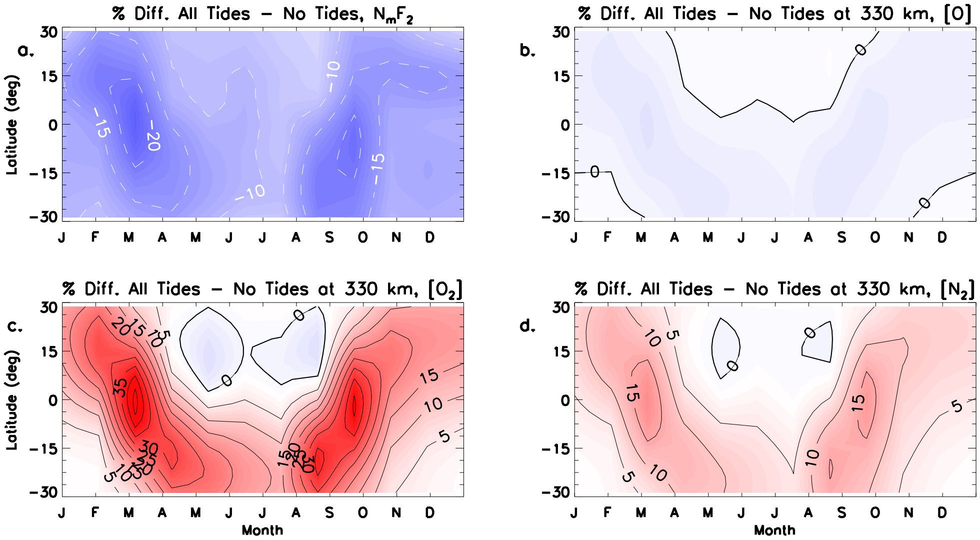

Figure 6.16: Percent difference fields between TIE-GCM simulations including and excluding CTMT lower boundary tidal forcing in N_mF_2 (a), [O] (b), [O_2] (c), and [N_2] (d) at 330 km as a function of month and latitude. Percent differences are contoured every ±5%.

forcing. The N_mF_2 experiences a 10 to 22% decrease due to vertically propagating tides at low latitudes throughout the year, with the exception of a smaller decrease (8–9%) in July (Figure 6.16a). This minimum in the N_mF_2 differences results from reduced O number densities at 330 km (Figure 6.16b). The biggest N_mF_2 differences occur during February, March, August, and September when [O] ([O_2] and [N_2]) differences experience their largest depletion (enhancement) (Figures 6.16b, 6.16c, and 6.16d). The mechanism by which these changes in the mean compositional structure occur due to vertically propagating tides is described in Section 6.4.

Figure 6.17 depicts difference fields in the N_mF_2, [O], [O_2], and [N_2], at 300 and 400 km, for TIE-GCM simulations with and without CTMT lower boundary tidal forcing under solar minimum (left column) and maximum (right column) conditions. Please note that altitude of the N_mF_2 changes with solar cycle due to variations in the neutral density. N_mF_2 decreases are more pronounced (suppressed) during solar minimum (maximum) with the largest decreases occurring of 30-35% (10-15%) on or around the equinoxes (Figures 6.17a 6.17b). The larger decreases in solar minimum versus those calculated for solar maximum result from more reduced O number densities at the F_2-layer peak altitude (Figures 6.17c and 6.17d). Once again, the biggest N_mF_2 decreases occur when $[O_2]$ and $[N_2]$ differences experience their largest enhancements, which are ~2 factor larger during solar minimum than in solar maximum (Figures 6.17e-h).

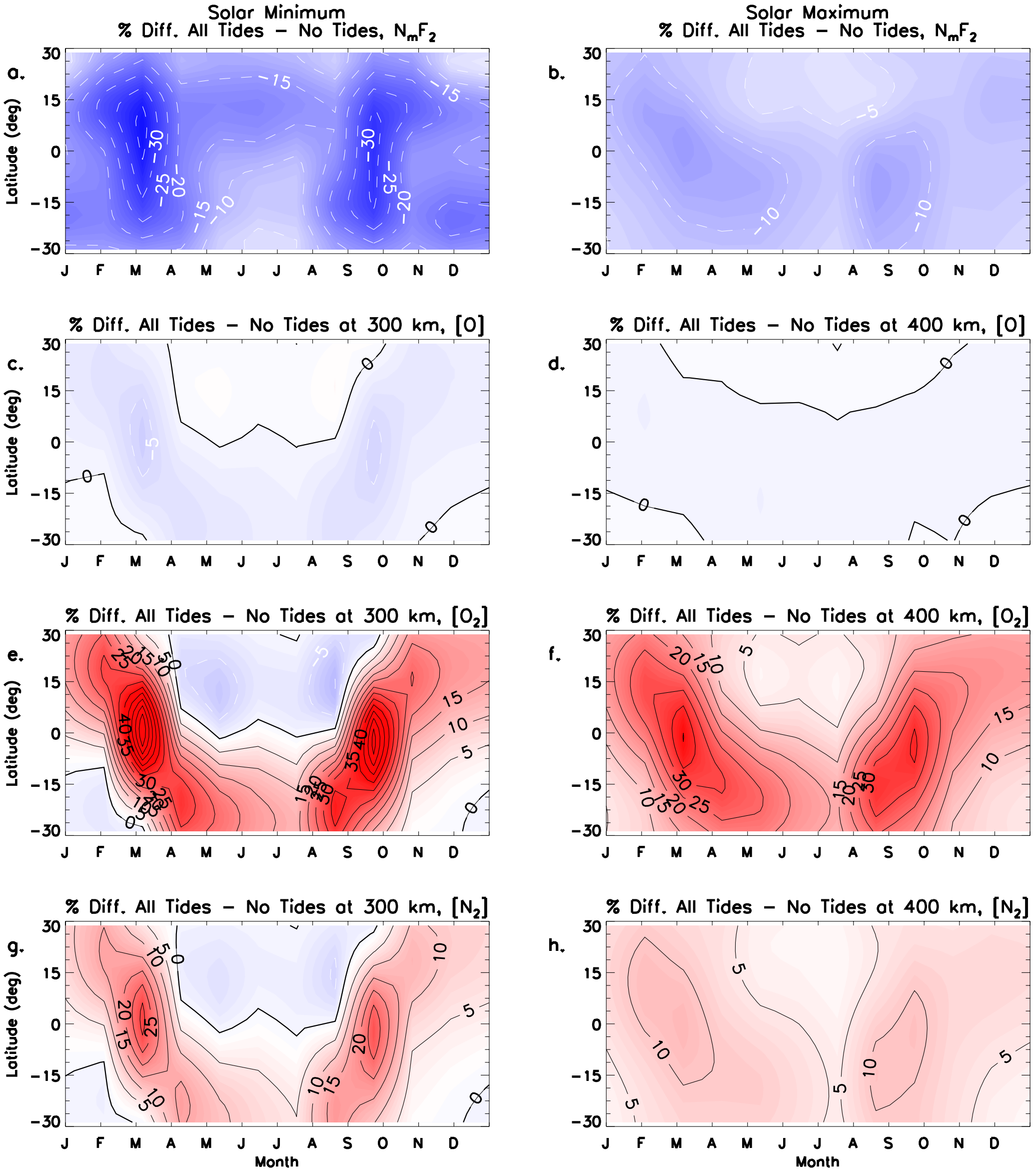

Figure 6.17: Same as Figure 6.16, except under solar minimum (Left Column) and maximum (Right Column) conditions. Neutral constituent density percent changes are calculated at 300 km (400 km) for the TIE-GCM simulations under solar minimum (maximum) conditions.

6.8 Summary of Important Results

The consequences of tidal dissipation on the zonal-mean compositional structure and the mechanisms by which these tides act to change the zonal-mean composition in the IT have only been the focus of a few prior research efforts. Hence, this chapter address science question (2c), which focuses on elucidating and quantifying the effects vertically-propagating tides have on the composition of the IT. By calculating difference fields in the individual constituent densities, as well as the flux divergences in the continuity equation between TIE-GCM simulations with and without CTMT tidal lower boundary we were able to evaluate the different ways by which the tides act to alter the zonal-mean composition of the IT system. The major results and conclusions are as follows:

1.) The dissipating tides drive clockwise (counterclockwise) flow at low- and mid-latitudes in the southern (northern) hemisphere extending from 110 to 250 km during September. This results in a convergence of the mass flow stream function centered over the equator, which implies a net increase in the major constituent densities at a given altitude, as higher density N_2 and O_2 are transported upward and equatorward at low- and mid-latitudes between 110 and 250 km.

2.) At low-latitudes, up to a 13% decrease (16% increase) in mean [O] ([O_2]) number density is produced in the presence of upward propagating tides. The percent change in [O] ([O_2]) extends well into the F-region ionosphere, where a maximum difference of -5% (40%) is achieved. The decrease in [O] and increase in [O_2] and [N_2] lead to a $\sim$25% decrease in mean [N_e] at F-region altitudes. Temperature differences produced by vertical propagating tides partially explain the increase in [N_2] and [O_2] number densities at equatorial latitudes. The migrating tides are responsible for driving the changes in the major constituent densities, although the results presented above differ from previous studies in that the effects of SW2 are playing a noticeable role. The changes in the major constituents are highly dependent upon solar cycle as percent changes in [O], [O_2], and [N_2] can vary by up to 10% (30%) in the lower (upper) thermosphere between solar maximum and solar minimum conditions during September, with the migrating tides having their largest effects during solar minimum.

3.) We have revealed through a series of TIME-GCM simulations a new mechanism by which the tides can act to change [O] throughout the thermosphere, i.e., a *net* meridional and vertical transport of [O] is induced by the tides themselves, in addition to the *advective* transport of [O] due to the mean circulation induced by the dissipation of the tides. The largest terms in the continuity equation are calculated for between 80 and 105 km. Due to its large meridional and vertical wind amplitudes, we conclude that DW1 is the primary tidal component responsible for driving constituent changes in the TIME-GCM during September. DW1 tends to be the dominant tidal component contributing to constituent changes in the MLT region around the equinoxes; however, during the solstices SW2 plays a greater role, comparable to that of DW1.

4.) The solar cycle variations in the major constituents, particularly in O and O_2 leads to changes the NO concentration in the lower thermosphere. Specifically, enhanced NO abundance driven by O and O_2 during solar maximum acts to more efficiently cool the lower IT. Solar cycle variations of up to 30° K exist in the TIE-GCM between solar minimum and maximum zonal-mean temperature differences, which ultimately result from this tidal modulation of NO cooling.

5.) A 10 to 22% decrease in the N_mF_2 persists at low-latitudes throughout the year, which arises from a decrease in the production (-4% in O) and an increase in the loss (40% in O_2 and 15% in N_2) at the F_2-layer peak for TIE-GCM simulations under solar medium conditions. Strong solar cycle variations also exist in the N_mF_2, as the reduction in electron density at the F_2-layer peak reaches values up to -35% around the equinoxes during solar minimum, as opposed to -15% during solar maximum. This distinctive solar cycle variation in N_mF_2 results from larger reductions (enhancements) in the [O] ([O_2] and [N_2]) in the F-region during solar minimum, whereas the opposite is true (i.e., smaller reductions (enhancements in the [O] ([O_2] and [N_2])) for solar maximum. The absolute magnitude of the solar cycle variations in N_mF_2 (up to 20%) calculated by the TIE-GCM needs to be validated against observations.

Chapter 7

Conclusions

7.1 Summary and Discussion

The IT system is subject to regular and repeatable forcing from the lower atmosphere in terms of vertically propagating tides. As these propagate upward from their source regions in the troposphere, stratosphere, and mesosphere, they interact non-linearly with the background atmosphere, plasma, and other waves. This dissertation constitutes a study to answer the main question **what role do non-linear tidal interactions play in determining the mean state, longitudinal, seasonal, and solar cycle variability of the IT system?** The NCAR TGCMs are used to examine this question. A series of numerical experiments using the TIME-GCM are conducted to evaluate how, and to what extent, the offset between the geographic and geomagnetic coordinate systems introduce complexities via ion-neutral coupling process that project onto diurnal and semidiurnal tides in the neutral atmosphere. Numerical experiments from the TIME-GCM are also conducted to examine the tidal-induced net transport effects on the O distribution in the thermosphere. A series of numerical experiments performed with the TIE-GCM and forced with observationally-based background and tidal lower boundary conditions, from WINDII-HRDI, SABER, and CTMT are used to evaluate the impacts that vertically-propagating tides have on the zonal-mean thermal, dynamical, and composition structure of the IT system. Additional insight into the physical mechanisms responsible for driving the tidally-induced zonal-mean wind, temperature, and composition changes in the IT is provided through a difference field analysis of the forcing terms in the zonal-mean momentum, thermodynamic energy, and continuity equations. Sections 3.6, 4.5, 5.4, and 6.8 summarize the important results of this study in detail. The broader contributions and implications of these dissertation results are discussed below in the context of previous work.

(1) ***Magnetic control of ion-neutral interactions in the IT system produce diurnal and semidiurnal non-migrating solar tides that reconcile existing data-model inconsistencies.*** Motivated by the discussion of potential in-situ non-migrating tidal sources offered by Oberheide et al. [87], Chapter 3 demonstrates that diurnal and semidiurnal non-migrating pseudo-tides are generated by the interaction between the zonally-symmetric wind circulation and a longitude-dependent ionosphere, resulting from the offset of the geographic and geomagnetic coordinate systems. These non-migrating pseudo-tides dominate over the tropospherically-generated non-migrating tides (i.e., DE3 and SE2) during solar maximum at upper IT altitudes. This result is consistent with the behavior of the non-migrating tidal amplitudes derived from CHAMP zonal wind measurements (Häusler and Lühr, [48] and Häusler et al., [49]). This in-situ generated non-migrating tidal source must be taken into account in order to reconcile differences in data-model comparisons between CHAMP tidal density diagnostics and the CTMT (see Oberheide et al., [87]).

(2) ***Vertically-propagating tides undergoing dissipation act to modify the pressure gradient force via eddy heat transport leading to appreciable zonal-mean zonal wind differences in the dynamo region.*** Many previous studies (e.g., Miyahara [75]; [76]; [78], Groves and Forbes [39], Miyahara and Wu [80], Miyahara et al. [79], and references therein) claim that the dissipating tides act to alter the zonal-mean circulation of the IT system through the momentum flux divergence terms in the zonal-mean momentum equations (see equations 2.12 and 2.13). The results presented herein demonstrate that zonal-mean wind differences due to the dissipating tides are driven by tidally-induced changes to the pressure gradient force via the eddy heat source term in the thermodynamic energy equation. Some of the aforementioned studies including Groves and Forbes [39] and Miyahara et al. [79], calculate the heat flux divergences due to the dissipating tides, but do

not report on their consequences in terms of potential zonal-mean wind changes. Lindzen and Blake [67] were the first to show that the vertical heat flux divergence driven by tidal dissipation was important to maintaining exospheric temperatures. However, the results presented in Chapter 4 show that it is not through direct heat deposition by the dissipating tides (i.e., the eddy heat source term), but rather through the pressure gradient term that the tidal heat deposition is driving zonal-mean zonal wind differences in the dynamo region.

(3) ***Zonal-mean temperature differences induced by the dissipating tides vary considerably as a function of solar cycle, resulting from the combination of net eddy heat transport and variations in NO cooling.*** To date, Forbes et al. [31] was the only report on the effects that the vertically-propagating tides have on the zonal-mean temperature structure of the IT. However, they did not diagnose the underlying physical mechanisms responsible for such changes. Following their work Chapter 5 demonstrates that zonal-mean temperature differences of up to 30° K between solar minimum and maximum result from tidally-induced changes in the major chemical constituents of IT. These changes in the major constituents lead to changes in the minor constituents, including NO. In this way, increased NO abundance with increasing solar activity leads to increased IR cooling, which Mlynczak et al. [81] refer to as the thermosphere's natural thermostat. SABER NO measurements reported in Oberheide et al. [88] suggest that other tidal effects including temperature changes and vertical advection act to alter NO emissions, with neutral density variations playing a lesser role. Since we report that mainly neutral density tidal variations are driving NO changes in the thermosphere, the relative importance of the different tidal mechanisms responsible for modulating the "natural thermostat" of the thermosphere requires further investigation.

(4) ***The net transport of O due to the tides themselves acts to substantially alter the [O] in the lower thermosphere.*** The effects of eddy mixing, vertical winds, and atmospheric tides on the O distribution in the mesosphere and thermosphere have been

studied since the 1960s (e.g., Colegrove et al., [7]; Shimazaki, [114], and references therein). Similar to the role of dissipating gravity waves in producing wave-induced *dynamical* transport of sodium (Gardner and Liu, [37]), we reveal that the net meridional and vertical transport of O induced by the tides appreciably contributes to [O] changes in the lower thermosphere. When combined with recombination effects, these transport mechanisms drive a net reduction in [O] of ~25% that is transmitted to higher altitudes by molecular diffusion. Understanding and quantifying the different mechanisms that act to determine the O distribution in the thermosphere is important because changes in the neutral constituents can have a significant effect on the plasma density of the F-region (Forbes et al. [31], Yamazaki and Richmond [127], Siskind et al., [115]).

(5) ***Tidal-induced net changes in the major constituents of the thermosphere result in measurable solar cycle variations in N_mF_2.*** Strong solar cycle variations in zonal mean [O], [O_2], and [N_2] due to dissipating tides result in noticeable solar cycle variations of up to 20% in electron density at the F_2-layer peak. The veracity of these solar cycle variations in N_mF_2 (i.e., of ~20%) calculated from TIE-GCM simulations should to be validated against observations. Nonetheless, tidally-driven density variations and their associated solar cycle dependencies should be considered in the orbital determination of near Earth orbiting satellites and space debris (e.g., Leonard et al., [63]). Furthermore, tidal modifications to the mean state (specifically the neutral constituents) may be sufficiently large to warrant consideration when seeking to ascertain the origins of long-term trends in the IT system (cf. Laštovička, [62]). Other than zonal-mean wind and dissipative effects (Oberheide et al., [85]), little is known about the long-term trends in tides entering the thermosphere, with the exception of the southern polar region (Baumgaertner et al., [3]). Clearly, this represents an area of future research since the results presented herein show that such trends can have a prominent impact on the IT system.

And finally, an overarching implication of this dissertation is the impact these results will have on the interpretation of existing and future tidal measurements and related non-linear processes from a range of ground-based (e.g., lidar and radar) and space-based (e.g., TIMED, COSMIC, ICON, and GOLD) platforms.

7.2 Recommendations for Future Study

This study illustrates the impact of vertically-propagating tides on the mean state and variability associated with the dynamical, thermal, and compositional structure of the IT. However, this work also highlights a number of areas where future research efforts are warranted (some of which are discussed above in Section 7.1). For example, there is a need for a more rigorous analysis focused on understanding how tides act to drive changes in the zonal-mean temperatures as a function of solar cycle at mid-latitudes. A number of issues concerning the tidal effects on the zonal-mean composition of the IT also remain. These include the solar-cycle dependence of tidally-induced net transport of O, as well as if the tidally-induced net transport mechanism described above is an important driver for other major (e.g., O_2) and minor (e.g., NO) constituent changes in the IT. Such investigations, which are aimed at understanding how the tides act to change the zonal-mean composition and thermal structure of the IT system, are additionally motivated by the increased need for more accurate space weather forecasts to better track space debris, as these zonal-mean compositional and temperature changes in the lower IT also affect higher altitudes via molecular diffusion. Understanding and quantifying the effects that non-linear tide-tide interactions have on the mean state and variability of the IT system are unprecedented and, would directly compliment the results presented herein. Motivated by Moudden and Forbes [83] who showed that migrating terdiurnal tidal amplitudes are comparable to the migrating diurnal and semidiurnal tides in the MLT; a study similar to what is reported herein might show that these tidal components are just as effective as the diurnal and semidiurnal tides in producing changes in the zonal-mean wind, temperatures, and composition. Finally, many of the tidal processes described herein may be relevant to Mars' thermosphere, since vertical propagation and dissipation of thermally-excited tides and their associated impacts have been shown to play an even more important role in determining the structure of Mars' atmosphere than they play at Earth (Wang et al., [124] and Moudden and Forbes, [82]).

Bibliography

[1] R. A. Akmaev and G. M. Shved. Modelling of the composition of the lower thermosphere taking account of the dynamics with applications to tidal variations of the [OI] 5577 åairglow. Journal of Atmospheric and Terrestrial Physics, 42(8):705 – 716, 1980.

[2] M. Allen, J. I. Lunine, and Y. L. Yung. The vertical distribution of ozone in the mesosphere and lower thermosphere. Journal of Geophysical Research: Atmospheres, 89(D3):4841–4872, 1984.

[3] A. J. G. Baumgaertner, A. J. McDonald, G. J. Fraser, and G. E. Plank. Long-term observations of mean winds and tides in the upper mesosphere and lower thermosphere above Scott Base, Antarctica. Journal of Atmospheric and Solar-Terrestrial Physics, 67(16):1480–1496, 2005.

[4] L. C. Chang, C. H. Lin, J. Y. Liu, N. Balan, J. Yue, and J. T. Lin. Seasonal and local time variation of ionospheric migrating tides in 2007-2011 FORMOSAT-3/COSMIC and TIE-GCM total electron content. Journal of Geophysical Research: Space Physics, 118(5):2545–2564, 2013.

[5] S. Chapman and R. S. Lindzen. Atmospheric Tides: Thermal and Gravitational. Gordon and Breach, New York, 1970.

[6] B. K. Ching and Y. T. Chiu. A phenomenological model of global ionospheric electron density in the E-, F1- and F2-regions. Journal of Atmospheric and Terrestrial Physics, 35(9):1615–1630, 1973.

[7] F. D. Colegrove, F. S. Johnson, and W. B. Hanson. Atmospheric composition in the lower thermosphere. Journal of Geophysical Research, 71(9):2227–2236, 1966.

[8] K. H. Cook. Hadley circulation dynamics. In H. F. Diaz and R. S. Bradley, editors, The Hadley Circulation: Present, Past and Future, volume 21 of Advances in Global Change Research, pages 61–83. Springer Netherlands, 2004.

[9] National Research Council. Solar and Space Physics: A Science for a Technological Society. The National Academies Press, Washington, D.C., 2013.

[10] R. E. Dickinson, E. C. Ridley, and R. G. Roble. Meridional circulation in the thermosphere i. equinox conditions. Journal of Atmospheric Sciences, 32:1737–1754, 1975.

[11] R. E. Dickinson, E. C. Ridley, and R. G. Roble. Meridional circulation in the thermosphere ii. solstice conditions. Journal of Atmospheric Sciences, 34:178–192, 1977.

[12] R. E. Dickinson, E. C. Ridley, and R. G. Roble. Thermospheric general circulation with coupled dynamics and composition. Journal of the Atmospheric Sciences, 41(2):205–219, 1984.

[13] R. E. Dickinson and R. G. Roble. Thermospheric motion and temperature perturbations from global-scale winds flowing through F-region ionization anomalies. Space Research, 12:1079–1085, 1972.

[14] R.E. Dickinson, E. C. Ridley, and R. G. Roble. A three-dimensional general circulation model of the thermosphere. Journal of Geophysical Research: Space Physics, 86(A3):1499–1512, 1981.

[15] D. P. Drob, et. al. An empirical model of the earth's horizontal wind fields: HWM07. Journal of Geophysical Research: Space Physics, 113(A12), 2008.

[16] E. M. P. Ekanayake, T. Aso, and S. Miyahara. Background wind effects on propagation of nonmigrating diurnal tides in the middle atmosphere. Journal of Atmospheric and Solar Terrestrial Physics, 59(4):401–429, January 1997.

[17] S. L. England, T. J. Immel, J. D. Huba, M. E. Hagan, A. Maute, and R. DeMajistre. Modeling of multiple effects of atmospheric tides on the ionosphere: An examination of possible coupling mechanisms responsible for the longitudinal structure of the equatorial ionosphere. Journal of Geophysical Research: Space Physics, 115(A5), 2010.

[18] S. L. England, T. J. Immel, E. Sagawa, S. B. Henderson, M. E. Hagan, S. B. Mende, H. U. Frey, C. M. Swenson, and L. J. Paxton. Effect of atmospheric tides on the morphology of the quiet time, postsunset equatorial ionospheric anomaly. Journal of Geophysical Research: Space Physics, 111(A10), 2006.

[19] S. L. England, X. Zhang, T. J. Immel, J. M. Forbes, and R. DeMajistre. The effect of non-migrating tides on the morphology of the equatorial ionospheric anomaly: seasonal variability. Earth, Planets and Space, 61(4):493–503, 2009.

[20] D. S. Evans. Global statistical patterns of auroral phenomena. In Y. Kamide and R. A. Wolf, editors, Proceedings of the Symposium on Quantitative Modeling of Magnetospheric-Ionospheric Coupling Processes, pages 325–330, Kyoto, Japan, 1987. Kyoto Sangyo University.

[21] T.W. Fang, A.D. Richmond, J.Y. Liu, A. Maute, C.H. Lin, C.H. Chen, and B. Harper. Model simulation of the equatorial electrojet in the Peruvian and Philippine sectors. Journal of Atmospheric and Solar-Terrestrial Physics, 70(17):2203 – 2211, 2008.

[22] J. M. Forbes. Tidal variations in thermospheric O, O_2, N_2, Ar, He, and H. Journal of Geophysical Research: Space Physics, 83(A8):3691–3698, 1978.

[23] J. M. Forbes. Atmospheric tide: 2. The solar and lunar semidiurnal components. Journal of Geophysical Research: Space Physics, 87(A7):5241–5252, 1982.

[24] J. M. Forbes. Atmospheric tides 1. Model description and results for the solar diurnal component. Journal of Geophysical Research: Space Physics, 87(A7):5222–5240, 1982.

[25] J. M. Forbes. Tidal and planetary waves. In R. M. Johnson and T. L. Killeen, editors, The Upper Mesosphere and Lower Thermosphere: A Review of Experiment and Theory, volume 87 of Geophysical Monograph Series, pages 67–87. AGU, 1995.

[26] J. M. Forbes. Wave Coupling in Terrestrial Planetary Atmospheres, pages 171–190. American Geophysical Union, Washington, D. C., 2002.

[27] J. M. Forbes, S. L. Bruinsma, X. Zhang, and J. Oberheide. Surface-exosphere coupling due to thermal tides. Geophysical Research Letters, 36(15), 2009.

[28] J. M. Forbes and H. B. Garrett. Theoretical studies of atmospheric tides. Reviews of Geophysics and Space Physics, 17(8):1951–1981, November 1979.

[29] J. M. Forbes and M. E. Hagan. Thermospheric extensions of the classical expansion functions for semidiurnal tides. Journal of Geophysical Research: Space Physics, 87(A7):5253–5259, 1982.

[30] J. M. Forbes and M. E. Hagan. Diurnal propagating tide in the presence of mean winds and dissipation: A numerical investigation. Planetary and Space Science, 36(6):579–590, February 1988.

[31] J. M. Forbes, R. G. Roble, and C. G. Fesen. Acceleration, heating, and compositional mixing of the thermosphere due to upward propagating tides. Journal of Geophysical Research: Space Physics, 98(A1):311–321, 1993.

[32] J. M. Forbes, J. Russell, S. Miyahara, X. Zhang, M. Mlynczak, C. J. Mertens, and M. E. Hagan. Troposphere-thermosphere tidal coupling as measured by the SABER instrument on TIMED during july-september 2002. Journal of Geophysical Research: Space Physics, 111(A10), 2006.

[33] J. M. Forbes and R. A. Vincent. Effects of mean winds and dissipation on the diurnal propagating tide: An analytic approach. Planetary and Space Science, 37(2):197–209, September 1989.

[34] J. M. Forbes, X. X. Zhang, W. Ward, and E. R. Talaat. Climatological features of mesosphere and lower thermosphere stationary planetary waves within 40° latitude. Journal of Geophysical Research: Atmospheres, 107(D17):ACL 1–1–ACL 1–14, 2002. 4322.

[35] J. M. Forbes, X. Zhang, and S. L. Bruinsma. Middle and upper thermosphere density structures due to nonmigrating tides. Journal of Geophysical Research: Space Physics, 117(A11), 2012.

[36] J. M. Forbes, X. Zhang, S. Palo, J. Russell, C. J. Mertens, and M. Mlynczak. Tidal variability in the ionospheric dynamo region. Journal of Geophysical Research: Space Physics, 113(A2), 2008.

[37] C. S. Gardner and A. Z. Liu. Wave-induced transport of atmospheric constituents and its effect on the mesospheric Na layer. Journal of Geophysical Research: Atmospheres, 115(D20), 2010. D20302.

[38] G.V. Groves and J. M. Forbes. Equinox tidal heating of the upper atmosphere. Planetary and Space Science, 32(4):447–456, 1984.

[39] G.V. Groves and J. M. Forbes. Mean zonal and meridional accelerations and mean heating induced by solar tides for equinox and solstice conditions. Planetary and Space Science, 33(3):283–293, 1985.

[40] M. E. Hagan. Comparative effects of migrating solar sources on tidal signatures in the middle and upper atmosphere. Journal of Geophysical Research: Atmospheres, 101(D16):21213–21222, 1996.

[41] M. E. Hagan, M. D. Burrage, J. M. Forbes, J. Hackney, W. J. Randel, and X. Zhang. GSWM-98: Results for migrating solar tides. Journal of Geophysical Research: Space Physics, 104(A4):6813–6827, 1999.

[42] M. E. Hagan and J. M. Forbes. Migrating and nonmigrating diurnal tides in the middle and upper atmosphere excited by tropospheric latent heat release. Journal of Geophysical Research: Atmospheres, 107(D24), 2002.

[43] M. E. Hagan and J. M. Forbes. Migrating and nonmigrating semidiurnal tides in the upper atmosphere excited by tropospheric latent heat release. Journal of Geophysical Research: Space Physics, 108(A2), 2003.

[44] M. E. Hagan, J. M. Forbes, and F. Vial. On modeling migrating solar tides. Geophysical Research Letters, 22(8):893–896, 1995.

[45] M. E. Hagan, A. Maute, and R. G. Roble. Tropospheric tidal effects on the middle and upper atmosphere. Journal of Geophysical Research: Space Physics, 114(A1), 2009.

[46] M. E. Hagan, A. Maute, R. G. Roble, A. D. Richmond, T. J. Immel, and S. L. England. Connections between deep tropical clouds and the Earth's ionosphere. Geophysical Research Letters, 34(20), 2007.

[47] HAO. TIEGCM V1.94 Model Description. National Center for Atmospheric Research, Boulder, CO, 2011.

[48] K. Häusler and H. Lühr. Nonmigrating tidal signals in the upper thermospheric zonal wind at equatorial latitudes as observed by CHAMP. Annales Geophysicae, 27:2643–2652, 2009.

[49] K. Häusler, H. Lühr, M. E. Hagan, A. Maute, and R. G. Roble. Comparison of CHAMP and TIME-GCM nonmigrating tidal signals in the thermospheric zonal wind. Journal of Geophysical Research: Atmospheres, 115(D1), 2010.

[50] P. B. Hays, V. J. Abreu, M. E. Dobbs, D. A. Gell, H. J. Grassl, and W. R. Skinner. The high-resolution doppler imager on the Upper Atmosphere Research Satellite. Journal of Geophysical Research: Atmospheres, 98(D6):10713–10723, 1993.

[51] A. E. Hedin, H. G. Mayr, C. A. Reber, N. W. Spencer, and G. R. Carignan. Empirical model of global thermospheric temperature and composition based on data from the OGO-6 quadrupole mass spectrometer. Journal of Geophysical Research, 79(1):215–225, 1974.

[52] C. O. Hines. Dynamical heating of the upper atmosphere. Journal of Geophysical Research, 70(1):177–183, 1965.

[53] J. R. Holton. The dynamic meteorology of the stratosphere and mesosphere. In Meteorological Monographs, volume 15, chapter 2, pages 27–38. American Meteorological Society, Boston, MA, August 1975.

[54] M. Angelats i Coll and J. M. Forbes. Nonlinear interactions in the upper atmosphere: The s = 1 and s = 3 nonmigrating semidiurnal tides. Journal of Geophysical Research: Space Physics, 107(A8):1–18, 2002.

[55] J. M. Russell III, M. G. Mlynczak, L. L. Gordley, Jr. J. J. Tansock, and R. W. Esplin. Overview of the SABER experiment and preliminary calibration results. volume 3756, pages 277–288, 1999.

[56] T. J. Immel, E. Sagawa, S. L. England, S. B. Henderson, M. E. Hagan, S. B. Mende, H. U. Frey, C. M. Swenson, and L. J. Paxton. Control of equatorial ionospheric morphology by atmospheric tides. Geophysical Research Letters, 33(15), 2006.

[57] L. G. Jacchia. Static diffusion models of the upper atmosphere with empirical temperature profiles. Smithsonian Contributions to Astrophysics, 8(9):215–257, 1965.

[58] M. Jones Jr., J. M. Forbes, and M. E. Hagan. Tidal-induced net transport effects on the oxygen distribution in the thermosphere. Geophysical Research Letters, 41(14):5272–5279, 2014.

[59] M. Jones Jr., J. M. Forbes, M. E. Hagan, and A. Maute. Non-migrating tides in the ionosphere-thermosphere: In situ versus tropospheric sources. Journal of Geophysical Research: Space Physics, 118(5):2438–2451, 2013.

[60] M. Jones Jr., J. M. Forbes, M. E. Hagan, and A. Maute. Impacts of vertically propagating tides on the mean state of the ionosphere-thermosphere system. Journal of Geophysical Research: Space Physics, 119(3):2197–2213, 2014.

[61] G. Kockarts. Nitric oxide cooling in the terrestrial thermosphere. Geophysical Research Letters, 7(2):137–140, 1980.

[62] J. Laštovička. Trends in the upper atmosphere and ionosphere: Recent progress. Journal of Geophysical Research: Space Physics, 118(6):3924–3935, 2013.

[63] J. M. Leonard, J. M. Forbes, and H. G. Born. Impact of tidal density variability on orbital and reentry predictions. Space Weather, 10(12), 2012. S12003.

[64] C. H. Lin, W. Wang, M. E. Hagan, C. C. Hsiao, T. J. Immel, M. L. Hsu, J. Y. Liu, L. J. Paxton, T. W. Fang, and C. H. Liu. Plausible effect of atmospheric tides on the equatorial ionosphere observed by the FORMOSAT-3/COSMIC: Three-dimensional electron density structures. Geophysical Research Letters, 34(11), 2007.

[65] R. S. Lindzen. Thermally driven diurnal tide in the atmosphere. Quarterly Journal of the Royal Meteorological Society, 93(395):18–42, 1967.

[66] R. S. Lindzen. Turbulence and stress owing to gravity wave and tidal breakdown. Journal of Geophysical Research: Oceans, 86(C10):9707–9714, 1981.

[67] R. S. Lindzen and D. Blake. Mean heating of the thermosphere by tides. Journal of Geophysical Research, 75(33):6868–6871, 1970.

[68] R. S. Lindzen and S. S. Hong. Effects of mean winds and horizontal temperature gradients on solar and lunar semidiurnal tides in the atmosphere. Journal of the Atmospheric Sciences, 31(5):1421–1446, 1974.

[69] R. S. Lindzen, S. S. Hong, and J. M. Forbes. Semidiurnal hough mode extensions in the thermosphere and their application. NRL Memorandum Report 3442, Naval Research Laboratory, Washington, D.C., 1977.

[70] A. Z. Liu and C. S. Gardner. Vertical dynamical transport of mesospheric constituents by dissipating gravity waves. Journal of Atmospheric and Solar-Terrestrial Physics, 66(3-4):267–275, 2004.

[71] H. L. Liu, T. Li, C. Y. She, J. Oberheide, Q. Wu, M. E. Hagan, J. Xu, R. G. Roble, M.G. Mlynczak, and J. M. Russell. Comparative study of short-term diurnal tidal variability. Journal of Geophysical Research: Atmospheres, 112(D18), 2007. D18108.

[72] X. Liu. The Effects of Composition on Thermosphere Mass Density Response to Geomagnetic Activity. PhD thesis, University of Colorado at Boulder, 2013.

[73] H. Lühr, M. Rother, K. Häusler, P. Alken, and S. Maus. The influence of nonmigrating tides on the longitudinal variation of the equatorial electrojet. Journal of Geophysical Research: Space Physics, 113(A8), 2008.

[74] C. McLandress. The seasonal variation of the propagating diurnal tide in the mesosphere and lower thermosphere. Part I: The role of gravity waves and planetary waves. Journal of the Atmospheric Sciences, 59(5):893–906, 2002a.

[75] S. Miyahara. Zonal mean winds induced by vertically propagating atmospheric tidal waves in the lower thermosphere. Journal of the Meteorological Society of Japan, 56(2):86–97, 1978a.

[76] S. Miyahara. Zonal mean winds induced by vertically propagating atmospheric tidal waves in the lower thermosphere, Part II. Journal of the Meteorological Society of Japan, 56(6):548–558, 1978b.

[77] S. Miyahara. Solar diurnal tides and the induced zonal mean flows. Journal of the Meteorological Society of Japan, 58(4):302–306, 1980.

[78] S. Miyahara. Zonal mean winds induced by solar diurnal tides in the lower thermosphere. Journal of the Meteorological Society of Japan, 59(3):303–319, 1981.

[79] S. Miyahara, Yu. I. Portnyagin, J. M. Forbes, and T. V. Solovjeva. Mean zonal acceleration and heating of the 70- to 100-km region. Journal of Geophysical Research: Space Physics, 96(A1):1225–1238, 1991.

[80] S. Miyahara and D. H. Wu. Effects of solar tides on the zonal mean circulation in the lower thermosphere: Solstice conditions. Journal of Atmospheric and Terrestrial Physics, 51(7/8):635–648, 1989.

[81] M. Mlynczak, J. Martin-Torres, J. Russell, K. Beaumont, S. Jacobson, J. Kozyra, M. Lopez-Puertas, B. Funke, C. Mertens, L. Gordley, R. Picard, J. Winick, P. Wintersteiner, and L. Paxton. The natural thermostat of nitric oxide emission at 5.3 μm in the thermosphere observed during the solar storms of April 2002. Geophysical Research Letters, 30(21), 2003. 2100.

[82] Y. Moudden and J. M. Forbes. Effects of vertically propagating thermal tides on the mean structure and dynamics of Mars' lower thermosphere. Geophysical Research Letters, 35(23), 2008. L23805.

[83] Y. Moudden and J. M. Forbes. A decade-long climatology of terdiurnal tides using TIMED/SABER observations. Journal of Geophysical Research: Space Physics, 118(7):4534–4550, 2013.

[84] J. Oberheide and J. M. Forbes. Thermospheric nitric oxide variability induced by nonmigrating tides. Geophysical Research Letters, 35(16), 2008. L16814.

[85] J. Oberheide, J. M. Forbes, K. Häusler, Q. Wu, and S. L. Bruinsma. Tropospheric tides from 80 to 400 km: Propagation, interannual variability, and solar cycle effects. Journal of Geophysical Research: Atmospheres, 114(D1), 2009.

[86] J. Oberheide, J. M. Forbes, X. Zhang, and S. L. Bruinsma. Wave-driven variability in the ionosphere-thermosphere-mesosphere system from TIMED observations: What contributes to the "wave 4? Journal of Geophysical Research: Space Physics, 116(A1), 2011a. A01306.

[87] J. Oberheide, J. M. Forbes, X. Zhang, and S. L. Bruinsma. Climatology of upward propagating diurnal and semidiurnal tides in the thermosphere. Journal of Geophysical Research: Space Physics, 116(A11), 2011b.

[88] J. Oberheide, M. G. Mlynczak, C. N. Mosso, B. M. Schroeder, B. Funke, and A. Maute. Impact of tropospheric tides on the nitric oxide 5.3 μm infrared cooling of the low-latitude thermosphere during solar minimum conditions. Journal of Geophysical Research: Space Physics, 118(11):7283–7293, 2013.

[89] J. Oberheide, Q. Wu, T. L. Killeen, M. E. Hagan, and R. G. Roble. Diurnal nonmigrating tides from TIMED Doppler Interferometer wind data: Monthly climatologies and seasonal variations. Journal of Geophysical Research: Space Physics, 111(A10), 2006.

[90] S. E. Palo. Analysis of the equatorial semiannual oscillation and quasi two-day wave in the mesosphere lower thermosphere using a spectral model and data collected with the christmas island radar systems. PhD thesis, University of Colorado at Boulder, 1994.

[91] D. Pancheva, P. Mukhtarov, and A. K. Smith. Nonmigrating tidal variability in the SABER/TIMED mesospheric ozone. Geophysical Research Letters, 41(11):4059–4067, 2014. 2014GL059844.

[92] N. M. Pedatella, J. M. Forbes, M. E. Hagan, A. D. Richmond, T. W. Fang, K. M. Larson, and G. Millward. Longitudinal variations in the F region ionosphere and the topside ionosphere-plasmasphere: Observations and model simulations. Journal of Geophysical Research: Space Physics, 116(A12), 2011.

[93] N. M. Pedatella, J. M. Forbes, and J. Oberheide. Intra-annual variability of the low-latitude ionosphere due to nonmigrating tides. *Geophysical Research Letters*, 35(18), 2008.

[94] N. M. Pedatella, M.E. Hagan, and A. Maute. The comparative importance of DE3, SE2, and SPW4 on the generation of wavenumber-4 longitude structures in the low-latitude ionosphere during september equinox. *Geophysical Research Letters*, 39(19), 2012.

[95] J. M. Picone, A. E. Hedin, D. P. Drob, and A. C. Aikin. NRLMSISE-00 empirical model of the atmosphere: Statistical comparisons and scientific issues. *Journal of Geophysical Research: Space Physics*, 107(A12):SIA 15–1–SIA 15–16, 2002.

[96] Yu. I. Portnyagin, J. M. Forbes, T. V. Solovjeva, S. Miyahara, and C. DeLuca. Momentum and heat sources of the mesosphere and lower thermosphere regions 70–110 km. *Journal of Atmospheric and Terrestrial Physics*, 57(9):967–977, 1995.

[97] L. Qian, R. G. Roble, S. C. Solomon, and T. J. Kane. Calculated and observed climate change in the thermosphere, and a prediction for solar cycle 24. *Geophysical Research Letters*, 33(23), 2006. L23705.

[98] L. Qian, et. al. *The NCAR TIE-GCM: A Community Model of the Coupled Thermosphere/Ionosphere System*, pages 73–83. John Wiley & Sons, Ltd, 2013.

[99] A. D. Richmond. *Geomagnetic crochets and ionospheric tidal winds*. PhD thesis, University of California, Los Angeles, 1970.

[100] A. D. Richmond. Tidal winds at ionospheric heights. *Radio Science*, 6(2):175–189, 1971.

[101] A. D. Richmond and A. Maute. *Ionospheric Electrodynamics Modeling*, pages 57–71. John Wiley & Sons, Ltd, 2013.

[102] A. D. Richmond, E. C. Ridley, and R. G. Roble. A thermosphere/ionosphere general circulation model with coupled electrodynamics. *Geophysical Research Letters*, 19(6):601–604, 1992.

[103] R. G. Roble. Energetics of the mesosphere and thermosphere. In R.M. Johnson and T. L. Killeen, editors, *The Upper Mesosphere and Lower Thermosphere: A Review of Experiment and Theory*, Geophysical Monograph Series, pages 1–21. American Geophysical Union, Washington, D.C., 1995.

[104] R. G. Roble. The NCAR thermosphere-ionosphere-mesosphere-electrodynamics general circulation model. In R. W. Schunk, editor, *STEP Handbook on Ionospheric Models*, pages 207–216. Utah State Univ., Logan, 1996.

[105] R. G. Roble and R. E. Dickinson. The effect of displaced geomagnetic and geographic poles on the thermospheric neutral winds. *Planetary Space Science*, 22:623–631, 1974.

[106] R. G. Roble, E.C. Ridley, A. D. Richmond, and R. E. Dickinson. A coupled thermosphere/ionosphere general circulation model. *Geophysical Research Letters*, 15(12):1325–1328, 1988.

[107] R. G. Roble and G. G. Shepherd. An analysis of wind imaging interferometer observations of o(^1s) equatorial emission rates using the thermosphere-ionosphere-mesosphere-electrodynamics general circulation model. Journal of Geophysical Research: Space Physics, 102(A2):2467–2474, 1997.

[108] R.G. Roble and E.C. Ridley. A thermosphere-ionosphere-mesosphere-electrodynamics general circulation model (time-GCM): Equinox solar cycle minimum simulations (30-500 km). Geophysical Research Letters, 21(6):417–420, 1994.

[109] E. Sagawa, T. J. Immel, H. U. Frey, and S. B. Mende. Longitudinal structure of the equatorial anomaly in the nighttime ionosphere observed by IMAGE/FUV. Journal of Geophysical Research: Space Physics, 110(A11), 2005.

[110] R. D. Sharma, H. Dothe, and J. W. Duff. Model of the 5.3 μm radiance from no during the sunlit terrestrial thermosphere. Journal of Geophysical Research: Space Physics, 103(A7):14753–14768, 1998.

[111] G. G. Shepherd. Thermospheric observations of equatorial wavenumber 4 density perturbations from WINDII data. Geophysical Research Letters, 38(8), 2011. L08801.

[112] G. G. Shepherd and Y. M. Cho. Global thermospheric atomic oxygen variations observed with the WIND Imaging Interferometer (WINDII): Wave 4 at low and high latitudes. Journal of Geophysical Research: Space Physics, 116(A10), 2011. A10314.

[113] G. G. Shepherd, et. al. WINDII, the wind imaging interferometer on the Upper Atmosphere Research Satellite. Journal of Geophysical Research: Atmospheres, 98(D6):10725–10750, 1993.

[114] T. Shimazaki. Dynamic effects on height distributions of neutral constituents in the Earth's upper atmosphere: a calculation of atmospheric model between 70 km and 500 km. Journal of Atmospheric and Terrestrial Physics, 30:1279–1292, 1968.

[115] D. E. Siskind, D. P. Drob, K. F. Dymond, and J. P. McCormack. Simulations of the effects of vertical transport on the thermosphere and ionosphere using two coupled models. Journal of Geophysical Research: Space Physics, 119(2):1172–1185, 2014.

[116] D. E. Siskind, D. P. Drob, J. T. Emmert, M. H. Stevens, P. E. Sheese, E. J. Llewellyn, M. E. Hervig, R. Niciejewski, and A. J. Kochenash. Linkages between the cold summer mesopause and thermospheric zonal mean circulation. Geophysical Research Letters, 39(1), 2012.

[117] A. K. Smith, D. R. Marsh, M. G. Mlynczak, and J. C. Mast. Temporal variations of atomic oxygen in the upper mesosphere from SABER. Journal of Geophysical Research: Atmospheres, 115(D18), 2010. D18309.

[118] A. A. Svoboda, J. M. Forbes, and S. Miyahara. A space-based climatology of diurnal MLT tidal winds, temperatures and densities from UARS wind measurements. Journal of Atmospheric and Solar-Terrestrial Physics, 67(16):1533–1543, 2005.

[119] H. Teitelbaum and F. Vial. Momentum transfer to the thermosphere by atmospheric tides. Journal of Geophysical Research: Oceans, 86(C10):9693–9697, 1981.

[120] H. Teitelbaum and F. Vial. On tidal variability induced by nonlinear interaction with planetary waves. Journal of Geophysical Research, 98(A8):14169–14178, 1991.

[121] F. Vial. Numerical simulations of atmospheric tides for solstice conditions. Journal of Geophysical Research: Space Physics, 91(A8):8955–8969, 1986.

[122] F. Vial, J. M. Forbes, and S. Miyahara. Some transient aspects of tidal propagation. Journal of Geophysical Research: Space Physics, 96(A2):1215–1224, 1991.

[123] R. L. Walterscheid, G. G. Sivjee, G. Schubert, and R. M. Hamwey. Large-amplitude semidiurnal temperature variations in the polar mesopause: evidence of a pseudotide. Nature, 324(6095):347–349, 1986.

[124] L. Wang, D. C. Fritts, and R. H. Tolson. Nonmigrating tides inferred from the Mars Odyssey and Mars Global Surveyor aerobraking data. Geophysical Research Letters, 33(23), 2006. L23201.

[125] Wenbin Wang. A Thermosphere-Ionosphere Nested Grid (TING) Model. PhD thesis, University of Michigan, 1998.

[126] Q. Wu, D.A. Ortland, B. Foster, and R.G. Roble. Simulation of nonmigrating tide influences on the thermosphere and ionosphere with a TIMED data driven TIEGCM. Journal of Atmospheric and Solar-Terrestrial Physics, 90-91(0):61 – 67, 2012. Recent Progress in the Vertical Coupling in the Atmosphere-Ionosphere System.

[127] Y. Yamazaki and A. D. Richmond. A theory of ionospheric response to upward-propagating tides: Electrodynamic effects and tidal mixing effects. Journal of Geophysical Research: Space Physics, 118(9):5891–5905, 2013.

[128] X. Zhang, J. M. Forbes, and M. E. Hagan. Longitudinal variation of tides in the mlt region: 1. Tides driven by tropospheric net radiative heating. Journal of Geophysical Research: Space Physics, 115(A6), 2010a.

[129] X. Zhang, J. M. Forbes, and M. E. Hagan. Longitudinal variation of tides in the mlt region: 2. Relative effects of solar radiative and latent heating. Journal of Geophysical Research: Space Physics, 115(A6), 2010b.

[130] X. Zhang, J. M. Forbes, M. E. Hagan, J. M. Russell, S. E. Palo, C. J. Mertens, and M. G. Mlynczak. Monthly tidal temperatures 20-120 km from TIMED/SABER. Journal of Geophysical Research: Space Physics, 111(A10), 2006.

Appendix A

Glossary of Atmospheric Variables and Symbols

All the frequently used variables in this dissertation are defined below. Please note variables that are only used or referenced a couple times are defined in the text where they are used.

u - Zonal wind velocity;

v - Meridional wind velocity;

w - Vertical wind velocity;

$\mathbf{V}$ - Vector wind $(u\hat{\imath},\ v\hat{\jmath},\ w\hat{k})$;

$\mathbf{V_h}$ - Vector wind $(u\hat{\imath},\ v\hat{\jmath})$;

T - Temperature;

ρ - Density;

ρ_0 - Basic state density;

p - Pressure;

$\mathbf{p}$ - Vector pressure $(p_x\hat{\imath},\ p_y\hat{\jmath},\ p_z\hat{k})$;

$\mathbf{g}$ - Vector gravity $(0\hat{\imath},\ 0\hat{\jmath},\ g\hat{k})$;

$\mathbf{OF_{V_h}}$ - Other forces in the horizontal momentum equations;

$\mathbf{OF_T}$ - Other forces in the thermodynamic energy equation;

Φ - Geopotential;

$\Phi_z = \frac{\partial \Phi}{\partial z}$ - Vertical derivative of the geopotential;

H - Atmospheric scale height;

J - Diabatic heating rate;

R - Gas Constant for Dry Air;

f - Coriolis frequency/parameter;

c_p - Specific heat at constant pressure;

κ - $\frac{R}{c_p}$;

Z_g - Geopotential Height;

$[N_i]$ - Individual constituent number density;

ζ_i - Individual constituent mass mixing ratio;

m_i - Individual constituent molecular mass;

Ψ - Mass flow stream function;

τ - Time constant variable referenced to a number of difference processes;

λ_{xx}, λ_{xy}, λ_{yx}, λ_{yy}, ϵ_1, ϵ_2 - Components of the ion drag tensor;

u_i - Zonal plasma drift velocity;

v_i - Meridional plasma drift velocity;

$\mathbf{V_i}$ - Plasma drift velocity vector $(u_i\hat{i},\ v_i\hat{j},\ w_i\hat{k})$;

$\mu \equiv (\mu_0 + \rho_0 \nu_{eddy})$ - Dynamic viscosity including both eddy and molecular diffusion;

K_T - Thermal conductivity;

K_E - Eddy diffusion coefficient;

$\overline{S} = (\frac{\partial \overline{T}}{\partial z} + \frac{\kappa \overline{T}}{H})$ - Static stability;

$\overline{F}_x$, $\overline{F}_y$ - Eddy momentum source terms;

$\overline{G}$ - Eddy heat source term;

$\mathbf{J}$ - Current density;

$\mathbf{B}$ - Magnetic field;

B - Magnetic field strength;

$\hat{b}$ - unit vector along $\mathbf{B}$;

δ - Magnetic declination angle;

I - Magnetic inclination or dip angle;

$\mathbf{E}$ - Electric field;

$\mathbf{E}_{\parallel}$ - Electric field parallel to the $\mathbf{B}$;

$\mathbf{E}_{\perp}$ - Electric field perpendicular to the $\mathbf{B}$;

σ_0 - Direct conductivity, parallel to $\mathbf{B}$;

σ_1, σ_P - Pedersen conductivity, parallel to $\mathbf{E}$ and perpendicular to $\mathbf{B}$;

σ_2, σ_H - Hall conductivity, perpendicular to both $\mathbf{E}$ and $\mathbf{B}$;

N - Neutral number density;

N_i - Ion number density;

ν_{in} - Ion-neutral collision frequency;

ω_i - Ion gyrofrequency;

a - Radius of the Earth;

λ - Longitude;

$\theta =$ Latitude;

$\theta_{co} = (90^\circ - \theta) =$ Colatitude;

$z = H \ln \frac{p_0}{p}$ - Height in log-pressure coordinates;

t - Time;

t_{LT} - Local time;

Ω - Rotation rate of the Earth;

a - Radius of the Earth;

n - Meridional index;

s - Zonal wavenumber;

m - Integer subharmonic of a solar day.

Primed (Barred) quantities represent the perturbation (zonal and diurnal mean) of atmospheric variables (e.g., u', $\overline{u}$, T', $\overline{T}$). Complex amplitudes are denoted by hat terms (e.g., $\hat{u}$, $\hat{v}$, $\hat{\Phi}$).

Appendix B

Supplemental Figures: Non-migrating Tides in the IT Study

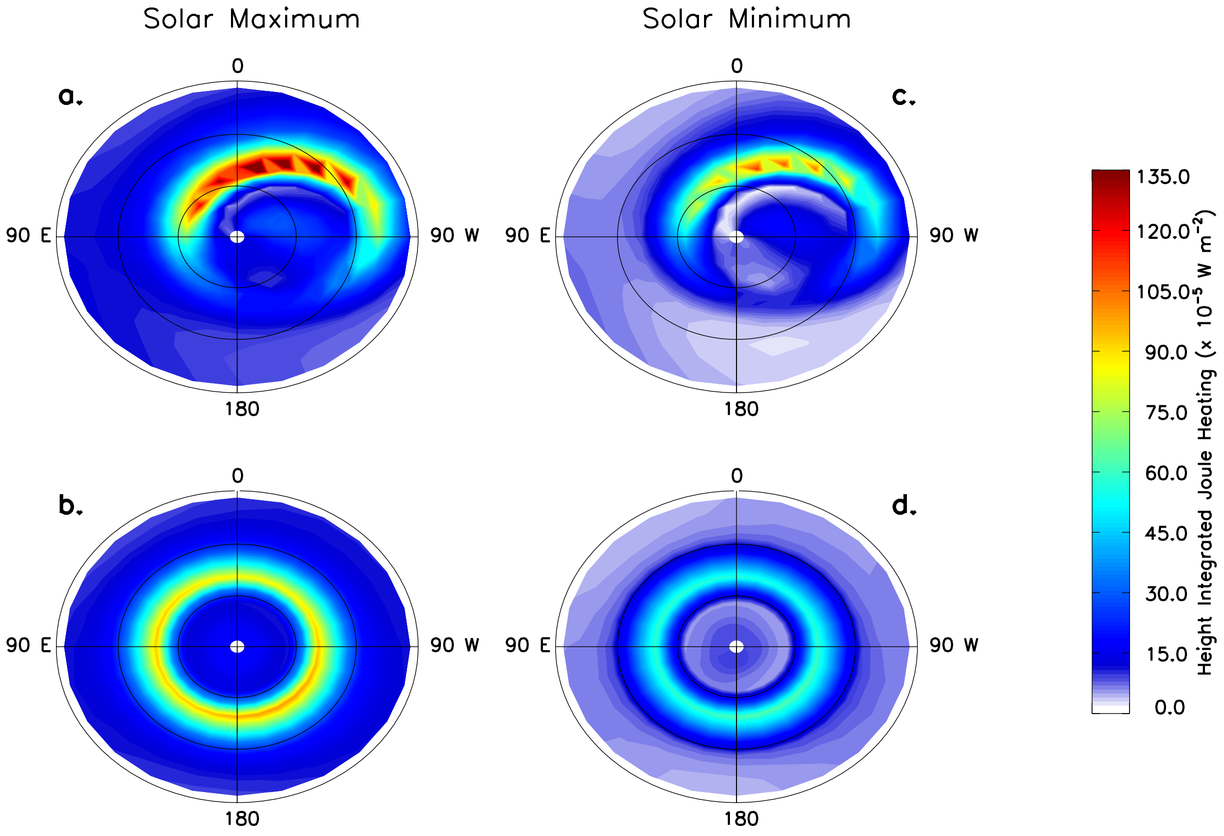

Figure B.1: Height integrated joule heating at high northern latitudes (>60° N) from the TIME-GCM during September under solar maximum (left column) and solar minimum (right column) conditions; a and c are from the modified simulation; b and d are from the idealized simulation.

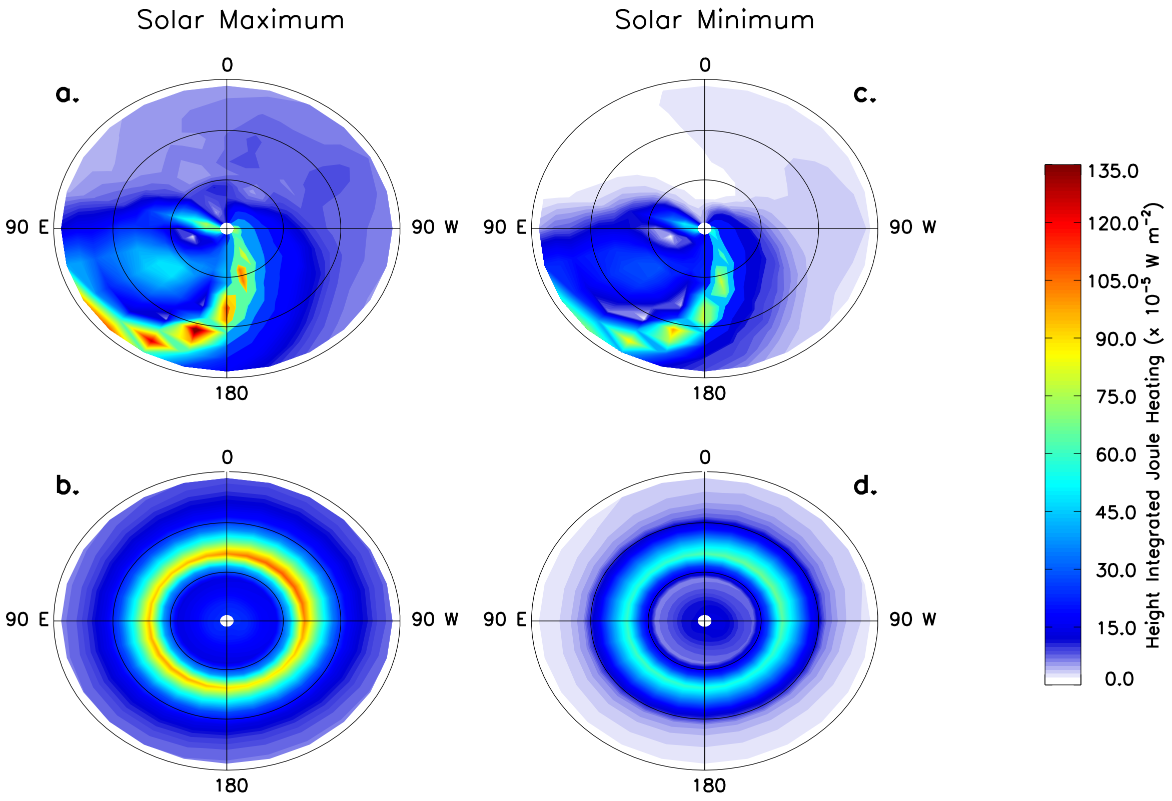

Figure B.2: Same as Figure B.1 except at high southern latitudes (>60° S).

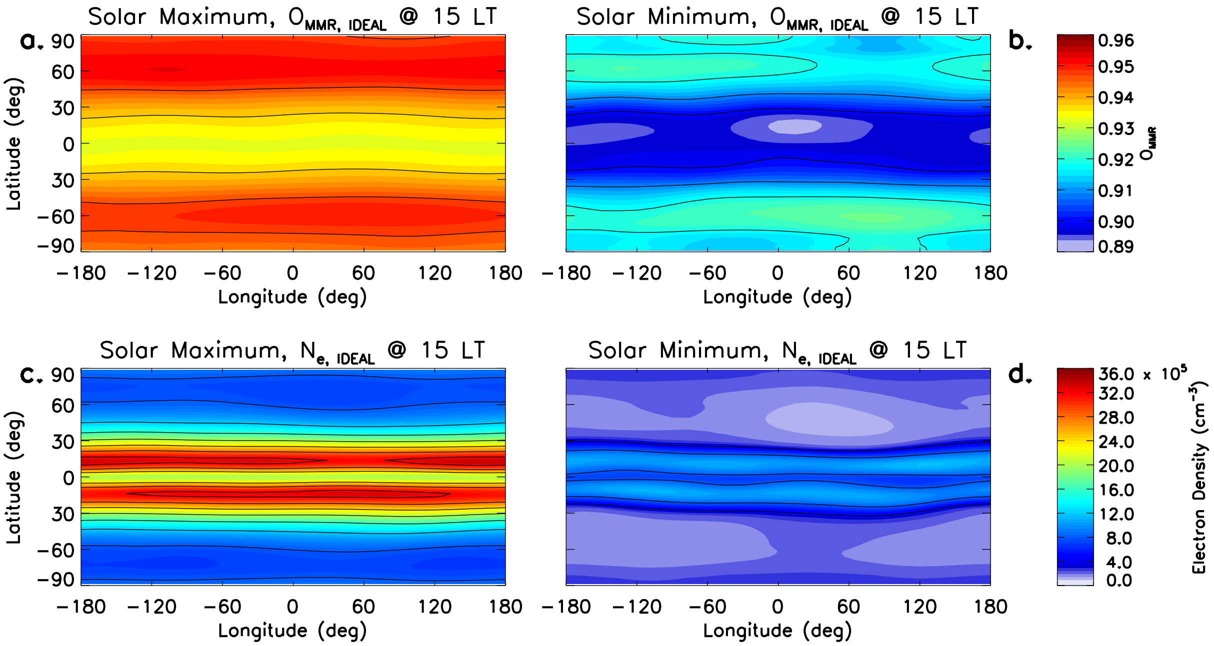

Figure B.3: Atomic oxygen mass mixing ratio (a and b) and electron density (c and d) at 15 LT and log-pressure level 3.5 from the TIME-GCM during September under solar maximum (left column, ~500 km) and solar minimum (right column, ~350 km) conditions. Atomic oxygen mass mixing ratio (electron density) is contoured every 0.1 (4×10^5 cm^{-3}).

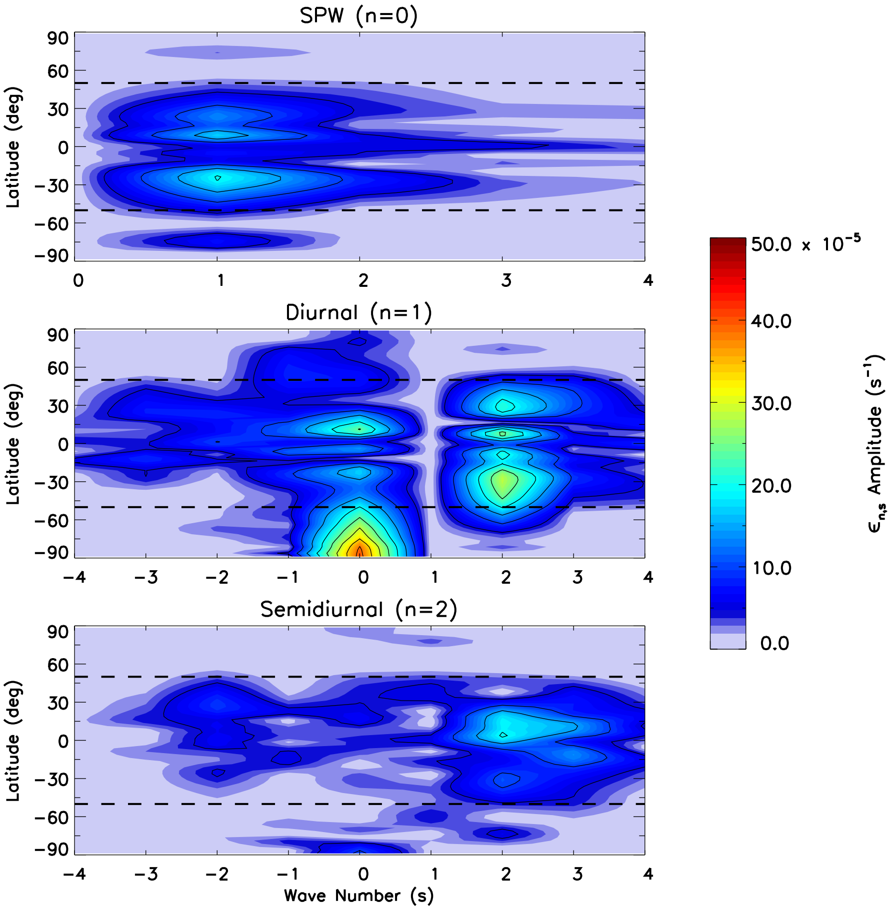

Figure B.4: Same as Figure 3.3, except for the realistic flow.

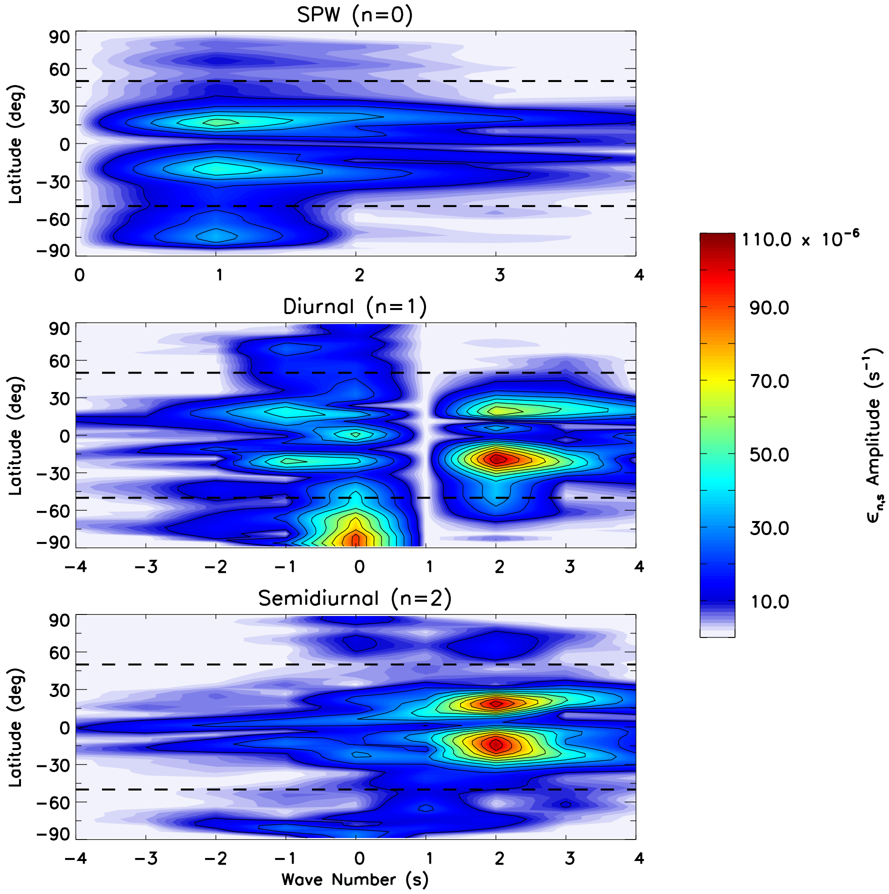

Figure B.5: Same as Figure 3.3, except for the modified flow during solar minimum conditions (∼350 km). Components are contoured every 10×10^{-6} s^{-1}.

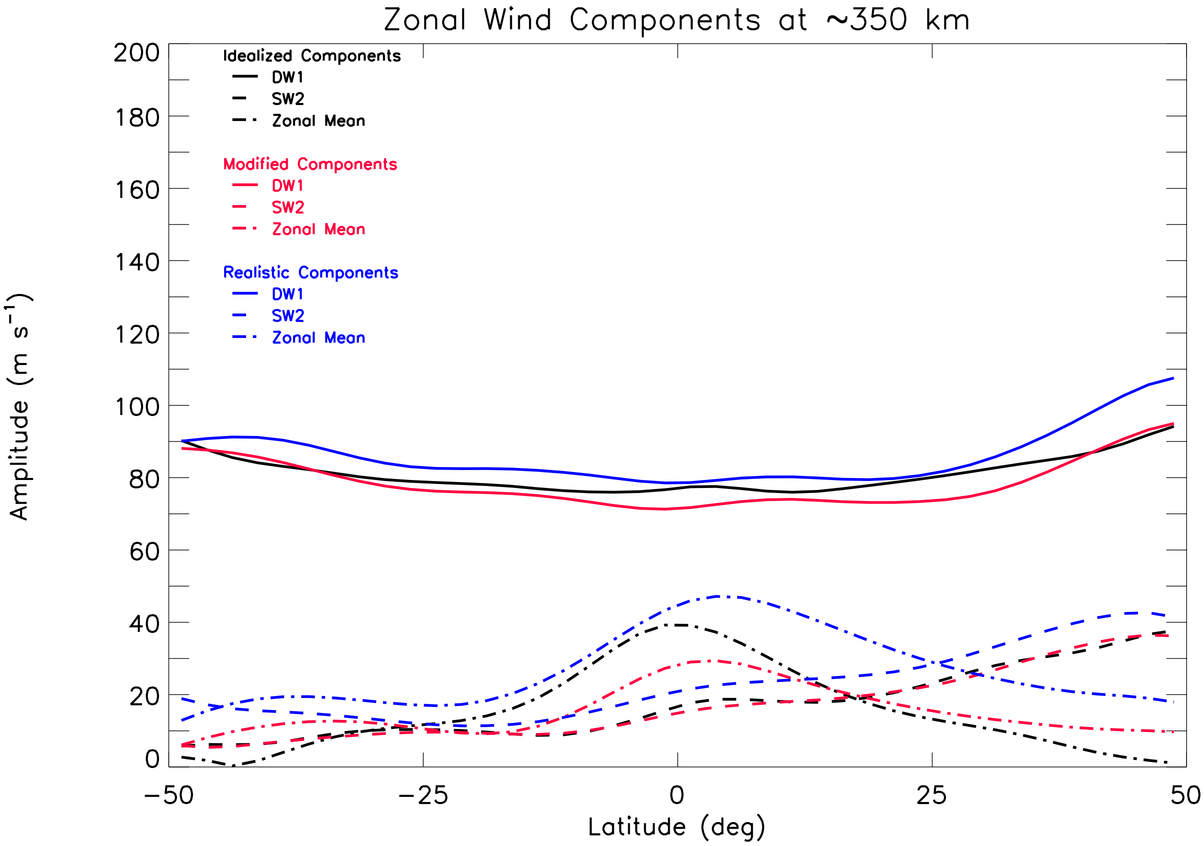

Figure B.6: Same as Figure 3.4, except under solar minimum conditions (~350 km).

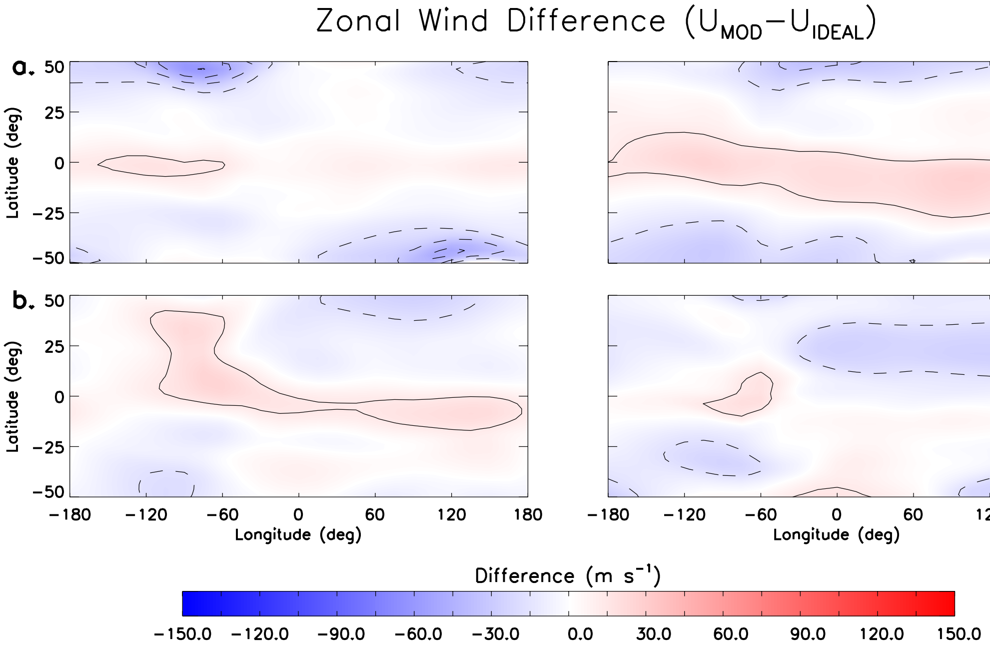

Figure B.7: Same as Figure 3.7, except under solar minimum conditions (~350 km).

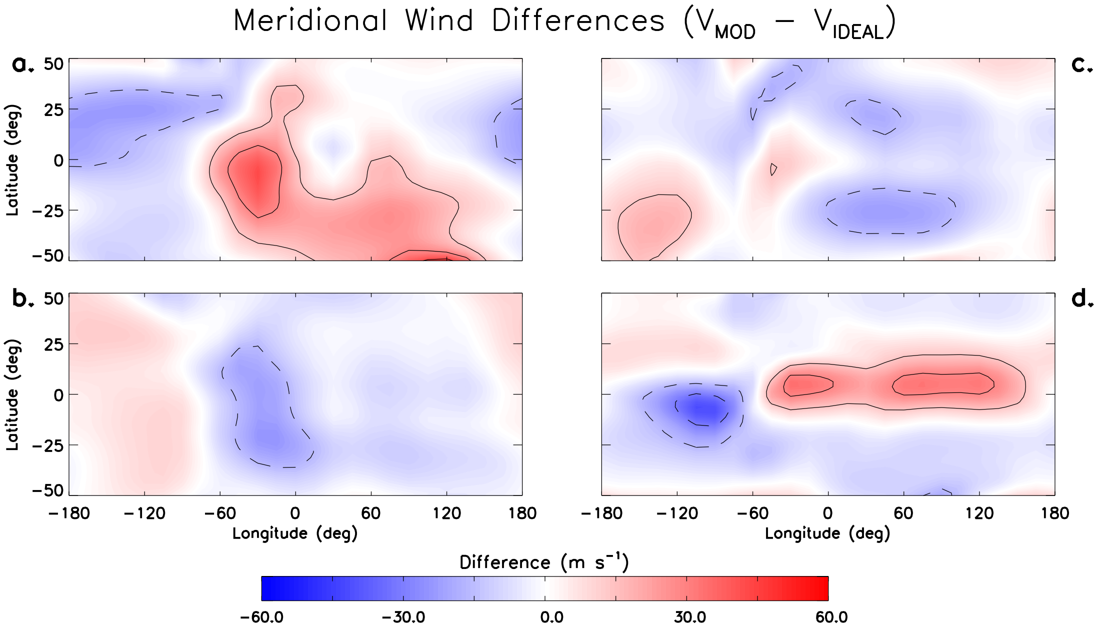

Figure B.8: Same as Figure 3.7, except for the meridional winds.

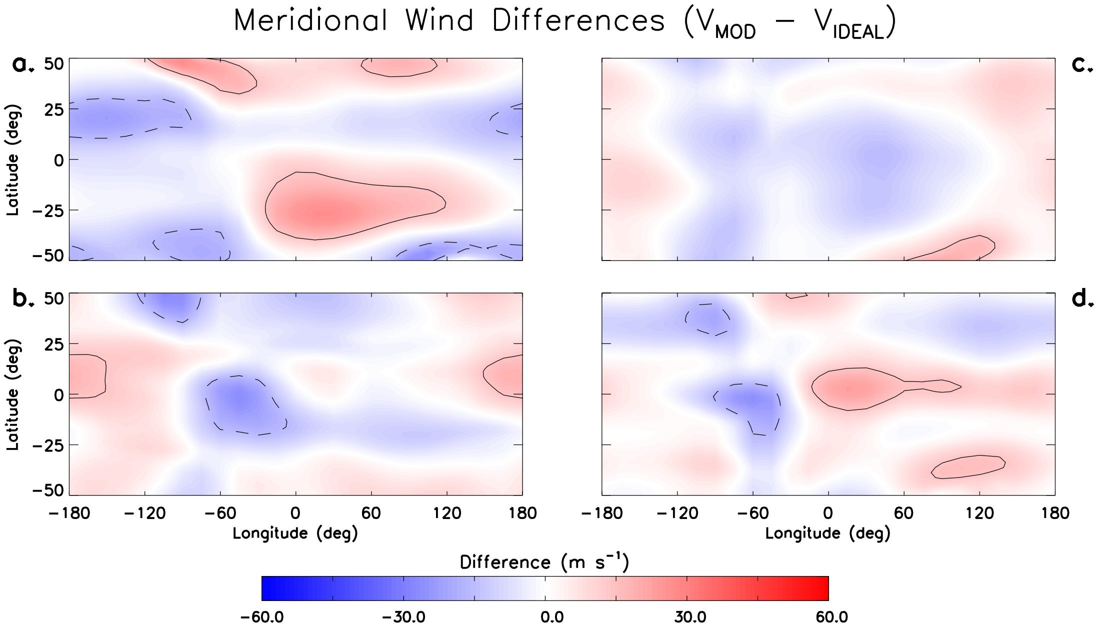

Figure B.9: Same as Figure 3.7, except for the meridional winds under solar minimum conditions (∼350 km).

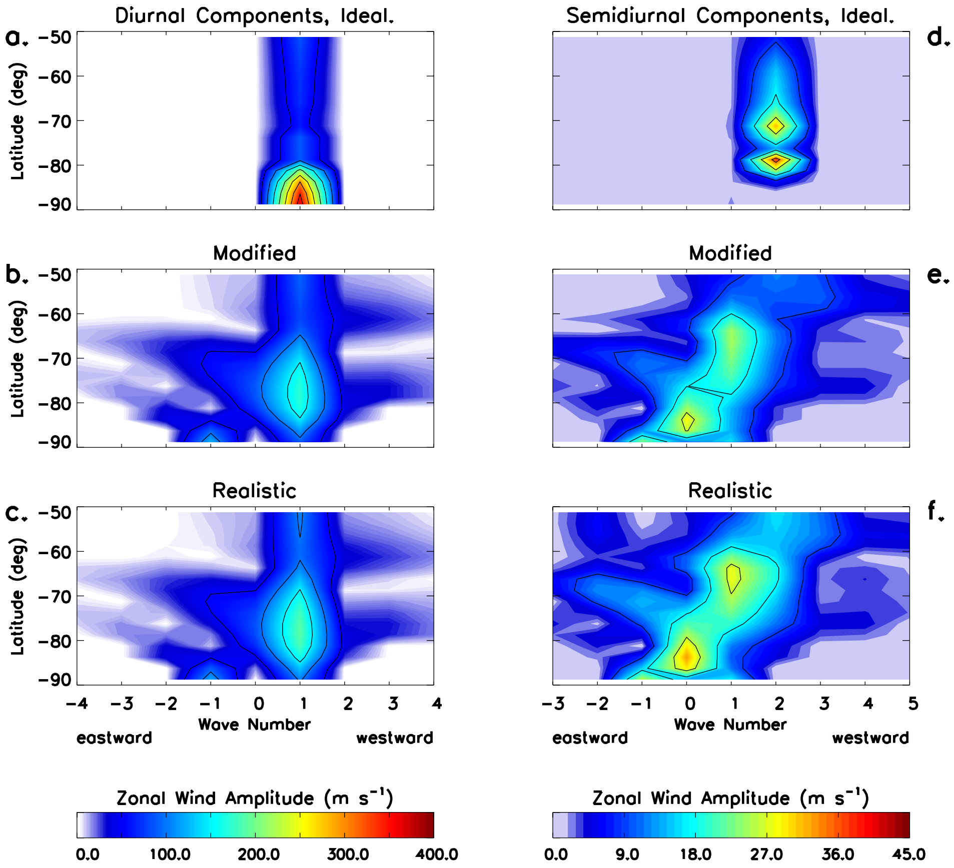

Figure B.10: Same as Figure 3.11, except at high southern latitudes.

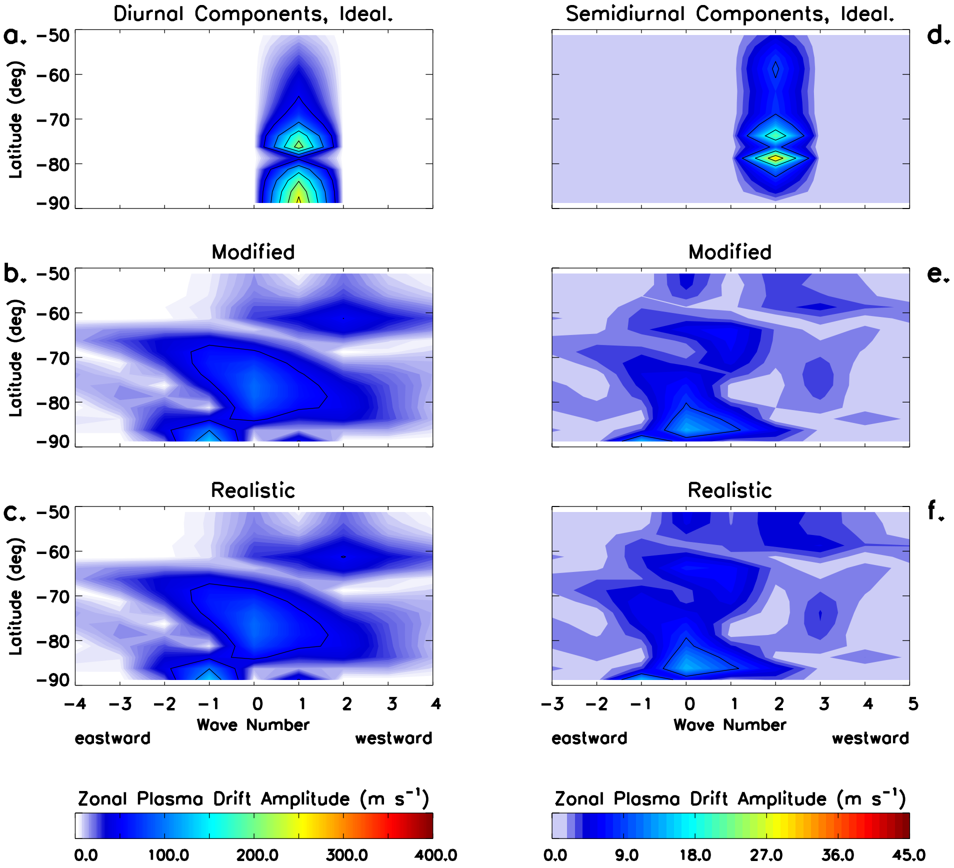

Figure B.11: Same as Figure 3.12, except at high southern latitudes.

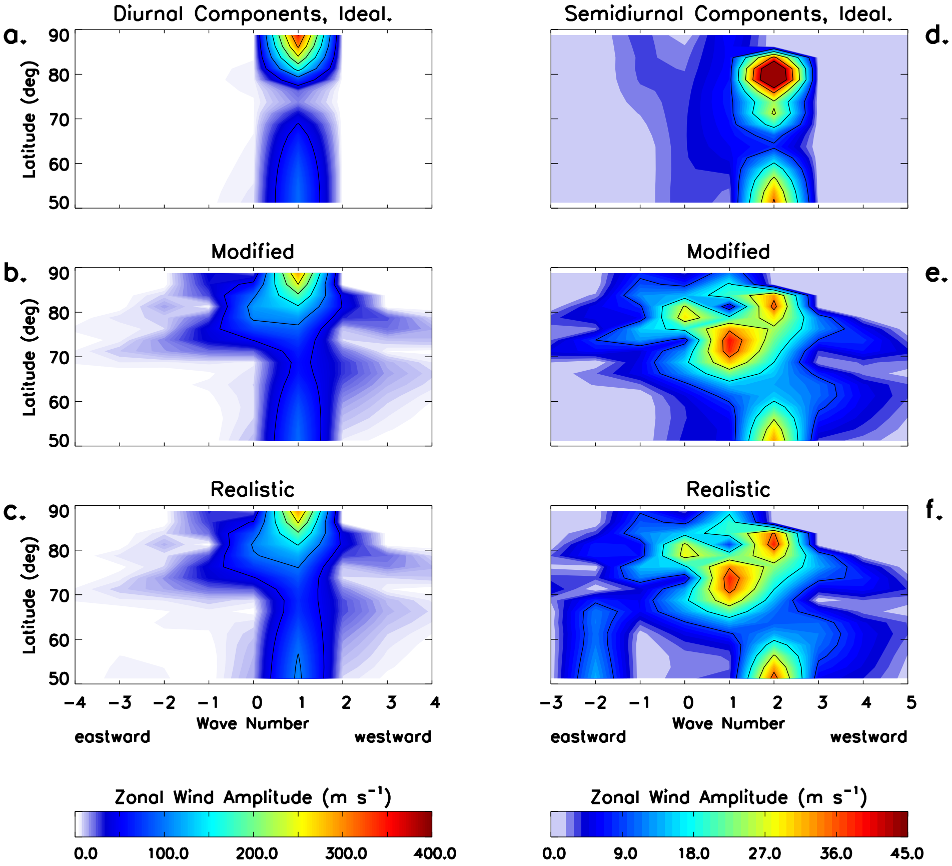

Figure B.12: Same as Figure 3.11, except under solar minimum conditions (∼350 km).

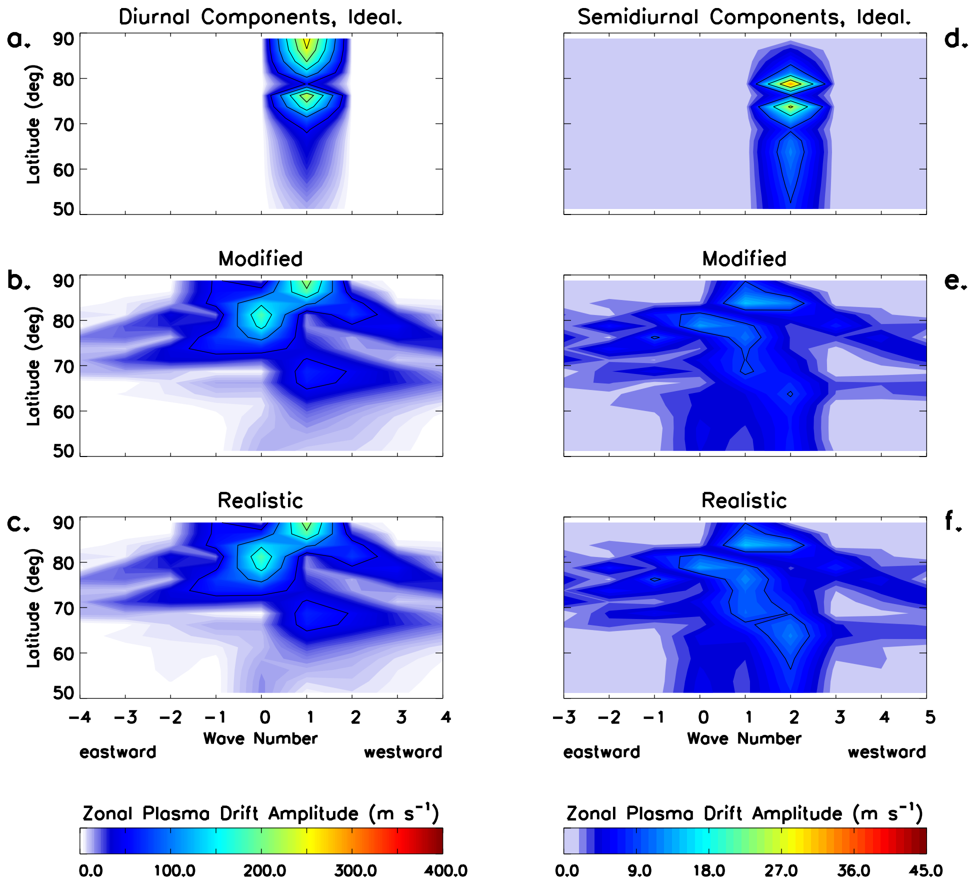

Figure B.13: Same as Figure 3.12, except at high southern latitudes (∼350 km).

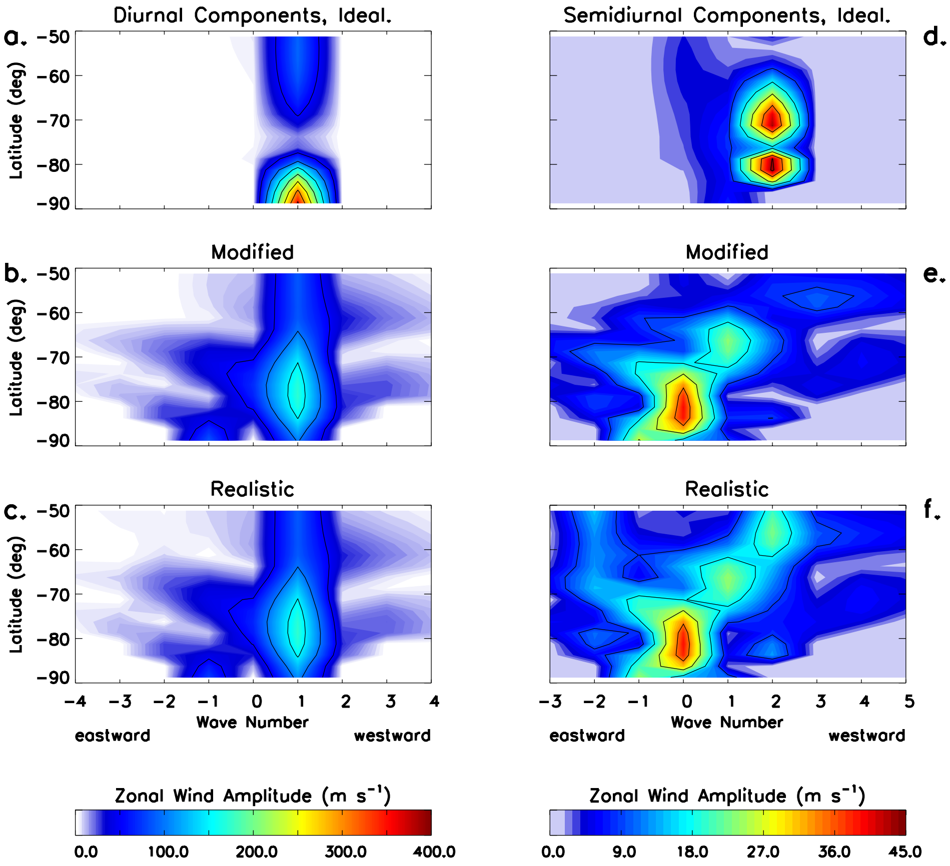

Figure B.14: Same as Figure 3.11, except at high southern latitudes and under solar minimum conditions (~350 km).

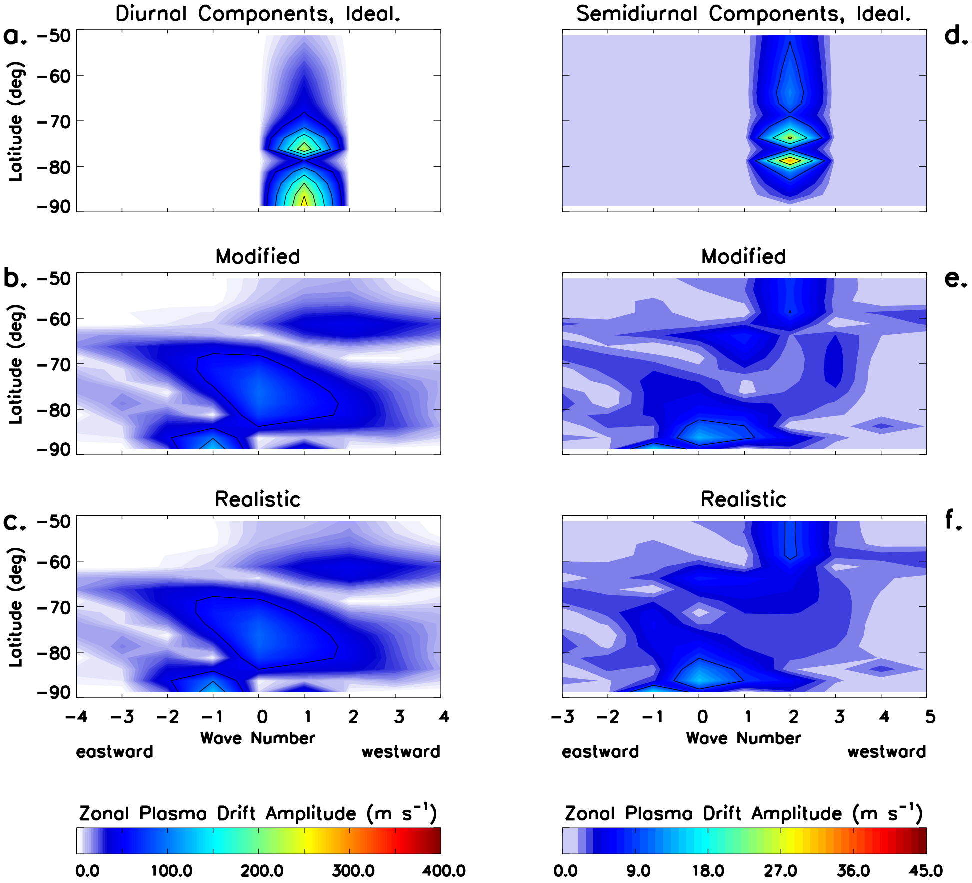

Figure B.15: Same as Figure 3.12, except at high southern latitudes and under solar minimum conditions (~350 km).

Appendix C

Supplemental Figures: Tidal Impacts on the Zonal-Mean Winds

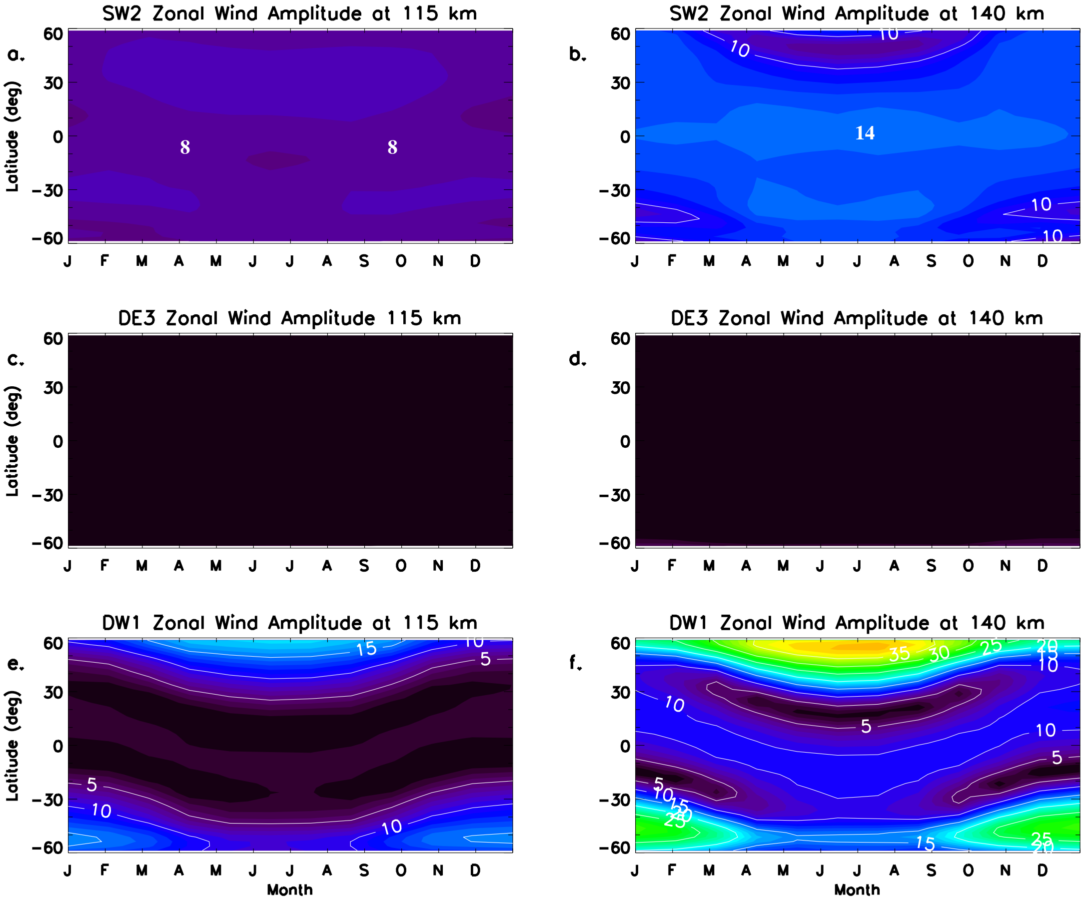

Figure C.1: Same as Figure 4.3, except for TIE-GCM simulations that exclude CTMT lower boundary tidal forcing.

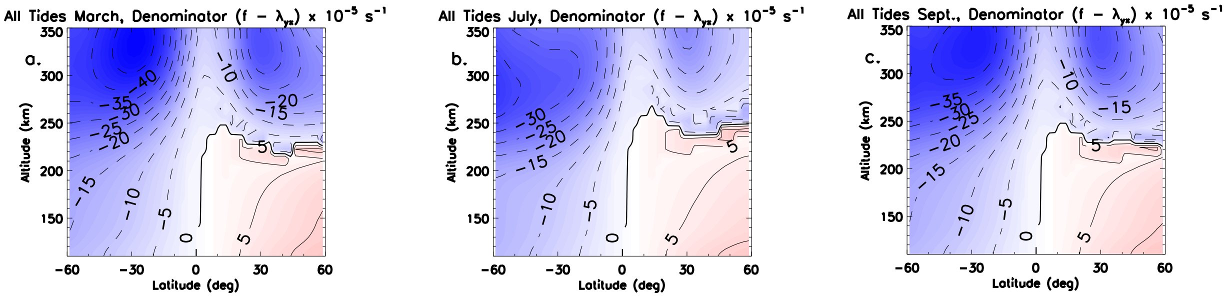

Figure C.2: $f - \overline{\lambda_{yx}}$ from the TIE-GCM during March (a), July (b), and September (c) under solar medium conditions including CTMT lower boundary tidal forcing.

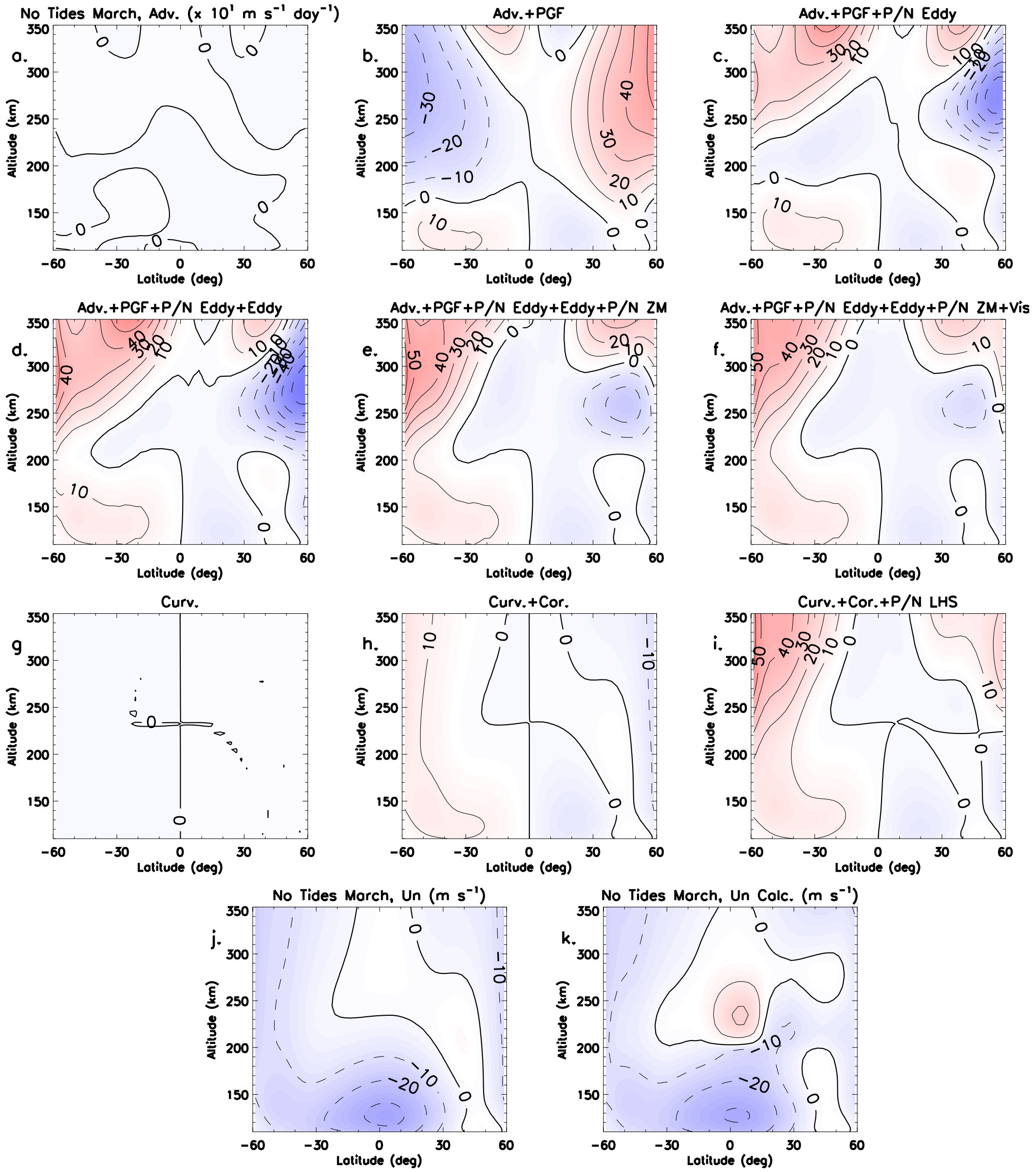

Figure C.3: Same as Figure 4.4, except for a TIE-GCM simulation excluding CTMT lower boundary tidal forcing.

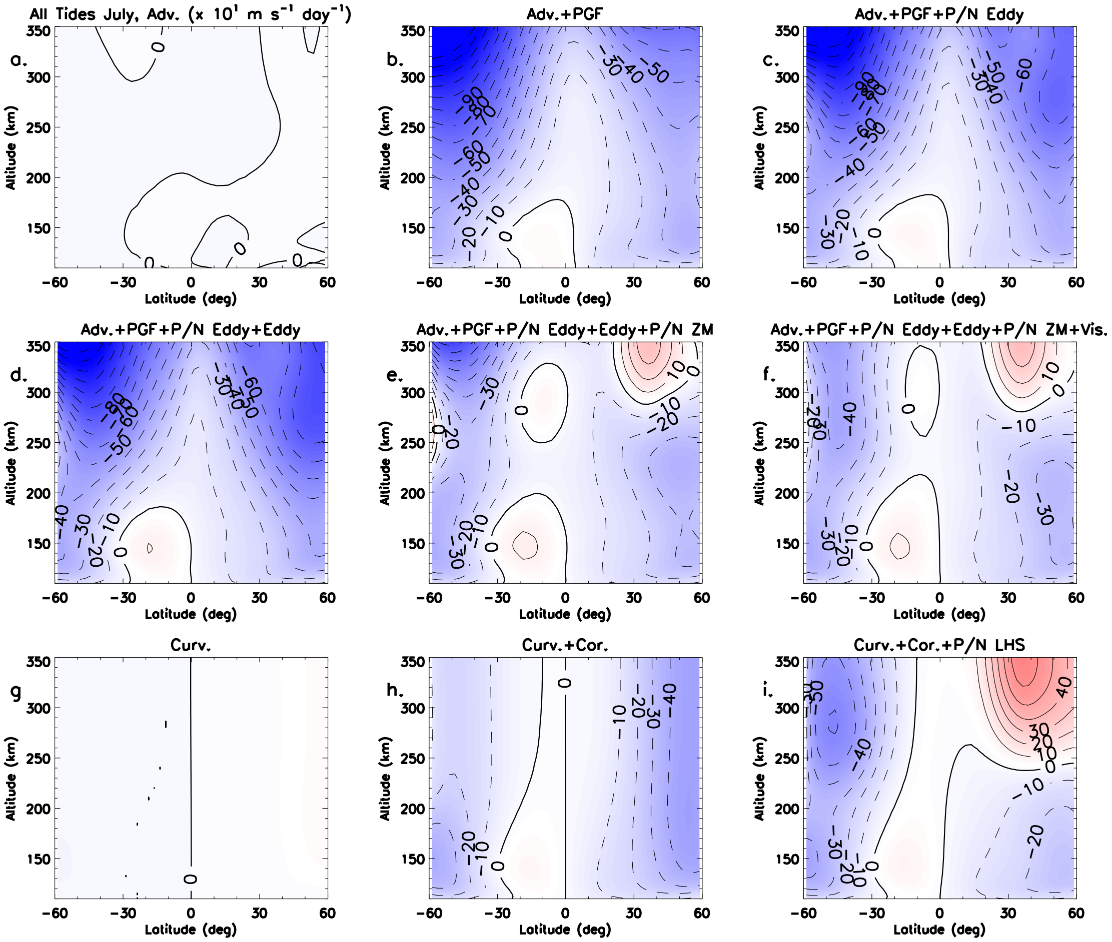
All Tides July, Adv. ($\times 10^1$ m s^{-1} day^{-1})

Adv.+PGF

Adv.+PGF+P/N Eddy

Adv.+PGF+P/N Eddy+Eddy

Adv.+PGF+P/N Eddy+Eddy+P/N ZM

Adv.+PGF+P/N Eddy+Eddy+P/N ZM+Vis.

Curv.

Curv.+Cor.

Curv.+Cor.+P/N LHS

Figure C.4: Same as Figure 4.4, except for a TIE-GCM simulation during July and excluding the zonal mean zonal winds.

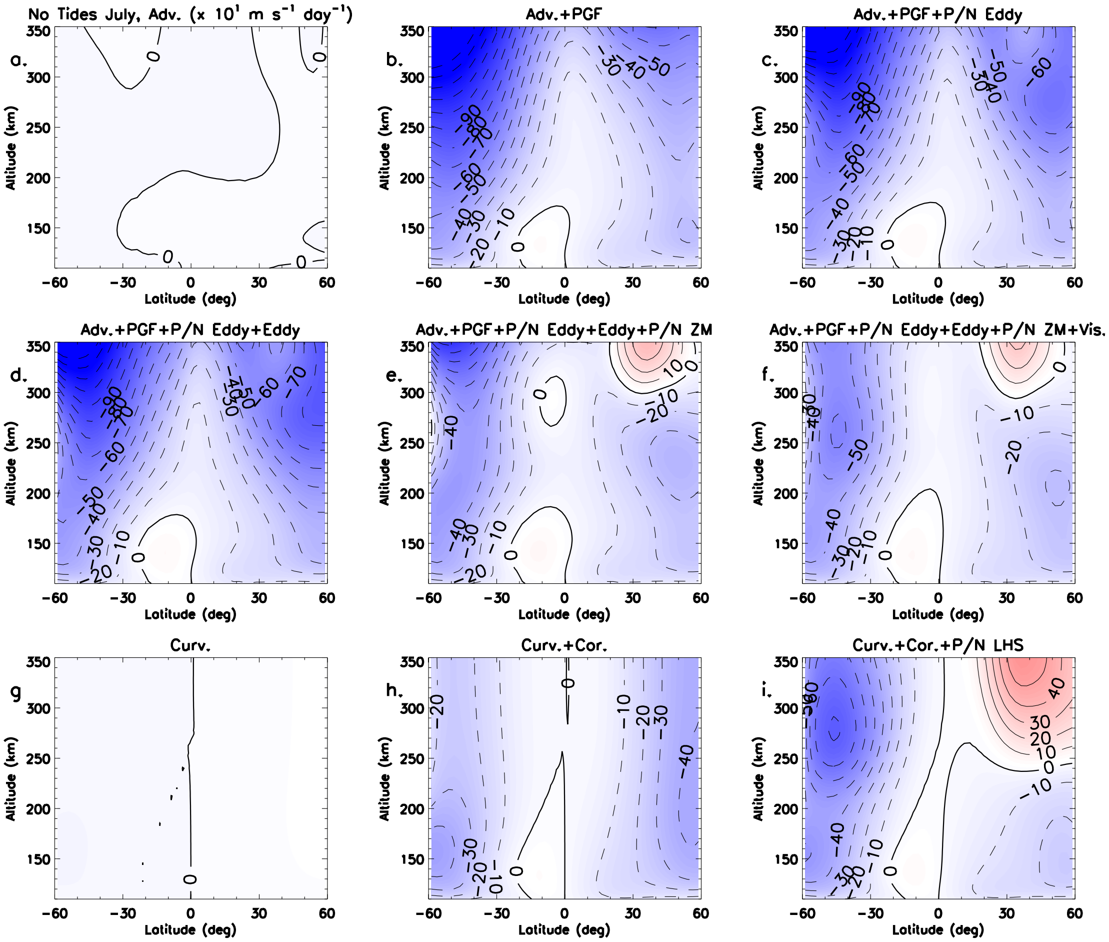

Figure C.5: Same as Figure C.3, except for a TIE-GCM simulation during July and excluding the zonal mean zonal winds.

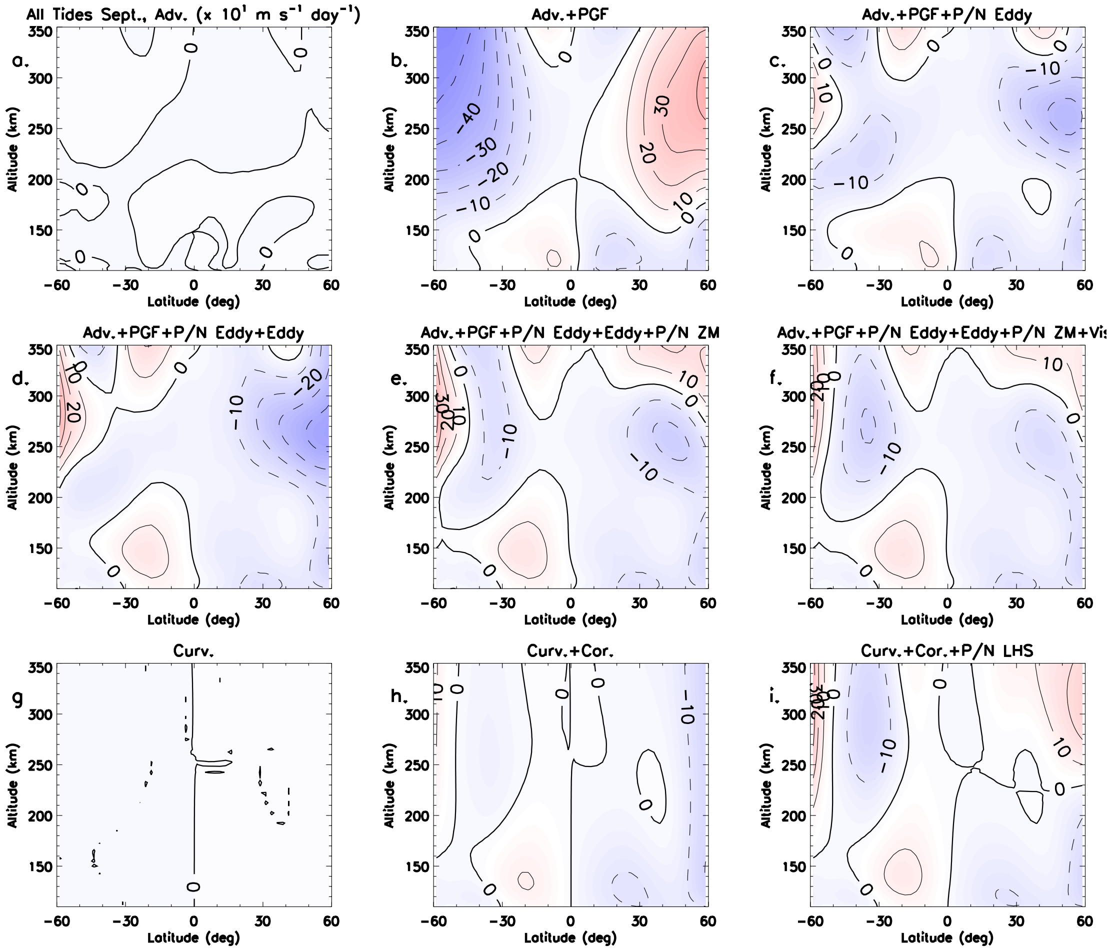

Figure C.6: Same as Figure C.4, except for a TIE-GCM simulation during September.

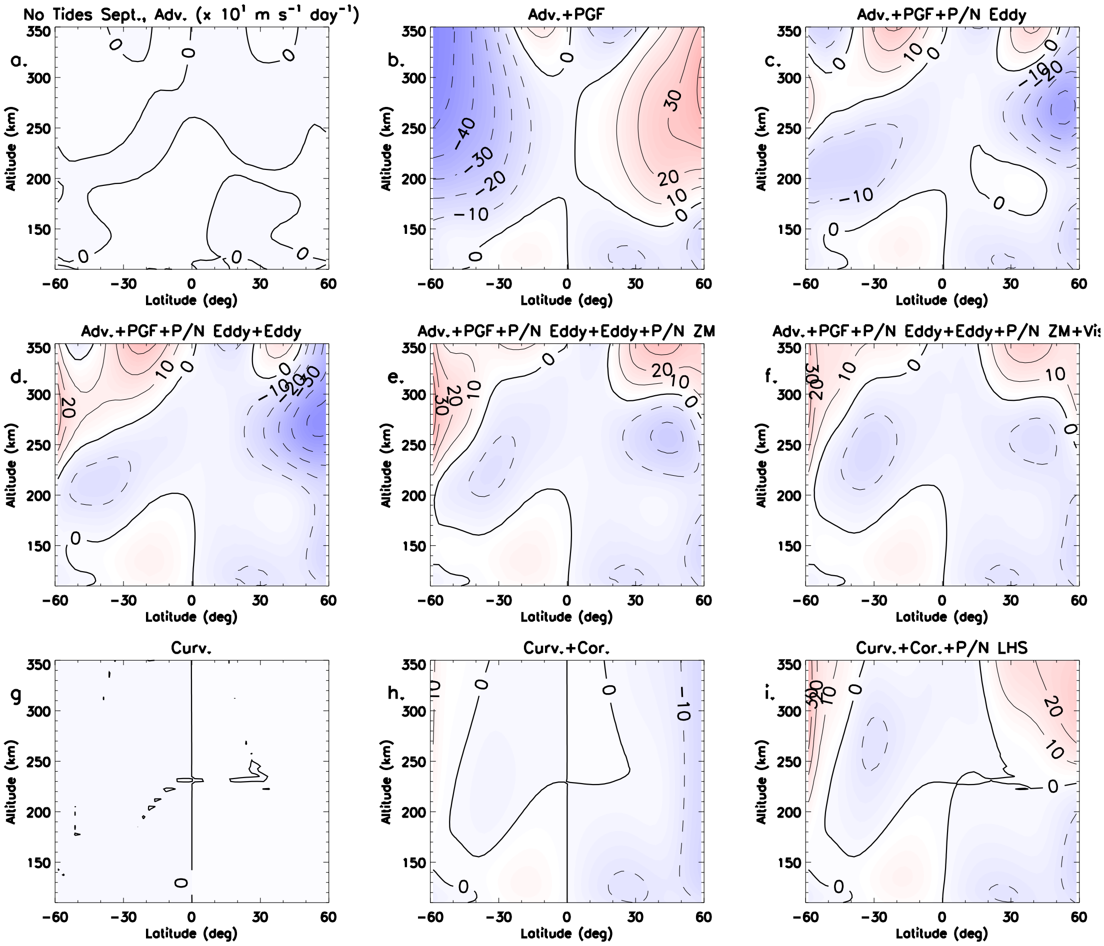

Figure C.7: Same as Figure C.5, except for a TIE-GCM simulation during September.

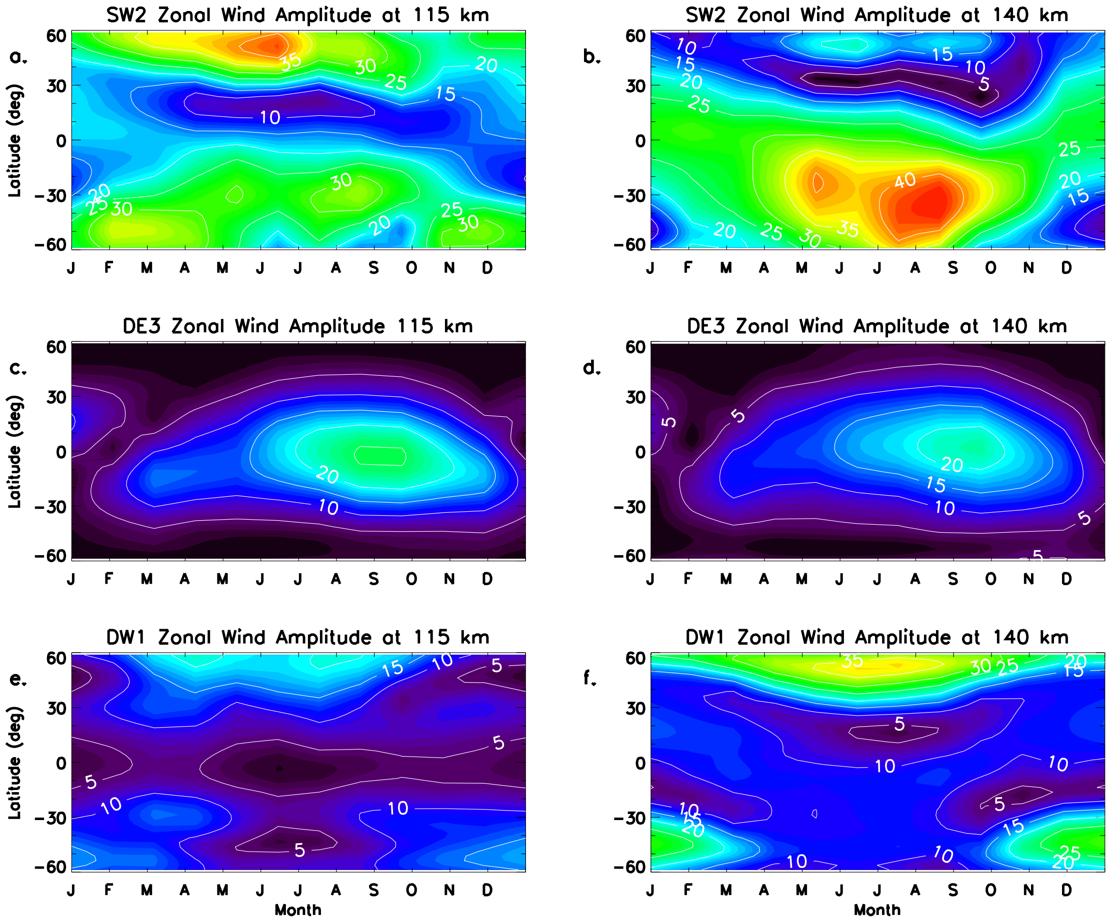

Figure C.8: Same as Figure 4.3, except for a TIE-GCM simulations under solar minimum conditions.

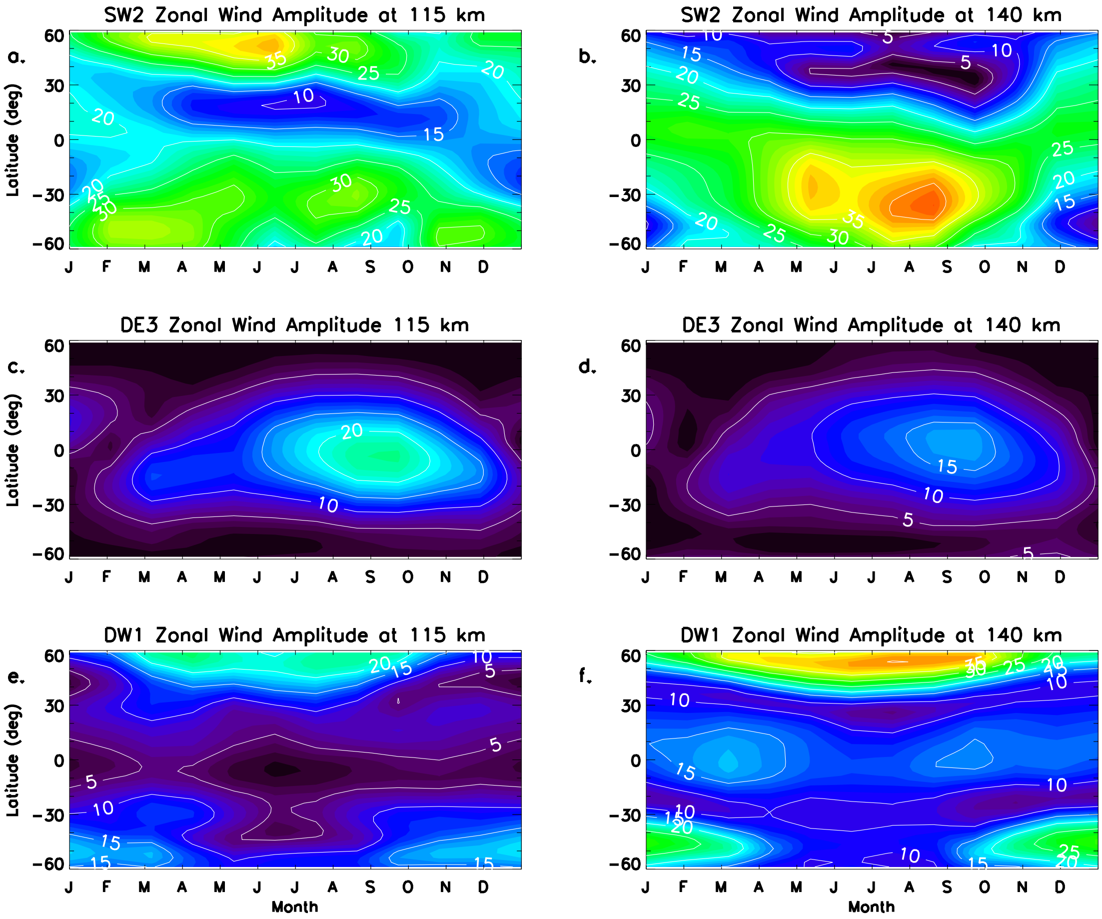

Figure C.9: Same as Figure C.8, except for a TIE-GCM simulations under solar maximum conditions.

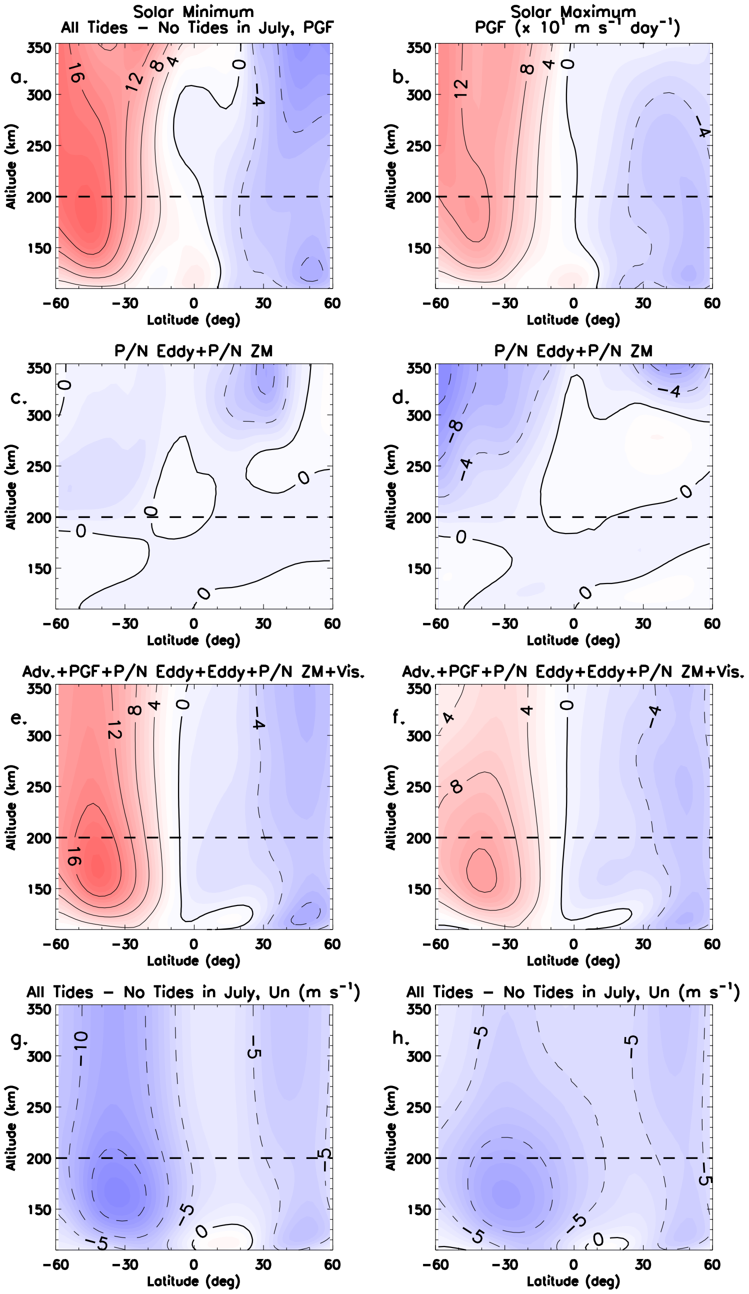

Figure C.10: Same as Figure 4.10, except for a TIE-GCM simulation during July.

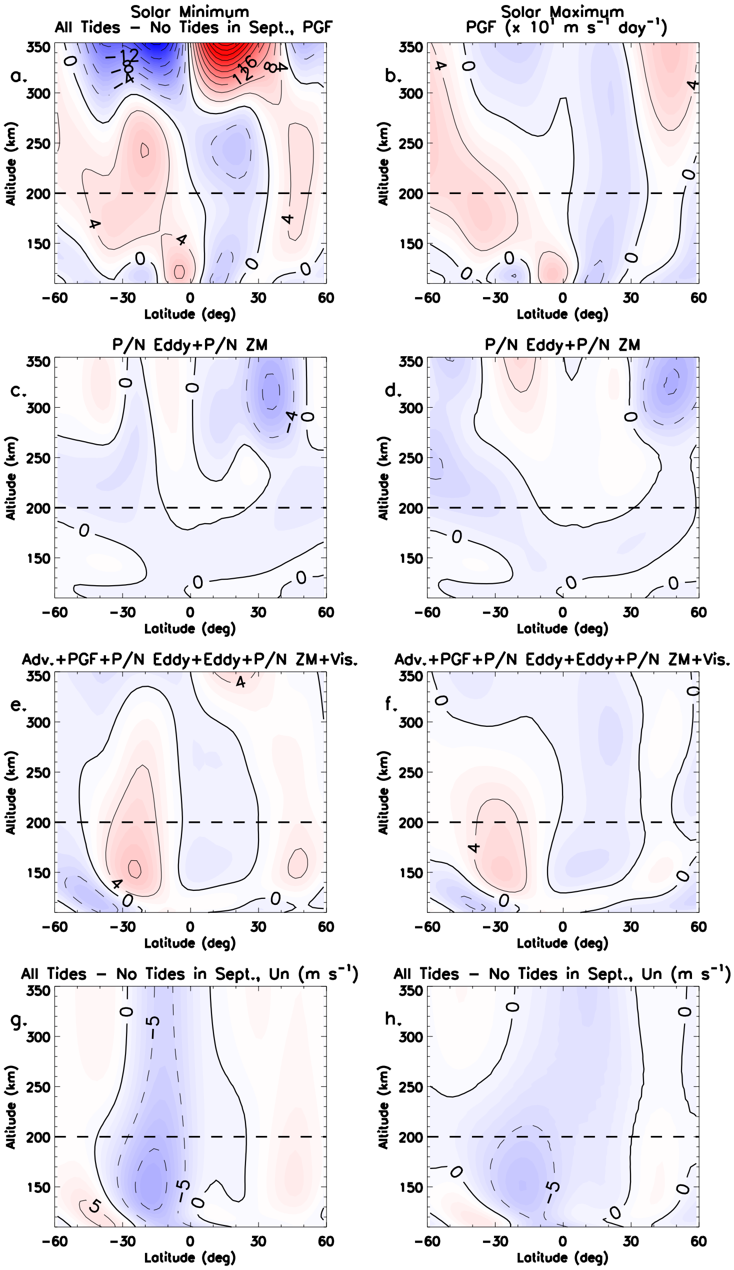

Figure C.11: Same as Figure C.10, except for a TIE-GCM simulation during September.

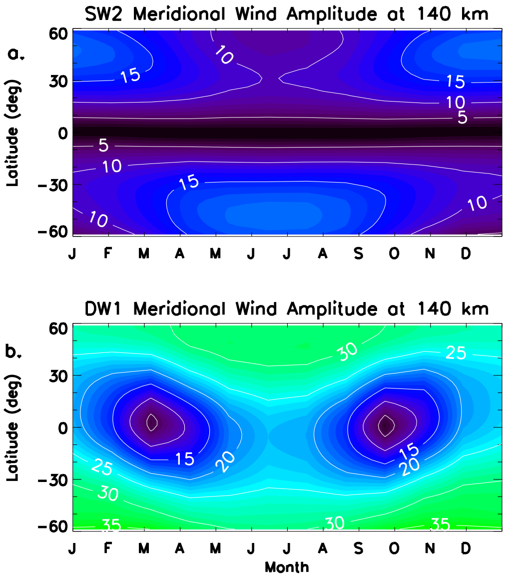

Figure C.12: Same as Figure 4.13, except for TIE-GCM simulations that exclude CTMT lower boundary tidal forcing.

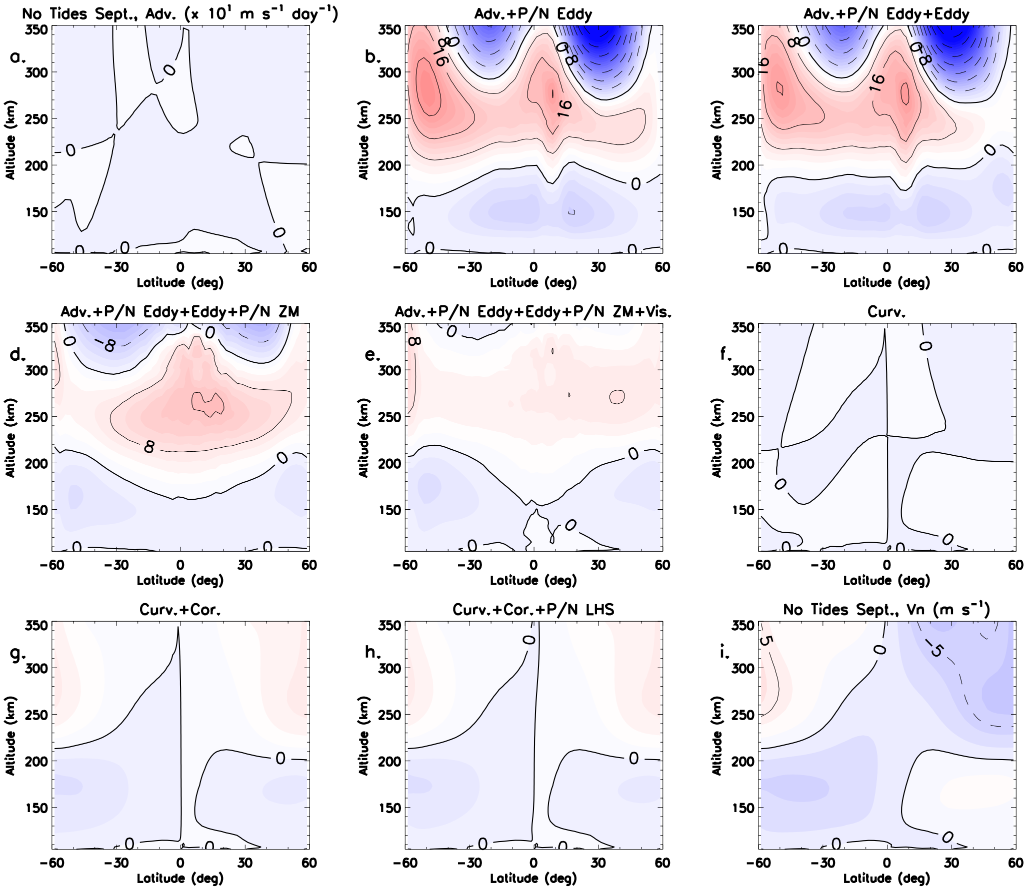

Figure C.13: Same as Figure 4.14, except for a TIE-GCM simulation excluding CTMT lower boundary tidal forcing.

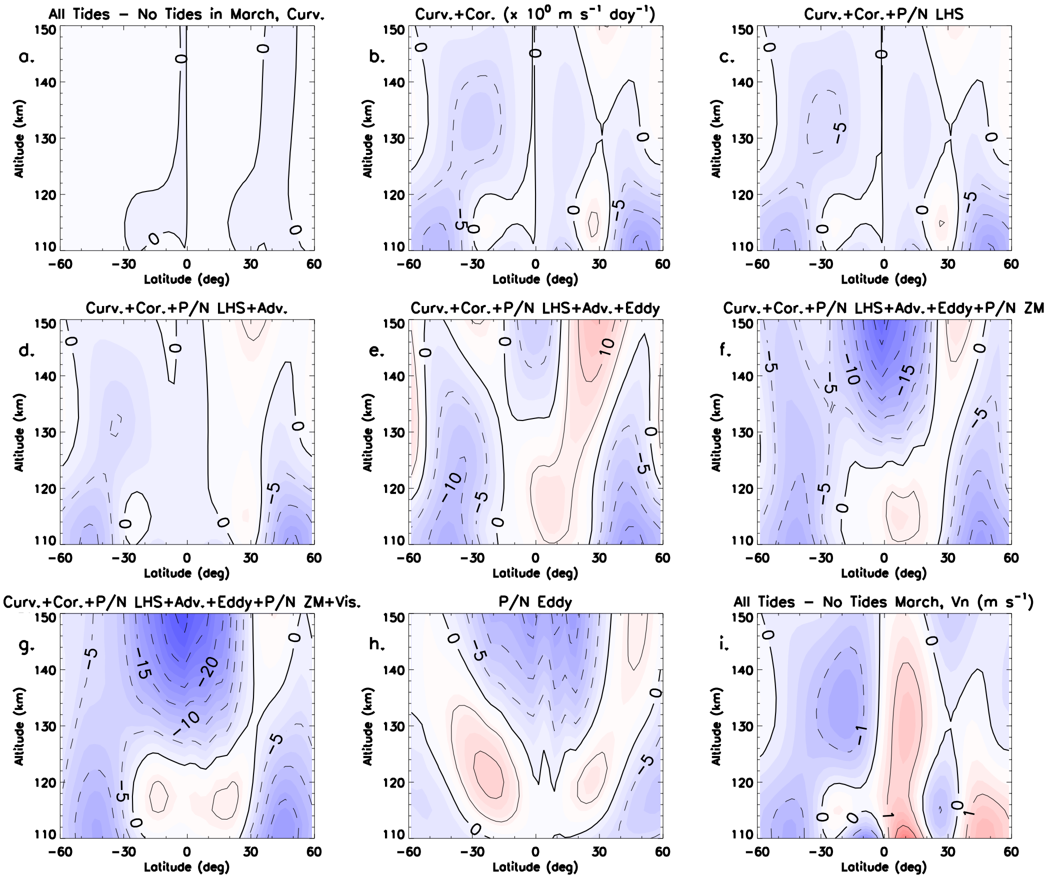

Figure C.14: Same as Figure 4.15, except for a TIE-GCM simulation under March conditions.

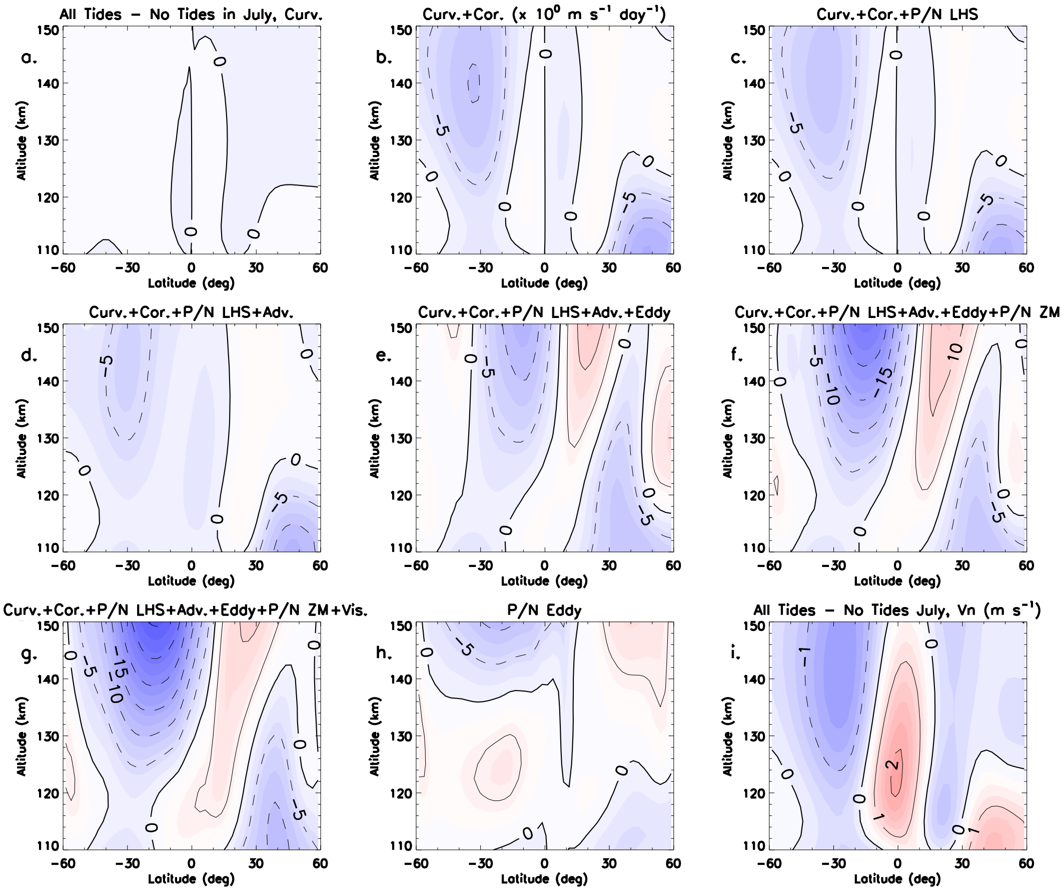

Figure C.15: Same as Figure 4.15, except for a TIE-GCM simulation under July conditions.

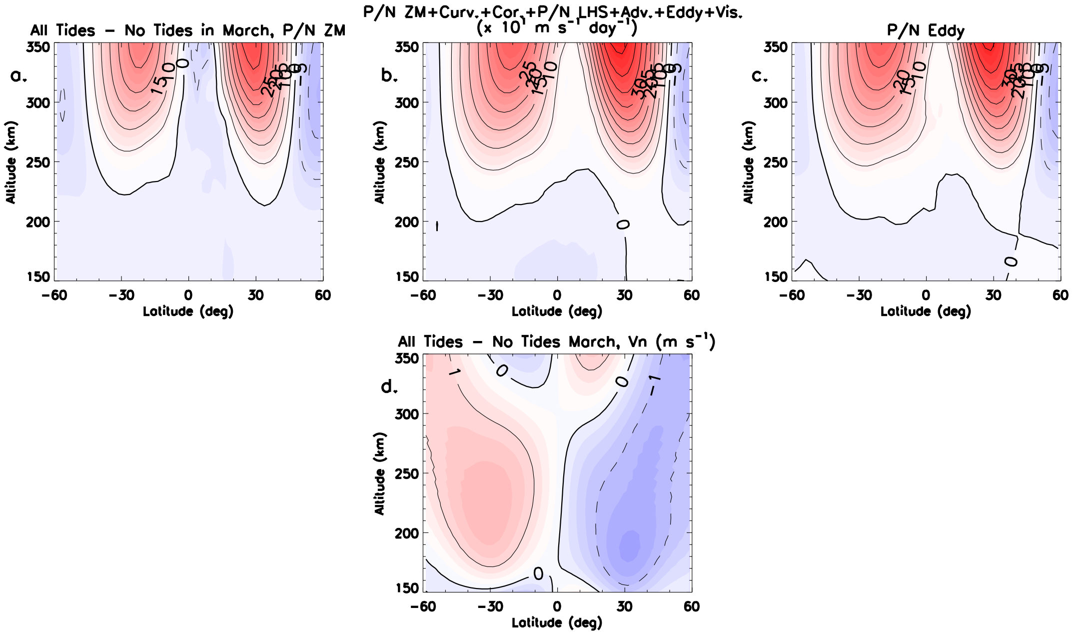

Figure C.16: Same as Figure 4.16, except for a TIE-GCM simulation under March conditions.

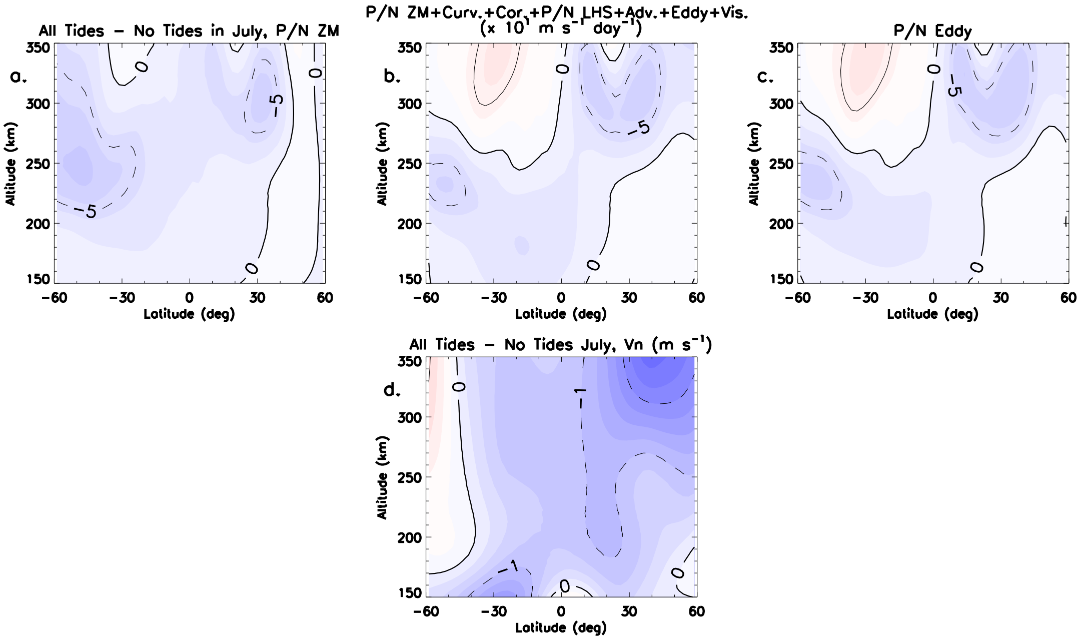

Figure C.17: Same as Figure 4.16, except for a TIE-GCM simulation under July conditions.

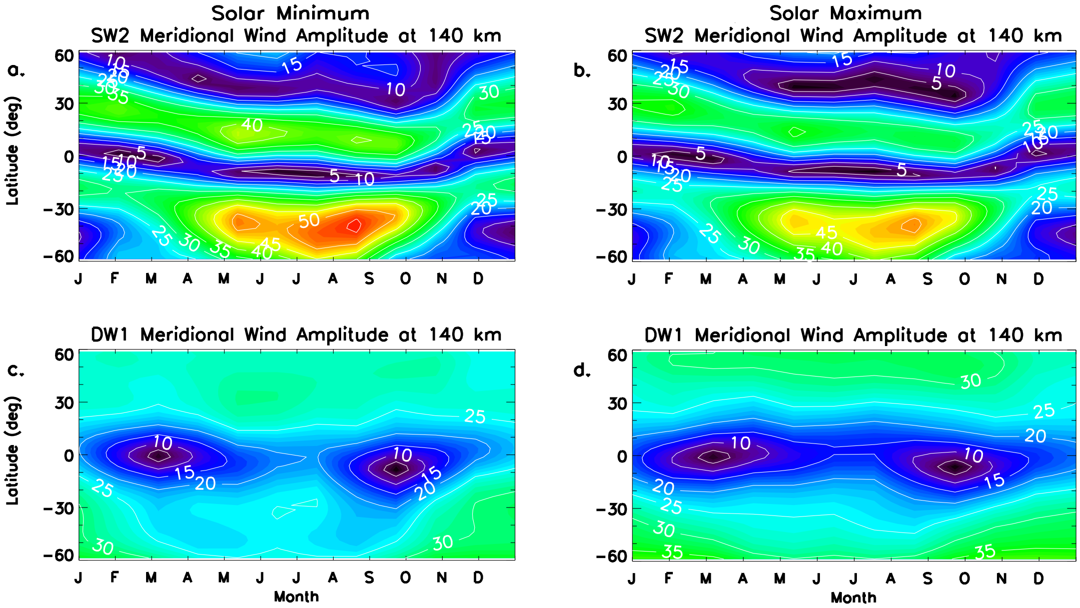

Figure C.18: Same as Figure 4.13, except for the SW2 (a) and (b), and the DW1 (c) and (d) meridional wind amplitudes under both solar minimum (Left Column) and solar maximum (Right Column) conditions.

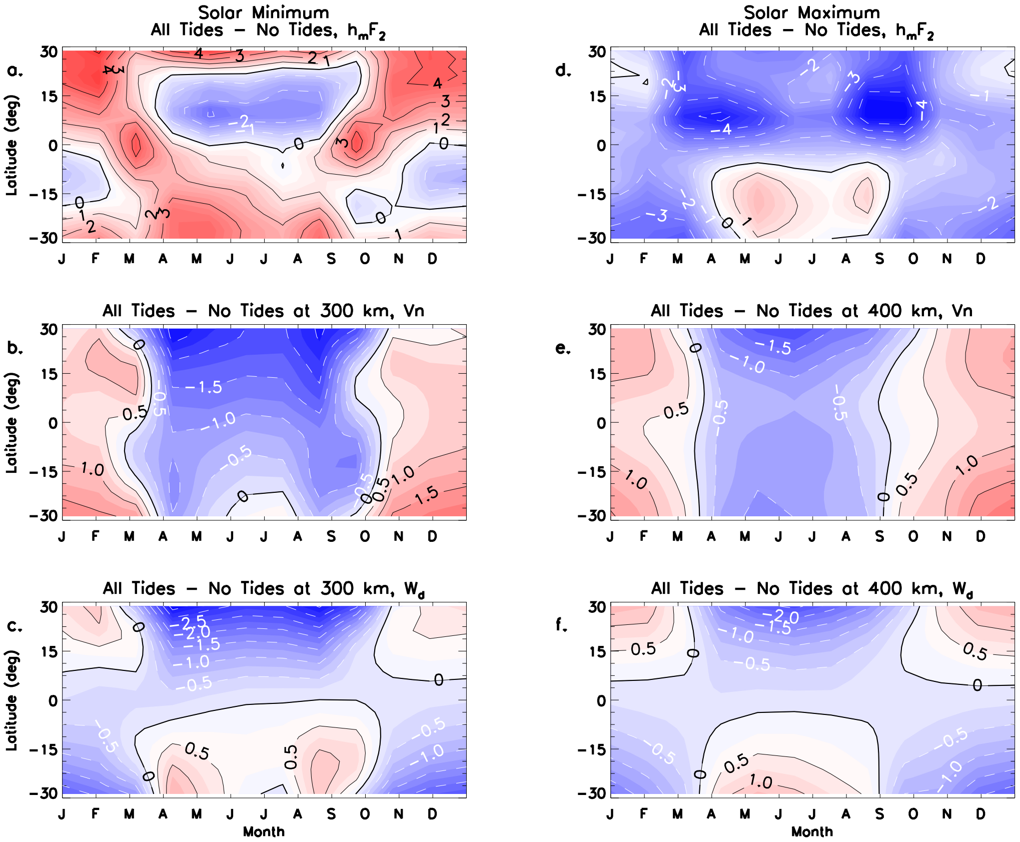

Figure C.19: Same as Figure 4.18, except for TIE-GCM simulations under solar minimum (Left Column) and solar maximum (Right Column) conditions. Meridional wind and parallel field-aligned plasma motions shown in (b) and (c) (e and f) are shown at 300 (400) km during solar minimum (maximum).

Appendix D

Supplemental Figures: Tidal Impacts on the Zonal-Mean Temperatures

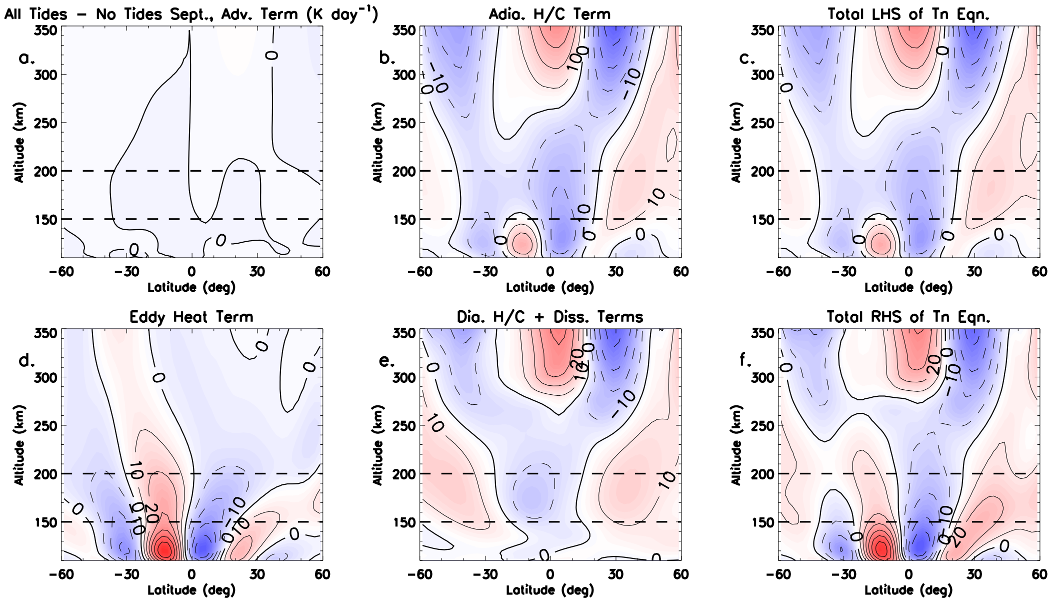

Figure D.1: Forcing term difference fields from the thermodynamic energy equation between TIE-GCM simulations including and excluding CTMT tidal lower boundary forcing under September and solar medium conditions as a function of latitude and altitude. The Adv. term is shown in (a); the Adia. H/C term is shown in (b); the sum of Adv. and Adia H/C terms on the left hand side of equation 2.12 is shown in (c); the Eddy Heat term is shown in (d); the sum of the Dia. H/C and Diss. terms is shown in (e); the sum of the Eddy Heat, Dia. H/C, and Diss. terms is shown (f). Forcing term differences are contoured every ±10 K day^{-1}.

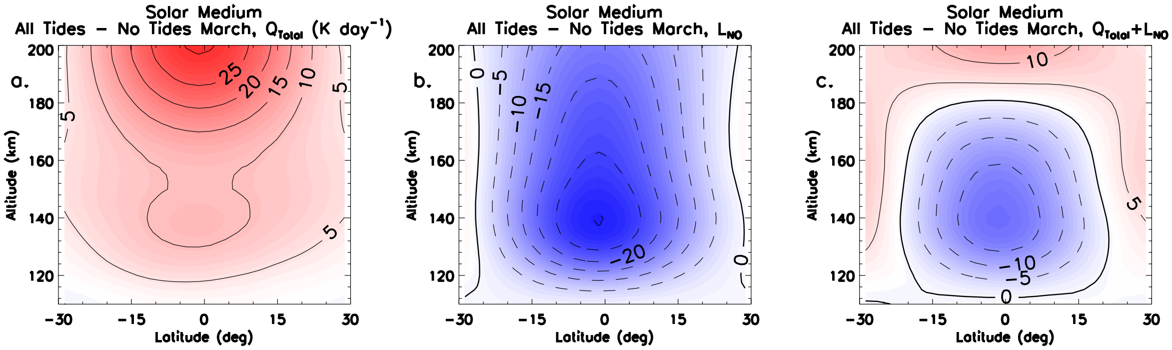

Figure D.2: Same as Figure 5.5, except during the month of March.

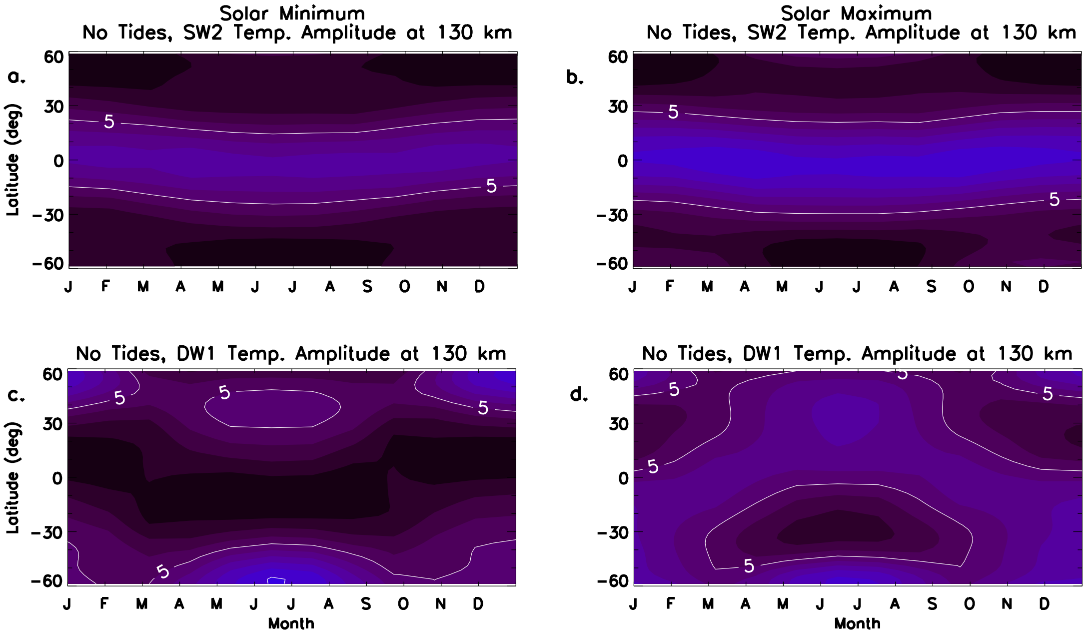

Figure D.3: Same as Figure 5.9, except for TIE-GCM simulations that exclude CTMT lower boundary tidal forcing.

Appendix E

Supplemental Figures: Tidal Impacts on the Zonal-Mean Composition

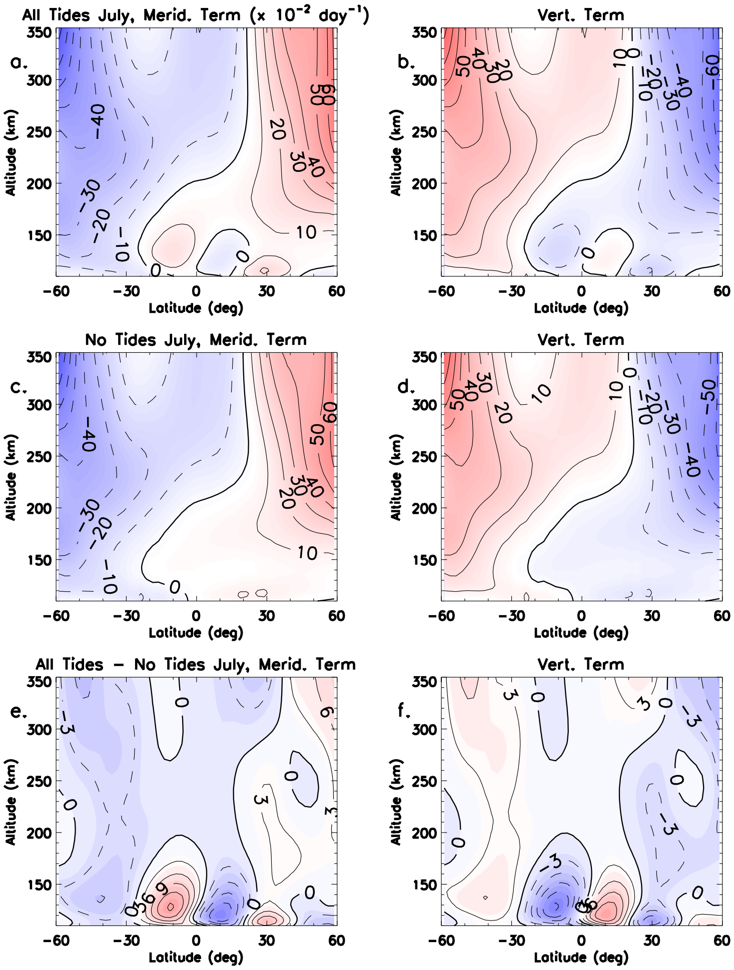

Figure E.1: Same as Figure 6.1, except during the month of July.

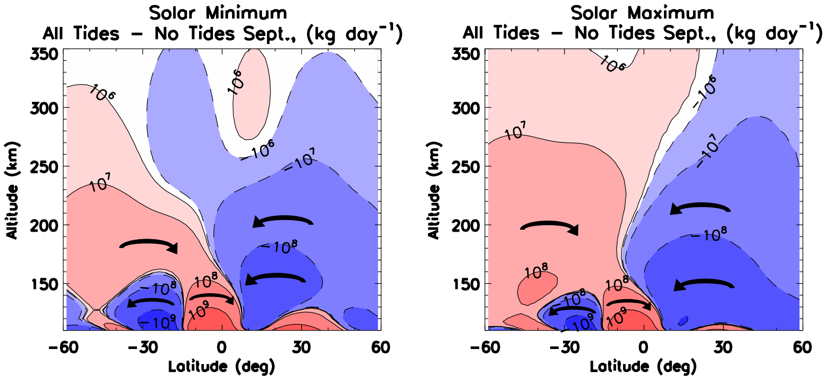
Solar Minimum
All Tides – No Tides Sept., (kg day^{-1})

Solar Maximum
All Tides – No Tides Sept., (kg day^{-1})

Figure E.2: Same as Figure 6.2c, except for mass flow stream function difference fields calculated under solar minimum (Left) and solar maximum (Right).

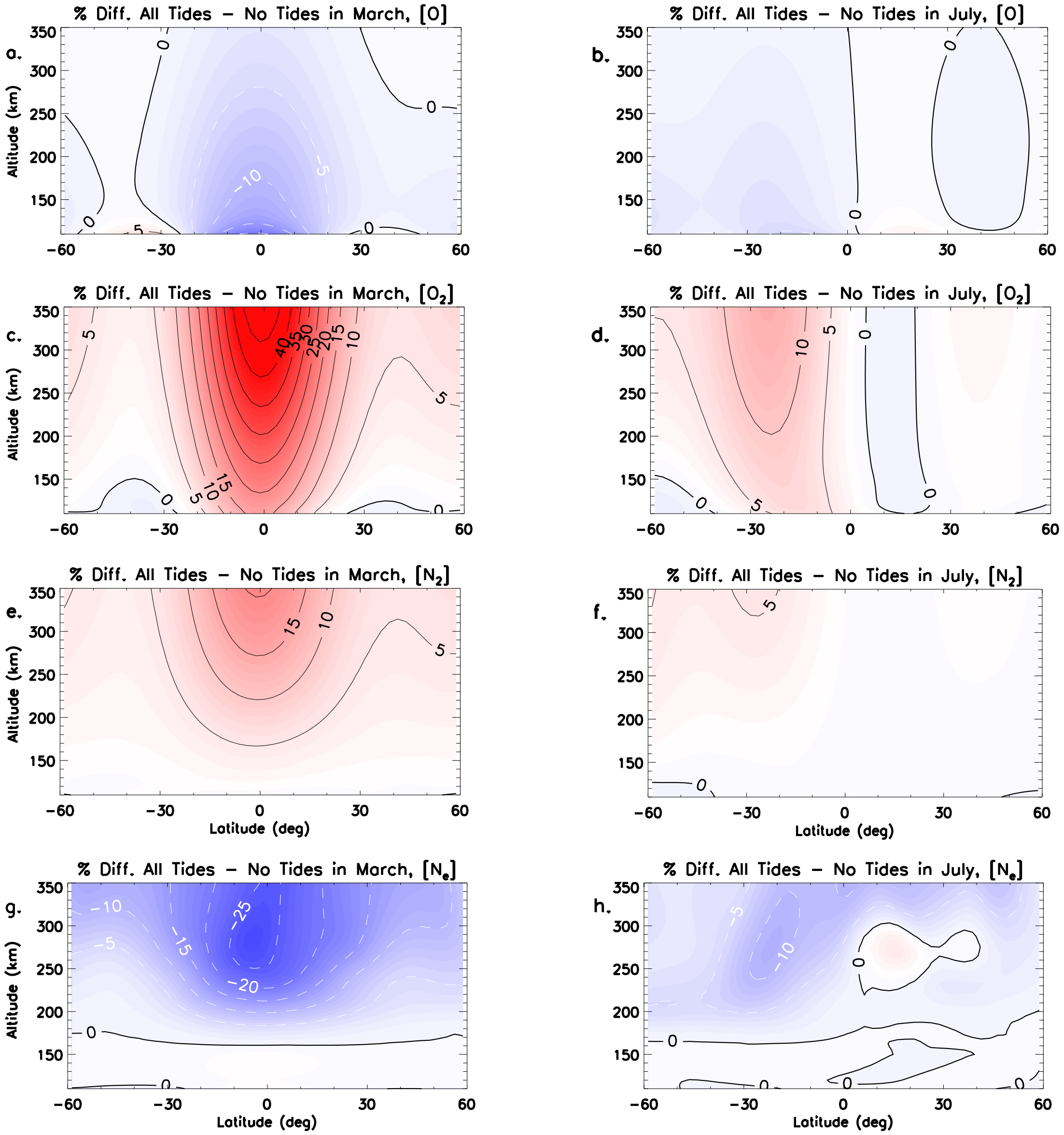

Figure E.3: Same as Figure 6.4, except for constituent percent differences during March (First Column) and July (Second Column). [O] differences are shown in (a) and (b), [O_2] differences in (c) and (d), [N_2] differences in (e) and (f), and electron density differences in (g) and (h). Percent difference are contoured every ±5%.

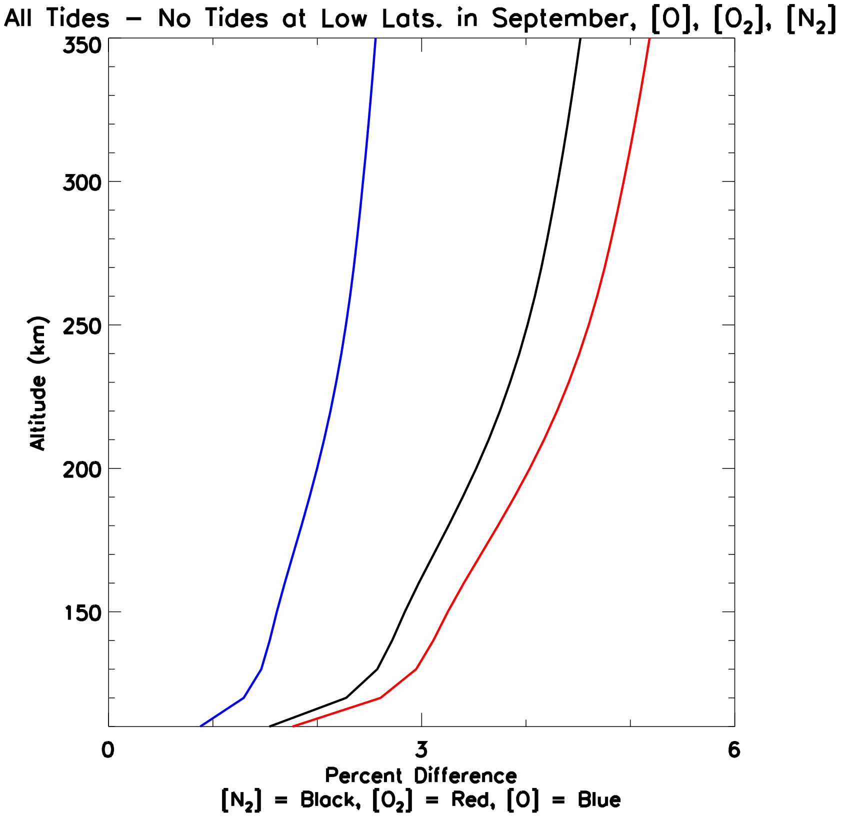

Figure E.4: Percent changes in [O] (blue), [O_2] (red), and [N_2] (black) averaged between ±30° latitude calculated via the hydrostatic law assuming tidally-induced changes in the zonal mean temperatures as a function of altitude under September and Solar Medium Conditions.

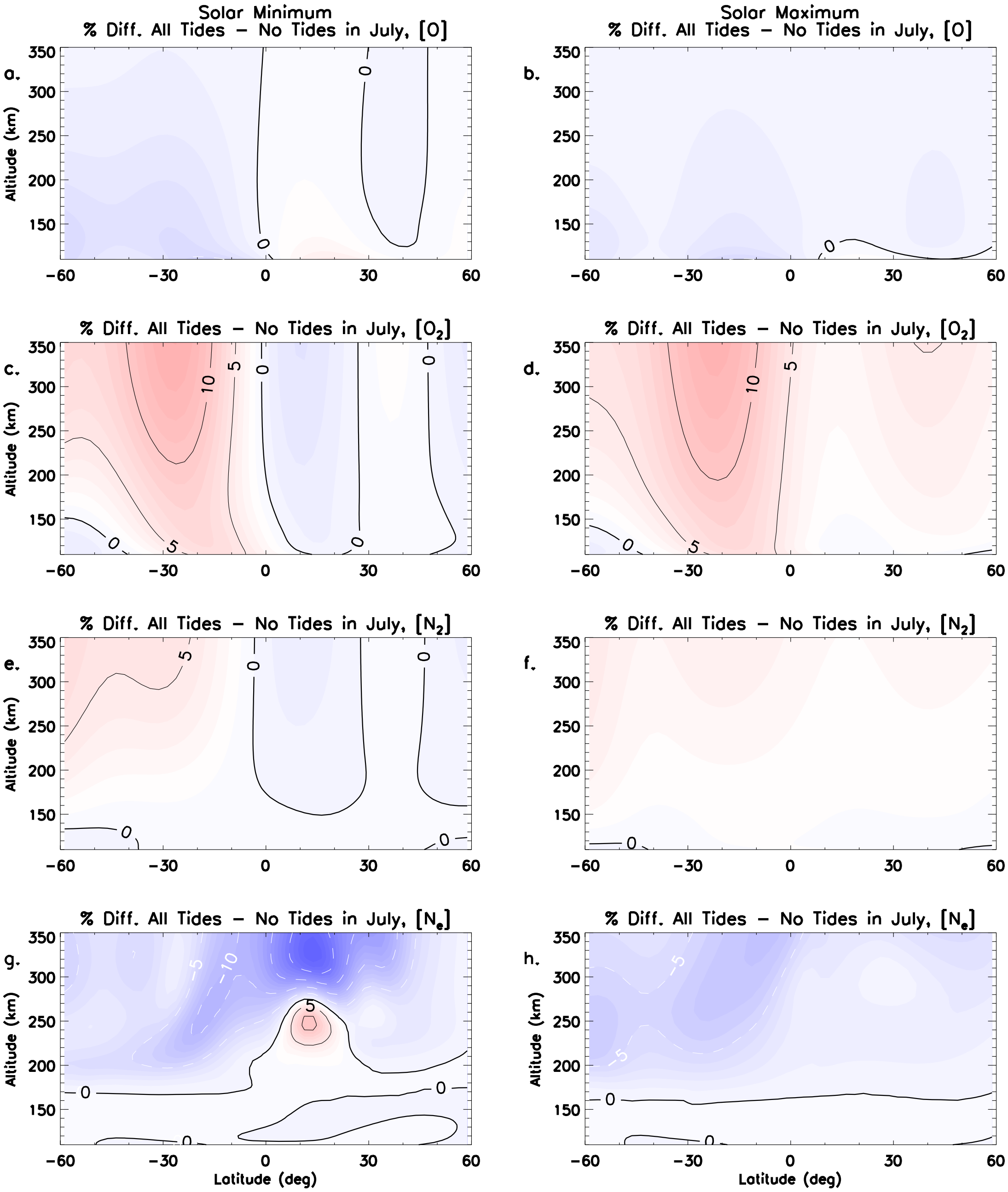

Figure E.5: Same as Figure 6.12, except during the month of July.

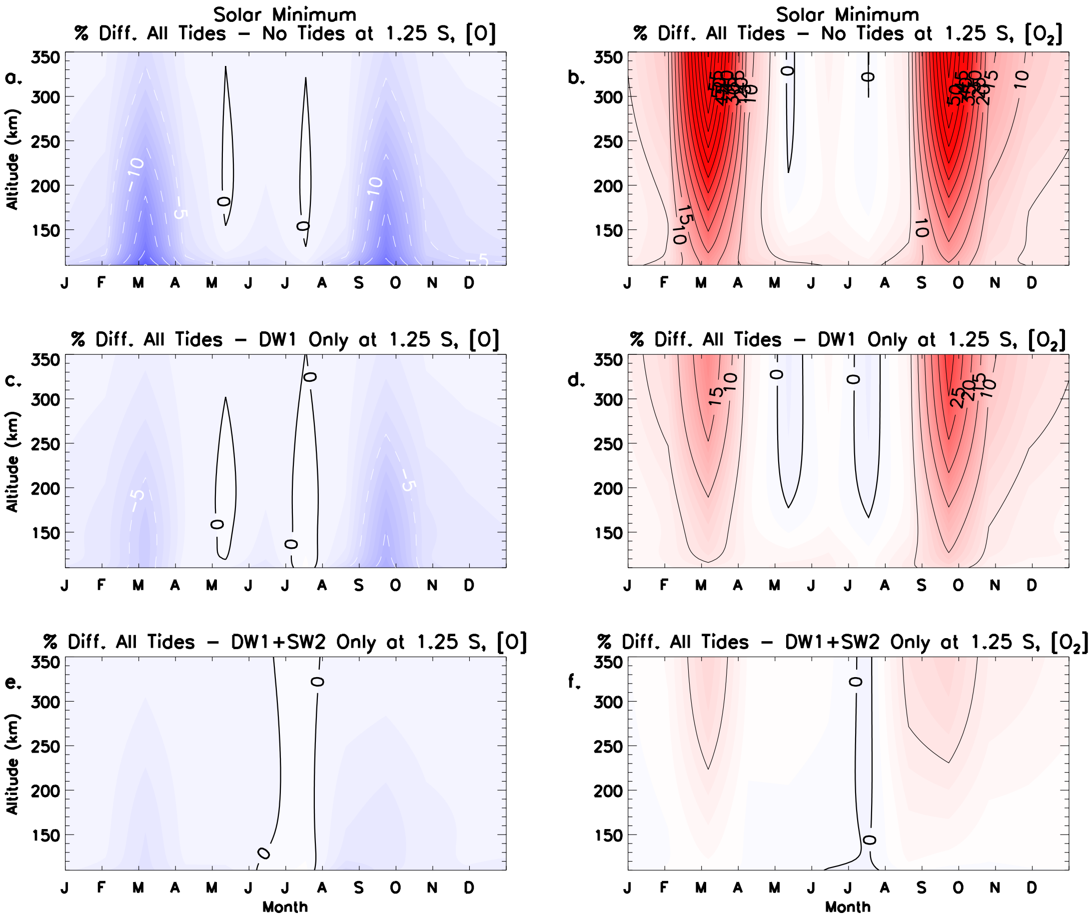

Figure E.6: Same as Figure 6.5, except under solar minimum conditions.

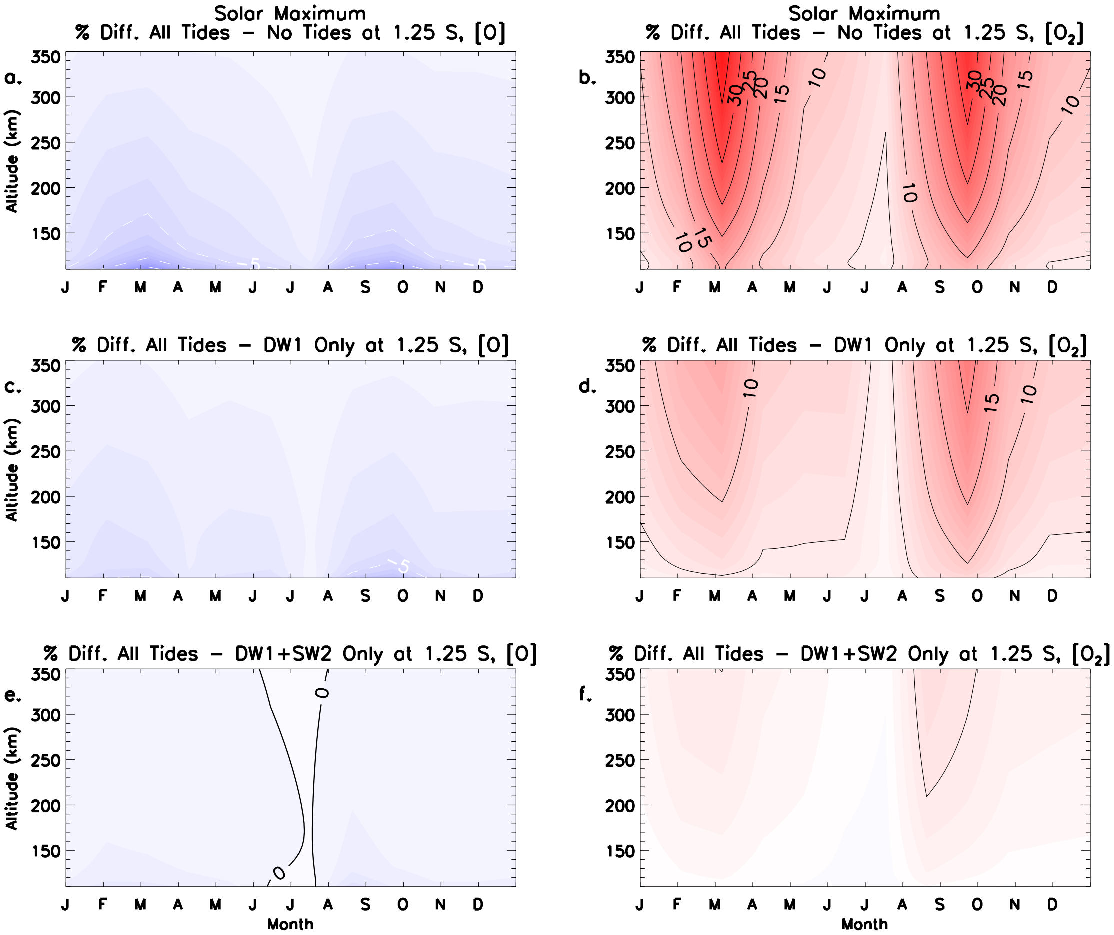

Figure E.7: Same as Figure 6.5, except under solar maximum conditions.

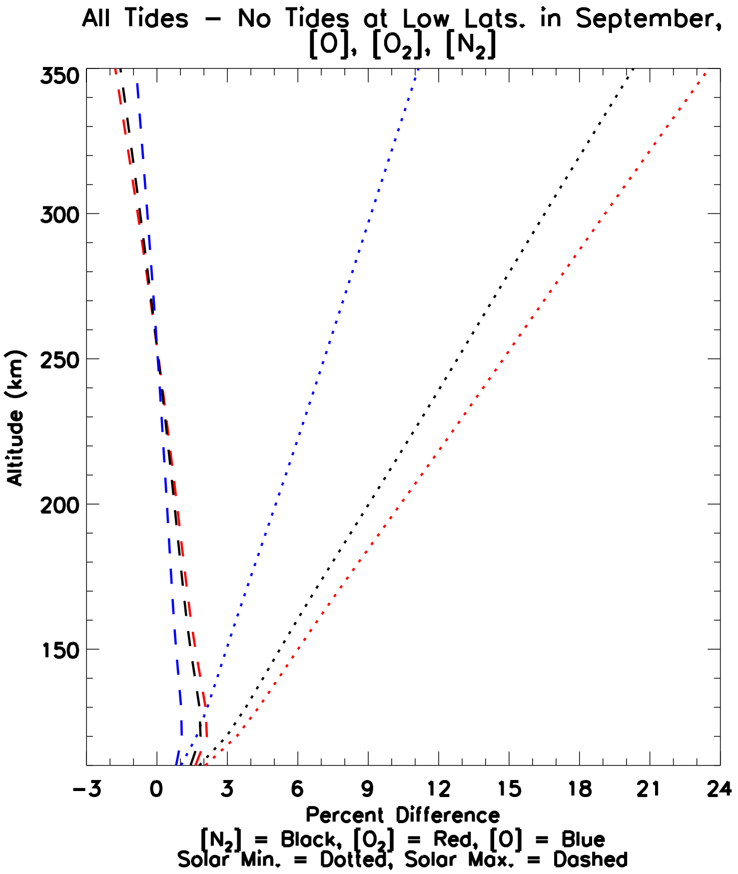

Figure E.8: Same as Figure E.4, except under solar minimum (dotted lines) and maximum (dashed lines) conditions.

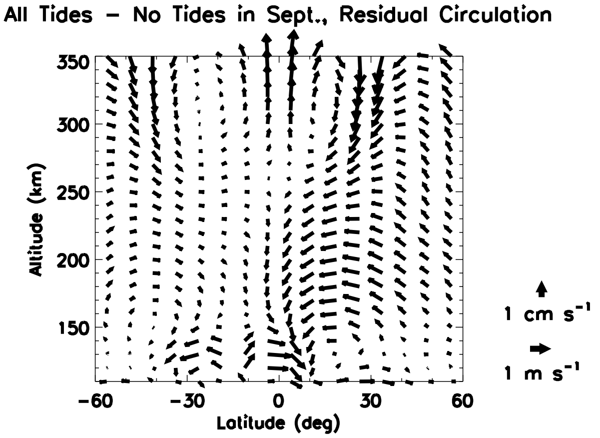

Figure E.9: The residual meridional circulation calculated from TIE-GCM simulations that include and exclude CTMT tidal lower boundary forcing as a function of latitude and altitude during September and under solar medium conditions.